ABSTRACT

FACULTY OF SCIENCE

PHYSICS

Doctor of Philosophy

THE ADSORPTION OF MONOLAYER FILMS OF URANIUM AND ZIRCONIUM ON TUNGSTEN

by Adrian John Sargood

The form and magnitude of the potential change at the surface of a metal is of paramount importance in electron and atom interactions in this region. The theoretical activity in the study of these surface potentials has increased in recent years, stimulated mainly by the plethora of data now available as well as the upsurge in the technological applications of surface phenomena. However there has been a need for a few accurate measurements of the dependence of the surface potential, that is the variation in work function, on the condition of well-defined surfaces. This thesis not only fills this gap but assesses the many phenomenological theories presently available. New lines of enquiry, both in the development of these theories and in the form of future experiments capable of unambiguous interpretation, are suggested.

The change in work function on adsorption of uranium and zirconium on single crystal and polycrystal tungsten surfaces has been exhaustively investigated, the measurement technique being, for the most part, the Zisman vibrating capacitor modification of the Kelvin method. The majority of the work concerned films of up to one atomic layer, evaporated on to (110) and (100) oriented tungsten crystals.

The use of ultra-high vacuum techniques, essential to the achievement of the extreme cleanliness required for this work, is described in some detail.

Pressures of below 1×10^{-10} torr were routinely obtained, and allowed measurements to be made on surfaces that were atomically clean. The way in which the work function was affected through contamination by residual gases has also been studied.

In the course of this work a relationship was established which enabled the work function change due to adsorption of a wide range of materials to be predicted. For each orientation of the tungsten substrate a unique number exists which, together with the adsorbate electronegativity, makes this calculation possible.

The relevant adsorption theories concerning work function changes in bimetallic adsorption systems are discussed and assessed. Despite recent activity in fundamental many-body concepts no theory is yet sufficiently developed to allow comparison with experiments. It is concluded that even the phenomenological theories reviewed in this work cannot as yet adequately predict work function/coverage data.

THE ADSORPTION OF MONOLAYER FILMS OF URANIUM AND ZIRCONIUM ON TUNGSTEN

adrian sargood

PhD thesis/University of Southampton/1969

'... everyone is convinced of the immense practical importance of the principles of Natural Philosophy at present known. We must not, however, by considerations of this kind be led to regard applications to the ordinary purposes of life as the proper object and end of science. Nothing could more effectually stop the advancement of knowledge than the prevalence of such views; even the desired practically useful discoveries would not be made if researches obnoxious to the fatal question cui bono were to be uniformly avoided ...'

'... No great law in Natural Philosophy has ever been discovered for its practical applications ...'

from introductory lecture to the course on Natural Philosophy by Professor Thomson (Baron Kelvin of Largs) at Glasgow University

CONTENTS

CONTENTS PAGE

CONTENTS PAGE

CONTENTS PAGE

CONTENTS PAGE

INTRODUCTION

In the last decade there has been considerable interest in the use of thermionic conversion in nuclear reactors[1]. In particular 'in-core' convertors in which the reactor fuel U^{235} is contained in the emitter of the conversion cell have received much attention[2]. A suitable emitter material must be capable of withstanding the long periods at high temperatures necessary in nuclear reactors. An investigation into the effect of such heat treatment on a possible emitter, sintered uranium carbide/zirconium carbide[3], was carried out several years ago in this laboratory[4,5]. The project demonstrated that material, probably uranium and zirconium, evaporated from the emitter, and that when deposited on to polycrystalline tungsten foil this material displayed unusual effects. In order to study these effects further, pure uranium and zirconium were evaporated directly on to tungsten foil. In the case of uranium it was found that the work function of very thin films, only a few monolayers in thickness, was appreciably different from the accepted value for uranium[6]. More interestingly, after heating these films to temperatures very close to those at which crystallographic phase changes occur in bulk uranium (938 K, 1043 K) the work function changed abruptly and irreversibly[7]. Although it is tempting to suggest that this effect was due to 'freezing-in' of the bulk phase structure in the thin film it is difficult to see how films of only a few monolayers thickness can exhibit such structure.

The work reported here is a continuation of the study of monolayer films of uranium and zirconium evaporated on to tungsten, and in particular the measurement of work function/coverage curves. Since the latter are dependent on the orientation of the substrate and since a comparison of

these curves with the predictions of the relevant adsorption theories requires a substrate of known surface structure, single crystal substrates are used in most of this work.

A thorough examination is also made of the effect of heating these films in order to ascertain under what conditions the abrupt work function changes occur.

In order to obtain the necessary purity of evaporated films, ultra-high vacuum techniques are used and these are described in some detail.

CHAPTER 1

1.1 work function

The observation that metals have a high electrical conductivity led to the conclusion that a large number of electrons are free to move about in the interior. The energy distribution of these free electrons is given by Fermi-Dirac statistics[8] and is characterized by the Fermi energy E_f. At the absolute zero of temperature the maximum energy of an electron is E_f where at this temperature E_f is the chemical potential, μ. At all temperatures the probability of an electron having an energy μ is one half, where for common metals μ is close to E_f[9]. Since additional energy is required to remove electrons from a metal, a potential barrier must exist at the surface. The magnitude of this electron-constraining barrier is given by the work function. Herring and Nichols[10] defined the 'true work function' of a uniform surface as the difference in energy between an electron at the Fermi level and an electron at rest in a vacuum just outside the surface. Although the Fermi energy is characteristic of all the atoms in the metal the work function is only a surface property. Thus if a negatively charged layer is placed on the surface the Fermi energy is unchanged but electrons require a greater energy to escape. Figure 1.1 shows the Sommerfeld free electron potential well diagram of a metal.

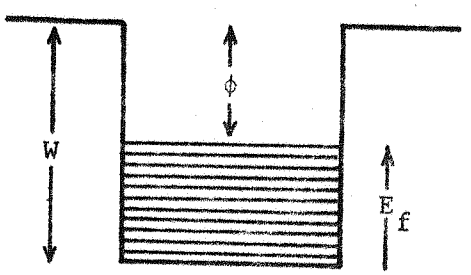

figure 1.1
Sommerfeld free electron model of a metal

The work function is given by:

$$\phi = W - E_f \qquad 1.1$$

where W is the well depth. Anderson et al[11] proposed that W consists of bulk and surface components, W_b and W_s. Then

$$\phi = (W_b - E_f) + W_s$$

Here W_b includes the classical image potential of an electron outside a perfectly conducting surface as well as the attraction of the lattice for its electrons. W_s is due to the surface dipole and equals D/ε_o where D is the dipole moment per unit area[12]. It is only this last term which changes when a charged layer is added to the surface. In the absence of such an externally applied surface charge a dipole layer still exists because of the deviation of the charge distribution of the surface atoms from the symmetrical form found in the bulk. Clearly this dipole moment is dependent on the surface structure. Smoluchowski[13] identified two components of the dipole:

a the electron distribution does not end abruptly at the surface but 'spreads' out perpendicular to it. This produces a dipole with the negative end outermost which increases the work function. The magnitude of this effect is independent of the surface orientation;

b the electron distribution 'smooths' out an atomically rough surface with negative charge accumulating between positive ion cores. The resulting dipole has its positive end outermost and lowers the work function. This smoothing effect is greater on rougher surfaces. Since high index planes have a low surface density of atoms, they are the most rough and so have the lowest work functions. Smoluchowski's calculations also showed that the low index planes are the most stable since they have the highest surface energy.

Stranski and Suhrman[14] calculated the surface energy of individual crystal faces by summing the bond energies between an atom in the surface and its nearest and next nearest neighbours. They found the free surface energy was linearly related to the experimentally determined work function of the crystal face as is shown in figure 1.2. Table 1.1 lists their free surface energy values in column 2, and in column 3 the experimental work functions determined in the author's laboratory by the Kelvin method. The surface free energy values have since been confirmed by Müller amd Drechsler[17] both experimentally and theoretically, a Mie potential (section 2.1.2.2) giving the best theoretical fit.

Recently Steiner and Gyftopoulos[18] have developed a theory for predicting the work functions of metal surfaces. The theory is discussed fully in section 1.5.2 but it is interesting to note here their interpretation of the anisotropy of work function with orientation. It is proposed that the work function is a measure of the number and strength of bonds between an atom in the surface and neighbouring atoms. Thus a high work function surface also has a high surface free energy. For body-centred-cubic metals they find, as did Stranski and Suhrman, that only the nearest and next nearest neighbours need be considered. Values of work function calculated from this theory are also shown in figure 1.2 as well as in column 5 of table 1.1.

An exact calculation of work function involves the solution of the Schrödinger equation for electrons in a lattice. Most of the attempts made to date[19-30] are restricted to the simple alkali atoms where the charge distribution can be treated at symmetric. Even here difficulties arise from the asymmetric nature of surface atoms and the lack of knowledge

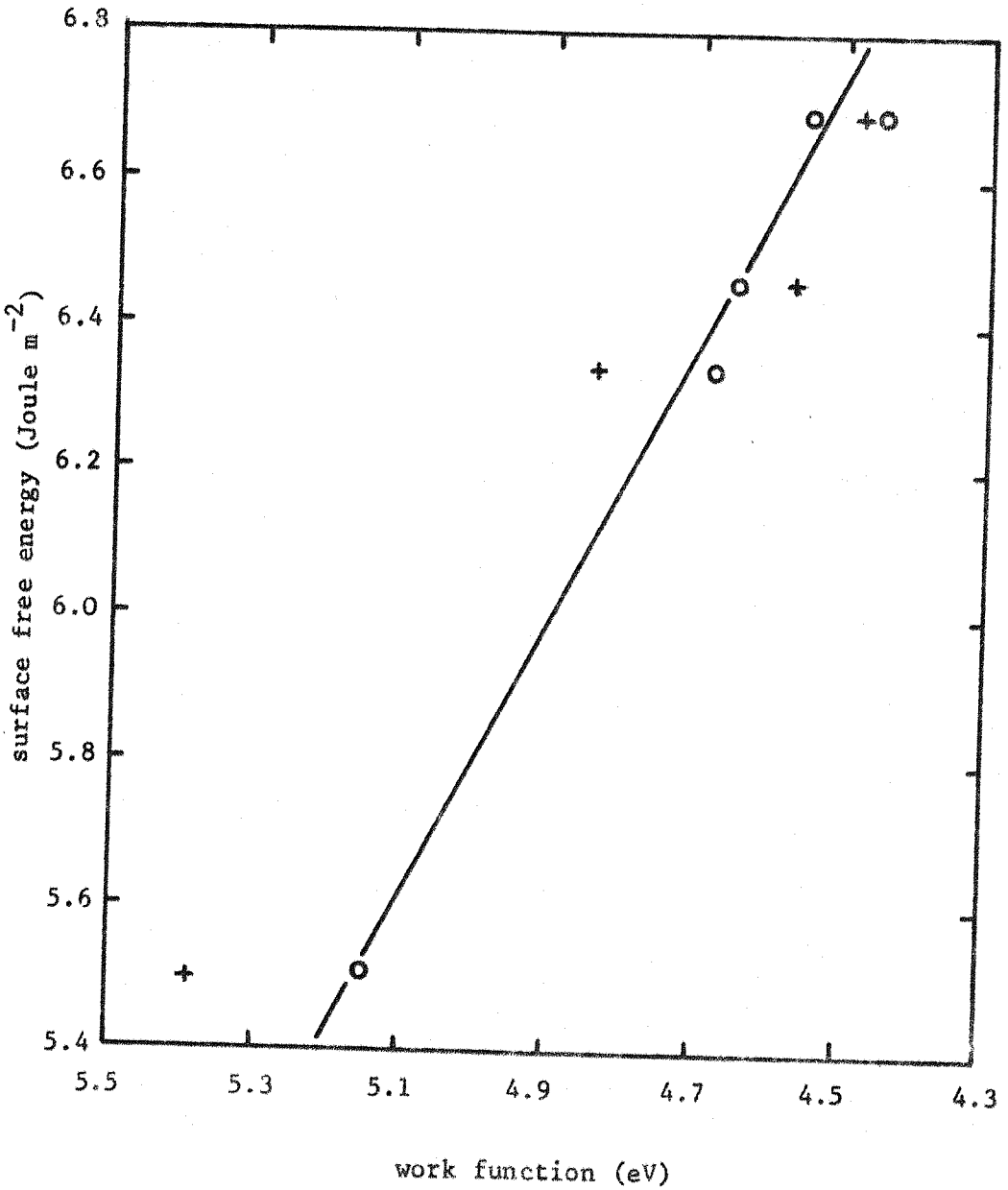

figure 1.2 work function versus surface free energy for 4 crystal planes of tungsten

o experimental work function

\+ theoretical work function

table 1.1 values used in figure 1.2

surface orientation	free energy[14] Joule m^{-2}	w.f.(exptl) eV	reference	w.f.(theor)[18] eV
110	5.51	5.15	†	5.39
211	6.34	4.68	15	4.84
100	6.43	4.65	†	4.57
111	6.69	4.45	16	4.38
611	6.69	4.55	†	4.38

† present work

of the atomic arrangement at the surface. The problem becomes very much more difficult for transition elements where the charge distribution can be strongly asymmetric. Consequently, most progress is being made using the semi-empirical concepts of chemistry (eg the nature of surface bonding, electronegativity, polarizability).

Neglecting the anomalous field emission work function of (110) tungsten (section 4.2), work functions of clean metal surfaces vary from ~ 2 eV for caesium to ~ 5.5 eV for platinum[31]. The change in work function with surface structure is however at the most 1 eV. This implies that although work function is a surface property it is strongly dependent on the nature of the bulk. This has been confirmed by many investigators. A review of the correlations between work function and bulk physical and chemical properties is given by Michaelson[32]. References 33-46 contain a more complete list of the relevant material. The most important of these from the present viewpoint, the correlation of work function and electronegativity[44], is discussed in section 1.5.1.

1.2 contact potential

When two metals at the same temperature are in electrical contact, electrons in one cannot exist at a higher energy than in the other. Consequently, at equilibrium, the Fermi levels attain equal energy. A contact potential difference will then appear between the two surfaces, given by:

$$V(c\ p\ d) = \phi_1 - \phi_2 \qquad 1.2$$

(see figure 1.3)

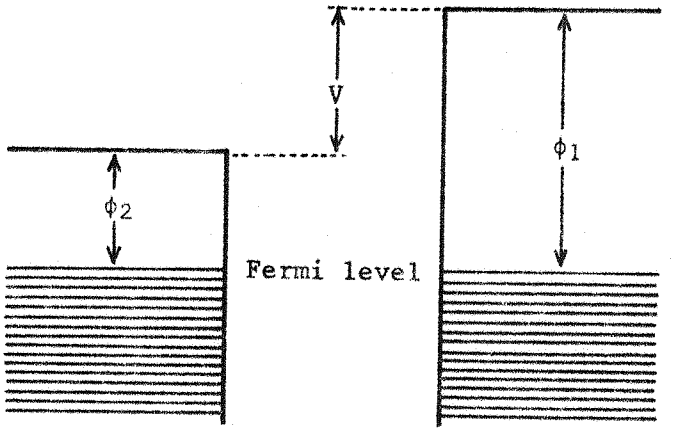

figure 1.3
c p d between two
free electron metals

1.3 electronegativity

Electronegativity is described by Pauling[47] as 'the power of an atom in a molecule to attract electrons to itself'. The electronegativity difference between two atoms forming a bond can be regarded as the degree of electron transfer between them. Elements with the lowest electronegativity are metals and are situated at the lower left of the periodic table whereas those at the upper right are non-metallic and are the most electronegative.

1.3.1 Pauling's scale

The electronegativity scale first set up by Pauling was derived from considerations of two types of bond: ionic and covalent. A pure ionic or heteropolar bond involves only the transfer of charge and the consequent coulomb interaction provides the bond energy. Covalent or homopolar bonding is due to the 'sharing' of charge and arises from the quantum mechanical exchange interaction. A typical bond is part covalent and part ionic and is described in terms of Pauling's resonance bond theory as

resonating between the two extremes. The electronegativity difference $\Delta\chi_p$ between two atoms forming a bond is related to the ionic content, i, of the bond. The ionic bond energy is greater than that of the 'normal covalent' bond by an amount δ called the extra-ionic or resonance energy†. Pauling proposed:

$$\Delta\chi_p = c\delta^{\frac{1}{2}}$$

where c is the constant of proportionality and δ was taken from single-bond energies determined by thermochemical methods. The electronegativity scale for the elements was chosen for convenience such that χ_p (hydrogen) = 2.1 and χ_p (fluorine) = 4.0. A bond with 50% ionic character (i = $\frac{1}{2}$) corresponds to $\Delta\chi_p$ = 1.7. The same method was used by Hafssinsky[49] for a further investigation into the subject. He found that for elements having more than one stable valence state the electronegativity increased with valence. The realisation that electronegativity is strictly only a constant of individual atomic orbitals and is not a single valued quantity for each element led to the modern concept of orbital electronegativity[50] (section 1.4).

† Here Pauling defined the 'normal covalent' bond energy between atoms A and B as the arithmetic mean of the individual covalent bond energies of A-A and B-B:

$$D(A\text{-}B) = \tfrac{1}{2}\{D(A\text{-}A) + D(B\text{-}B)\} \qquad 1.3$$

However in the case of the alkali metal hydrides this definition gives negative values for δ. As a result Pauling and Sherman[48] redefined the normal covalent bond energy as the geometric mean of the individual covalent bond energies:

$$D(A\text{-}B) = \{D(A\text{-}A).D(B\text{-}B)\}^{\frac{1}{2}} \qquad 1.4$$

However Pauling never recalculated his electronegativity scale using the new definition.

1.3.2 Mulliken's Scale

Mulliken[51] put the electronegativity concept on a firmer theoretical foundation and at the same time recognised the dependence on the valence state of the atom. He was able to show that the condition for equal electronegativity of two atoms, p and q, is:

$$I_p + A_p = I_q + A_q$$

where I_p and A_p are the ionization potential and electron affinity of the valent state of the atom p. He then proposed an 'absolute electronegativity':

$$\chi_a = \tfrac{1}{2} (I + A) \qquad 1.5$$

where I and A are in units of electron volts. This definition can be extended to molecular orbitals[52] since the latter can be expressed as a linear combination of atomic orbitals (L.C.A.O.). Mulliken related his absolute electronegativity (χ_a) to Pauling's value (χ_p) by:

$$\chi_a = 2.78\ \chi_p \qquad 1.6$$

Pritchard and Skinner[50], using more recent data, have re-evaluated the constant in equation 1.6 and found:

$$\chi_a = 3.15\ \chi_p \qquad 1.7$$

Coulson[53] points out that Mulliken's scale is a better measure of electronegativity than that of Pauling in view of the entirely empirical nature of the latter.

1.3.3 Malone's Scale

Since charge transfer in a bond gives it a dipole moment Malone[54] suggested

that for single covalent bonds the measured dipole moment M was proportional to $\Delta\chi$, or

$$M = \Delta\chi_p \qquad 1.8$$

where M is in Debye (1 Debye = 3.33×10^{-30} C.m). This is not a reliable measure for the following reasons:

a a pure covalent bond has zero dipole moment only when the atomic radii are equal. The overlap of orbitals of atoms of unequal size produces a homopolar dipole. This was first pointed out by Mulliken[55];

b at high values of $\Delta\chi$ self-depolarization occurs[56];

c a bonding orbital consists of a hybrid of atomic orbitals. Coulson[57] has shown that hybridization leads to asymmetrical charge distribution and hence a dipole moment. Further, hybridization of bonding orbitals affects non-bonding orbitals with the result that unshared electron pairs can produce a very large dipole moment. In practice, equation 1.8 applies well to a few cases of which the hydrogen halides are one, but fails badly in others[58].

1.3.4 Gordy's Scale

Gordy[59] attributed the electronegativity of an atom to the potential, z^*e/r, at the valence shell of radius r, due to the effective nuclear charge z^*. r is taken as the single-bond covalent radius and z^* is calculated assuming that all electrons in shells other than the valence shell exert full screening, and that the screening constant of one valence electron for another is 0.5: then

$$z^* = n - 0.5\,(n-1) = 0.5\,(n+1)$$

where n is the number of valence electrons.

Gordy then proposed:

$$\chi_a = 0.98 \left(\frac{n+1}{r}\right) + 1.57 \qquad 1.9$$

where r is in Å and where the constants are evaluated empirically. Although the expression for z* is an over simplification its use here is justified by the agreement between Pauling's electronegativities and those calculated from equation 1.9 for the majority of elements. The agreement is, however, poor for some of the transition metals; for example copper, silver and gold. This is to be expected since the use of Gordy's z* is least justified in these cases[44]. According to Gordy and Thomas[44] Gordy's electronegativities for tungsten, zirconium and uranium agree well with Pauling's values.

Slater[60] gives a more realistic evaluation of z* but its use does not lead to a single universal expression for electronegativity[50].

1.4 orbital electronegativity

Hinze, Whitehead, Jaffe[61] define orbital electronegativity by analogy with Pauling's original definition: 'Orbital electronegativity is a measure of the power of an atom as it exists in a molecule to attract an electron in a given orbital to itself'. It is therefore the derivative of the energy of the atom with respect to the charge q in the orbital; or

$$(\chi_a)_j = \frac{dE}{dq_j} \qquad 1.10$$

where q_j is the fractional charge in the jth orbital. This equation implies that the energy E is a continuous function of charge within the limits $0 \leq j \leq 2$ laid down by the Pauli exclusion principle. Assuming a second order approximation for E:

$$E(q) = a + bq + cq^2 \qquad 1.11$$

E is chosen to be zero for the neutral state of the orbital (q = 0). In the ionized state (q = e) and the doubly occupied state (q = -e) the energy E is eI and -eA respectively, where I is the ionization potential and A is the electron affinity. With these boundary conditions equation 1.11 becomes:

$$E(q) = \tfrac{1}{2}(I + A)\, q + \tfrac{1}{2}e(I - A)\, q^2$$

and

$$\chi_a(q) = \frac{dE(q)}{dq} = \frac{I+A}{2} + \frac{I-A}{e}\, q \qquad 1.12$$

On formation of a bond, charge transfer takes place until the orbital electronegativity of both atoms is equal. Sanderson[62] has named this effect the principle of electronegativity equalization. The definition of electronegativity as a function of the charge in the orbital is more general than earlier definitions and in the special case of the neutral atom reduces to Mulliken's value (equation 1.5): that is, neutral electronegativity

$$\chi_a(0) = \tfrac{1}{2}(I+A) \qquad 1.13$$

1.5 electronegativity and the work function of metals

1.5.1 the Gordy-Thomas relationship

From Michaelson's[32] values of work function ϕ, Gordy and Thomas[44] found the approximate relation:

$$\phi = 2.27\, \chi_p + 0.34 \qquad 1.14$$

or in terms of Mulliken's absolute electronegativity:

$$\phi = 0.817\, \chi_a + 0.34 \qquad 1.15$$

The relationship between recent values of ϕ and Gordy-Thomas values of χ is shown in figure 1.4 where all metals whose work function has been

measured are included. The data used in this figure is presented in table 1.2. The work function values are taken from Rivière[31], Michaelson[32] or Fomenko[63] (in that order of preference) except in the cases of uranium and zirconium where the present† values are used and in the case of ytrium where a recent value[64] is available.

Gyftopoulos and Levine[65] make use of this relationship in calculating the work function of metals coated by metallic films. They propose a simple physical interpretation of equation 1.15: the electronegativity is the energy required to remove an electron from an atom but in the case of a metal surface it is modified in two ways:

a electrons are shared by more than one lattice site and so are less strongly bound to the lattice atoms. Only 80% of the electronegativity energy is required to remove them from the lattice;

b the electron produces an image potential at a conducting surface. The energy required to overcome this is the same for all surfaces and equals 0.34 eV.

Clearly equation 1.15 cannot take account of the anisotropy of work function with orientation, and deviations from this relation may well be due to this effect. The observation that less than the electronegativity energy is required to remove an electron from the surface atom is interpreted by Steiner and Gyftopoulos[18] as a lowering of the bulk electronegativity at the surface. This reduction is attributed to the fact that there are fewer bonds to a surface atom than to one in the bulk. They propose that the work function of a clean metal surface equals the neutral electronegativity of the surface atom (see below). The concept of the double layer is implicit in this definition of work function.

† films evaporated on to polycrystalline tungsten

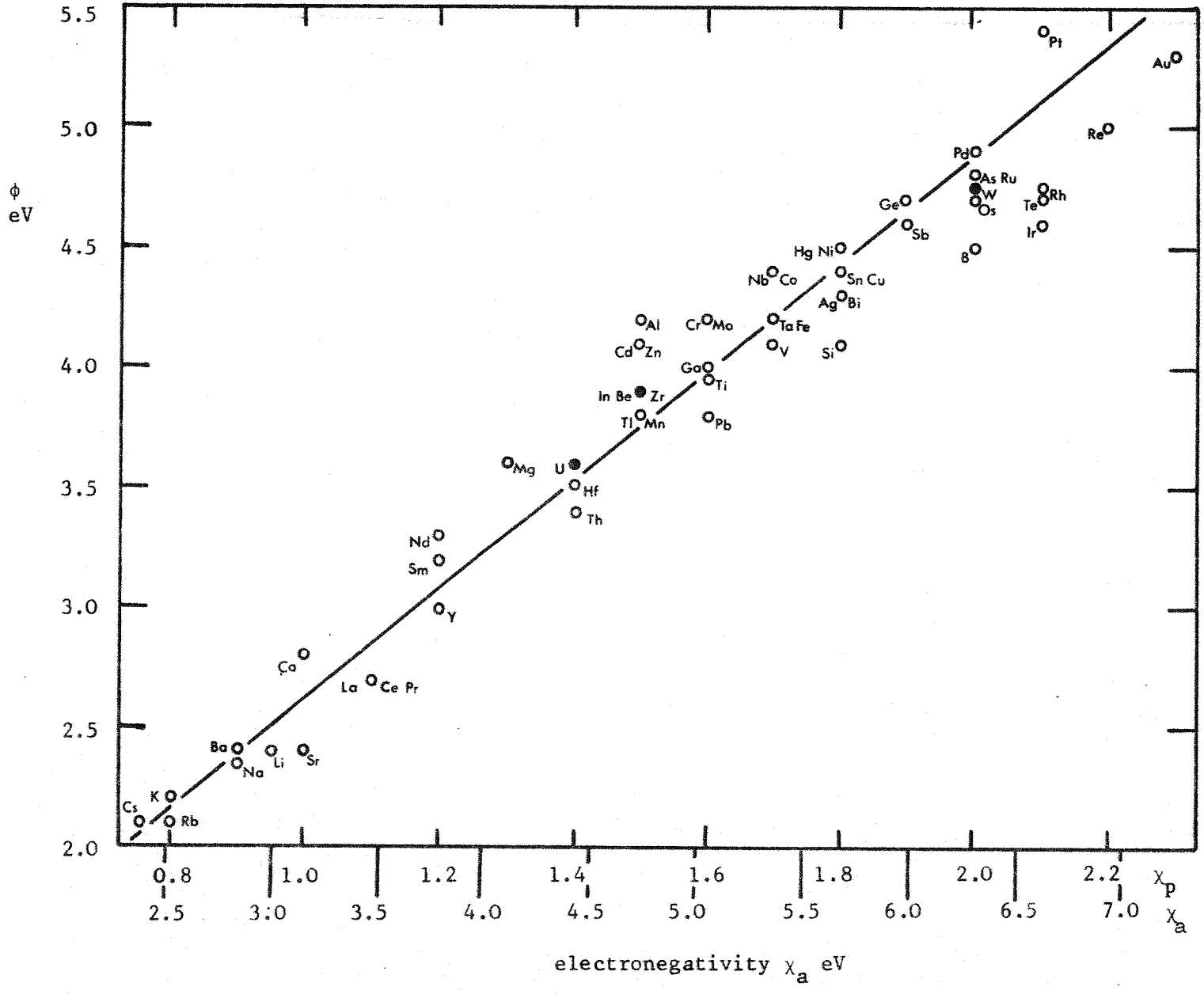

figure 1.4
Gordy-Thomas
relationship.

$\phi = 2.27\chi_p + 0.34$
(equation 1.14)

$\chi_a = 3.15\chi_p$
(Pritchard and
Skinner[50])

table 1.2

electronegativity and work function of the elements used in figure 1.4

series	atomic no.	element	ϕ (eV)	ref.	χ_p	χ_a	ref.
	3	Li	2.4	63	0.95	2.99	44
2	4	Be	3.9	31	1.5	4.73	44
	5	B	4.5	32	2.0	6.30	44
	11	Na	2.35	63	0.9	2.84	44
	12	Mg	3.6	31	1.3	4.10	50
3	13	Al	4.2	31	1.5	4.73	44
	14	Si	4.1	32	1.8	5.67	44
	19	K	2.2	31	0.8	2.52	44
	20	Ca	2.8	32	1.0	3.15	44
	22	Ti	3.95	63	1.6	5.04	44
	23	V	4.1	32	1.7	5.36	44
	24	Cr	4.2	31	1.6	5.04	44
	25	Mn	3.8	31	1.5	4.73	44
4	26	Fe	4.2	31	1.7	5.36	44
	27	Co	4.4	63	1.7	5.36	44
	28	Ni	4.5	63	1.8	5.67	44
	29	Cu	4.4	63	1.8	5.67	44
	30	Zn	4.1	31	1.5	4.73	44
	31	Ga	4.0	31	1.6	5.04	50
	32	Ge	4.7	31	1.9	5.99	50
	33	As	4.8	31	2.0	6.30	44
	37	Rb	2.1	32	0.8	2.52	44
	38	Sr	2.4	32	1.0	3.15	44
	39	Y	3.0	64	1.2	3.78	44
	40	Zr	3.9	†	1.5	4.73	44
	41	Nb	4.4	31	1.7	5.36	44
	42	Mo	4.2	31	1.6	5.04	44
	44	Ru	4.8	31	2.0	6.30	44
5	45	Rh	4.75	63	2.1	6.62	44

table 1.2 (continued)

series	atomic no.	element	ϕ (eV)	ref.	χ_p	χ_a	ref.
	46	Pd	4.9	31	2.0	6.30	44
	47	Ag	4.3	31	1.8	5.67	44
	48	Cd	4.1	63	1.5	4.73	44
	49	In	3.9	31	1.5	4.73	44
	50	Sn	4.4	31	1.8	5.67	44
	51	Sb	4.6	31	1.9	5.99	50
	52	Te	4.7	32	2.1	6.62	44
	55	Cs	2.1	31	0.75	2.36	44
	56	Ba	2.4	31	0.9	2.84	44
	57	La	2.7	31††	1.1	3.47	44
	58	Ce	2.7	32	1.1	3.47	44
	59	Pr	2.7	32	1.1	3.47	44
	60	Nd	3.3	32	1.2	3.78	44
	62	Sm	3.2	32	1.2	3.78	44
	72	Hf	3.5	63	1.4	4.41	44
	73	Ta	4.22	31	1.7	5.36	44
	74	W	4.55	31	2.0	6.30	44
	75	Re	5.0	63	2.2	6.93	44
6	76	Os	4.7	63	2.0	6.30	44
	77	Ir	4.6	31	2.1	6.62	44
	78	Pt	5.4	31	2.1	6.62	44
	79	Au	5.3	31	2.3	7.25	44
	80	Hg	4.5	32	1.8	5.67	44
	81	Tl	3.8	32	1.5	4.73	44
	82	Pb	3.8	31	1.6	5.04	44
	83	Bi	4.3	31	1.8	5.67	44
7	90	Th	3.4	31	1.4	4.41	44
	92	U	3.6	†	1.4	4.41	44

† present work - films evaporated on to polycrystalline tungsten

†† value taken as that for lanthanum hexofluoride - ie assuming that the emitting surface of LaF_6 cathodes is lanthanum

1.5.2 the Steiner and Gyftopoulos theory of work function

Previous calculations of work function[19-30] are based on the premise that the work function is the energy required to remove an electron from the sea of valence electrons in the metal. Steiner and Gyftopoulos[18] propose that the electron is removed from a valence orbital of a surface atom. The important parameter, the energy state of this atom, differs from that of the bulk atom since there are fewer neighbouring atoms with which it can bond. Thus the work function calculation is reduced to that of computing the change in energy of a surface atom caused by the removal of a valence electron. One important condition must be satisfied: the energy state of the surface atom is not altered by the removal of an electron. For an isolated atom this cannot happen since the atom alters its energy from the ground state to the ionized state; the implication is that for atoms in a metal the removal of a valence electron is counterbalanced by the collective interactions of other atoms.

The change in energy dE caused by the removal of charge dq is the orbital electronegativity (equation 1.10):

$$\frac{dE}{dq} = \chi_a$$

In the present case the charge on the atom remains constant (neutral) and the work function is given by the neutral orbital electronegativity[66] (equation 1.9):

$$\phi = \frac{dE(0)}{dq} = \chi_a(0)$$

From equation 1.13:

$$\phi = \tfrac{1}{2}(I_s + A_s) \qquad 1.16$$

where I_s and A_s are the ionization potential and the electron affinity of the valence state of the surface atom. Clearly these values will not equal those for an isolated atom nor those in the bulk. Since I_s and A_s are not known Steiner and Gyftopoulos suggest the extension of Gordy's electronegativity (equation 1.9) to surface atoms. Specifically they propose:

$$\phi = 0.98 \frac{v_s + 1}{r_m} + 1.57 \quad \text{eV} \qquad 1.17$$

where v_s is the number of electrons per surface atom which participate in bonding and r_m is the effective radii of these atoms in Å. The problem now reduces to that of calculating v_s, the 'surface valence'.

In the bulk the metallic valence, v_m, is divided between the neighbouring atoms. The strength of each bond depends on the interatomic distance and is given by the fractional bond number, n, which is defined[67] such that 2n equals the average number of bonding electrons shared by two interacting atoms at an interatomic separation R. Pauling[68] found the empirical relation:

$$R_b - R_a = 0.60 \log_{10}(n_a/n_b) \qquad 1.18$$

where a and b refer to atoms a and b. Considering only nearest and next nearest neighbours, for which the fractional bond numbers are n_a and n_b, v_m is given by:

$$v_m = P_a n_a + P_b n_b \qquad 1.19$$

where P_a and P_b are the numbers of nearest and next nearest neighbours. In the body centred cubic (b c c) structure $P_a = 8$ and $P_b = 6$, so that equation 1.19 becomes:

$$v_m = 8n_a + 6n_b \qquad 1.20$$

Since v_m for metals is known n_a and n_b can be calculated from equations 1.18 and 1.20. In the particular case of tungsten (b c c):

$$n_a = 0.65$$

$$n_b = 0.13 \qquad 1.21$$

Again considering only nearest and next nearest neighbours, of which there are N_a and N_b respectively, v_s is given by:

$$v_s = N_a n_a + N_b n_b \qquad 1.22$$

N_a and N_b can be found directly for each surface from consideration of the crystal structure. Putting v_s and (known) r_m into equation 1.17 gives the work function. It can easily be shown that for body centred cubic metals the effect of the 3rd nearest neighbours is negligible.

A discussion of the values obtained from this theory is given in section 8.1.

CHAPTER 2 ADSORPTION

2.1 types of binding forces

Usually surface binding forces are divided into two categories, physical and chemical. In the latter, charge is exchanged or shared on the formation of a bond between two atoms whereas physical bonding involves no charge transfer but only the polarization of one atom by the other. In principle this distinction is unambiguous, but from observation of atoms adsorbed on metal surfaces the division is not an easy one. As far as dipole moments are concerned polarization looks identical to charge transfer. Indeed, polarization is the same as charge transfer in the sense that the electron distribution in the diatomic system is altered. Since the work function change on adsorption is directly related to the dipole moment, work function measurements alone cannot distinguish chemisorption from physisorption. There are, however, differences and these will be discussed in section 2.1.3.

It is often held that physisorption is characterized by low adsorption energies and chemisorption by high. The forces involved in physisorption are those which cause liquefaction and so the binding energies are of the same order as the heats of liquefaction. These are, at the maximum, 1 eV. Certainly chemisorption energies can be very much higher but they can also be negative (endothermic reactions[69]) and can have any intermediate value.

2.1.1 physical adsorption

An atom which has no permanent (time-averaged) dipole possesses continually

changing transient dipoles. In effect, the charge distribution at any instant is not symmetrical. Such a dipole induces a similar dipole in a neighbouring atom, the interaction of the two leading to an attractive force. These transient phenomena have been discussed by London[70] in connection with their effect on optical dispersion. For this reason they are sometimes known as dispersion forces. London showed that the potential between two atoms (1 and 2) due to dipole-dipole interactions obeys an inverse sixth power law of distance of separation r:

$$E = -\frac{C}{r^6} \quad \text{where} \quad C \simeq \frac{3\alpha_1\alpha_2}{2} \cdot \frac{I_1 I_2}{I_1+I_2}$$

and α = polarizability, I = ionization potential.

Forces produced by quadrupole interactions are smaller and are usually neglected.

Where atoms are physisorbed on a metal surface the dipole layer at the surface induces a permanent dipole in the adatom. The mechanism is the same as with dispersion forces except that the dipole is permanent. An inverse 6th power law is similarly obeyed. At smaller separations the repulsive force between electron distributions becomes dominant, the force increasing rapidly as the separation is reduced. Lennard-Jones[71] calculated the potential, regarding the metal as completely polarizable and the interaction as a classical image problem. From this highly simplified model he derived:

$$E = 4E_o \{ -(\frac{\sigma}{r})^6 + (\frac{\sigma}{r})^{12} \} \qquad 2.1$$

where E_o is the depth of the energy well and σ is the value of separation r at zero energy. A typical Lennard-Jones potential is shown in figure 2.1. Equation 2.1 is most useful at long ranges ($r > \sigma$) since for E>0 it gives too high a repulsive potential[72].

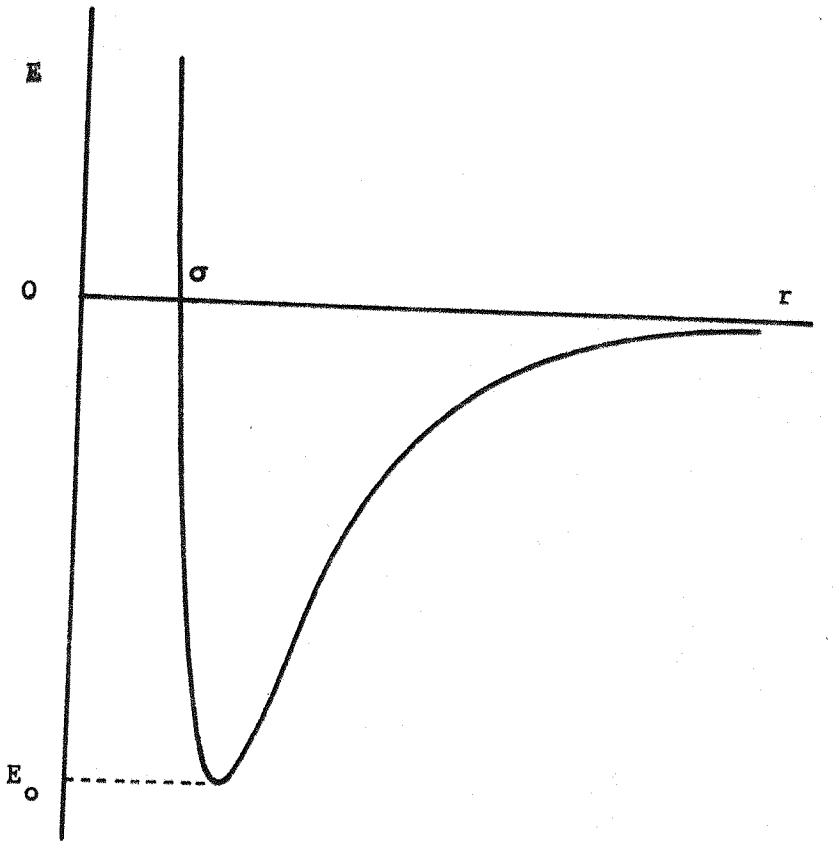

figure 2.1 Lennard-Jones potential

2.1.2 chemisorption

Chemical bonding between two atoms is usually separated into two categories: ionic and covalent bonding. A further category, metallic bonding, will also be discussed.

2.1.2.1 ionic bond (heteropolar binding forces)

In a single ionic bond an electron is transferred from the influence of one

atom to that of the other, producing negatively and positively charged ions. The coulomb interaction between these ions provides the bond energy. Thus the wave functions for the two atoms (Ψ_a and Ψ_b) are independent, there being no overlap.

The potential energy of an atom which adsorbs on to a metal surface forming an ionic bond is shown in figure 2.2 and figure 2.3 for the cases of caesium on tungsten and sodium on tungsten. The separation of the atom from the surface is given by r.

Figure 2.2 shows that at zero Kelvin the caesium ion is always energetically more favourable than the atom so that an atom is ionized as it comes up to the surface. The energy required to remove the electron (ionization potential I = 3.89 eV) is less than the energy recovered as the electron is transferred into the metal (electron work function ϕ = 4.55 eV). The surface ionization potential I_s is the energy required to ionize the atom when it is at its equilibrium position and in this case is -0.55 eV. Figure 2.3 shows that sodium is ionized when it reaches $\sim 5\text{Å}$ and conversely as the ion desorbs it transfers to an atom at the same point. Clearly, an atom which is not ionized on the surface must have a lower energy in the atomic state than in the ionic state when at equilibrium.

2.1.2.2 covalent bond (homopolar binding forces)

Covalent bonding involves the sharing of charge between the two atoms. In a single covalent bond each atom donates an electron, the two being shared equally by both atoms. If both atoms are identical the resulting covalent

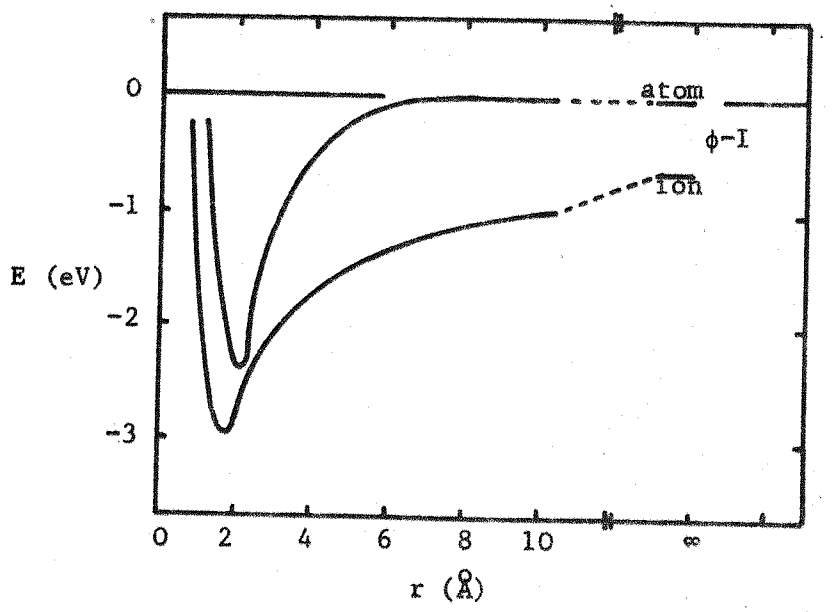

figure 2.2

potential for adsorption of caesium on tungsten

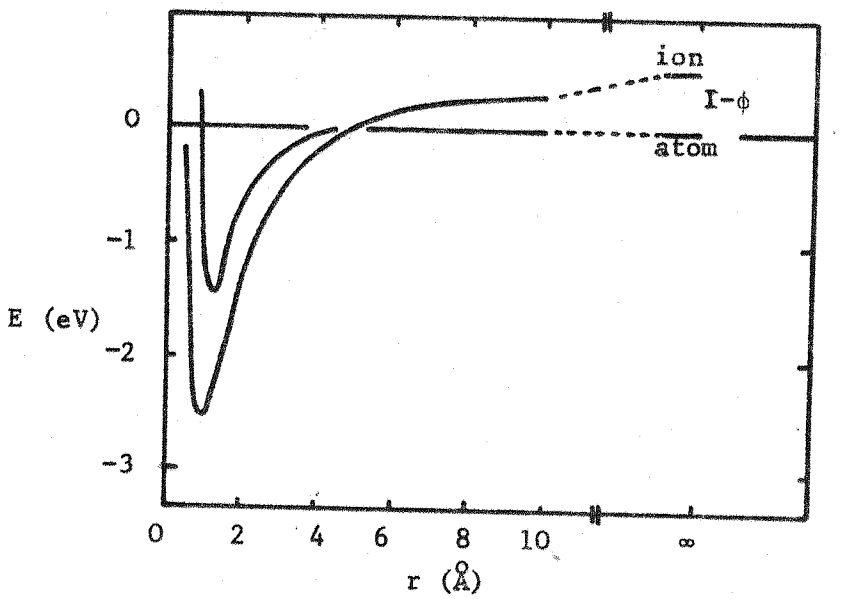

figure 2.3

potential for adsorption of sodium on tungsten

bond produces no net charge transfer and hence no dipole moment. The hydrogen molecule is the simplest example of such a bond. The two electrons come under the influence of both atoms so that the wave functions are not independent but overlap. The interaction due to this overlap is termed the exchange interaction which is attractive when the electrons are of opposite spin and repulsive when the spin is the same[73]. Although the exchange force is quantum mechanical in derivation and has no classical analogue, the associated energy is a direct product of the coulomb interaction between electrons, the spin dependence being a result of the Pauli exclusion principle.

The potential energy for a diatomic molecule is given by Morse[74] as:

$$E = E_o \left[\exp\{-2a(r-r_o)\} - 2\exp\{-a(r-r_o)\}\right] \qquad 2.2$$

where the minimum energy $-E_o$ occurs at a separation of $r = r_o$ and where a is a constant of the atom. Morse derived this equation as an approximate solution to the Schrödinger wave equation using the Heitler-London[73] model for a diatomic molecule. The equation predicts reasonable values of potential and produces the required boundary conditions $E \to 0$ as $r \to \infty$. However, it does not produce $E = \infty$ at $r = 0$ but this is of little consequence since the region $r << r_o$ is not of interest.

According to field-ion measurements of surface free energy by Drechsler and Nichols[75] the Morse function does not describe the potential for metals as well as a generalised Lennard-Jones (Mie[76]) potential of the form:

$$E = \frac{E_o}{m-n}\left[n\left(\frac{r_o}{r}\right)^m - m\left(\frac{r_o}{r}\right)^n\right] \qquad 2.3$$

Equation 2.3 reduces to the 6-12 potential of equation 2.1 when $n = 12$, $m = 6$ and where $r_o = 2^{1/6}\sigma$.

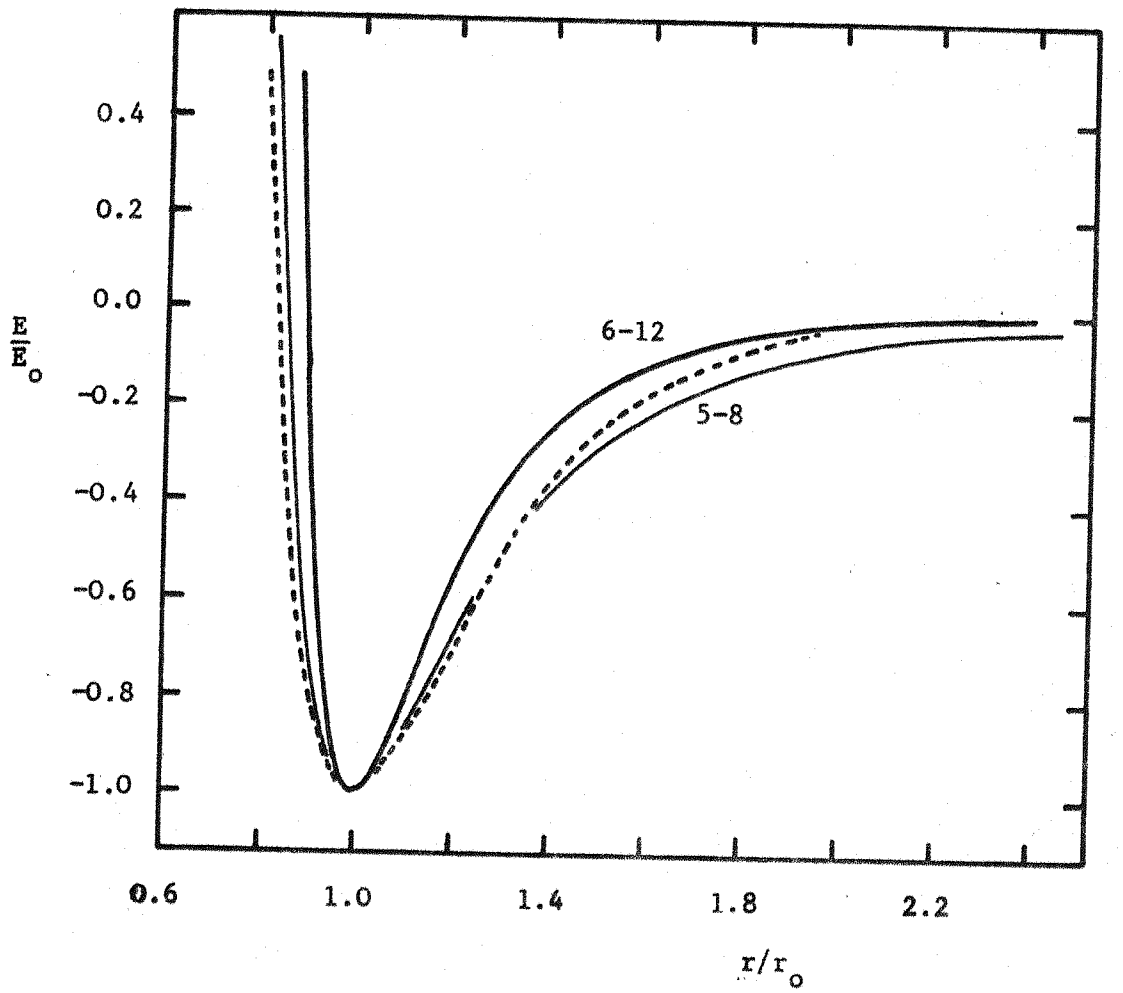

figure 2.4

Morse potential (equation 2.2) for $a/r_o = 4$ and Mie 6-12 and 5-8 potentials (equation 2.3)

Morse: dashed line Mie: full lines

Figure 2.4 shows the Lennard-Jones 6-12 and 5-8 potentials as well as the Morse potential for tungsten ($^a/r_o = 4$).

The two cases, ionic and covalent, described above are ideal, there being no sharp dividing line between them. Both arise from coulomb interactions. It

is of interest at this stage to discuss the generalized bond (part ionic, part covalent) in terms of molecular orbital theory. According to this theory a molecular orbital wave function of a diatomic molecule is a linear combination of the normalized atomic orbitals of each atom, Ψ_A and Ψ_B (L C A O):

$$\Psi_{AB} = C_A\Psi_A + C_B\Psi_B$$

then:

$$\Psi_{AB}^*\Psi_{AB} = C_A^2\Psi_A^*\Psi_A + C_AC_B\Psi_A^*\Psi_B + C_AC_B\Psi_B^*\Psi_A + C_B^2\Psi_B^*\Psi_B$$

Integrating over all space τ:

$$\int\Psi_{AB}^*\Psi_{AB}d\tau = C_A^2\int\Psi_A^*\Psi_Ad\tau + C_AC_B\int\Psi_A^*\Psi_Bd\tau + C_AC_B\int\Psi_B^*\Psi_Ad\tau + C_B^2\Psi_B^*\Psi_Bd\tau$$

Since the wave functions are normalized

$$\int\Psi_{AB}^*\Psi_{AB}d\tau = \int\Psi_A^*\Psi_Ad\tau = \int\Psi_B^*\Psi_Bd\tau = 1$$

and so

$$C_A^2 + 2C_AC_BS_{AB} + C_B^2 = 1 \qquad 2.4$$

where S_{AB} is the overlap integral. This term is negative or positive according to whether the electron spins are parallel or antiparallel.

C_A^2 and C_B^2 are then the electron populations of the orbitals of each atom so that the charge transfer F (and hence the coulomb energy) is given by:

$$F = C_A^2 - C_B^2 \qquad 2.5$$

This represents the ionic part of the bond. The overlap population $2C_AC_BS_{AB}$ determines the covalent bond energy[77]. As an approximation to this energy the Coulson[78] bond order P is often used[79], where:

$$P = 2C_AC_B \qquad 2.6$$

and where C_A and C_B are calculated from equation 2.4 assuming the overlap integral is zero.

In terms of the charge transfer F (equation 2.5) P is then

$$P_{S=0} = (1-F^2)^{\frac{1}{2}} \qquad 2.7$$

Thus for a pure covalent bond (F=0) P=1 and for a pure ionic bond (F=1) P=0. However a direct result of the neglect of the overlap integral is that the covalent bond energy is too large, especially for strongly ionic bonds. For instance, when F=0.98, P=0.2. If the opposite extreme of complete overlap (S_{AB}=1) is used to calculate C_A and C_B equation 2.4 becomes:

$$C_A^2 + 2C_AC_B + C_B^2 = 1 \qquad 2.8$$

and in terms of F, P is given by $P = \frac{1}{2}(1-F^2)$. Since the Coulson expression for a pure covalent bond gives P = 1, $P_{S=1}$ is defined:

$$P_{S=1} = (1-F^2) \qquad 2.9$$

With this definition F = 0.98 produces P = 0.04

Calculation of P explicitly in terms of F is not possible for values of S other than 0 or 1.

2.1.2.3 the metallic bond

Metals possess the requirement for covalent bonding to one another: they have vacancies and unpaired valence electrons which could be shared. However, the number of vacancies exceeds the number of unpaired electrons. For example sodium has one valence electron and seven vacancies. With this configuration one might expect that the single electrons are shared between two atoms forming a diatomic molecule, but in the metallic state the sodium atoms become very close packed with 8 atoms in contact. This close packing, together with the apparent lack of electrons to form covalent bonds between all the atoms in contact, characterizes the metallic state. The other

important characteristic is the high mobility of these electrons which do not become localized between any pair of atoms but act as if jointly held by the cations of the metal.

2.1.2.4 covalent bonding involving transition elements

The covalent bond between an adsorbed atom and a metal surface is made through the sharing of valence electrons from the adatom and from the atoms of the metal. In the case of transition elements these electrons are in the d band. Covalent bonds formed with d electrons are known to be particularly strong[80]. As the d character of a metal substrate increases more d electrons are used in the mutual cohesion of the metal atoms leaving fewer available for the formation of other bonds[81]. Consequently, increasing substrate d character produces a lowering in the adsorption bond energy. Conversely, increasing d character in the adsorbate produces an increase in the bond energy as is elegantly demonstrated in the study by Plummer and Rhodin[82].

2.1.2.5 exchange and correlation interactions

For electrons of the same spin the exchange force is repulsive. In effect, electrons of the same spin tend to stay apart from one another. The Hartree[83] method of calculating the energy of electrons in a lattice assumes that each electron moves in an average potential due to all the other electrons. This is known as the self-consistent field method. The Hartree-Fock[84] method takes into account electron spin and produces a different value from the Hartree method. The difference is said to be due

to exchange. Wigner and Seitz[19] calculated the electron energy for sodium including the exchange interaction but found that the energy was not low enough to agree with experiment. A mechanism was required to keep electrons apart, so reducing the coulomb interaction and lowering the total energy. An interaction which was repulsive for electrons of unlike spin was found to be adequate and was termed the correlation interaction. Thus the effect of correlation is to keep electrons apart. It should be realised that exchange and correlation are the result of mathematical approximations in calculating the electron energy. If the energy could be calculated exactly it would not be possible to distinguish between the parts due to exchange and those due to correlation.

2.1.3 work function change on adsorption - physisorption and chemisorption

The work function change which occurs when atoms are physisorbed on a metal surface is a result of the polarization of the adsorbed atom by the field at the surface. Thus the magnitude of the change is dependent on the polarizability of the adatom (which is related to its volume[85]) and on the surface field. The latter, according to the Smolochowski smoothing concept, has its positive pole outermost and is greatest for the orientations of lowest work function. Since the adatom will be polarized in the same direction as the surface dipole the work function is lowered, the decrease being greatest for large adatoms on low work function orientations. However this effect may be negated when the substrate surface structure is so porous that the adatoms no longer protrude from the surface but contribute to the smoothing effect.

The work function change associated with chemisorption is a result of the dipole moment due to charge transfer between the adatom and the substrate and may be treated to a first approximation by utilizing the concept of electronegativity. Thus the electronegativity difference $\Delta\chi$ between the adsorbate and the substrate atoms determines the direction and magnitude of the charge transfer. Examples are caesium on tungsten[86] where $\Delta\chi$ is large and negative and the work function is lowered, and oxygen on tungsten[87] where the sign is reversed.

However, the real situation is more complex since on the above basis the effective electronegativities of metal surfaces appear to be considerably greater than the quoted (isolated atom) values (appendix 2). The magnitude of the work function change is proportional to the density and strength of the dipole. The latter is simply the product of charge transfer and dipole length. The density, however, is determined by two factors: the size of the adsorbate particles and the substrate geometry. Clearly, if the adsorbate size is not the limiting factor, the adsorbate density increases with substrate density (section 2.3). On this simple basis the work function change is greatest on high work function orientations (which have the highest surface density) in contrast with the case of physisorption. This discussion has been greatly over-simplified since charge transfer is not dependent on $\Delta\chi$ alone (section 1.3.3), and since the effects of depolarization (section 2.2.1), penetration and reconstruction (appendix 2) have been neglected.

2.1.4 chemisorption and band theory

Gurney[88] first pointed out that the interaction of an atom with a metal

surface causes the valence level of the atom to become broadened, and he was thus able to explain how charge transfer occurred in bonds which were not considered as ionic. Gomer and Swanson[89], on a semi-empirical basis, classified types of bond by means of the position of the broadened and shifted valence level relative to the Fermi level in the metal. An electron at the shifted energy level resonates between the atom and the metal states. Because of the uncertainty principle the finite lifetime of the electron in this 'resonance' state results in a broadening of the discrete level into a band. At small separations the interaction becomes strong and the bandwidth, Γ, large. When the bandwidth approaches the width of the conduction band in the metal it is no longer meaningful to view the atomic band as a separate state but must be considered as an integral part of the band structure of the metal. Physically the electron can be regarded as tunnelling between the metal conduction band and the atomic valence level. The energy shift is a consequence of the coulomb interactions involved in the ion-electron and ion-electron-image systems. The amount that the shifted and broadened level overlaps the conduction band determines the nature of the chemical bond. Gadzuk[90] distinguishes three cases. In the first the broadened and shifted level falls below the Fermi level as shown in figure 2.5(a). There is no net charge on the adsorbate and the bond is metallic (covalent). When the broadened level partially overlaps the Fermi level, as shown in figure 2.5(b), the atomic band is filled only up to the position of the Fermi level and so the adsorbate has a net positive charge. This represents a partially ionic-partially covalent bond. The third case, shown in figure 2.5(c), occurs when the broadened level lies totally above the Fermi level and none of the atomic states are filled. This corresponds to an ionic bond. All three cases described by figure 2.5 are at zero Kelvin. At non-zero temperatures some electrons exist above the Fermi level so that even in the ionic case

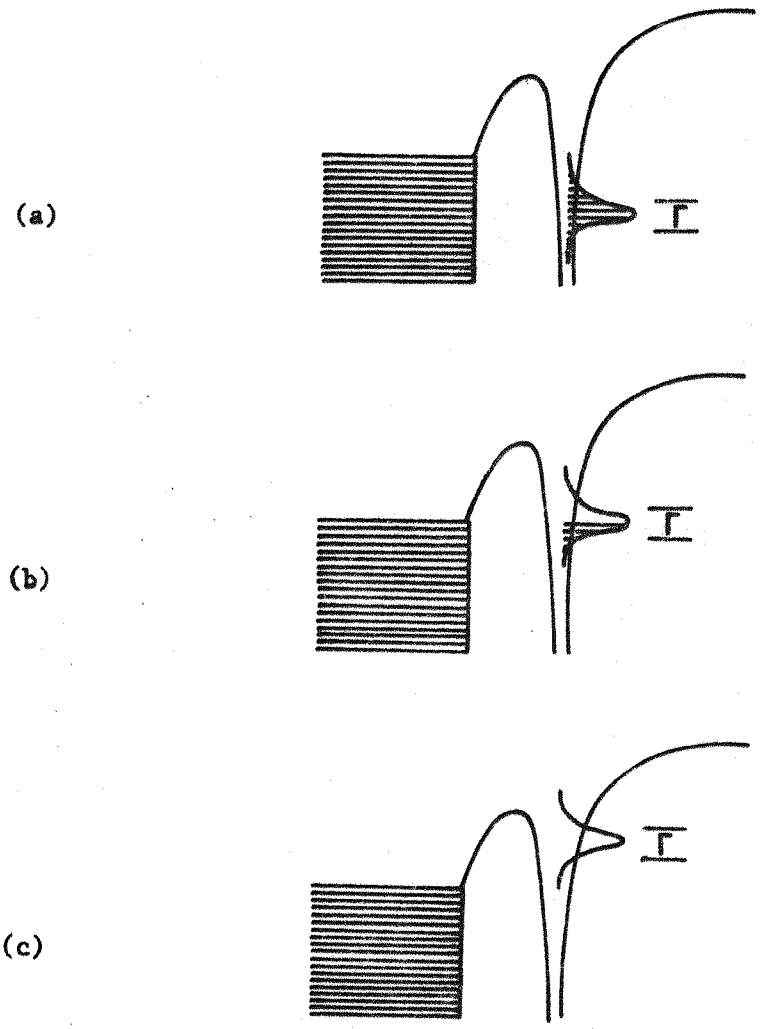

figure 2.5
position of the broadened valence level of an atom adsorbed at a metal surface

(a) metallic or covalent bond
(b) partially covalent - partially ionic bond
(c) ionic bond

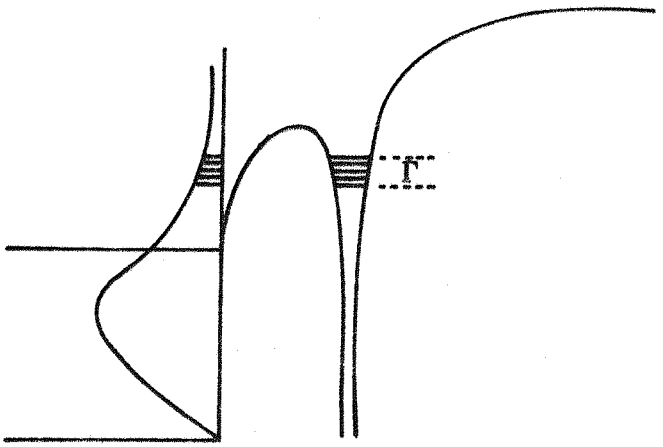

figure 2.6(a)
ionic adsorption at a metal surface
broadened valence level and Fermi-Dirac electron distribution for non-zero temperature

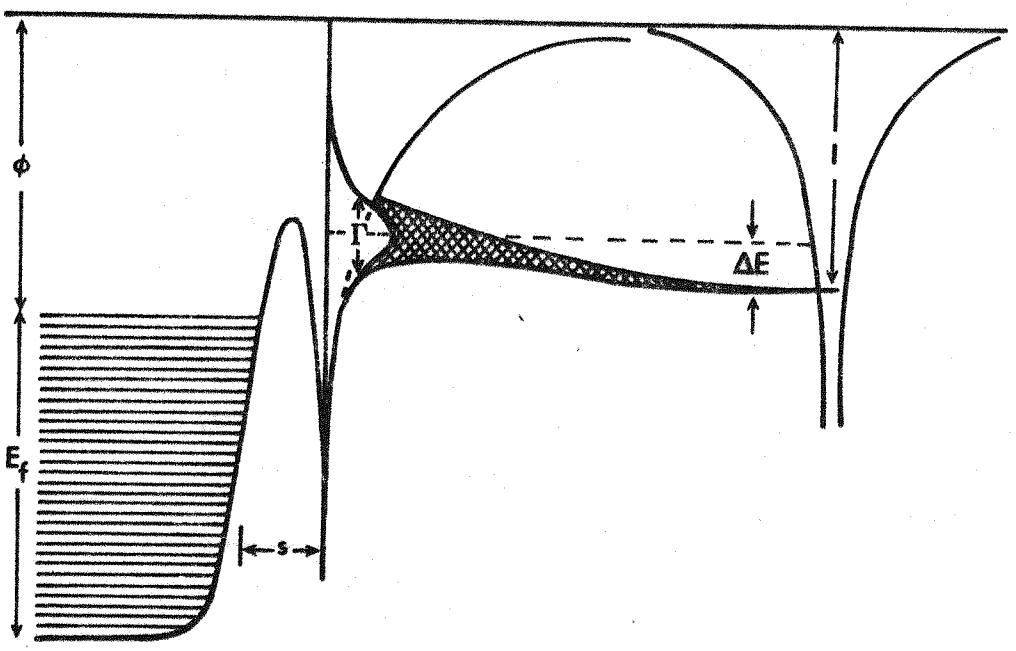

figure 2.6(b)
valence level shift and broadening for adsorption of caesium on tungsten

some electrons will be found in the broadened valence level. The electron distribution corresponding to this state is shown in figure 2.6(a). It is clearly important to calculate the extent of the energy level shift and broadening in order to establish the nature of the bond. For the case of caesium on tungsten Rasor and Warner[91] calculate the bandwidth as negligible in comparison with kT which justifies their proposition that the bond is entirely ionic. However Gomer[89,92] suggests that the overlap is large and Gyftopoulos and Levine[65] by postulating a partially ionic-partially covalent bond also imply considerable overlap. Gadzuk[90] has made a detailed calculation of the shift and broadening based on the Sommerfeld model and using perturbation theory. The electron wave function is considered as perturbed by the coulomb interactions between the electron and the ion, the electron and the ion image, and the electron and its own image. The calculation shows that near the equilibrium position the broadening Γ increases rapidly as the separation reduces whereas the shift ΔE is very weakly dependent on separation. For caesium on tungsten the broadening Γ = 1-2 eV, a smaller value than suggested by Gomer but greater than estimated by Raser. The shift ΔE = 0.7 eV. These values produce an atomic energy band entirely above the Fermi level, the bond thus being completely ionic. Figure 2.6(b) shows the energy diagram for caesium on tungsten as calculated by Gadzuk[104], demonstrating the shift ΔE and broadening Γ of the valence level as the separation s is reduced. The unperturbed adatom, ionization potential I, is shown on the right of this diagram.

2.2.1 early adsorption theories

The first attempt to explain the decrease in work function on adsorption

was made by Langmuir[93] in order to interpret Taylor and Langmuir's work on caesium on tungsten[86]. Elementary electrostatics applied to a continuous dipole sheet leads to the Helmholtz formula:

$$\Delta\phi = \frac{M_o \theta \sigma_f}{2\varepsilon_o} \qquad 2.10$$

where M_o is the dipole moment formed by the ion and its image in the conducting surface. The coverage θ is here defined as unity when the density of adsorbed particles equals the density of adsorption sites. At $\theta = 1$ the coverage is described as a monolayer and the adsorbate surface density is σ_f. The dipole moment $M_o = 2e\ell$ where e is the electronic charge and ℓ is the separation of the ion centre from the imaging plane. The 2 appears in equation 2.10 since the effective potential barrier is half the total barrier between the ion and its image because half the field is screened from electrons by the substrate.

It is immediately obvious that the linear relationship between $\Delta\phi$ and θ of equation 2.10 is obeyed only at very low coverages, there actually being a minimum in the experimental ϕ versus θ data. This failure is due to the discrete and polarizable nature of real adsorbate particles. As the number of adatoms $\theta\sigma_f$ increases the effect of mutual depolarization of dipoles must be considered. Topping[94] calculated the depolarizing field due to an infinite array of ideal (point) dipoles. The fields for random and regular arrays are respectively:

$$E_d = \frac{\delta \sigma_f^{3/2} \theta M}{4\pi\varepsilon_o} \qquad 2.11$$

and

$$E_d = \frac{\delta \sigma_f^{3/2} \theta^{3/2} M}{4\pi\varepsilon_o} \qquad 2.12$$

where $\delta = 9.034$ for a square array and 8.894 for a hexagonal array. δ is

usually approximated to 9 so that equations 2.11 and 2.12 can be written:

$$E_d = \frac{9\sigma_f^{3/2}\theta^H M}{4\pi\varepsilon_o} \qquad 2.13$$

where H = 1.5 for mobile and 1 for immobile adsorbates. The effective dipole moment is now:

$$M = M_o + \alpha E_d \qquad 2.14$$

where α is the polarizability. Re-arranging

$$M = \frac{M_o}{\varepsilon} \qquad \text{where } \varepsilon = 1 + \frac{9\alpha\sigma_f^{3/2}\theta^H}{4\pi\varepsilon_o} \qquad 2.15$$

and

$$\Delta\phi = \frac{M_o\theta\sigma_f}{2\varepsilon\varepsilon_o} \qquad 2.16$$

A good fit to Taylor and Langmuir's data is obtained for $\theta < 0.6$ using equation 2.16. However this equation cannot produce a minimum in the work function/coverage curve.

2.2.2 MacDonald and Barlow

The most thorough treatment of adsorption based on Langmuir's classical approach is given in a series of papers by MacDonald and Barlow[95]. Adsorbate particles are treated as discrete entities and dipoles are not assumed to be ideal. The total depolarizing field E_d at an adsorbed particle is subdivided into six components. These are the 'natural' field E_n at the surface before any adsorption occurs; the field E_1 due to the image of the particle:

$$E_1 = -\frac{ze}{4\pi\varepsilon_o(2\ell)^2} \quad ; \qquad 2.17$$

the field E_2 due to the image of the ideal dipole possessed by the particle:

$$E_2 = \frac{\alpha E_d}{4\pi\varepsilon_o 4\ell^3} \quad ; \qquad 2.18$$

the field E_3 due to all surrounding ideal dipoles:

$$E_3 = -\frac{\alpha E 9\theta^H \sigma_f{}^{3/2}}{4\pi\varepsilon_o} \quad ; \qquad 2.19$$

the field E_4 due to all surrounding non-ideal dipoles formed by the particles and their images and finally the field E_5 due to the images of all surrounding ideal dipoles. E_4 and E_5 are calculated approximately using Grahame's cut-off model rather than making a complex complete summation. Putting the total E_d into equation 2.14 and re-arranging:

$$\Delta\phi = -\frac{M_o \theta\sigma_f}{2\varepsilon_o}\left[1-g(\theta)\right] \qquad 2.20$$

where $M_o = 2ze\ell$ and where

$$g(\theta) = \frac{1}{2\varepsilon_{eff}} \frac{\alpha}{4\pi\varepsilon_o \ell^3}\left[\left[0.9117 + \left(\frac{2\pi}{11.034\sqrt{3}\ell}\left[\frac{11.034}{9\theta^H \sigma_f{}^{3/2}}\right]^{1/3}\right)^2\right]^{1/2} + \frac{1}{2} - \frac{4\pi\varepsilon_o E_n 2\ell^2}{ze}\right] \qquad 2.21$$

and

$$\varepsilon_{eff} = 1 + \frac{\alpha}{4\pi\varepsilon_o \ell^3}\left(9\theta^H \sigma_f{}^{3/2}\ell^3 - \frac{1}{4} + \frac{8\pi^3}{3^{3/2}(11.034)^2}\left[1 + \left(\frac{2\pi}{11.034\sqrt{3}\ell}\left[\frac{11.034}{9\theta^H \sigma_f{}^{3/2}}\right]^{\frac{1}{3}}\right)^2\right]^{-\frac{3}{2}}\right) \qquad 2.22$$

The first term in $g(\theta)$ arises from E_4, the second term from E_1 and the third from E_n. The terms inside the brackets in the expression for ε_{eff} are respectively due to E_3, E_2 and E_5. The fact that the second term ($-\frac{1}{4}$) is of negative sign is because the ideal dipole produces an image dipole of the same polarity, thus increasing the polarizing field. This negative

feedback effect leads to the unfortunate result that ε_{eff} becomes zero for $\alpha/4\pi\varepsilon_o \ell^3 \simeq 4$ and hence $\Delta\phi$ becomes infinite. Since polarizabilities of this magnitude are physically very feasible for atomic caesium it must be concluded from this analysis either that the atom becomes ionized on adsorption or that the polarizing field reduces the polarizability sufficiently to avoid the effect. For this reason MacDonald and Barlow do not attempt a detailed fit of the theory to experiment. For $E_n = 0$ an excellent fit can be made to the data of Taylor and Langmuir, the parameters emerging as:

$$\ell = .23\ \text{Å} \qquad \alpha = .026 \times 10^{-40}\ \text{Fm}^2 \qquad \sigma_f = 129 \times 10^{18}\ \text{m}^{-2}$$

These must be compared with the physically realistic values:

$$\ell = 2\ \text{Å} \qquad \alpha = 3 \times 10^{-40}\ \text{Fm}^2 \qquad \sigma_f = 2.5 \times 10^{18}\ \text{m}^{-2}$$

However a good fit can be obtained using the latter values, in the range $\theta < 0.6$. MacDonald and Barlow suggest that at higher coverages the increasing proportion of atom to ions on the surface causes the theory to become subject to the above-mentioned difficulty.

In general terms this failure of linear polarization theory is a result of the neglect of the quantum features of adsorption. It appears that the concept of discrete particles on the surface is only meaningful for highly ionic adsorption.

2.2.3 Rasor and Warner

The essence of Rasor and Warner's theory[91] is the proposition that completely ionic and completely atomic particles can exist simultaneously

on the substrate surface. The total work function change is then the sum of the dipole contributions M_i and M_a of the ions and atoms respectively. Again the classical Helmholtz formula is used:

$$\Delta\phi = \frac{\sigma_f}{2\varepsilon_o}(M_i\theta_i + M_a\theta_a) \qquad 2.23$$

where θ_i and θ_a are the ionic and atomic coverages. The effective dipole moment is given by an equation of the form of 2.14

$$M_i = M_{io} + \alpha_i E_d \qquad 2.24$$

where $$M_{io} = 2e\ell \qquad 2.25$$

The charge centre of an adsorbed ion does not reach the imaging surface because of its finite size. A quantity $f(\theta)$ is defined as the fraction of the total dipole barrier $\Delta\phi$ penetrated by the ion. The depolarizing field at the ion is then given by:

$$E_d = -\frac{(1-f)\Delta\phi}{\ell} \qquad 2.26$$

In order to evaluate the ratio of atoms to ions on the surface Rasor and Warner use a statistical mechanical method given by Dobretsov[96]. The result is a Boltzman type factor:

$$\frac{\theta_a}{\theta_i} = q \exp\left(-\frac{E}{kT}\right) \qquad 2.27$$

where E is the energy difference between the atomic and ionic states on the surface (surface ionization energy) and q is a quantum mechanical weighting factor nearly equal to 2. The use of equation 2.27 with q = 2 is only justified when the amount of overlap between the broadened valence level of the adsorbed atom and the conduction band of the metal is small; that is when the bandwidth $\Gamma \ll kT$. An approximate calculation by Rasor and Warner shows this condition holds for caesium on tungsten, an assumption which, as mentioned in section 2.1.4, is made doubtful by Gadzuk's more exact

calculation. The energy E is evaluated in terms of the atom adsorption energy ϕ_a, the ionization potential I, the ion adsorption energy ϕ_i and the electron work function ϕ by considering the following hypothetical cycle. An adsorbed atom is ionized on the surface and the ion and electron removed separately from the surface. The free electron neutralizes the free ion and the resulting free atom is re-adsorbed on to the surface.

Then $$E + \phi_a + I - \phi_i - \phi = 0 \qquad \text{at a coverage } \theta \qquad 2.28$$

and $$E_o + \phi_{ao} + I - \phi_{io} - \phi_o = 0 \qquad \text{for } \theta = 0 \qquad 2.29$$

From equations 2.28 and 2.29 and putting $\Delta\phi = \phi_o - \phi$; $\Delta\phi_a = \phi_{ao} - \phi_a$; $\Delta\phi_i = \phi_i - \phi_{io} = f\Delta\phi$,

then $$E = E_o - (1-f)\Delta\phi + \Delta\phi_a \qquad 2.30$$

Combining equations 2.23 - 2.27:

$$\Delta\phi = \frac{\sigma_f e \ell \theta \left[1-\alpha_i \frac{(1-f)\Delta\phi}{2e\ell^2}\right]\left[1+\frac{M_a\theta_a}{M_i\theta_i}\right]}{\varepsilon_o\left[1 + q \exp(-E/kT)\right]} \qquad 2.31$$

where E is given by equation 2.30. In equation 2.31 the depolarization is determined by the factor $f(\theta)$. Rasor and Warner estimate this function from Taylor and Langmuir's data and support the result using a detailed statistical analysis based on the coulomb repulsion between ions. Equation 2.31 is fitted to the caesium on tungsten data assuming only values for σ (3.56×10^{18} m^{-2}) and the function $f(\theta)$. Good agreement is found, the parameters having unique best values of:

$\ell = 1.4 \times 10^{-10}$ m ; $\alpha_i = 31 \times 10^{-40}$ Fm^2 ; $E_o = 1.05$ eV ;

$\Delta\phi_a << kT$; $M_a\theta_a / M_i\theta_i << 1$.

Thus according to this theory there is no atomic contribution to the dipole moment. Physically the reduction in work function on adsorption is

accounted for by the classical dipole barrier, the slope falling off as the coverage increases because of depolarization and finally falling off further because the ratio of atoms to ions increases as the value of E is reduced. This theory can predict a minimum in the work function/coverage curve because of the last effect. A final point in the theory's favour is that it predicts the temperature dependence of the work function change (again in terms of the atom/ion ratio).

Criticism of the theory arises from four factors. Firstly particles are treated as either ionic or atomic, not as partially ionic as would be more realistic. This is probably justified in the case of caesium on tungsten where the adsorption is almost entirely ionic. Secondly the bandwidth of the valence level of the adsorbed atom is taken to be very small, an assumption which may be justified for caesium on tungsten, but is certainly not for adsorbates other than alkalis. Thirdly, as was pointed out with the MacDonald and Barlow theory, quantum features of adsorption are neglected and so it is only fully applicable at lower coverages where ionic adsorption is dominant. Finally, no account is taken of the short range attractive interaction between adsorbed particles which is important where the repulsive coulomb interaction is small. Thus, again at high coverages where the adsorbate particles are more closely spaced and there is less coulomb repulsion from the ionic species, the theory breaks down. In general, for systems where E_o is small or negative or where the ionization potential is high, the atomic species becomes dominant and the theory is no longer applicable.

Although it is found from fitting to experimental data that $\Delta\phi_a << kT$ this cannot be assumed for systems other than caesium on tungsten. As a first

approximation

$$\Delta\phi_a = -c\Delta\phi$$

where c is a constant is reasonable.

Equation 2.30 then becomes:

$$E = E_o - (1-f+c)\,\Delta\phi \qquad 2.32$$

Gadzuk and Carabateas[107] have made a calculation of the function f for both mobile and immobile ions. The values for caesium on tungsten are similar to those calculated by Rasor and Warner.

For the case of an immobile adsorbate:

$$f = 1 - \frac{4.5}{\pi}\,\ell\,(\theta\sigma_f)^{\frac{1}{2}} \qquad 2.33$$

Finally neglecting $M_a\theta_a$ / $M_i\theta_i$, equation 2.31 can be re-arranged as:

$$\Delta\phi = \frac{\frac{1}{\varepsilon_o}\, e\sigma_f \ell\theta}{1 + \frac{1}{\varepsilon_o}\,\frac{\sigma_f\alpha_i}{2\ell}\,(1-f)\theta + q\,\exp\left[-\frac{E}{kT}\right]} \qquad 2.34$$

Equation 2.34 is used to fit to the uranium and zirconium coverage curves (section 9.2) where E is given by equation 2.32 and f is given by equation 2.33.

2.2.4 Gyftopoulos and Levine

Gyftopoulos and Levine[65] point out that for coverages greater than one monolayer the work function of an adsorbed film is constant and equal to that of the bulk adsorbate. It is suggested that at $\theta = 1$ there is no dipole contribution to the work function, its value being determined only by the electronegativity of the adsorbate. Similarly at $\theta = 0$ the bare work function is determined by the electronegativity of the substrate. For

$0 < \theta < 1$ an homogenized composite surface is proposed in which the adsorbate particles are partially ionic-partially covalent and whose work function has two components: the electronegativity barrier $e(\theta)$ and the dipole barrier $d(\theta)$. Then:

$$\phi(\theta) = e(\theta) + d(\theta) \qquad 2.35$$

The electronegativity barrier is due to the effective electronegativity of the composite surface and is taken as the simplest polynomial to which it can be fitted:

$$e(\theta) = a + b\theta + c\theta^2 + d\theta^3 \qquad 2.36$$

At zero coverage the work function is characterized by the electronegativity of the substrate:

$$e(0) = \phi_m$$

At a monolayer coverage the work function is given by the electronegativity of the adsorbate:

$$e(1) = \phi_f$$

where the subscript refers to the adsorbate. Since the addition of the first few atoms to the clean surface does not appreciably alter the electronegativity of the homogenized surface

$$\left.\frac{de(\theta)}{d\theta}\right|_{\theta=0} = 0$$

and since the work function is constant at one monolayer

$$\left.\frac{de(\theta)}{d\theta}\right|_{\theta=1} = 0 \quad .$$

Putting the above boundary conditions into equation 2.36:

$$e(\theta) = \phi_f + (\phi_m - \phi_f)G(\theta) \qquad 2.37$$

where $$G(\theta) = 1-3\theta^2 + 2\theta^3 \qquad 2.38$$

In order to deduce the dipole barrier Malone's relation between electronegativity difference and dipole moment is evoked (section 1.3.3):

$$\Delta\chi_p = M \qquad \text{where M is in Debye}$$

Thus

$$M(\theta) = M_o \frac{\chi(\theta)-\chi_f}{\chi_m-\chi_f} \quad .$$

Since according to the Gordy-Thomas relation (equation 1.14) electronegativity is proportional to work function, and making use of equation 2.37:

$$M(\theta) = M_o G(\theta) \qquad 2.39$$

Dipole-dipole depolarization is taken into account in the usual way. From equation 2.16 the dipole barrier is:

$$d(\theta) = \frac{M_o G(\theta)\theta\sigma_f}{2\varepsilon\varepsilon_o} \qquad 2.40$$

where

$$\varepsilon = 1 + \frac{9\alpha\sigma_f{}^{3/2}{}_\theta H}{4\pi\varepsilon_o} \qquad 2.41$$

M_o is the component of the dipole perpendicular to the surface. Gyftopoulos and Levine estimate this component in terms of the total dipole between adsorbate and substrate atoms, M_{fm}, using a model in which the adsorbate atom is in contact with four substrate atoms as shown in figure 2.7:

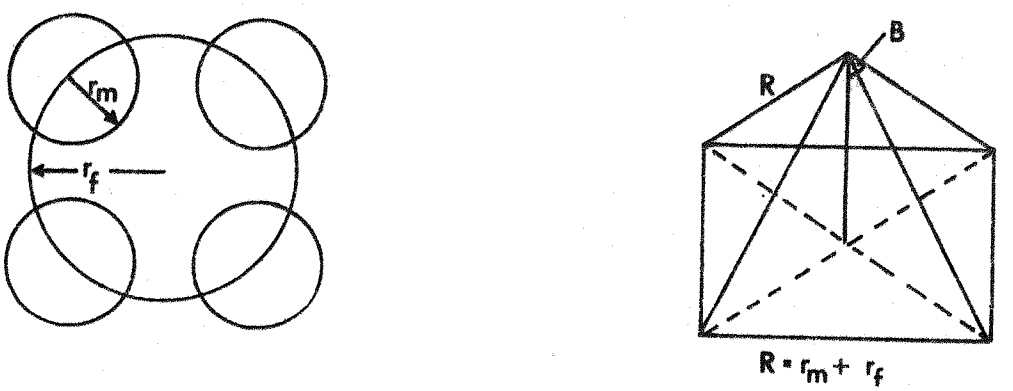

figure 2.7

Then $$M_o = 4 \cos B \, M_{fm} \qquad 2.42$$

The Malone and Gordy-Thomas relations are again used to calculate M_{fm}. Malone gives $M = 3.33 \times 10^{-30} \Delta\chi_p$ where M is in coulomb-metres. From more recent data Gyftopoulos and Levine deduce: $M = 3.83 \times 10^{-30} \Delta\chi_p$.

Using the Gordy-Thomas relation (equation 1.14):

$$M = \frac{3.83 \times 10^{-30}}{2.27} \Delta\phi \quad .$$

Putting this into equation 2.42:

$$M_o = 4 \cos B \frac{3.83 \times 10^{-30}}{2.27} (\phi_m - \phi_f)$$

The Malone relation was determined for diatomic molecules and does not take into account self-depolarization of dipoles on a conducting surface. The field due to self-depolarization is given by an equation of the form of 2.18. Thus the effective dipole moment perpendicular to the surface is given by:

$$M_o = \frac{4 \cos B \; 3.83 \times 10^{-30} (\phi_m - \phi_f)}{2.27 \; (1 + \alpha/4\pi\varepsilon_o R^3)} \quad . \qquad 2.43$$

Combining equations 2.35, 2.37, 2.40, 2.41, 2.43 and putting $\varepsilon_o = 1/(36\pi \times 10^9)$:

$$\frac{\phi}{\phi_m - \phi_f} = 1 - G(\theta)\left[1 - \frac{k_1 \theta}{1 + k_2 \theta^H}\right] \qquad 2.44$$

where H = 1 for immobile, 1.5 for mobile adsorbates,

$$G(\theta) = 1 - 3\theta^2 + 2\theta^3 \; ;$$

$$k_1 = \frac{0.765 \times 10^{-18} \sigma_f \cos B}{1 + \alpha/4\pi\varepsilon_o R^3} \; ; \quad k_2 = \frac{9\alpha\sigma_f^{3/2}}{4\pi\varepsilon_o} \quad . \qquad 2.45$$

Equation 2.44 generally gives excellent agreement with experiment[97]. This is partly due to the arbitrary nature of the $G(\theta)$ term used for the electronegativity barrier. However neither MacDonald and Barlow nor Rasor and

Warner include any term of this nature which is not directly due to the dipole effect. This term implicitly contains the attractive interaction between adsorbate particles since it assumes that the composite surface has a characteristic metallic nature somewhere between the clean substrate and pure adsorbate surfaces whose work function is independent of the dipole term. Physically the theory explains the initial drop in the work function by the dipole effect with the usual depolarization terms. At higher coverages the dipole term decreases and the adsorbate takes on the bulk metallic band structure with a characteristic work function of its own. Thus the quantum nature of adsorption is implicitly assumed in this theory. For this reason the theory has a better physical basis than those which consider adsorbate particles as independent classical elements. Further support for the Gyftopoulos and Levine 'chemical' approach is given by Kaplit et al[98]. The total energy of the adsorption bond is calculated using the Thomas-Fermi-Dirac theory corrected for exchange and correlation interactions in such a way as to be able to distinguish between the coulombic and quantum mechanical contributions. This is done for the systems caesium on (100) tungsten, caesium on (110) tungsten, barium on (100) tungsten and barium on (110) tungsten. The coulomb energy (sum of electron-electron and ion-electron interactions) is found to be between 70 and 95 per cent of the total energy. The remainder is due to the sum of the quantum mechanical kinetic, exchange and correlation energies. The total charge transfer to the substrate is calculated as 20 per cent of the available valence charge, a value consistent with the Gyftopoulos and Levine view of a partially ionic-partially covalent adsorption bond. It is clear from this analysis that even in the cases considered to be highly ionic, quantum mechanical forces cannot be neglected.

MacDonald and Barlow[95] criticize Gyftopoulos and Levine for three reasons:

a the theory does not predict the final work function but uses the experimental value;

b a minimum in the work function/coverage curve only appears when the surface is assumed to be rough;

c it is unlikely that a single layer of adsorbate atoms would shield out all the effects from the underlying material and exhibit bulk behaviour.

The first criticism is valid in that both MacDonald and Barlow and Rasor and Warner do predict a final value for the work function and in this sense Gyftopoulos and Levine is a less general theory. However they only do so at the expense of good agreement with experiment In both cases, if Taylor and Langmuir's data is fitted to the theory at low coverages where there should be good agreement, the final work function predicted is far too low.

The second point is incorrect although higher surface densities do produce larger minima if the other parameters are held constant. Whether or not this is correct can only be ascertained from experiment.

The last criticism is the most serious. As will be seen later, the final values on differently oriented substrates are not the same and so cannot be characteristic of the bulk adsorbate. However this does not invalidate the theory as long as the monolayer work function remains unchanged at higher coverages. The final value then corresponds to an adsorbate structure which is characteristic of the orientation of that substrate. In this sense the theory is better than those of MacDonald and Barlow and Rasor and Warner since neither can account for such structural effects.

A final criticism of Gyftopoulos and Levine is that the relation between dipole moment and work function is entirely empirical, Malone's equation in particular being especially dubious (section 1.3.3).

The real advantage of the theory is that it is applicable to the cases where other theories fail: that is for systems which are not predominantly ionic. The arbitrary nature of the $G(\theta)$ term and empirical nature of the dipole moment are overcome in the subsequent theory of Gyftopoulos and Steiner.

2.2.5 Gyftopoulos and Steiner

This theory[99] is an extension of Gyftopoulos and Levine but with an improved physical foundation. Gyftopoulos and Steiner identify the work function of the bare surface with the neutral orbital electronegativity of the valence orbitals of the surface atoms (section 1.5.2). The work function of a composite surface is then taken as the perturbed neutral electronegativity of the substrate atoms. This perturbation by the adsorbate arises from two factors. Firstly the adsorbate-substrate interaction which, as in Gyftopoulos and Levine, is assumed to be partially ionic-partially covalent. The charge transfer F associated with this bond gives rise to a dipole moment and hence a work function change of bF

where $$bF = -\frac{\sigma_f \theta M_o}{2\varepsilon_o} \qquad 2.46$$

The dipole moment of the adsorbate-substrate bond is FezR where, as before, R is the sum of the adsorbate and substrate atomic radii and z is the number of bonding orbitals per adatom. M_o in equation 2.46 refers to the dipole moment perpendicular to the surface. Taking into account dipole-dipole

depolarization and self-depolarization in the same way as in the Gyftopoulos and Levine theory, M_o is then given by:

$$M_o = \frac{FezR\ \cos B}{\left[1 + \frac{\alpha}{4\pi\varepsilon_o R^3}\right]\left[1 + \frac{9\alpha\sigma_f^{3/2}\theta^H}{4\pi\varepsilon_o}\right]}$$

Putting M_o into equation 2.46

$$b = -\frac{ezR\ \cos B\ \sigma_f\theta}{2\varepsilon_o\left[1 + \frac{\alpha}{4\pi\varepsilon_o R^3}\right]\left[1 + \frac{9\alpha\sigma_f^{3/2}\theta^H}{4\pi\varepsilon_o}\right]} \qquad 2.47$$

The second contribution to the perturbation arises from the entirely covalent adsorbate-adsorbate interaction. This is assumed to produce a work function change cQ linearly proportional to the overlap charge Q in the adsorbate-adsorbate bond.

Then $\phi = \phi_m + cQ + bF$ 2.48

Gyftopoulos and Steiner take z = 1 for the univalent but highly ionic alkali adsorbates but for all other metals they take z as half the metallic valence. The basis of the latter assumption is that on average metal atoms form half as many bonds on the surface as they do in the bulk.

The second contribution to the perturbation, the overlap charge, is determined by the covalent bond energy[100] (section 2.1.2.2). This is often taken as proportional to the Morse function M (equation 2.2):

$$M = 2\exp\{-a(d-d_o)\} - \exp\{-2a(d-d_o)\} \quad . \qquad 2.49$$

M is a minimum when the separation d between adsorbate atoms equals d_o, this being taken as the monolayer situation; a is a constant of the adatoms. For atoms in a square array:

$$d = d_o\theta^{-\frac{1}{2}} \quad .$$

Putting this into equation 2.49

$$M = 2\exp\{ad_o(1-\theta^{-\frac{1}{2}})\} - \exp\{2ad_o(1-\theta^{-\frac{1}{2}})\} \quad . \qquad 2.50$$

Since the constant $\underline{a}$ is not known for adatoms on a metal surface, ad_o cannot be evaluated. However Gyftopoulos and Steiner point out that experimental data on many metallic adsorbates indicate that at one monolayer d_o approaches the interatomic distance in the bulk adsorbate. Tabulated values of the latter and of $\underline{a}$[101] in the bulk show that the product ad_o varies only from 2.29 to 3.65 for most adsorbates. As will be seen later the perturbations bF and cQ are interrelated in such a way that changes in the Morse function tend to be compensated for by opposite changes in these two functions. Consequently Gyftopoulos and Steiner propose that an average value of ad_o is taken:

$$ad_o = 2.97 \qquad 2.51$$

Figure 2.8 shows the Morse function for three values of ad_o: 2.97, 2.29 and 3.65. As in Gyftopoulos and Levine the initial and final work functions are determined respectively by the substrate and by the adsorbate only, there being no dipole component. This gives the boundary conditions:

$$\phi_{\theta=0} = \phi_m \quad , \qquad 2.52a$$

$$\phi_{\theta=1} = \phi_f \quad . \qquad 2.52b$$

Clearly from equation 2.48 these conditions are obeyed when cQ is of the form:

$$cQ = -(\phi_m - \phi_f)M \qquad 2.53$$

Comparing equation 2.53 with equations 2.37 and 2.38 shows how the Morse function replaces the $G(\theta)$ term in Gyftopoulos and Levine. Explicitly M is equivalent to 1 - G. For comparison (1 - G) is included in figure 2.8 (dashed line).

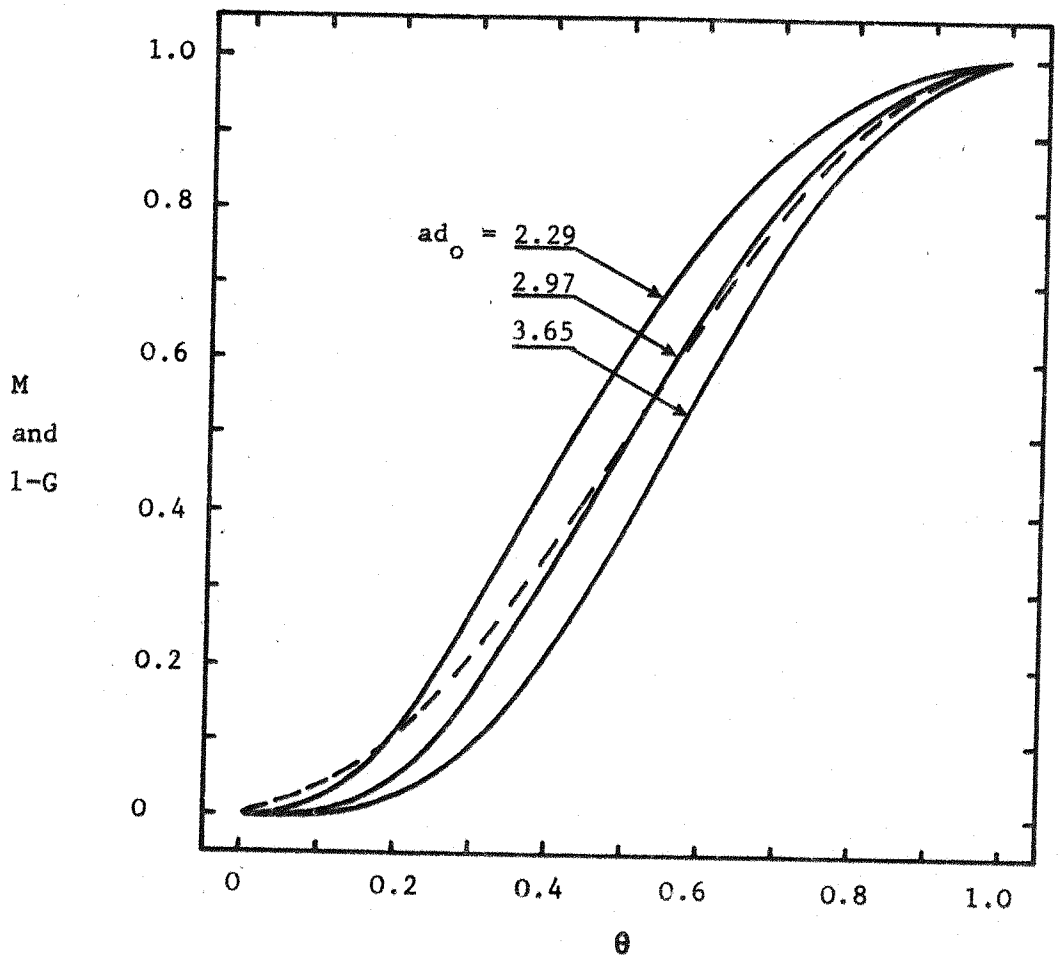

figure 2.8
Morse function M(θ) for 3 values of the parameter ad_o and the Gyftopoulos and Levine 1-G(θ) function

——————— M(θ)
— — — — — 1-G(θ)

It only remains now to compute the charge transfer F. This is done by maximising the adsorbate-substrate bond energy with respect to F. The total bond energy can be divided into homopolar and heteropolar parts. The former, discussed in section 2.1.2.2 for the cases of zero overlap (S = 0) and

complete overlap (S = 1) is given by equations 2.8 and 2.9:

$$D(\text{homopolar})_{S=0} = D_o (1-F^2)^{\frac{1}{2}} \qquad 2.54$$

$$D(\text{homopolar})_{S=1} = D_o (1-F^2) \qquad 2.55$$

where D_o is the energy of the purely covalent bond. Gyftopoulos and Steiner use equation 2.54.

The heteropolar component can again be divided into two components[79]:

a the coulomb interaction energy between the charged atoms:

$$\frac{kF^2e^2}{4\pi\varepsilon_o R} \qquad 2.56$$

where the coefficient k ($k \leq 1$) is introduced to account for the repulsion between overlapping orbitals;

b the energy required to effect the transfer of charge F between bonding orbitals.

In section 1.4 orbital electronegativity was defined (equation 1.12) as:

$$\chi(q) = \frac{dE(q)}{dq} = \frac{I+A}{2} + \frac{I-A}{e} q$$

where E(q) is the energy of the bonding orbital containing charge q. Before charge transfer the electronegativity of the substrate is perturbed by an amount cQ. Thus the energy required to increase the charge in the substrate orbital from -Fe to the final value zero is:

$$\int_{-Fe}^{0} dE(q)\, dq = \int_{-Fe}^{0} \left[\frac{I_m+A_m}{2} + cQ + \frac{I_m-A_m}{e} q \right] dq$$

$$= \left[\frac{I_m+A_m}{2} + cQ \right] Fe - \frac{I_m-A_m}{2e} F^2e^2 \quad . \qquad 2.57$$

Similarly the charge in the adsorbate valence orbital decreases from Fe to zero so that:

$$\int_{-Fe}^{0} dE(q)\, dq = \int_{0}^{Fe} \left[\frac{I_f+A_f}{2} + \frac{I_f-A_f}{e} q \right] dq$$

$$= -\frac{I_f+A_f}{2} Fe - \frac{I_f-A_f}{2e} F^2e^2 \quad . \qquad 2.58$$

The complete orbital charge transfer energy is then:

$$\left[\frac{I_m+A_m}{2} + cQ - \frac{I_f+A_f}{2} \right] Fe - \left[\frac{I_m-A_m}{2e} + \frac{I_f-A_f}{2e} \right] F^2e^2 \quad . \qquad 2.59$$

Combining equations 2.54, 2.56 and 2.59 the total bond energy is:

$$D = D_o(1-F^2)^{\frac{1}{2}} + \frac{kF^2e^2}{4\pi\varepsilon_o R} + \left[\frac{I_m+A_m}{2} + cQ - \frac{I_f+A_f}{2} \right] Fe - \left[\frac{I_m-A_m}{2e} + \frac{I_f-A_f}{2e} \right] F^2e^2 \qquad 2.60$$

As the charge transfer F increases, the ionic contribution (second term) is increased. However, there is then less charge available for overlap so that the first (covalent) term is decreased. The last terms are due to changes in the electron populations of the bonding orbitals.

Differentiating D with respect to F and setting equal to zero, the charge transfer for maximised bond energy is given by:

$$F = \frac{(\phi_m-\phi_f)(1-M)}{D_{o/e}(1-F^2)^{-\frac{1}{2}} + D_{1/e}} \qquad 2.61$$

where use has been made of equation 2.53 and where:

$$D_1 = I_m - A_m + I_f - A_f - ke/(2\pi\varepsilon_o R) \quad . \qquad 2.62$$

D_1 is not calculable since the quantities involved refer to particular bonding orbitals and are not known. In the present work D_1 is found by adjusting its value until a good fit between theory and experiment is obtained (section 9.4).

D_o, the purely covalent adsorbate-substrate bond energy, is calculated using an extension of Pauling's postulate of the geometric mean (section 1.3.1):

$$D_o = \frac{\left[D(f\text{-}f).D(m\text{-}m)\right]^{\frac{1}{2}} S_{fm}}{z} \qquad 2.63$$

where D(f-f) and D(m-m) are here taken as heats of sublimation of the adsorbate and substrate respectively and where the number of bonding orbitals per adatom, z, is included since D_o refers to a single bond. The angular efficiency S_{fm} [48,102] accounts for the eccentricity of the atomic orbitals due to hybridization and is defined in terms of the angular strength S of the orbitals. According to Pauling and Sherman[48] the magnitude of the angular part of the orbital along the bond axis is a measure of the bond-forming power. The normalized value of this quantity is the angular strength S and is 1 for s orbitals, 1.732 for p orbitals and 2 for the best bond-forming hybrid s-p orbitals. Theoretical one-electron-bond energy calculations show that for s-p hybridization the bond energy is closely proportional to S^2 although this relation is not so good for s-p-d hybridization. For bonds between unlike adsorbate and substrate orbitals it is proposed that the energy is proportional to the geometric mean of the individual S^2 terms: viz. $S_f S_m$. In order that this 'angular efficiency' should equal unity for bonds between identical orbitals it is re-defined as:

$$S_{fm} = \frac{2S_f S_m}{S_f^2 + S_m^2} \qquad 2.64$$

Thus the angular efficiency decreases from unity as the disparity between angular strengths increases.

Summarizing equations 2.47, 2.48, 2.50, 2.53 and 2.55:

$$\phi = \phi_m - (\phi_m - \phi_f)M + bF \qquad 2.65$$

where $M = 2\exp\{ad_o(1-\theta^{-\frac{1}{2}})\} - \exp\{2ad_o(1-\theta^{-\frac{1}{2}})\}$, 2.66

$$b = -\frac{ezR\cos B\,\sigma_f\theta}{2\varepsilon_o\left[1+\frac{\alpha}{4\pi\varepsilon_o R^3}\right]\left[1+\frac{9\alpha\sigma_f^{3/2}\theta^{\frac{3}{2}}}{4\pi\varepsilon_o}\right]} \qquad 2.67$$

and $$F = \frac{(\phi_m-\phi_f)(1-M)}{D_{o/e}(1-F^2)^{-\frac{1}{2}} + D_{1/e}} \qquad 2.68$$

If equation 2.55 is used for the homopolar bond energy (complete overlap) equation 2.68, after minimizing the bond energy, becomes:

$$F = \frac{(\phi_m-\phi_f)(1-M)}{2D_{o/e} + D_{1/e}} \qquad 2.69$$

The effect of neglecting overlap can now be seen. Equation 2.68 places an upper limit on the maximum value of F (θ=0). For example, the values of $(\phi_m-\phi_f)$, D_o and D_1 for caesium on (110) tungsten[97] are 3.155 eV, 1.75 eV and 1.56 eV where this value of D_1 gives the best least-squares fit as shown by the full line in figure 2.8. Putting these values into equation 2.68 gives a maximum F of 0.74. However this amount of charge transfer is not great enough to produce the required initial slope in the work function/coverage curve. Larger F values can be obtained by reducing D_1 but this has the effect of lowering the work function below the experimental value in the region of the minimum. At the opposite extreme of complete overlap the best fit gives D_1 as -0.37 eV which, put into equation 2.69, produces a charge transfer of 0.98 and consequently a much better fit (dashed line in figure 2.8). Thus although both cases, no overlap and complete overlap, are extreme, the latter gives a better fit because the form of equation 2.69 is less restrictive on the F values than that of 2.68.

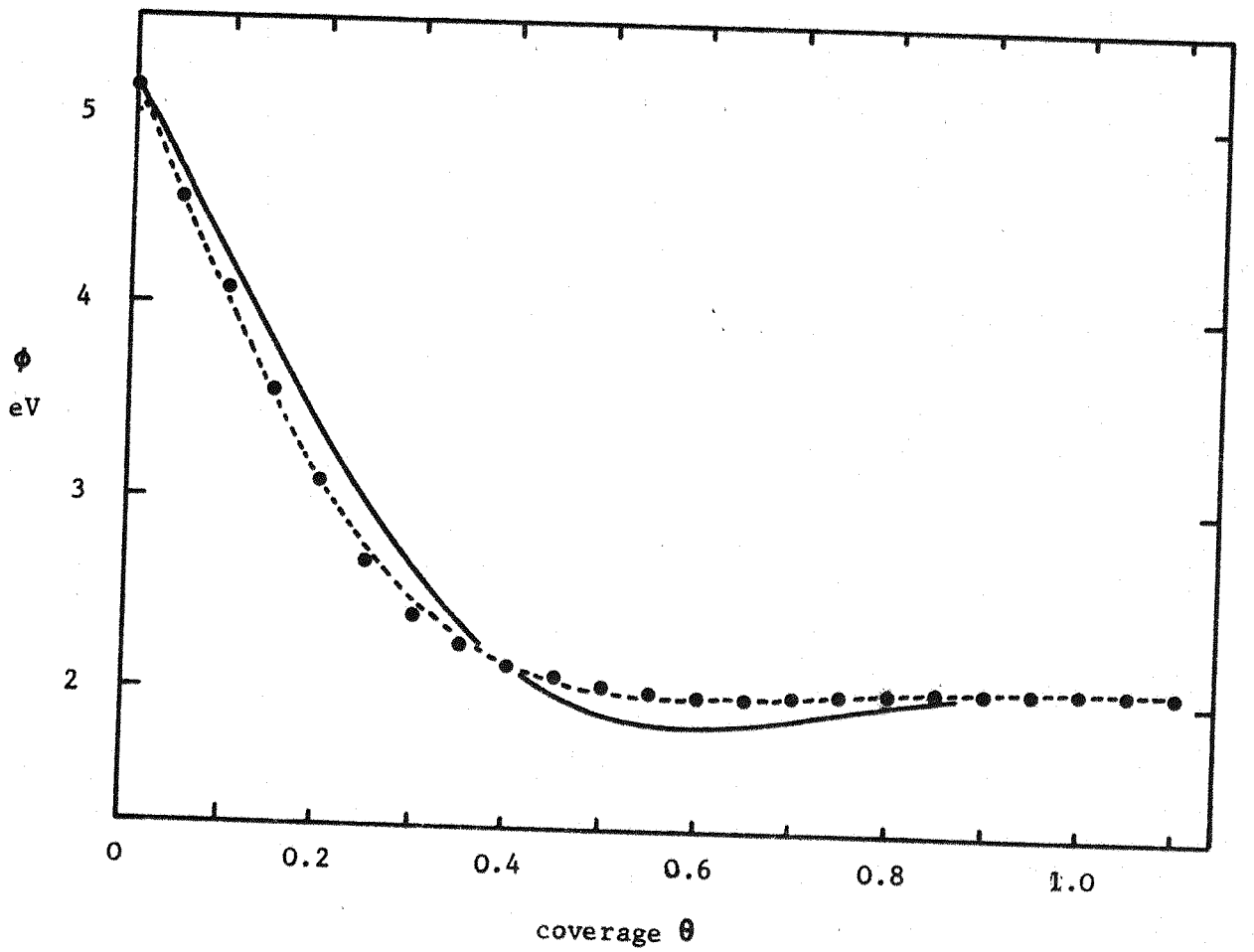

figure 2.8

comparison of the theory of Gyftopoulos and Steiner (equation 2.65) with the experimental data of Lee[97] for caesium on (110) tungsten

σ_f = 5.43×10^{18} m^{-2}

z = 1

R = 3.95×10^{-10} m

cos B = 0.88

D_o = 1.75 eV

– – – – – – complete overlap. Least squares fit: D = −0.37 eV
α = 25.4×10^{-40} Fm^2

———— zero overlap. Least squares fit: D_1 = 1.56 eV
α = 19.4×10^{-40} Fm^2

● ● ● ● experimental

The Gyftopoulos and Steiner theory is an improvement on the Gyftopoulos and Levine theory in four major respects:

a the $G(\theta)$ term used for the adsorbate-adsorbate interaction is replaced by the more specific Morse function;

b the dipole moment is no longer derived from empirical relations but by maximising the bond energy;

c electronegativity is treated as a variable property and its orbital dependence is considered. In the Gyftopoulos and Levine theory electronegativity is taken as an invariant property of the metal;

d because work function is defined as the neutral electronegativity of the surface atoms the theory can be extended to include systems other than bimetallic[103] (appendix 1).

2.2.6 limitations of the classical ion-image model

In all adsorption theories the dipole length must be known in order to calculate the dipole moment. This length is taken either as the ion-image distance (MacDonald and Barlow[95], Rasor and Warner[91]) or as the sum of the adsorbate and substrate metallic radii (Gyftopoulos and Levine[65], Gyftopoulos and Steiner[99]). Gadzuk[104] has made a detailed calculation of dipole moment based on a model in which the metal tends to screen the field due to the ion at the surface. In the limit of the metal being a perfect conductor the screening charge becomes equal to the classical ion-image charge. However, for an ion only a few Angstroms from a real metal surface the image model is of limited usefulness. The screening mechanism is a combination of two processes: the broadened and shifted valence level of the adsorbed atom is partially filled with charge by an amount depending

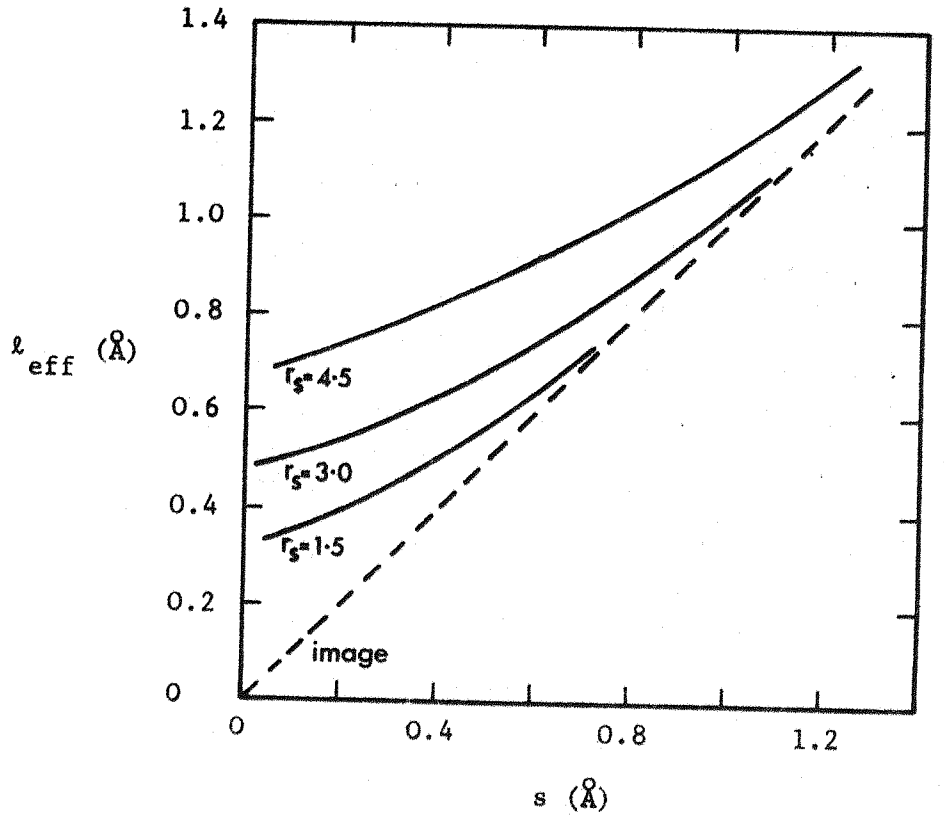

figure 2.9
effective dipole length as a function of adatom-metal separation s for 3 values of inter-electron separation r_s

on the extent of its overlap with the metal conduction band (section 2.1.4). The screening produced by this charge is the first process. The effective charge left on the adatom polarizes the electrons in the metal causing a redistribution of charge that also screens the ion. A self-consistent treatment applied to this model produces the result shown in figure 2.9 where s is the adatom-metal separation, ℓ_{eff} is the effective charge separation and r_s is the interelectron separation, a dimensionless quantity defined by the electron density N:

$$\frac{1}{N} = \frac{4}{3}\pi(r_s a_o)^3$$

where a_o is the Bohr radius. The dashed line represents the classical image dipole. For the highest electron density (that closest to a perfect conductor) the volume polarization effects die out most rapidly as the adatom moves away from the surface and the polarization looks like surface charge and hence image dipoles. As the density of electrons decreases, the ion field penetrates farther into the metal and hence the dipole length formed by the adatom and its screening charge appears larger than that of the image dipole.

2.3 effect of substrate structure on adsorption

All the adsorption theories discussed so far have been concerned with particles adsorbed on to a substrate surface which has a density of sites σ_f. Consequently it is important to establish the position of adsorption sites on each surface so that the number of adatoms of a given size that can be accommodated by the surface can be estimated. Provided that the adsorbing atoms have sufficient mobility on striking the surface they will move to the local positions of highest binding energy. Neustadter and Bacigalupi[105] have calculated the binding energy for a large number of positions on the surfaces of body-centred-cubic metals and so have deduced the positions of adsorption sites. A Lennard-Jones 6-12 potential (equation 2.1) is assumed which, because it is derived for physisorption, can only be expected to give qualitative results for chemisorption. However, as was pointed out in section 2.1.2.2, a generalized form of the Lennard-Jones potential does accurately describe metallic adsorption.

Neustadter, Luke and Sheahan[106] have used the 6-12 potential to calculate adsorption energies in agreement with experiment for low coverages of alkali metals on tungsten. In the present case only the position of the maximum adsorption energy is required.

The minimum, $E = E_o$, in the Lennard-Jones potential (equation 2.1) occurs at $r = 2^{1/6}\sigma$. This separation is taken as the sum of the adsorbent and adsorbate radii R so that $\sigma = 2^{-1/6}R$. Thus equation 2.1 can be written:

$$E_i = 4E_o\left[-\frac{1}{2}\left(\frac{R}{r_i}\right)^6 + \frac{1}{4}\left(\frac{R}{r_i}\right)^{12}\right]$$

Assuming pairwise additivity of the interactions between the adsorbate and substrate atoms i, the total energy E is given by:

$$\frac{E}{4E_o} = \frac{1}{4}\left(\frac{R}{a}\right)^{12}\sum_i\left(\frac{1}{d_i}\right)^{12} - \frac{1}{2}\left(\frac{R}{a}\right)^6\sum_i\left(\frac{1}{d_i}\right)^6 \qquad 2.70$$

where a is the lattice constant of the substrate and $d_i = r_i/a$. Thus the ratio R/a defines the adsorbate-substrate system. In the present work the summation in equation 2.70 is made over all substrate atoms contained in a hemisphere of radius L lattice constants centred on the adsorbate position. For each prospective site the energy is calculated as the adsorbate particle is moved along an axis perpendicular to the surface; the minimum in the curve then defines the binding energy. This whole procedure was carried out for 400 prospective sites in the unit cell for each surface. The binding energy for positions between these points was found by interpolation. Using this procedure topographical maps of the normalized energy $E/4E_o$ were constructed for each substrate orientation and for each adsorbate-substrate system. The calculation was performed on an ICL 1907 computer at Southampton University Computation Department and the results are discussed

in section 9.1. It is interesting to note here that increasing L from 5 to 7 produced less than 1% change in the binding energy, and that even for L = 2 the topographical map contained the important features. The number of atoms involved in the summations for L = 2, 5, 7 are 30, 450 and 1040 respectively. Since the computation time is directly related to the number of atoms summed there seems little point in using twice the amount of time required for L = 7 (as was done by Neustadter and Bacigalupi) rather than L = 5. Consequently the latter value was used in this work.

CHAPTER 3 MEASUREMENT OF WORK FUNCTION

introduction

A comprehensive review of methods of determining work function is given by Rivière[31]. There are six basic methods:

a thermionic emission

b photoelectric emission

c field emission

d contact potential difference

e retarding field technique

f surface ionization[217]

although these can be further subdivided. In this work methods which come under categories (d) and (e) were used: the Zisman[108] modification of the Kelvin[109] contact potential difference technique (d), and the Anderson[110] retarding field technique (e).

Since the conditions under which measurements are made (temperature, applied field, preparation of specimen) are different, each method cannot be expected to yield the same value. In practice most surfaces do not have a uniform work function, and since each method averages the work functions of a collection of patches, each with its own work function in a different way, the resulting values can be very different. Calculation of the effect of patches in each of the six cases is complex. Herring and Nichols[10] discuss these effects for cases (a) and (e) above and Rivière[31] summarizes them for cases (b), (d) and (f). The following is a brief review of the material relevant to this work.

3.1 thermionic emission

The saturation current from a metal under zero field conditions is given by the Richardson-Dushman equation as:

$$i = As\,(1-r_e)\,T^2 \exp(-e\phi/kT) \qquad 3.1$$

where $A = \frac{4\pi mek^2}{h^3} = 1.20 \times 10^6$ A m^{-2} deg K^{-2}

$= 120$ A cm^{-2} deg K^{-2} ,

s is the emitting area, r_e the reflection coefficient at the emitting surface with zero field, T the absolute temperature and ϕ the true work function of a uniform surface (section 1.1).

3.1.1 Richardson work function

According to equation 3.1 if $r_e = 0$ and ϕ is not temperature dependent then a plot of $\log_e (i/T^2)$ versus 1/T (Richardson line) yields a straight line of slope $-e\phi/k$ and intercept $\log_e(As)$. In practice, equation 3.1 with $r_e = 0$ and ϕ independent of temperature does not accurately describe emitting surfaces with the result that A determined from the intercept is rarely equal to the theoretical value. (This situation is complicated by the fact that s, the emitting area, is not measurable because of surface roughness). Consequently an apparent (or Richardson) work function ϕ^* and emission constant A^* are defined:

$$\phi^* = \frac{d\,(\log_e i/T^2)}{d(1/T)} \qquad 3.2$$

and $\log_e A^* = (\log i/T^2)_{1/T \to 0}$ 3.3

3.1.2 effective work function

Hensley[111] has advocated the use of an effective work function defined as the value obtained by direct substitution into equation 3.1 with $r_e = 0$ and $A = 1.20 \times 10^6$ A m^{-2} deg K^{-2}.

Thus $$i = AsT^2 \exp(-e\phi_E/kT) \qquad 3.4$$

The relationship between ϕ^* and ϕ_E can be calculated by substituting i from equation 3.4 into equation 3.2:

$$\phi^* = \phi_E - T\frac{d\phi}{dT} \qquad 3.5$$

From equations 3.3, 3.4, 3.5:

$$A^* = As \exp\left(-\frac{e}{k}\frac{d\phi}{dT}\right) \qquad 3.6$$

Combining equations 3.5 and 3.6:

$$\phi_E = \phi^* + \frac{kT}{e}\log_e\left(\frac{As}{A^*}\right) \qquad 3.7$$

ϕ_E is of more use than ϕ^* since it alone determines the emission, whereas ϕ^* is of little value unless A^* is also quoted. ϕ_E and ϕ^* are clearly equal only at T = 0 or if $A^*/s = A$. Deviations of A^*/s from A are attributed in this analysis only to the dependence of ϕ on T, with the consequence that ϕ_E is independent of T but dependent on r_e.

3.1.3 Schottky effect

When the field at the surface is non-zero the work function is altered. The potential at a distance x from the surface is modified by the image potential $-e^2/4x$ and the applied potential $-eEx$ as shown in figure 3.1.

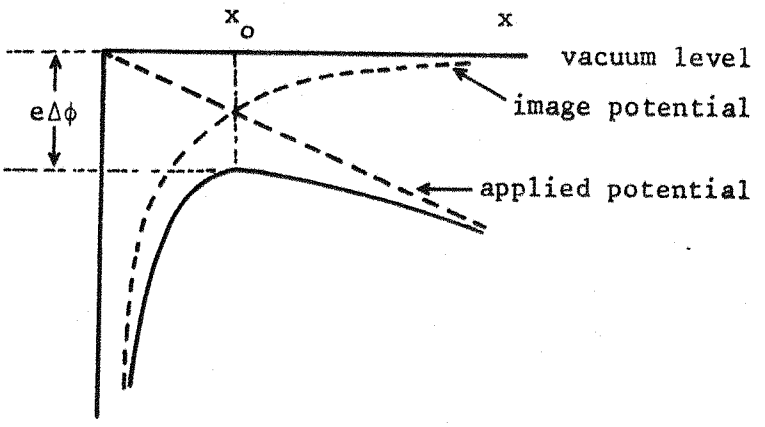

figure 3.1
Schottky lowering of the work function

There is then a maximum potential at $x_o = \frac{1}{2}(e/E)^{\frac{1}{2}}$ which is below the vacuum level by an amount $(eE)^{\frac{1}{2}}$. The work function is reduced by this amount so that equation 3.1 becomes:

$$i = As\,(1-r_e)\,T^2 \exp\left[-\frac{e\{\phi - (eE)^{\frac{1}{2}}\}}{kT}\right] \qquad 3.8$$

3.2 retarding field (Anderson) technique

The current in the retarding field region of the current/voltage characteristic of a diode is given by[42]:

$$i_r = As_c\,(1-r_c)\,T^2 \exp\left[-\frac{e}{kT}(\phi_c - V_a)\right] \qquad 3.9$$

where s_c is the area of the electron beam at the collector, r_c is the reflection coefficient at the collector, ϕ_c is the collector work function and V_a is the applied voltage (V_a is negative in the retarding field region). Equation 3.9 demonstrates that i_r is independent of emitter work function. This can be seen in figure 3.2 where the potential is shown for two emitter work functions ϕ_e and ϕ_e'. In order to be collected electrons must pass over a barrier of height $\phi_c - V_a$. The retarding field technique is thus

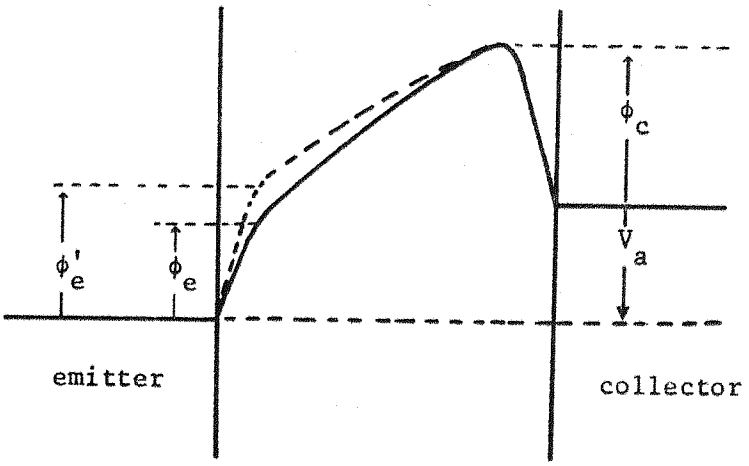

figure 3.2
potential in a
retarding field diode

only capable of measuring changes in the collector work function. The current i_r and emitter temperature T are kept constant as the collector work function is changed. From equation 3.9, a change from ϕ_{c1} to ϕ_{c2}, assuming s_c and r_c remain constant, causes a displacement in the current/voltage characteristic of:

$$-(V_{a1} - V_{a2}) = \phi_{c1} - \phi_{c2}$$

Thus a decrease in collector work function is compensated by a displacement to more negative V_a. The accuracy of this technique is determined by the parallelism of the current/voltage characteristics since any deviation from parallelism makes it impossible to decide what value of displacement is the correct one. Generally, the difficulty with this method is that the reflection coefficient r_c is not constant during adsorption on to the collector[112-114].

3.3 photoelectric technique

At T = 0 K the maximum energy attained by an electron after adsorbing a

photon of energy $h\nu$ and overcoming a potential barrier $e\phi$ is[115]:

$$E_{max} = h\nu - e\phi$$

In principle the photoelectric method consists of lowering the frequency until the photoelectric current falls to zero. At this point: $E_{max} = 0$, $\nu = \nu_o$ and $e\phi = h\nu_o$.

However for T > 0 K electrons can be emitted from higher energy levels by photons with $\nu < \nu_o$, causing the photoelectric cut-off to be gradual rather than sharp. In order to overcome this difficulty Fowler[116] developed a theory to account for the temperature dependence of photoelectric emission. The Fowler equation is the basis for photoelectric work function measurements. The photoelectric current near the threshold is given by:

$$i_p = H T^2 p \{(h\nu - h\nu_o)/kT\} \qquad 3.10$$

where H is a constant independent of T and ν, and p is a universal function of the quantity $(h\nu - h\nu_o)/kT$, where ν is close to ν_o.

3.4 field emission technique

Application of very high fields causes the surface potential barrier width to decrease so that the probability of tunnelling increases to the point at which the emitted electrons are easily measurable. The field emission current is given by the Fowler-Nordheim[117,118] equation as:

$$i_f = 1.54 \times 10^{-6} \frac{\beta^2 V^2 s}{\phi t^2(y)} \exp\left[-6.83 \times 10^7 \frac{\phi^{3/2}}{\beta V} f(y)\right] \qquad 3.11$$

where V is the applied voltage, s is the emitting area, β is the geometrical factor relating the surface field to the applied voltage, and

t and f are image correction terms. To a first approximation equation 3.11 can be written:

$$i_f = A_f V^2 \exp \frac{\phi^{3/2}}{CV} \qquad 3.12$$

A Fowler-Nordheim plot ($\log_e i_f/V^2$ versus $1/V$) has slope $\phi^{3/2}/C$. Principle difficulty with this method lies in the assumption that the pre-exponential term A_f in equation 3.12 is constant on adsorption. Variation of A_f due to the field dependence of ϕ is analogous to the variation of A in equation 3.1 due to the temperature dependence of ϕ in the Richardson method.

3.5 the Kelvin technique

When two metals at the same temperature are in electrical contact the Fermi levels are the same and the contact potential difference between the two is given by equation 1.2:

$$V_{c\ p\ d} = \phi_1 - \phi_2 \qquad 3.13$$

If the two metals are formed into a parallel plate condenser of capacitance C then the charge due to the contact potential difference is:

$$q = C\, V_{c\ p\ d}$$

If then a potential V_a is applied externally:

$$q = C\,(V_{c\ p\ d} + V_a)$$

A change in capacitance ΔC then causes the displacement of charge Δq in the external circuit given by:

$$\Delta q = \Delta C\,(V_{c\ p\ d} + V_a) \quad .$$

V_a is then adjusted until there is no charge flow, ie $\Delta q = 0$.

Then $V_{c\ p\ d} = -V_a$

In the Zisman modification[108] C is continually altered by vibrating one of the plates of the capacitor, the resulting alternating current being amplified and used to detect the null.

The limitation of this method is that one of the surfaces, the reference, must have a work function which is known.

3.6 effect of patchy surfaces on work function measurements

Generally real surfaces are not of uniform work function but can be considered as a collection of patches, each with its own true work function ϕ_i. The existence of adjacent patches of different work function gives rise to a patch field E_p, the effect of which dies out exponentially with distance from a flat surface[10]. The measured work function depends on the averaging process involved in the measurement techniques. These are briefly summarized.

3.6.1 Kelvin technique - patches

When the distance between the two plates is large in comparison with the dimensions of the patch field then the contact potential difference measured is the difference between the area averaged true work functions, given by:

$$\bar{\phi} = \sum_i f_i \phi_i$$

where f_i is the fractional area occupied by the ith patch.

3.6.2 Richardson method - patches

Herring and Nichols[10] discuss two limiting cases:

a collecting field strong in comparison with the patch field. $E >> E_p$;

b collecting field so weak that the position of the Schottky potential energy maximum (x_o in figure 3.1) lies outside the patch field.

Figure 3.3 shows the potential energy through high and low work function patches for the two cases. In the first case each patch emits independently according to equation 3.8 (figure 3.3a). The apparent work function of the composite surface is then given by:

$$\phi^{**} = \sum_i \omega_i \phi_i^{*}$$

where ϕ_i^{*} is the zero field apparent work function of the ith patch and ω_i is the fraction of the total emission from the ith patch. Thus ϕ^{**} is heavily weighted towards low work function patches so that $\phi^{**} < \bar{\phi}$.

In case (b) all patches ($i < k$) with work functions $\phi_i < \bar{\phi}$ see a potential energy maximum $\bar{\phi}$ (low work function patch figure 3.3b) and so emit as a single patch with effective work function $\bar{\phi}$. The remaining patches ($i \geq k$) with work functions $\phi_i > \bar{\phi}$ (high work function patch figure 3.3b) emit as in case (a). The complete apparent work function is then given by:

$$\bar{\phi}^{**} = \sum_{i \geq k} \omega_i \phi_i^{*} + \omega \bar{\phi}^{*}$$

where ω is the fraction of the total emission from patches $\phi_i < \bar{\phi}$ and $\bar{\phi}^{*}$ is the apparent work function of these patches defined by analogy with equation 3.2. Thus $\bar{\phi}^{**}$ is a little larger than $\bar{\phi}$. The difference between ϕ^{**} and $\bar{\phi}^{**}$ is approximately equal to the maximum work function difference between patches.

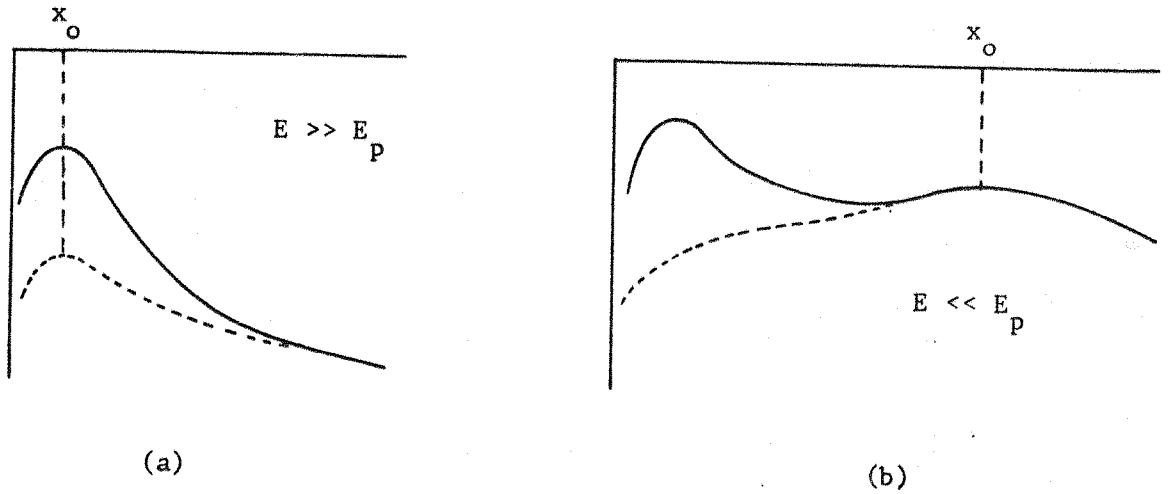

figure 3.3
potential energy through high work function patch
and low work function patch
for (a) strong field $E >> E_p$
(b) weak field $E << E_p$

3.6.3 photoelectric technique - patches

Just as for thermionic emission there is a photoelectric Schottky effect causing a reduction in the work function[119-121]. The effect of patches can again be discussed in the two limiting cases of (a) strong and (b) weak collecting fields. In case (a) each patch emits independently with the result that the apparent photoelectric threshold $h\nu_o^{**}$ is slightly greater than the lowest work function in the surface. As the temperature is raised $h\nu_o^{**}$ decreases towards the lowest work function (c.f. effective thermionic work function increases with temperature). In case (b) all patches with apparent thresholds $(h\nu_o^{*})_i < \bar{\phi}$ emit as one patch with effective threshold $\bar{\phi}$ whereas the others emit as in case (a). Generally the apparent weak field

photoelectric threshold $\overline{\overline{h\nu_o}}^{**} < \bar{\phi}$. As the temperature is raised the measured threshold approaches $\bar{\phi}$. Just as $\bar{\phi}^{**} > \phi^{**}$ so $\overline{\overline{h\nu_o}}^{**} > h\nu_o^{**}$.

3.6.4 Anderson (retarding field) technique - patches

Herring and Nichols[10] deduce that for a collector consisting of large patches each patch can be considered independently and the total current is given by the sum of currents to individual patches (equation 3.9). However, for patches small in comparison with the electrode spacing all patches on the collector with work function $\phi_i < \bar{\phi}$ are hidden from the emitter by a potential barrier $\bar{\phi}$. Thus in general the current corresponds to a collector work function greater than $\bar{\phi}$. Zingerman and Morozovskii[122] point out that electrons approaching the collector will be diverted by the patch field to patches of lower work function, thus yielding a current corresponding to a collector work function closer to $\bar{\phi}$. The situation is complicated by the fact that the reflection coefficient r_c varies in usually an unknown way with patches. This should not be confused with the equivalent reflection coefficient which is the value obtained for r_c from equation 3.9 assuming a collector work function of $\bar{\phi}$ (ie this definition takes account of patch effects in the reflection coefficient). The Anderson technique is usually used to determine the contact potential difference caused by adsorption on the collector. The resulting c p d clearly depends in a complex way on the work functions and reflection coefficients of the patches of both initial and final surfaces. Anderson[123], in a comparison of the retarding field technique with the Kelvin technique, found there was no observable difference for the silver-barium system. However, since both surfaces were presumably patchy to an unknown extent no wider conclusions can be drawn.

Hopkins and Smith[124] attempted the same comparison for the barium on tungsten adsorption system but simplifying the situation by using a tungsten single crystal substrate. Thus only the final barium covered surface was patchy. For barium on (110) tungsten the contact potential difference obtained by the Kelvin method was 150 mV greater than that obtained by the Anderson method. This could be accounted for either by the existence of barium patches whose work function differed by $\sim$ 1.0 eV, or by a change in the average reflection coefficient from zero for tungsten to 0.6 for barium.

A study of the adsorption of uranium on single crystals of tungsten has been made by Lea and Mee[125] using Kelvin, Anderson and photoelectric methods. In all cases the contact potential measured increased in the order Anderson, Kelvin, photoelectric, thus confirming the above.

Since the Kelvin technique is the only method in which the simple area averaged work function $\bar{\phi}$ at zero field is measured, it was used for most of the present work. Some considerations of the suitability of Kelvin and Anderson methods are discussed in sections 7.1.1 and 7.2.4.

CHAPTER 4 PREVIOUS MEASUREMENTS

4.1 structure of uranium

A review of the metallurgy of uranium is given by Holden[126]. The bulk metal is known to exist in 3 allotropic forms, α, β and γ. The α-phase, stable below 938 K, has an orthorhombic structure[127] and consists of corrugated rows of atoms as shown in figure 4.0. The lattice constants are a_o = 4.945, b_o = 5.865, c_o = 2.852 Å. The structure of the β-phase, which exists in the temperature range 938-1043 K, is complex and has not yet been resolved. However, Tucker[128-130] has shown that it is tetragonal with lattice constants $a_o = b_o$ = 10.52 Å, c_o = 5.57 Å and has a unit cell containing 30 atoms. Above 1043 K the γ-phase exists. Wilson and Rundle[131] first established the structure as body-centred-cubic with a lattice constant of 3.48 Å at 1100 K.

Addition of chromium or molybdenum in trace amounts depresses the phase transformation temperatures considerably. Tucker[129] used this method in conjunction with 'quenching' in order to study the structure of β-uranium at room temperature. Holden[132] describes in detail the procedure for manufacturing large crystallites of β-uranium but points out that at ambient temperatures they are only quasi-stable. Wilson and Rundle[131] used the same technique to lower the β-γ transition point but state that it is not possible by this method to obtain the γ-phase at room temperature. Duwez[133] investigated how rapid quenching alone lowers the transition points. A cooling rate of 8000 K sec^{-1} lowers the α-β transformation temperature by 250 K and the β-γ temperature by 150 K. Again no work has been reported in which the β-γ transition point has been reduced to room temperature.

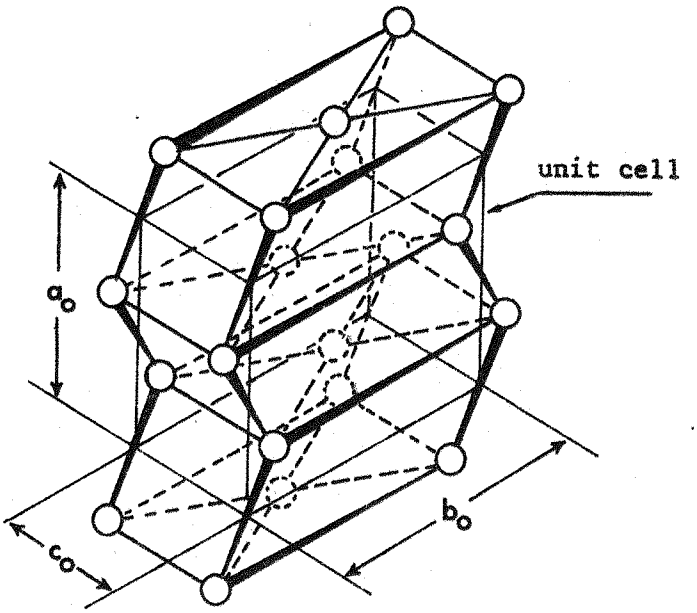

a_o = 4.945 Å

b_o = 5.865 Å

c_o = 2.852 Å

figure 4.0
crystal structure of alpha uranium

thin films of uranium

Chatterjee[134] evaporated films of uranium in a vacuum of 10^{-4} torr and observed them by electron diffraction. He reported microcrystallites of β-uranium existing at room temperature. However, Donohue[135] re-examined Chatterjee's diffraction patterns and showed they were not due to β-U nor to α-U, γ-U, UO_2, U_3O_8, UC or UN. Recently Rivière[136] also re-examined Chatterjee's work and concluded that the diffraction pattern was that of α-UH_3 (not considered by Donohue). The curious fact that no lines corresponding to UO_2 were reported by Chatterjee may mean that his vacuum conditions were very much better than he thought.

Kolomiets[137] also attempted to produce β-uranium films at room temperature. He evaporated uranium from a tungsten coil on to quartz and rock salt substrates in a vacuum of 2×10^{-5} torr. They were then transferred to an electron microscope for study. He was able to show that a film 200 Å thick, exposed to the atmosphere for one hour, was entirely transformed to UO_2. When the films were more rapidly transferred the diffraction patterns showed mainly UO_2 and some α-U but no β-U. He also attempted to evaporate uranium inside the microscope column (10^{-4}torr) but found that only UO could be observed. Rivière[136], for the purpose of comparison with Chatterjee's work, evaporated uranium in a vacuum of 10^{-5} torr on to carbon electron microscope grids, transferring them rapidly to the microscope. Using low beam intensity he observed α-UH_3 apparently grown epitaxially on α-U although the evidence for the presence of the latter was scant. UO_2 was also present, but in lower concentration than α-UH_3. After the film had been heated by the electron beam at full intensity, α-UH_3 rings had become faint, UO_2 strong and supposed α-U lost. Since the pressure in the microscope (10^{-3} torr) was predominantly due to water vapour, Rivière proposed that the following reaction occurred under beam heating:

$$U + 2H_2O \rightarrow UO_2 + 2H_2$$

$$2U + 3H_2 \rightarrow 2UH_3$$

evaporation of uranium

The problem with evaporation of uranium is that it is oxidized very readily by the residual gas in the vacuum system. Deiss[138] has shown that at 10^{-10} torr oxidation during evaporation by the collision of uranium atoms with oxygen molecules is negligible; most oxidation occurs in the solid phase. He also found that addition of 1 at % of carbon to the uranium was

very effective in preventing oxidation. Films evaporated in an electron microscope without carbon showed UO_2 only, whereas those with carbon showed α-U only. The suggested mechanism was:

$$2C + O_2 \rightarrow 2CO$$

$$UO_2 + 2C \rightarrow U + 2CO$$

Curiously Deiss never observed UH_3.

4.2 work function of uranium

Oxide contamination of uranium cannot be removed by heating below ∿2000 K[139] and since the melting point is only 1403 K it follows that no bulk sample can be free from oxide. For this reason work function measurements on bulk uranium are of little value. These are summarized in table 4.1. Of necessity Richardson measurements refer to the γ-phase.

table 4.1 work function measurements on bulk uranium

		α-U	β-U	γ-U	method
Dushman[140]	1923			3.28	Richardson
Dushman et al[141]	1927			2.84	Richardson
Rentschler[142]	1930	3.87			photoelectric
Klein and Lange[143]	1938	4.32			Kelvin
Hole and Wright[144]	1939			3.58†	Richardson
Rauh and Thorn[145]	1959			3.87†	Richardson
Fry and Cardwell[146]	1962	3.47	3.52	3.39	photoelectric
Rivière[6]	1962	3.09			Kelvin

† corrected to effective work function

Hole and Wright made an attempt to remove the oxide by heating uranium foil in dried hydrogen. The effect was to reduce the work function to 3.27 eV. Rauh and Thorn, in trying to reproduce Hole and Wright's work, succeeded only in reducing the work function to 4.07 eV and proposed that the 3.27 eV value must have been contaminated by oxide. Fry and Cardwell also noted that the work function decreased during the cleaning procedure. Initially 4.0 eV, after heating for 1000 minutes at 1250 K the α-phase work function had dropped to 3.47 eV. Rivière, however, found that electron bombarding uranium foil for 40 hours at 1350 K increased its work function from ∿2.1 to 3.09 eV. The initial low value, he suggested, was due to UO_2, and the increase the result of the reaction:

$$UO_2 + U \rightarrow 2UO$$

thus implying that UO has a higher work function than UO_2. Earlier photoelectric measurements by Rentschler and Henry[147] in which oxygen was adsorbed on to a sputtered uranium film confirmed this: small addition of oxygen reduced the work function whereas large amounts increased it. It is thus feasible that the uranium was coated in UO and heating in poor vacuum caused further oxidation to UO_2, reducing the work function.

It is well established[148,149] that atomic hydrogen, produced by dissociation of molecular hydrogen at a heated filament, readily combines with tungsten oxides in a vacuum tube, releasing water vapour. Thus in Hole and Wright's case reactions such as:

$$U + 2H_2O \rightarrow UO_2 + 2H_2$$

$$UO + H_2O \rightarrow UO_2 + H_2$$

may well have occurred, again causing a reduction in work function.

Work function measurements on evaporated films of uranium are summarized in

table 4.2 work function measurements on evaporated films of uranium

		α-U	β-U	γ-U	method	system
Rentschler et al[150]	1932	3.63			photoelectric	sputtered on to Ni in Ar
Rauh, Thorn[145]	1959			3.37†	Richardson	1 monolayer evaporated on to W foil
				3.47†	Richardson	10-200 monolayers on W foil
Rivière[6]	1962	3.19			Kelvin	thick film on W foil
Haas, Jensen[151]	1963			3.28†	Richardson	1 monolayer on W wire
				3.45†	Richardson	several monolayers on W wire
Blott, Hopkins[152]	1965	3.6			Anderson	1 monolayer evaporated from UC on to W foil
Barry et al[7]	1967			3.36†	Richardson	1-2 monolayers on W foil
				3.45†	Richardson	10-20 monolayers on W foil
		3.63	3.58		Kelvin	1 monolayer on W foil
		3.63	3.58	3.53	Kelvin	20 monolayers on W foil
Lea, Mee[153]	1967	3.65	3.59	3.45	photoelectric	several monolayers on W foil
Collins, Blott[154]	1968	3.60	3.53	3.43	field emission	1 monolayer - total emission - W tip ††
Collins, Blott[155]	1969	3.38			field emission	12 monolayers - total emission - W tip ††
Collins[156]	1968	4.04			field emission	1 monolayer on (110) W †††
		3.88			field emission	1 monolayer on (100) W
present work	1969	3.90			Kelvin	1 monolayer on (110) W single crystal
		3.80			Kelvin	1 monolayer on (100) W single crystal

† corrected to effective work function

†† substrate work function taken as 4.50 eV (c.f. 4.55 eV for W foil)

††† substrate work function taken as 5.20 eV (c.f. 5.15 eV in present work)

table 4.2. Kelvin, photoelectric and field emission values of β-U and γ-U refer to room temperature measurements on films which have been heated to temperatures in the β and γ ranges.

Rentschler et al[150] give no details of conditions and it is unlikely that at that date clean surfaces could be produced. Rauh and Thorn[145] took great care with their measurements: uranium was degassed at 2000 K and one third had evaporated before measurements were begun. The residual pressure was 2×5^{-10} torr. The Richardson work function increased from 3.0 eV at 1 monolayer, reaching a steady value of 3.47 eV at 15 monolayers. This latter value was maintained up to 200 monolayers (figure 4.1). However, when the Richardson work function is corrected to the effective work function using A values which have been published elsewhere[157], the variation with thickness is greatly reduced (figure 4.1) and can probably be accounted for by errors in the measurement of A. The final steady value, 3.47 eV, is the same as the Richardson work function since the A value is close to the theoretical 1.20×10^{6} A m^{-2} deg K^{-2}. Rauh and Thorn also noted a minimum in the work function/coverage curve at ∿0.5 monolayer although no detailed measurements are given. Haas and Jensen[151] evaporated uranium, degassed at 1800-2000 K, on to tungsten wire. The residual pressure was in the low 10^{-10} torr range. At 1 monolayer coverage they reported an effective work function of 3.28 eV but for thicker films the emission current was half an order lower, corresponding to an effective work function of 3.45 eV in good agreement with Rauh and Thorn.

Rivière[6] attempted to establish finally the work function of evaporated films of uranium. A very precise Kelvin technique with aged polycrystalline foil as a reference was used in conjunction with excellent vacuum conditions

(5×10^{-11} torr). After evaporating a thick film of uranium on to tungsten foil the work function (3.19 eV) remained unchanged for 30 hours. Although the residual pressure was undoubtedly very low, no indication is given of the pressure during evaporation, nor are details of the exact uranium degassing procedure available. However the 3.19 eV value was very reproducable.

Blott and Hopkins[152] report Anderson (retarding field) measurements on the evaporant, believed to be uranium, from UC. A monolayer film of this evaporant, produced by heating UC at 2200 K for 20 minutes, had a work function of $\sim$3.6 eV, considerably above Rivière's value for uranium. Lower values, down to 3.0 ev, were obtained if the film was oxide contaminated.

Barry, Hopkins and Sargood[7] made both Kelvin and Richardson measurements on uranium films evaporated on to tungsten foil. The uranium was degassed above 2000 K, $\frac{3}{4}$ of it having evaporated before measurements were begun. During evaporation the pressure was always $< 2 \times 10^{-10}$ torr. Richardson measurements produced effective work functions of 3.36 eV for a film of 1-2 monolayers and 3.45 eV for 10-20 monolayers, values in good agreement with Rauh and Thorn. Kelvin measurements on a film a few monolayers in thickness gave the work function as 3.63 eV. After this film was annealed, the (room temperature) work function showed abrupt changes at annealing temperatures close to the crystallographic phase transition temperatures of bulk uranium. However, unlike the phase transitions, these changes were irreversible. Kelvin work function versus annealing temperature is shown in figure 4.2. Above 1800 K the work function rose as the uranium was desorbed. Barry et al suggest that uranium is deposited in an amorphous state; at 950 K, close to the bulk α/β phase transition, the uranium

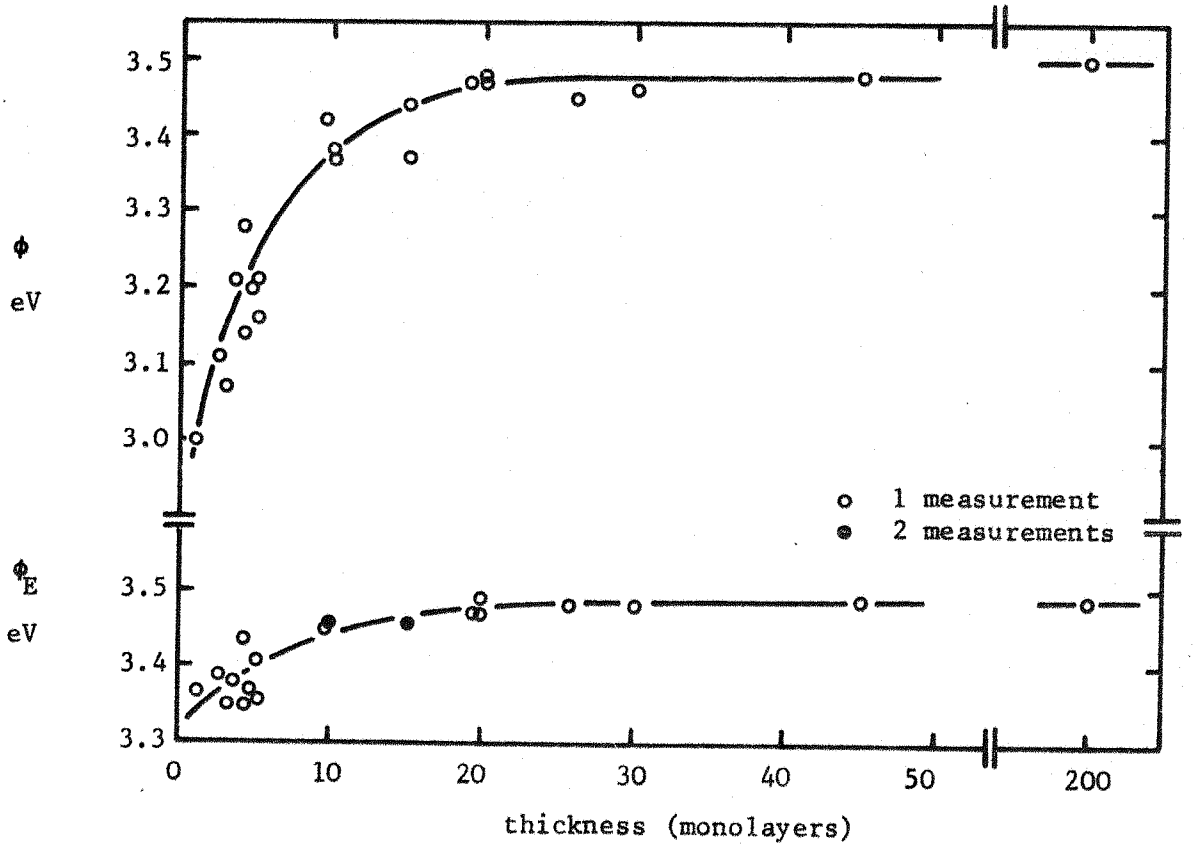

figure 4.1 Richardson work function ϕ, and effective work function ϕ_E, due to Rauh and Thorn. ϕ_E at 1300 K

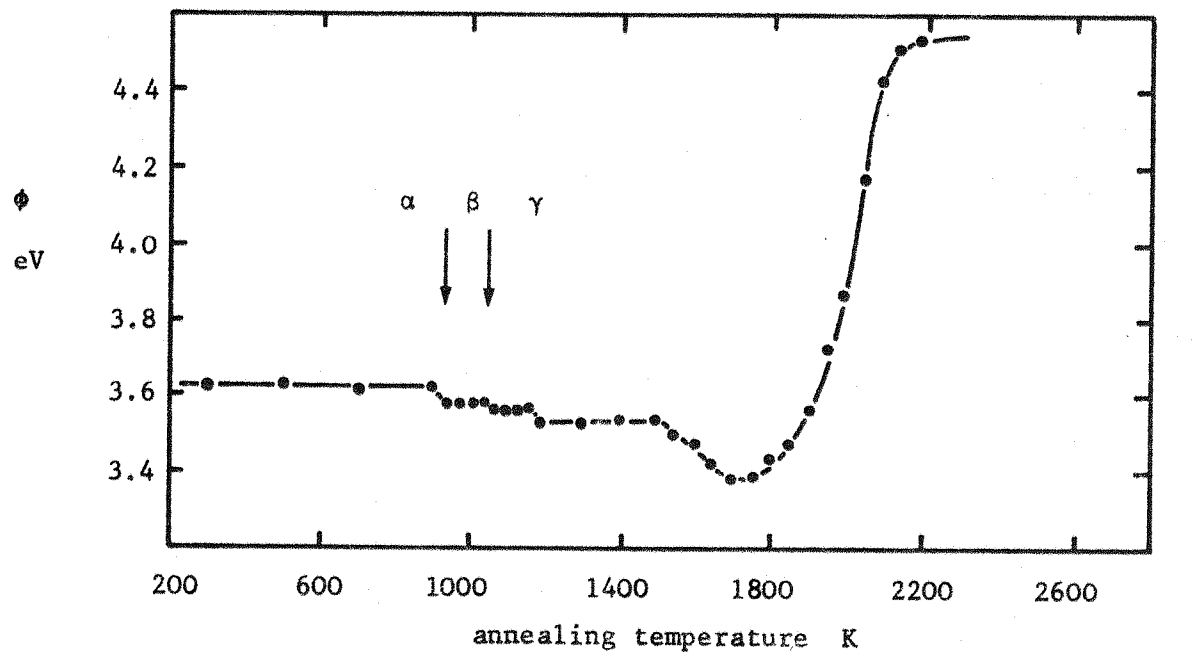

figure 4.2 Kelvin work function after annealing a monolayer film of uranium on polycrystalline tungsten due to Barry et al.

becomes mobile and forms a β-U structure possibly in islands; finally the β-U structure changes to γ-U.

Similar abrupt changes in work function for monolayer uranium films evaporated on to polycrystalline tungsten have been observed by Lea and Mee[153] using a photoelectric method, and by Collins and Blott[154] using field emission. However Collins and Blott[155] find that these changes, apparent at a coverage of 1.5, had completely disappeared at a coverage of 2. Collins and Blott[155] also found that as the coverage increased, the work function steadily dropped, reaching 3.38 eV at 12 monolayers and still falling. They suggested that the discrepancy between Rivière's 3.19 eV value and the higher values was simply due to thickness, monolayer films having a work function of ∿3.6 eV and thick films 3.19 eV.

Collins[156], using a probe-hole technique, measured the field emission work function of uranium on single crystal faces of tungsten. The values for (110) and (100) tungsten substrates were 4.04 eV and 3.88 eV respectively. These measurements were all made under clean conditions, the pressure during evaporation being $< 2 \times 10^{-10}$ torr.

4.3 structure of zirconium

A review of the metallurgy of zirconium is given by Miller[158]. Zwikker[159] first discovered that zirconium has two allotropic modifications. The α-form is close-packed-hexagonal with lattice constants 3.23 and 5.13 Å and is stable up to 1135 K. The β modification which is stable from this temperature to the melting point (2120 K) is body-centred-cubic with lattice

constant 3.62 Å. The temperature at which transformation begins can be depressed by rapid quenching, but not suppressed. Similarly, addition of small amounts of titanium lowers the transition point by 100 K. Oxygen, however, which is absorbed in very large amounts at elevated temperatures, raises the transition point. De Boer and Fast[160] reported that after absorbing 10 atomic per cent of oxygen the transition occurred as high as 1800 K. Hydrogen, unique in that it absorbs reversibly[161], lowered the transition point (according to Fitzwilliam et al[162]) by 200 K. However, it is not clear that the high temperature structure was that of β-Zr.

4.4 work function of zirconium

Zirconium forms a protective layer of oxide, ZrO_2, during exposure to the atmosphere. Although oxygen cannot be removed by heating in vacuum[163] the oxide dissolves into the bulk at ∿720 K[164] producing a surface closer to that of the clean metal. Work function measurements of zirconium are summarized in table 4.3. The first 8 of these measurements were made under vacuum conditions which preclude their interest. The field emission work of Shrednik[169] was performed in a sealed-off tube; no indication of pressure is given. The work function/coverage curves showed no minima and the final (monolayer) values varied in the range 3.2 - 3.5 eV. Shrednik[170] gives no details of the experiment in which the 3.84 eV value was measured although it is in good agreement with the present (polycrystalline tungsten substrate) work.

The first reported work in which well degassed zirconium was evaporated in good vacuum conditions is that of Collins and Blott[172]. The zirconium was

table 4.3 work function measurements of zirconium

		w f	method	system
Dushman[140]	1923	3.28	Richardson	ZrO_2 heated on W wire
Dushman et al[141]	1927	3.15	Richardson	ZrO_2 heated on W wire
Zwikker[165]	1929	4.13	Richardson	Zr wire
Rentschler et al[150]	1932	3.73	photoelectric	Zr sputtered on to Ni in Ar
Klein and Lange[143]	1938	3.60	Kelvin	Zr foil in Ar
Wahl[166]	1951	3.91†	Richardson	Zr wire
		3.88	photoelectric	Zr wire
Wright[167]	1953	3.51†	Richardson	thick film evaporated on to W foil
Malamund et al[168]	1954	4.33	photoelectric	Zr foil
Shrednik[169]	1958	3.2-3.5	field emission	total emission - 1 monolayer evaporated on to W tip
Shrednik[170]	1961	3.84	field emission	total emission - evaporated on to W tip - no details
Dyubua and Popov[171]	1962	4.0	Richardson	Zr wire
Collins and Blott[172]	1968	3.84	field emission	total emission - 1 monolayer evaporated on to W tip
Collins[156]	1968	4.46	field emission	1 monolayer on W(110) plane
		3.87	field emission	1 monolayer on W(100) plane
present work	1969	3.88	Kelvin	1 monolayer on poly-crystalline W foil
		4.28	Kelvin	1 monolayer on W(110) single crystal
		3.75	Kelvin	1 monolayer on W(100) single crystal

† corrected to effective work function

degassed at 2100 K and evaporated at a pressure of $< 1 \times 10^{-10}$ torr. A monolayer film evaporated on to a tungsten field emitter tip had a work function of 3.84 eV. Collins[156], using a probe-hole technique, also measured the work function of zirconium on single crystal faces of tungsten. For (110) and (100) faces the monolayer values were 4.46 eV and 3.87 eV respectively. In all cases a minimum in the work function/coverage curve was observed.

4.5 work function of tungsten single crystals

Measurements of the work function of tungsten single crystals made since 1940 are listed in table 4.4. It is clear that the values decrease in the order (110), (211), (100), (111) which is expected from the surface free energies (section 1.1). However there is far from good agreement on the absolute values. This is probably a reflection of the different surface preparation treatments, vacuum conditions and measurement techniques. Recent evidence[173] suggests that carbon can be removed from the surface only by heating above 3000 K, a procedure which has only been adopted in more recent measurements but which may cause thermal etching of the higher (less stable) index planes[174]. Carbon may also be removed by heating to lower temperatures in the presence of oxygen[175,176], but again this process causes surface damage: faceting[366]. (110) tungsten has the lowest surface free energy so it would be expected to be the most stable. However, field emission measurements on this orientation give values considerably higher than measurements on macroscopic single crystals, suggesting that the latter may be thermally damaged[178]. Plummer and Rhodin[179] concluded from direct observation in a field ion microscope that the work function of the (110)

face was very sensitive to the degree of surface perfection on an atomic scale. Included in table 4.4 are the values obtained in the present work as well as those derived from the Steiner and Gyftopoulos[18] theory. Both are discussed in section 8.1.

table 4.4

work functions of single crystals of tungsten measured since 1940

date	author	method	(100)	(110)	(111)	(211)	(311)	(611)	notes
1940	Nichols[180,181]	Richardson†	4.56	4.98	4.57	4.68		4.51	a
1943	Müller[182]	field emission		6.0					
1948	Apker et al[183]	photo-electric	4.49						b
1950	Brown et al[184]	Richardson	4.59						c
1951	Becker[185]	field emission	4.60	>4.9	4.40	4.8		4.2	
1952	Smirnov[187] et al	field emission	4.6	5.5	4.2	4.9			
1952	Andreev[188]	field emission		4.60	4.3				
1953	Wilkinson[189]	field emission	4.97	4.68	4.64	4.93		4.49	
1953	Drechsler[190] et al	field emission		5.70					
1954	Dyke et al[191]	field emission		5.0-5.5					d
1954	Smith[192]	Richardson†	4.54	5.26	4.50	4.65		4.45	e
1955	Hutson[193]	m v a	4.52	5.17	4.39	4.69		4.34	f
1955	Smith[194]	m v a							
1955	Müller[195]	field emission		5.70-5.99	4.39	4.65-4.88		4.30	
		s i (Al)		>5.96					g
1955	Houston[196]	field emission	4.71					4.26	
1956	Shuppe[197] et al	Richardson†		4.66		4.70			
		s i (Na)		5.14					

date	author	method	(100)	(110)	(111)	(211)	(311)	(611)	notes
1957	Eisinger[198]	photo-electric					4.54		
1958	Eisinger[199]	photo-electric					4.54		
1958	Eisinger[200]	photo-electric					4.53		
1959	Hughes[201] et al	Richardson†		5.43		5.39			
		s i (Na)		5.25		5.25			
1960	Gienapp[202]	Richardson	4.60	5.20	4.2	5.3			c
1961	Anthony[203] et al	Richardson		4.8					c
1962	Love et al[204]	Shelton					4.21		
1962	Sytaya[205] et al	Richardson†	4.66	5.30					
		s i (Ba)		4.82					
1962	Gavrilyuk[206] et al	Kelvin					4.55		
1962	Gofman[207]	field emission	4.6	5.6	3.9			4.3	
1962	Young et al[208]	field emission		5.96					
1962	Gofman[209]	field emission	4.7	6.0	4.0			4.3	
1963	Reynolds[210]	s i (Sr,Ca)		5.41	4.49				
1963	van Oostrom[211]	field emission			4.40			4.20	
1963	Stafford[212] et al	photo-electric			4.32				
1964	Sultanov[213]	Richardson†		5.10	4.48			4.39	
1964	Gorodetskii[214] et al	Anderson		5.3					h
1964	Holscher[215]	field emission	5.2		4.40		4.50	4.30	

date	author	method	(100)	(110)	(111)	(211)	(311)	(611)	notes
1964	Oguri[216]	field emission			4.46				
1965	Fine et al[217]	Shelton		5.18					c
		s i (NaCl)		4.87					
1965	Delchar[218] et al	Kelvin	4.7	5.9	4.7				
1966	Azizov[219] et al	Richardson†	4.54	5.33	4.41	4.88			
1966	Protopopov[220] et al	Richardson†	4.60	5.35	4.40	4.80		4.32	i
1966	Young et al[178]	field emission		7.1-8.7					
1966	Gavrilyuk[221] et al	field emission		5.2		4.6			j
1966	Schmidt[222] et al	field emission	4.82	5.85	4.41	4.85			
1966	Hopkins[223] et al	Kelvin		5.05					
1966	Hopkins[224] et al	Kelvin	4.65	5.11					
1966	Hopkins[225] et al	Kelvin	4.65	5.11	4.45		4.65		
1967	Love et al[226]	Shelton					4.21		
1967	Hopkins[227] et al	Kelvin	4.64			4.73			
1967	Lee et al[228]	Kelvin	4.65	5.10					
1967	Ovchinnikov[229]	field emission	4.77	5.9	4.4	4.95			
1967	Gavrilyuk[230] et al	field emission		5.30	4.4	4.8			o
1967	van Oostrom[231]	field emission	4.65	6.0	4.2				

date	author	method	(100)	(110)	(111)	(211)	(311)	(611)	notes
1967	Swanson[232] et al	field emission		5.79					k
		field emission		5.15				4.32	l
		field emission	4.59	5.02	4.49	5.00			m
1967	Ermich[233]	field emission	4.74		4.40		4.35		
1967	Hopkins[234] et al	Kelvin	4.65	5.10	4.45		4.65		
1967	Maday et al[235]	Shelton		5.25					n
1967	Schmidt[236]	field emission	4.70	6.0	4.43	4.87			
1968	Hopkins[124] et al	Kelvin	4.66	5.12					
1968	Swanson[237] et al	field emission	4.57	5.70					
1968	Smith[238]	Kelvin					4.62		
1968	Hopkins[239] et al	Kelvin						4.59	p
1968	Abey[240]	Shelton	4.55						
1968	Lea[174]	Kelvin	4.65	5.11			4.59		
1968	Hopkins[241] et al	Kelvin		5.10		4.77			
1969	Jowett[15]	Kelvin	4.65	5.13	4.44	4.68	4.56		
1969	Williams[16]	Kelvin	4.65	5.15	4.45				
present work		Kelvin	4.65	5.15				4.55	
Steiner and Gyftopoulos[18] theory			4.66	5.50	4.47	4.94	4.47	4.47	

† corrected to effective work function

Notes on table 4.4

abbreviations:
s i surface ionization
m v a magnetic velocity analyser

field emission microscope tips (110) oriented unless otherwise stated

a Smith (ref 192) pointed out that (110) value was erroneously low

b well aged foil with (100) oriented crystallites within 10^{o} of surface

c not corrected to effective work function as no A value given

d assumed (310) work function was 4.35 eV from Nichols (ref 180). (110) work function ranged from 5.0 - 5.5 eV. 5.0 eV value preferred.

e same tube as Nichols (ref 180). Spurious (110) value of 4.58 eV due to secondaries from inner walls of anode. Estimate of 5.26 eV (A=120) made.

f Hutson used magnetic velocity analyser (m v a) to measure contact potential difference between (111) and the 4 other crystals. Comparing these with the work function values of Nichols (ref 180) and Smith (ref 192) he suggested his own values. These were then corrected by Smith (ref 194).

g since the ionization potential of Al is 5.96 eV this showed that hot polycrystalline wire had regions of work function greater than 5.96 eV.

h assumed work function of Ba was 2.5 eV

i values are averages of the following:
1 Sytaya et al (ref 205)
2 Smorodinova, Sytaya (ref 242)
3 Sultanov (ref 213)
4 Sultanov, Shuppe (ref 243)
5 Azizov, Shuppe (ref 219)

j assumed work function (111) was 4.40 eV (most reliably consistent in literature)

k (110) tip

l (100) tip

m (113) tip

n assumed 4.60 eV for (100) work function

o assumed values

p (611) badly polygonized

CHAPTER 5 VACUUM TECHNIQUES

introduction

The central problem with surface studies is contamination. Adsorption of only one atomic layer of material drastically alters the electronic properties of a surface. According to Gyftopoulos and Levine[65], evaporation of one monolayer of a metal on to a metallic substrate produces a surface with a work function characteristic of the bulk evaporant. Typically, in this work, uranium and zirconium evaporated on to tungsten substrates produced a total work function change of $\sim$ 1 eV. Monolayer adsorption of chemically active gases also produces work function changes of this order[87]. Thus it is essential that during the period under which a surface is studied very much less than a monolayer of gas is adsorbed.

The rate at which atoms of a gas impinge on a surface is given by kinetic theory[244] as:

$$\text{rate} = 3.5 \times 10^{26} P (MT)^{-\frac{1}{2}} \quad m^{-2} sec^{-1}$$

where P is the pressure of the gas in torr, M is its molecular weight and T its absolute temperature. Thus for oxygen, a monolayer ($\sim 10^{19}$ m^{-2}) forms in 30 seconds at 10^{-7} torr. In order to obtain a surface covered by less than 1/100th of a monolayer of active gases after one hour the partial pressure of these gases must be $\sim 1 \times 10^{-11}$ torr. The gas desorbed from one cm^2 of such a surface into a one litre volume produces a pressure rise of $\sim 10^{-8}$ torr.

Measurement of pressure is described in the first section, vacuum systems used to attain these pressures in the second and operating techniques in the third.

5.1 measurement of pressure and partial pressure

The pressure in the backing line of a diffusion pumped system (section 5.2) was not normally measured. However, when in doubt as to whether pressure was sufficiently low to back the diffusion pumps, the discharge produced by a Tesla coil held against a glass section of the backing line was found adequate. If any discharge was apparent the pressure was too great. A faint X-ray glow on the opposite wall of the glass characterized good backing pressure (about 10^{-1} torr). It was however essential to measure the pressure in the roughing line of getter-ion pumped systems (section 5.2) since the pump would not start above 10^{-3} torr. A standard pirani gauge was used. For the measurement of total pressure in the vacuum system a Mullard UKG-1 inverted Bayard-Alpert[245] gauge was used. This is built in a glass envelope with a wide neck to reduce the effect of pumping by the gauge[246]. It was normally operated at an electron current of 0.5 mA, the sensitivity then being 10^{-2} amps/torr. Initially the circuit shown in figure 5.1 was constructed to operate the gauge. The filament current was adjusted manually by means of R_1 and R_2 to keep the emission current at 0.5 mA as the pressure varied. Later an AERE ionization gauge control unit type 1785A with automatic emission control was used. Ion currents were measured on an Edwards Speedivac ion-current amplifier model 2.

The X-ray limit[247] of the UKG-1 gauge is quoted as 1×10^{-10} torr. In order to measure pressures lower than this a Redhead[248] type modulated gauge was constructed using the larger electrode assembly of the Mullard IOG-1 gauge and a modulator electrode of the same size and material (tungsten) as the collector. However difficulty was found in establishing a reliable modulation constant and, since the electrode assembly required considerably

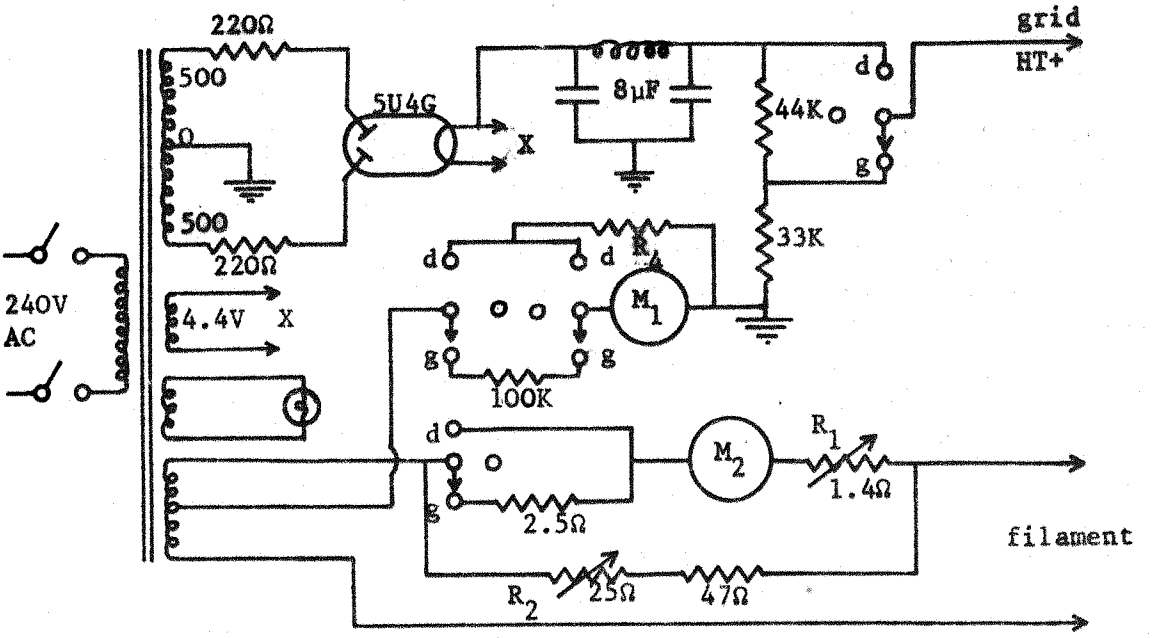

d degas

g gauge

M_1 emission current meter 1mA fsd

M_2 filament current meter 2A fsd

R_1 coarse current control

R_2 fine current control

R_4 shunt to give M_1 200mA fsd

figure 5.1

ion gauge supply unit

more outgassing, the UKG-1 gauge was found preferable. In practice the Bayard-Alpert gauge was used only down to 1×10^{-10} torr, the contamination due to residual gases being determined by:

a flashing a filament left cold for one hour. Typically, during measurements a filament of one cm^2 area produced a pressure rise of less than 1×10^{-10} torr when flashed to 3000 K into a one litre volume. This implied a gas coverage of less than 10^{-4} monolayers;

b observing the work function change produced by flashing clean a surface. No change (less than 10 mV) was seen on a surface left for one hour under measurement conditions;

c using a mass spectrometer. This was not subject to X-ray limitations.

Partial pressures of gases were measured with an AEI MS10 mass spectrometer or a Varian partial pressure gauge (p p g). Both were magnetic deflection instruments. The former had a sensitivity of 3.5×10^{-5} amp/torr and could completely resolve mass peaks up to mass 45. The latter had a sensitivity of 10^{-2} amp/torr but suffered from poor resolution; it could not completely resolve masses above 14. An electrometer with a noise level of 1×10^{-15} amp then produced a minimum detectable partial pressure of 3×10^{-11} torr with the MS10 and 1×10^{-13} torr with the p p g. Such an electrometer was provided with the MS10 but not with the p p g. In the latter case a Keithley 610 electrometer was used to give a detection limit of 5×10^{-13} torr. Essentially the MS10 is an analytical instrument, the low temperature rhenium filament producing only 5×10^{-5} amp being very suited for accurate measurement of relative peak heights without the carbon contamination that the tungsten filament of the p p g produces. However, for the measurement of residual gases in a vacuum system below 1×10^{-10} torr the greater sensitivity of the p p g is essential, resolution not being of great

importance for looking at simple gases. A big disadvantage of the p p g, however, was the difficulty found in outgassing it. A new instrument typically took 3 weeks of continued degassing before it could be operated below 1 x 10^{-10} torr without causing a detectable pressure rise.

Initially an MS10 only was available; several difficulties had to be overcome before it could be used successfully:

a leaks often developed on the gold wire seal flanges after bakeout;

b the scan rate was fixed at 13 minutes to scan masses 12-44; often it was required to measure residual gases during a 1 minute evaporation period;

c masses 2, 3 and 4 were switched, not scanned. This often resulted in these peaks being missed since the ion accelerating voltage was not set correctly for that particular spectrometer head;

d the atomic mass number was displayed on a potentiometer dial. Any electrical leakage in the head caused the true ion accelerating voltage to be lower than that implied by the dial.

The first problem was the most time-consuming. It was eventually found that leaks were prevented only by:

a electropolishing flange bolts before re-use;

b applying an anti-binding lubricant to the bolts (eg Acheson Colloids dag dispersion 654);

c increasing the diameter of the gold wire seal from 0.010" to 0.012";

d never allowing the bakeout temperature to exceed 300 C.

If the above were obeyed, this type of gold wire seal was found to be as reliable as the copper-gasket 'Conflat' flanges on the p p g.

The second, third and fourth problems were overcome by modifying the MS10

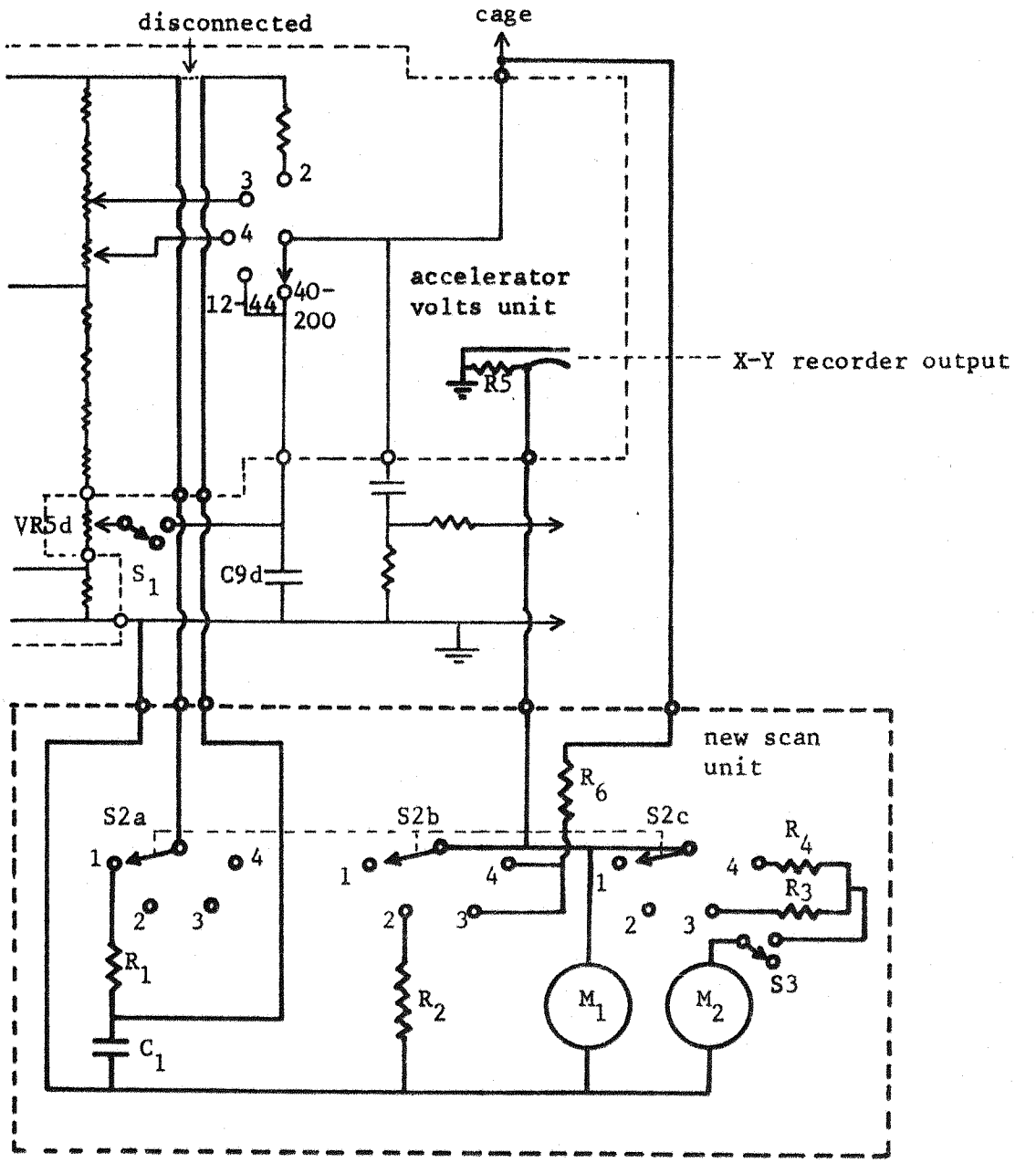

S_1	charge/discharge switch for mass ranges 12-44, 40-200		
S_2	mass range switch:	(1) mass 2	(3) range 12-44
		(2) mass 3, 4	(4) range 40-200
S_3	scan rate switch		
R_1	2 M	R_6	10 M
R_2	24.6 M	C_1	4 µF
R_3	7 M	M_1	electrostatic voltmeter 2 KV fsd
R_4	2 M	M_2	moving coil ammeter 50 µA fsd
R_5	100 K		

figure 5.2 modifications to MS10 control unit

control unit according to figure 5.2. In order to scan through mass 2 a capacitor C_1 was charged through R_1 to the maximum ion-accelerating voltage available, 2030 V. Masses 3 and 4 were scanned by discharging this capacitor through R_2. The voltage was displayed on an electrostatic voltmeter M_1. The mass range 12-45 was scanned by discharging the existing capacitor C9d through R_3 and R_5, and similarly the mass range 40-200 by discharging through R_4 and R_5. This provided 1 minute scans, the accelerating voltage being displayed on the meter M_2. 2 minute scans could only be achieved by switching out this meter by means of S_3, the capacitor now being discharged only by R_5. The original 13 minute scan, achieved by operating the potentiometer VR5d with an electric motor, was retained. The peak heights, x(t), for the new scan times (t) were reduced approximately by:

$$\frac{x(2)}{x(13)} \sim 0.8 \; ; \qquad \frac{x(1)}{x(13)} \sim 0.5 \quad .$$

In addition, a voltage output was provided for displaying the mass spectra on an X-Y recorder.

5.2 vacuum systems

The first vacuum system built was modelled on the design of Venema and Bandringa[249] and is shown in figure 5.3. A mechanical rotary pump backed two mercury diffusion pumps placed in series. The latter were two stage pumps with a nominal pumping speed of 30 litre sec^{-1} and were manufactured in Pyrex glass by T W Wingent Ltd. A single liquid nitrogen trap was adequate to prevent mercury diffusing into the experimental tube. In order to achieve high conductance 60mm tubing was used for all connections between the second diffusion pump and the experimental tube. The system was baked

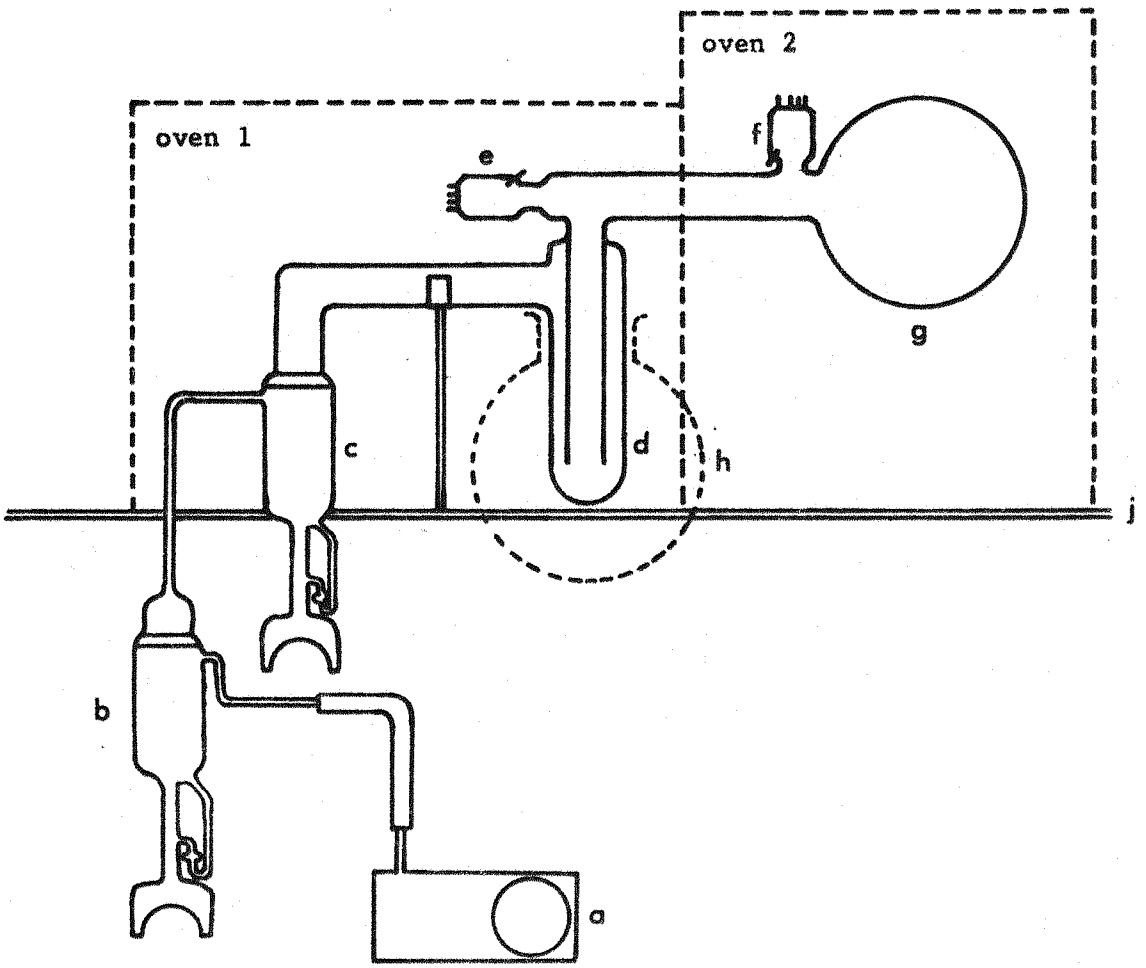

a rotary backing pump
b 1st diffusion pump
c 2nd diffusion pump
d cold trap
e ionization gauge 1
f ionization gauge 2
g experimental tube
h liquid nitrogen dewar
j syndanyo base

figure 5.3
first vacuum system

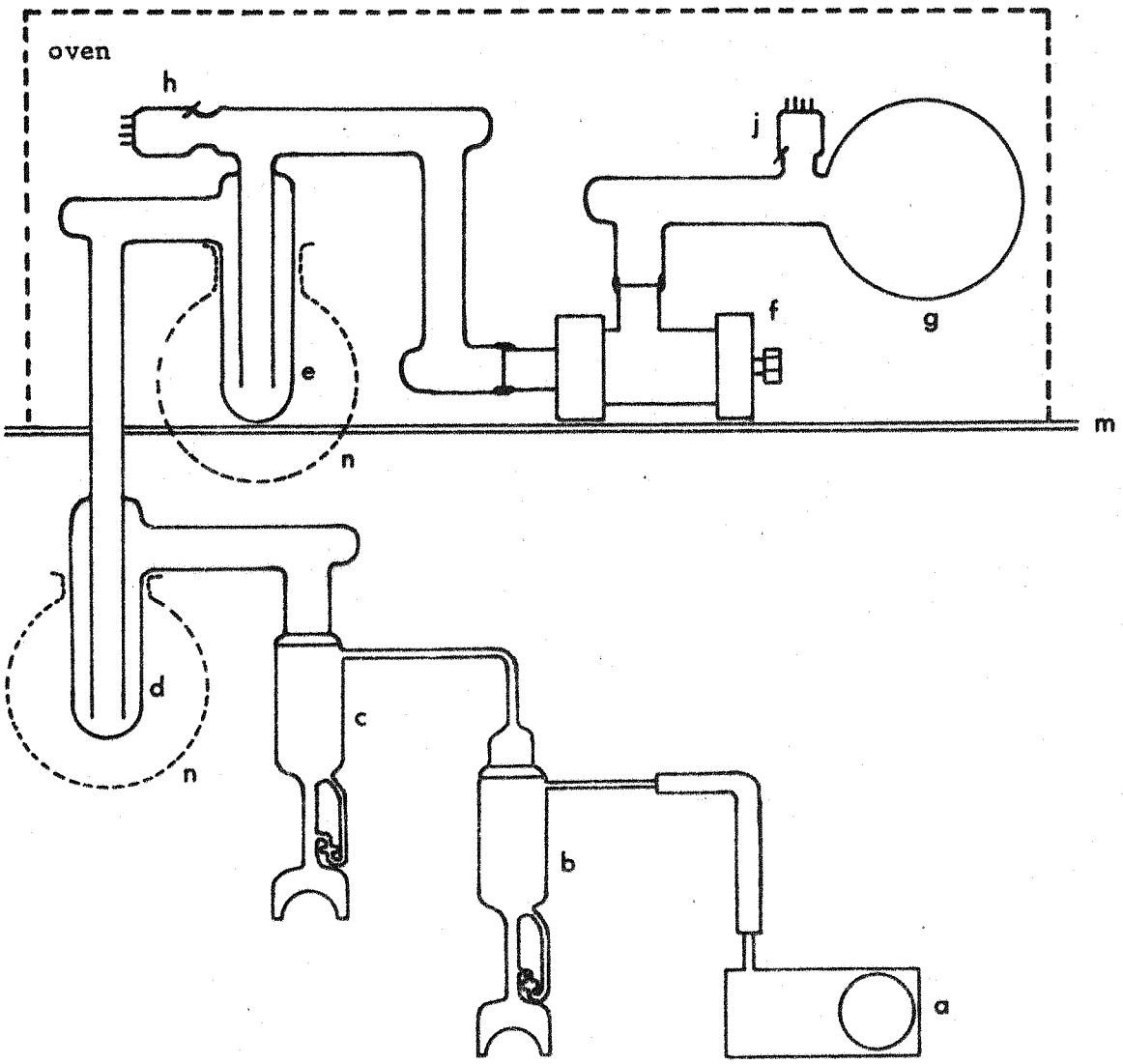

a	rotary backing pump	g	experimental tube
b	1st diffusion pump	h	1st ionization gauge
c	2nd diffusion pump	j	2nd ionization gauge
d	1st liquid nitrogen trap	m	syndanyo base
e	2nd liquid nitrogen trap	n	dewar
f	stainless steel u h v valve		

figure 5.4
second vacuum system

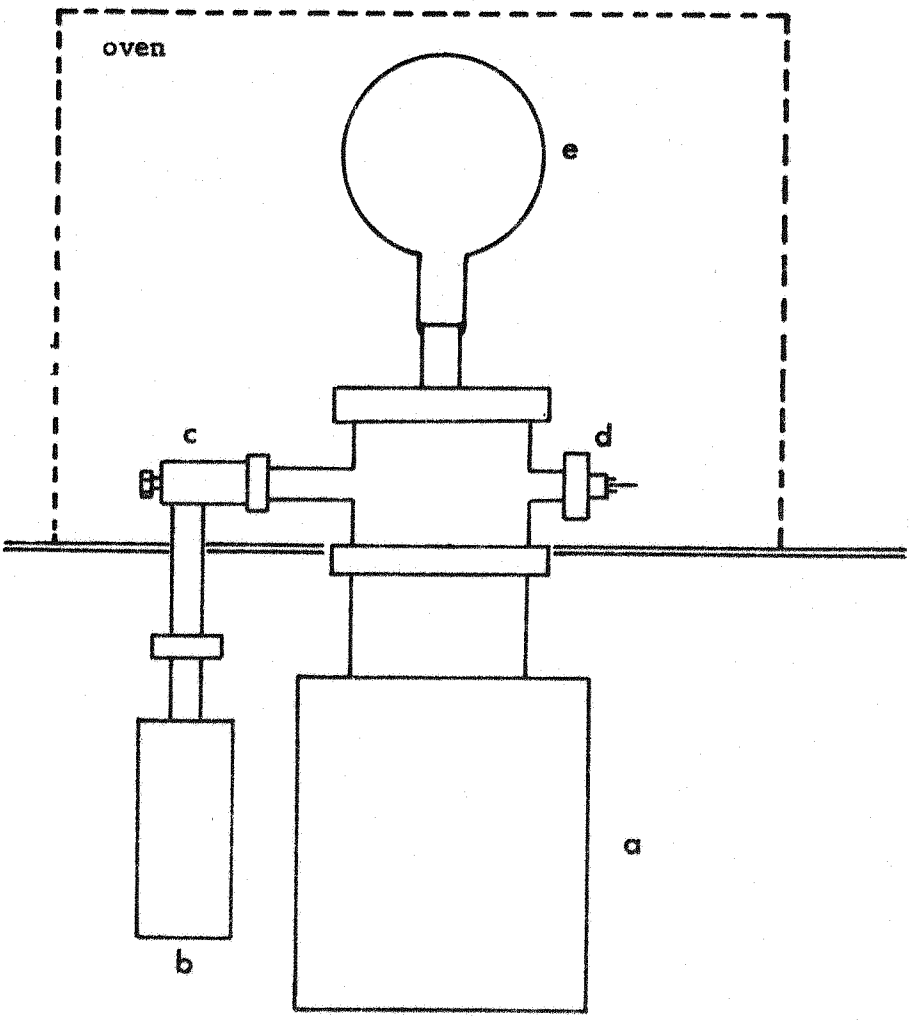

a getter-ion pump

b sorption pump

c u h v valve

d nude ionization gauge

e glass experimental tube

figure 5.5

third vacuum system

in two halves, one oven enclosing the second diffusion pump and the trap, the other the tube. The syndanyo base formed the bottom of the ovens.

It was decided to modify this system for two reasons: the experimental tube was exposed to mercury vapour during bakeout and an isolating valve was required between the pumping system and the tube. The advantages of the valve are discussed in section 5.3.2. This second system is shown in figure 5.4. Both diffusion pumps and the first trap were mounted below the syndanyo base, the second trap and tube only requiring bakeout. An incidental advantage of this system was that,since the second diffusion pump was not baked, its water cooling system did not have to be disconnected. Only one oven was needed, this being winched up and down as required. Thus the bakeout procedure was very much simplified. The valve was a Vacuum Generators type CRD64, constructed of stainless steel, which utilized a knife-edge seating on to a copper pad, giving a closed conductance of less than 10^{-14} litre sec^{-1}.

Finally, the third system, shown in figure 5.5, was employed. Apart from the experimental tube this was constructed entirely of stainless steel and was based on a Ferranti 140 litre sec^{-1} getter-ion pump incorporating an internal bakeout element. Vacuum Generators again supplied the valve, type CRPD38, as well as the sorption pumps.

5.3.1 operating procedure - diffusion pumped systems

After roughing out with the rotary pump a Tesla was used to test for 'pin-hole' leaks. The diffusion pumps were then switched on and the trap(s)

immersed in liquid nitrogen. Ten minutes later the Tesla was again employed to check that the system had pumped below discharge pressure. At this stage the ion gauge was switched on, it normally recording a pressure of about 10^{-5} torr. The system was then left to pump for several hours before testing for smaller leaks. This was done with a mass spectrometer, if fitted, using either argon or helium as the probe gas. When no mass spectrometer was available, leak testing was carried out by painting, with a small brush, the suspect area with industrial alcohol and observing the pressure with the ion gauge. Frequently leaks occurred at glass to metal seals and on applying alcohol the pressure normally fell rapidly. Careful heating of the seal with an oxy-hydrogen torch whilst the system was under vacuum usually sealed the leak. More rarely a larger leak occurred, the pressure rising on applying alcohol. Such leaks, as well as leaks other than on seals, could only be repaired with the system at atmospheric pressure. Several commercial leak sealers were tested but none was found that would withstand the bakeout procedure.

As soon as the pressure fell below 10^{-6} torr all filaments were given a quick degas (2400 K for 60 sec) to remove the surface contamination and aneal them. The latter was particularly important since filaments were often spot-welded under strain so that fracture of the weld would occur during bakeout or when manoeuvring ovens. Particularly susceptible were thermo-couple wires spot-welded on to filaments; frequently they would part from the filament when the latter was first heated. Much time could be saved by repairing these breakages before rather than after bakeout. At this stage the main gas in the system was water vapour (figures 5.6 and 5.7a) although a peak was observable at every mass number except 3 and 4. The substances most probably responsible are shown in table 5.1. According to Erents and

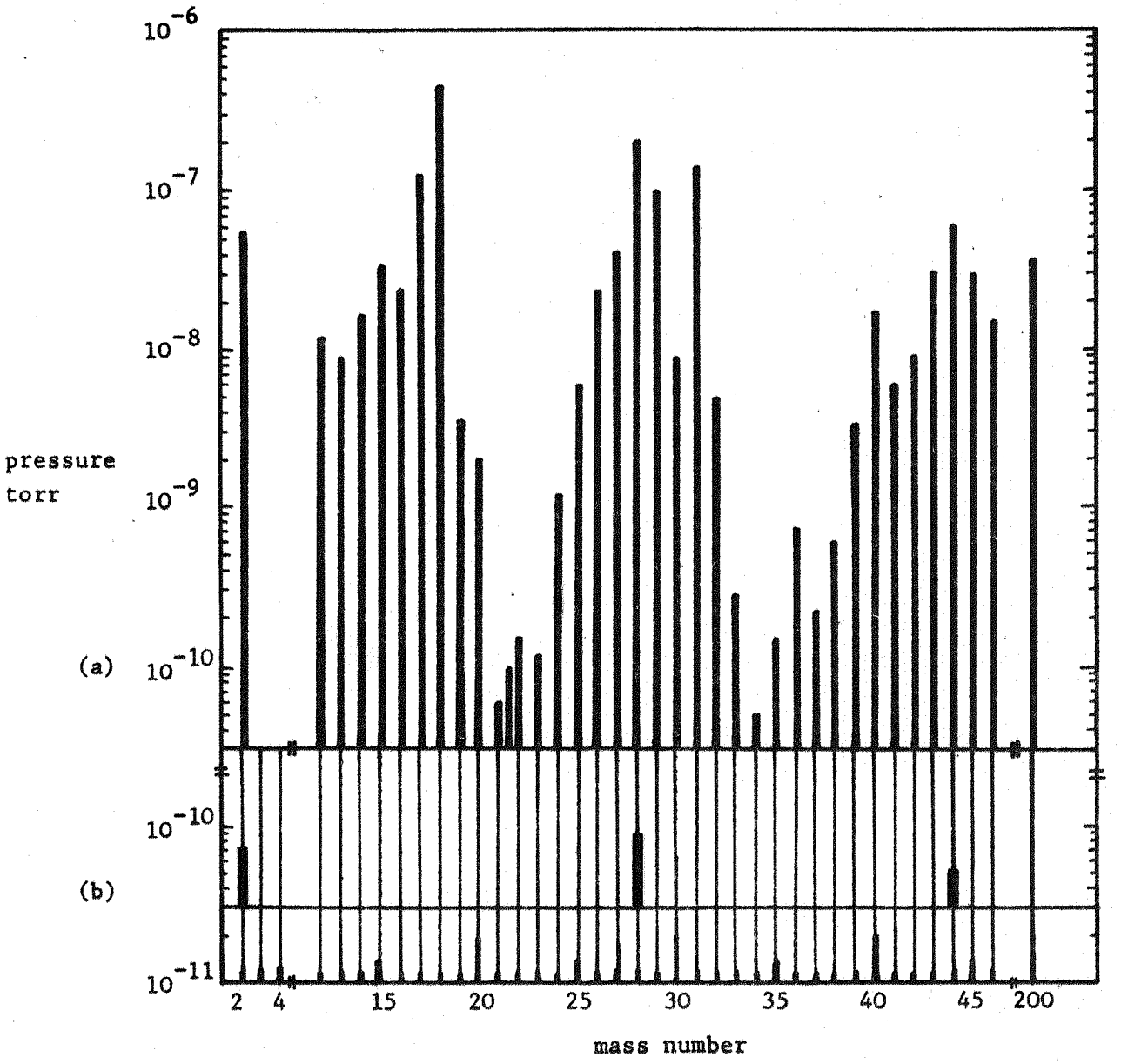

figure 6.5
residual gases in a glass mercury diffusion pumped system
measured on an MS10 mass spectrometer
electrometer noise level corresponds to 3×10^{-11} torr

(a) before bakeout; total pressure 5×10^{-7} torr
(b) clean system; total pressure 1×10^{-10} torr

table 5.1 probable ions in figure 5.6

a m u (m/e)	ion	a m u (m/e)	ion
2	H_2^+	28	$C_2H_4^+$, CO^+, N_2^+
3	He^+	29	$C_2H_5^+$
4	He^+	30	$C_2H_6^+$
		31	$C_2H_7^+$
12	C^+	32	O_2^+
13	CH^+	33	O_2^+
14	CH_2^+, N_2^{++}, N^+	34	O_2^+
15	CH_3^+, NH^+	35	Cl^+
16	CH_4^+, NH_2^+, O_2^{++}, O^+	36	C_3^+
17	NH_3^+, OH^+	37	C_3H^+, Cl
18	NH_4^+, HOH^+	38	$C_3H_2^+$
19	F^+	39	$C_3H_3^+$
20	Ne^+, Ar^{++}	40	$C_3H_4^+$, Ar^+
21	Ne^+	41	$C_3H_5^+$
21.5	$COCH_3^{++}$	42	$C_3H_6^+$
22	Ne^+	43	$C_3H_7^+$, $COCH_3^+$
23	hydrocarbon	44	$C_3H_8^+$, CO_2^+
24	C_2^+	45	hydrocarbon
25	C_2H^+	46	hydrocarbon
26	$C_2H_2^+$		
27	$C_2H_3^+$	200	Hg^+

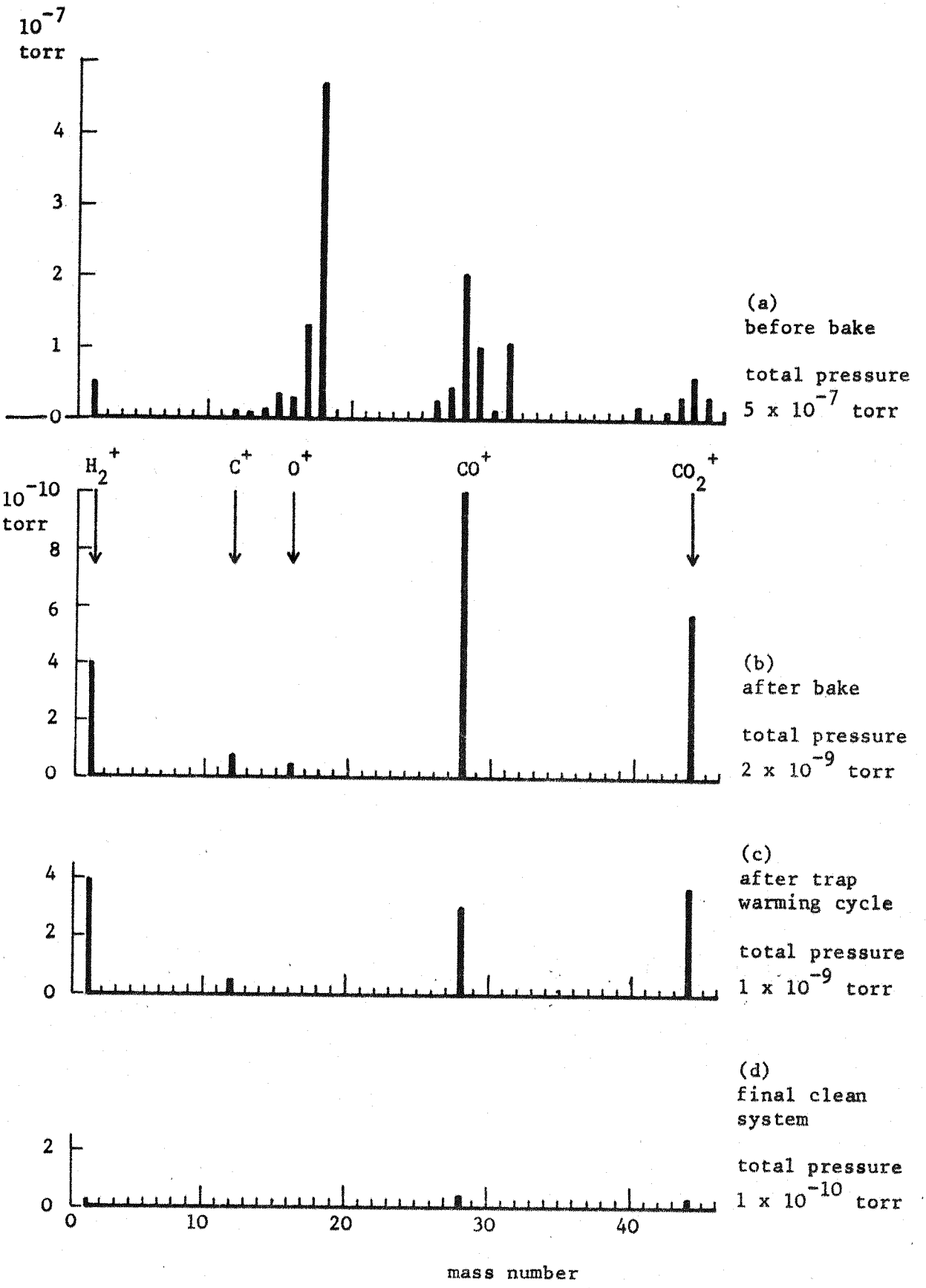

figure 5.7

mass spectra of a glass mercury diffusion pumped system (MS10)

Carter[250], water vapour is desorbed from the walls in two phases, the maximum evolution rates occurring at about 150 C and 260 C. Thus the next step was to bake the section of the system above the syndanyo base with the rotary pump on gas ballast. In the case of the first system (figure 5.3) this necessitated switching off the second diffusion pump, removing its water cooling connections and lowering the liquid nitrogen dewar. On the second system (figure 5.4) only the second dewar needed to be removed. An all-glass system was baked to 450 C overnight (8 hours), but one having metal components (mass spectrometer, valve) could only be taken safely to 300 C and so required a longer bakeout (12 hours).

Immediately after removing oven 1 (first system) the trap was immersed in liquid nitrogen and, after allowing some minutes to cool, the water system was re-connected and the second diffusion pump switched on. The second oven was left on for a further few minutes in order to bake all the mercury from the tube into the trap. In the second system the oven was simply raised and the trap cooled. In this case the first trap was always kept cold, even during bakeout, so preventing mercury ever reaching the second trap. Immediately following bakeout the pressure was typically 5×10^{-7} torr and after several hours had fallen to 2×10^{-9} torr. A mass scan (figure 5.7b) at this pressure showed that the bakeout had removed all water vapour, hydrocarbon contaminants and mercury, leaving only hydrogen, carbon monoxide and carbon dioxide.

Frequently bakeout caused the fracture of a tungsten/Pyrex seal. The mass spectrum characteristic of a leak at this stage is shown in figure 5.8. The presence of $18(H_2O^+)$, $40(Ar^+)$ and enlarged $32(O_2^+)$ and $14(N^+)$ peaks is typical. Again, leaking seals could be repaired by careful heating but the

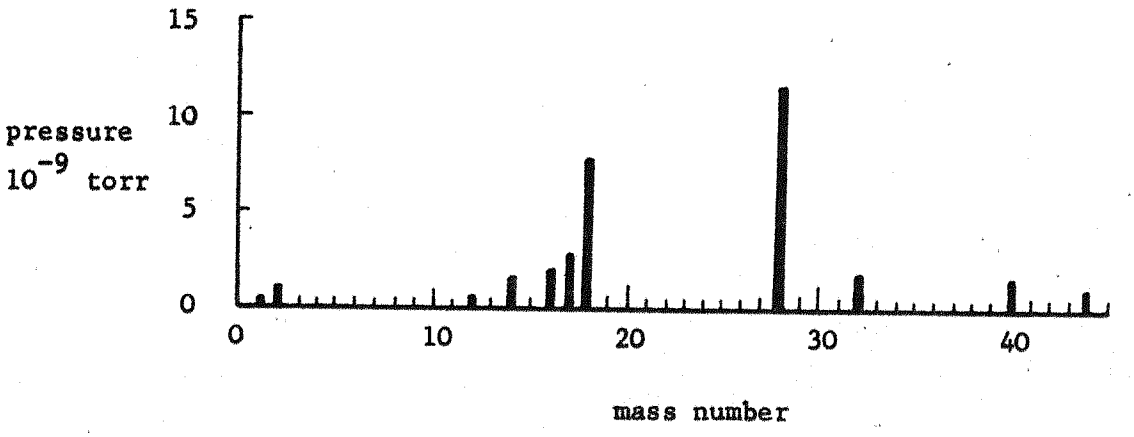

figure 5.8
mass spectrum characteristic of a leak after bakeout
total pressure 2 x 10^{-8} torr
glass, mercury-diffusion pumped system

water vapour contamination could only be removed by an additional short (4 hour) bake. However, since another bake was usually necessary later the normal procedure after sealing a leak was to start outgassing the electrodes. The purpose of outgassing was threefold:

1 to remove from all parts of the experimental tube those dissolved and adsorbed gases which would otherwise desorb during the experiment. Clearly, parts which were to become hot required the greatest amount of outgassing;

2 to act as a getter;

3 to prepare the surfaces for the experiment (chapter 6).

The first objective was the most time consuming. It was generally found that degassing was sufficient when the pressure, with all the tungsten electrodes at 2400 K, was $\sim 5 \times 10^{-9}$ torr. The procedure was, in principle, simple: all electrodes were left at that temperature until the required pressure was

reached. In addition, the second gauge was outgassed at an emission current of 40 mA while the pressure was recorded on the first gauge (figures 5.3 and 5.4). The length of time necessary depended largely on the power required for outgassing, a complex tube containing large electrodes (eg tube 8 section 7.2) consuming as much as 2 KW and taking up to 500 hours. It appeared that most of the gas came from the glass walls since an un-outgassed electrode in an otherwise well-outgassed tube could be degassed in only 12 hours at 2400 K, whereas a well-outgassed electrode in a new glass envelope required almost as long as an entirely new tube. For this reason the glass walls were kept as far as possible from the electrodes by using large tubes (1 litre flasks) and good geometry. However, heavy currents through the tungsten leadthroughs caused the glass in and around the seals to become hot. The maximum size of leadthrough, determined by the strain in the tungsten/Pyrex seal, was 2 mm and this appeared to be the limiting factor. Even 2 mm tungsten seals had a tendency to crack so that 1.5 mm seals were preferable. Experimental seals, using intermediate glasses in order to match the tungsten coefficient of expansion, were made but none proved as reliable as the simple tungsten/Pyrex seal. Thus the ideal tube was large with very small electrodes requiring low currents. The limiting factor here was the size that the electrodes could easily be made.

The minimum pressure reached by the system before outgassing commenced was about 2×10^{-9} torr, the constituent gases being mainly carbon monoxide and carbon dioxide (figure 5.7b). These gases accumulated in the trap and diffused back into the tube. This could be shown simply by removing the liquid nitrogen dewar from the last trap. The carbon monoxide partial pressure rose to a maximum, followed by carbon dioxide. The total pressure thus showed two maxima, the second larger one exceeding 10^{-5} torr. After

60 seconds the pressure had fallen to $\sim 10^{-8}$ torr but started to rise again as mercury vapour diffused into the tube. Cooling the trap, degassing the gauge and allowing the system to pump out for one hour showed that the carbon monoxide and carbon dioxide pressures had dropped considerably (figure 5.7c). This cycle, warming the trap for 60 seconds and then cooling, was essential to obtaining good vacuum and was carried out several times per day during outgassing. A similar procedure has been described by Dawson and Whetton[251].

When the pressure, with electrodes at 2400 K, reached 5×10^{-9} torr the temperature was increased to 2800 K for 12 hours, thus evaporating some tungsten over the walls of the tube. This had the effect of gettering the remaining active gases. The pressure (electrodes cold) was then in the low 10^{-10} torr range and the trap warming cycle produced no pressure rise or fall. Outgassing of gauge 2 was ceased and the pressure then measured on this gauge. Finally, the electrodes were flashed to 3000 K for short periods (2 seconds). The equilibrium vapour pressure of tungsten at this temperature is about 10^{-7} torr so that considerable gettering occurred without a great increase in the temperature of the rest of the tube. This procedure was continued until the maximum pressure rise on flashing electrodes left cold for 1 hour was 1×10^{-10} torr. A mass scan (figure 5.7d) revealed only hydrogen, carbon monoxide and carbon dioxide, the major constituent being carbon monoxide.

The above procedure removed all contaminants from the surface of the tungsten electrodes, flashing to 3000 K being necessary to remove carbon[173]. In addition, such 'aged' polycrystalline tungsten has a stable reproducable work function (section 6.2) which is suitable for use as a reference.

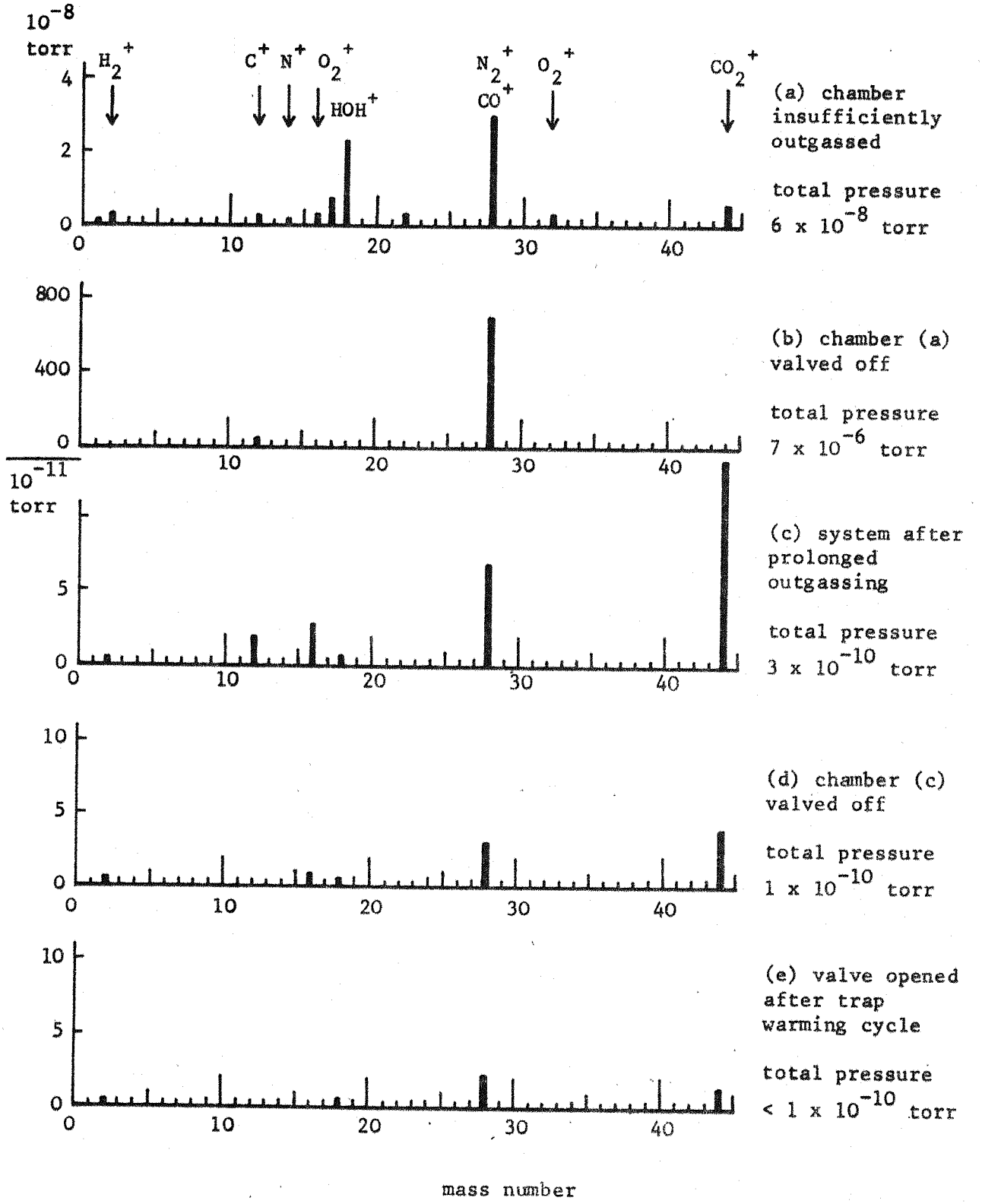

figure 5.9

effect of isolating experimental chamber from pumping system (figure 5.4)

a,b insufficiently outgassed chamber

c-e trap warming procedure used in conjunction with valve

In order to prevent complete oxidation of the electrodes in the case of an accidental rise in pressure, the current for all the outgassing supplies was drawn through a relay which was tripped off when the pressure, recorded on the ion gauge, exceeded a preset value.

5.3.2 use of an isolation valve

During the trap warming procedure some of the gas evolved adsorbed on the walls of the experimental tube and required further degassing to remove it. Some of this gas then condensed back into the trap. A convenient way of overcoming this problem was the installation of a valve between the trap and the tube as in the second system (figure 5.4). The effect of this valve in use is shown in figure 5.9. When the valve was closed on an insufficiently outgassed system (figure 5.9a) the pressure rose rapidly, the spectrum showing almost entirely carbon monoxide (figure 5.9b). After prolonged outgassing carbon monoxide and carbon dioxide accumulated in the trap, the carbon dioxide partial pressure eventually surpassing that of carbon monoxide (figure 5.9c). On closing the valve the pressure then dropped from 3 to 1 x 10^{-10} torr (figure 5.9d), presumably due to pumping by the gauge. The trap was warmed for 60 seconds and then allowed to pump out for 15 minutes. On opening the valve the pressure dropped still further, the mass spectrum (figure 5.9e) then showing predominantly carbon monoxide. Similar use of a valve in conjunction with the trap warming cycle has been described by Singleton and Lange[252]. Other uses of the valve were:

1 leak testing: small leaks could be missed even with a mass spectrometer. The absence of significant leaks in a well-outgassed system was indicated by a fall in pressure on closure of the valve;

2 in the event of an electricity or water supply failure the valve could be closed and the pressure held down in the latter case by gauge pumping;

3 gas contamination studies: the pressure of gas admitted to the system could be controlled by partial closure of the valve.

It has been suggested[253,254] that the limiting pressure in a glass system is determined by the diffusion of helium through the glass. However, no helium peak was observable. As a check, the valve was closed and the system allowed to stand for 1 hour. After this time the pressure of helium was only 1×10^{-10} torr, and on opening the valve it immediately fell below the detectable limit (5×10^{-13} torr).

High conductance stainless steel valves of the type used were expensive in comparison with the other components of the glass system. Further disadvantages were the necessity of a lower bakeout temperature, the long time taken to cool after bakeout and, in this particular case, the tendency of the valve to leak at the (gold wire seal) flanges. The last factor finally caused the writer to investigate a simple all-glass valve constructed from a Quickfit 25 mm ground glass ball and socket joint (MS41 and FS41). The valve is shown in the open position in figure 5.10. The glass encapsulated iron slug rested on a ledge, indented to hold the slug firmly. Closure was effected by magnetically rotating the slug off the ledge and lowering the assembly until the ball contacted the socket. The valve proved surprisingly effective, holding a pressure of 1×10^{-10} torr for several minutes against a pressure of 10^{-5} torr on the trap side. Thus it was adequate for the trap warming procedure.

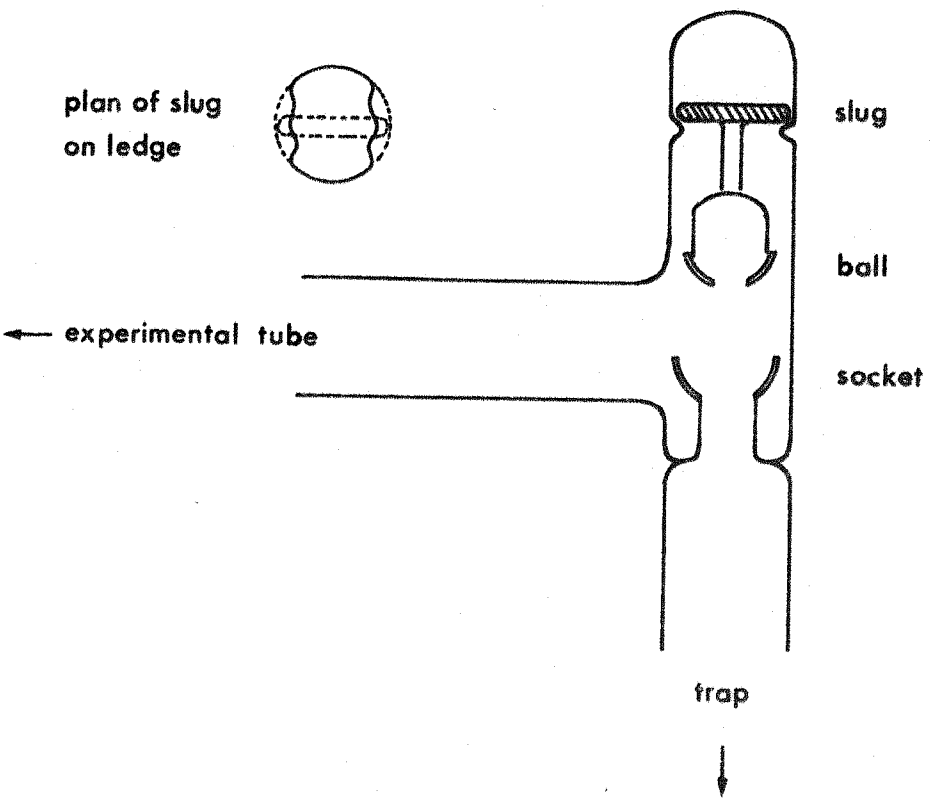

figure 5.10
high conductance glass valve

5.3.3 operating procedure - getter-ion pumped system (figure 5.5)

Operation of the getter-ion system was simple. The pressure was reduced to $\sim 10^{-3}$ torr by means of 2 sorption pumps used cyclicly. As soon as the pressure was low enough for the ion pump to start, the UHV valve was closed and leak testing began. The pressure before bakeout reached $\sim 2 \times 10^{-8}$ torr, nearly two orders lower than that achieved by the mercury diffusion pumped system. This greatly facilitated leak testing. The lower pressure was partly a reflection of the greatly increased pumping speed at this pressure (140 litre sec^{-1} for getter-ion, 30 litre sec^{-1} for diffusion) and also the absence of traps. A mass spectrum at this point was similar to that of the glass system; the dominant gas was water vapour. However a He^4 peak was detectable, a consequence of the low pumping speed for inert gases[255,256]. No mercury was observed. Care had to be taken during bakeout that the pressure did not exceed the critical value at which the ion pump cut out ($\sim 10^{-3}$ torr). In practice, because of the thermal time-lag, the heating elements were set to switch off at 10^{-5} torr. This was done with a Schmidt trigger circuit operated by the pump ion current. Bakeout temperature was not allowed to exceed 300 C inside the oven and 150 C inside the pump. The 24 hour bakeout found to be necessary was terminated by means of a time switch so that the system had cooled to a workable temperature (4 hours) before the oven was removed. The pressure while still hot was $\sim 2 \times 10^{-7}$ torr and after 24 hours had fallen to 2×10^{-10} torr. It appeared to be difficult to reduce the pressure below this value quickly. However, at the end of an outgassing procedure as described for the glass systems, the pressure was usually below 1×10^{-10} torr as is shown by the mass scan, figure 5.11b. The main residual gas was hydrogen, followed by carbon monoxide. Calder and Lewis[257] have demonstrated that hydrogen

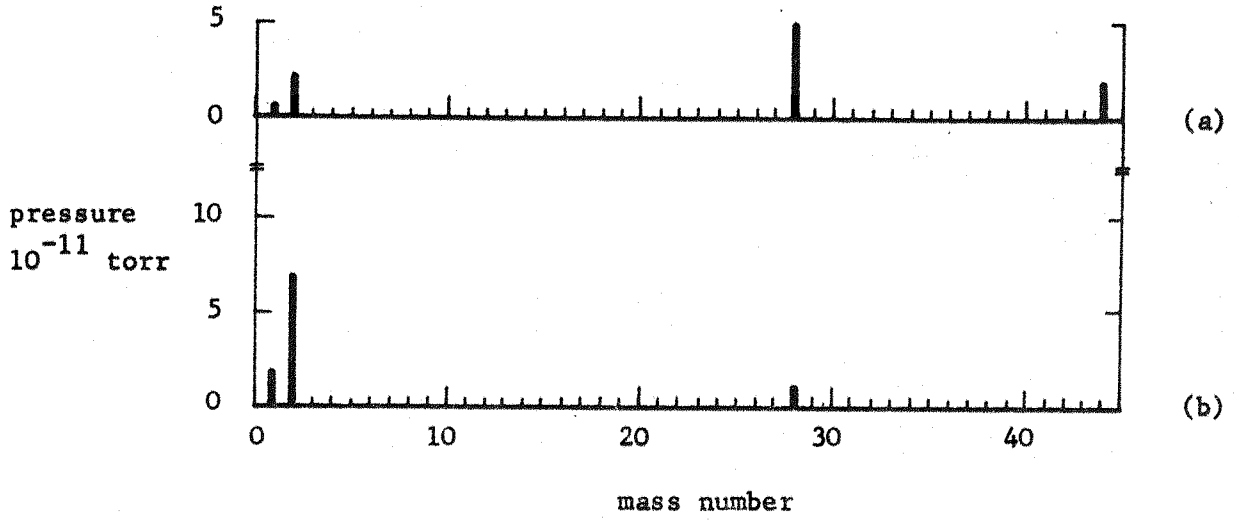

figure 5.11
comparison of residual gases in vacuum systems at a total pressure of 1×10^{-10} torr

(a) glass, mercury-diffusion pumped system
(b) stainless steel, getter-ion pumped system

diffuses from the interior of stainless steel, a situation which is aggravated by the reduction of pumping speed for hydrogen at low pressures[258].

Initially it was decided to use a getter-ion pumped system to check that mercury contamination[259] of uranium was not causing spurious measurements. However, since the main contaminant gas during deposition of uranium in this system was hydrogen (section 8.2) and since no mercury contamination was evident, it was decided to resume work on a mercury diffusion pumped system.

5.3.4 comparison of mercury diffusion and getter-ion pumped systems

At the time of writing the total cost of the glass system shown in

figure 5.4, but using the glass valve (figure 5.10) was £140. This did not include the services of a competent glass blower or the cost of the syndanyo base, its supporting frame and the oven. The equivalent metal system (figure 5.5), including the pump control unit and bakeout control unit, cost £1400 (again excluding syndanyo base, frame and oven). One might expect that for such a large price differential there would be significant performance differences. However these differences, detailed below, appeared to be small:

1 the ultimate pressure of both systems was about the same (less than 1×10^{-10} torr). However, since the (quoted) pumping speed of the ion pump is much greater this implies that the rate at which gas desorbed from the metal walls was also much greater. Consequently, for the same pressure, a glass system should produce less contamination. In practice, flash desorption experiments showed that the rate of contamination in the two systems was very similar. This suggests that the pumping speed of the ion pump falls off far more rapidly with reduction in pressure than that of the diffusion pump;

2 as described in section 5.3.1 the time required to achieve a clean experimental tube was dependent on the desorption rate from the tube, not on the pumping speed. Consequently there was no difference in outgassing time;

3 the predominant residual gas was hydrogen in the metal system and carbon monoxide in the glass system (figure 5.11);

4 roughing out the metal system was a time-consuming process. However, this was compensated by the lower pre-bake pressure facilitating quick leak testing;

5 the bakeout cycle was about 4 times longer for the metal system;

6 the performance of the ion pump slowly deteriorated with use. The lifetime of the pump was quoted as 2 torr minutes;

7 in contrast with a diffusion pumped system the metal system was 'fail safe'. An electricity failure caused only a slow increase in the pressure. When the supply was restored the pressure regained its initial value. No water supply was required;

8 probably the greatest attraction of the metal system was its simplicity, notably the absence of liquid nitrogen traps.

9 the 'memory-effect'[260] displayed by getter-ion pumps (sometimes a serious disadvantage) was not important in this work.

5.3.5 getters

Evaporation of chemically active metals is often used as a method of pumping[261]. Titanium is most frequently employed although it has been suggested[262] that tantalum would provide higher pumping speeds. An experimental getter was constructed in which titanium was evaporated on to the walls of a 500 ml glass bulb. Since titanium wire is not self-supporting at the temperatures required for evaporation a 15%/85% Mo/Ti alloy, developed for use as a getter[263] was employed. This was in the form of a wire 2 mm in diameter and 10 cm long. The system in which the getter was tested had previously been contaminated with hydrogen. The mass spectrum, after pumping out the system and thoroughly degassing the getter, is shown in figure 5.12a. A current of 50 amp was passed through the wire for 10 minutes, after which time the thickness of the evaporated titanium layer was at least 10,000 Å. The pressure during evaporation rose to 1×10^{-8} torr, the predominant gas being hydrogen (figure 5.12b). 5 hours after evaporation

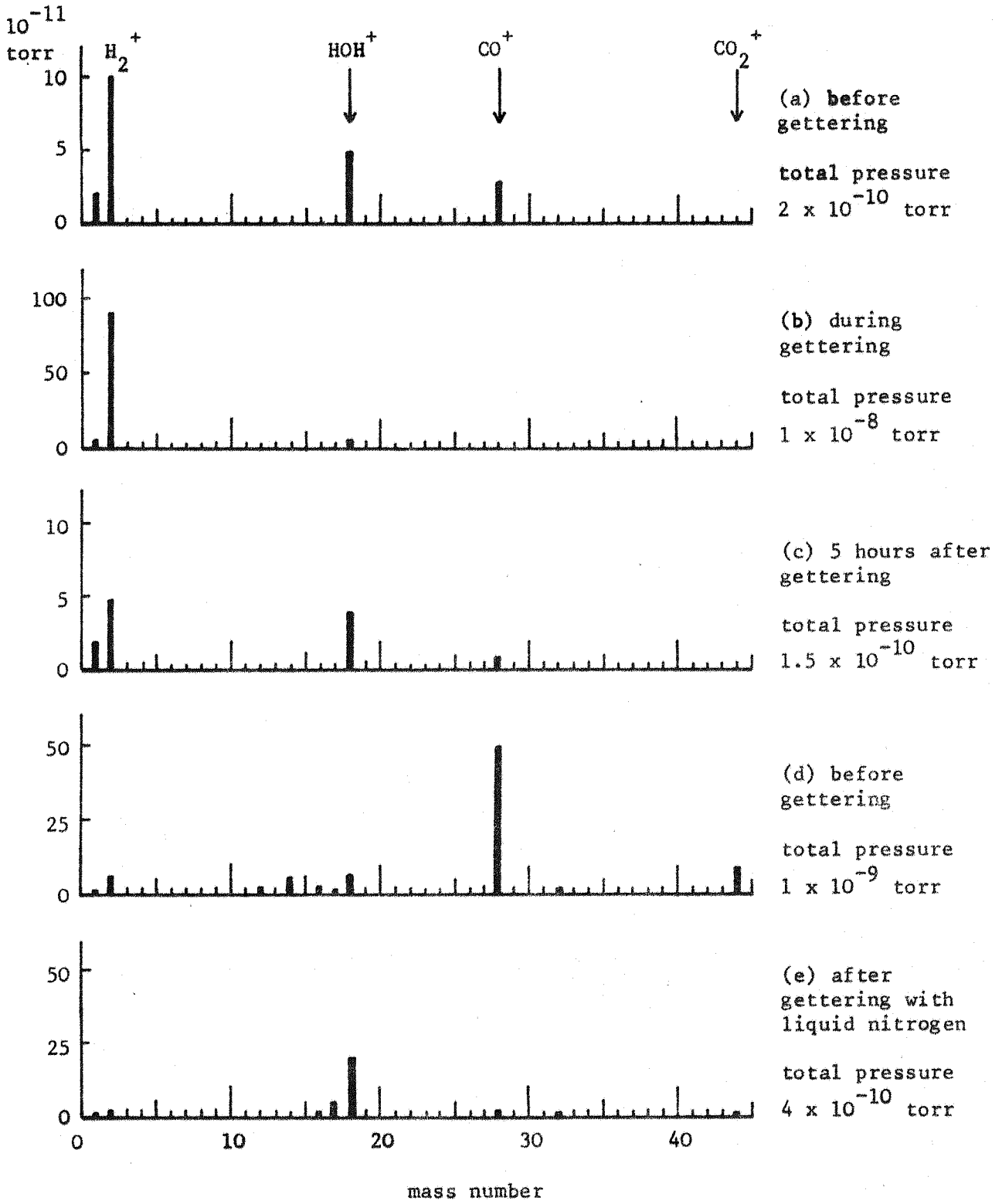

figure 5.12

effect of Mo/Ti getter on glass mercury diffusion pumped system

a-c without liquid nitrogen cooling

d,e with liquid nitrogen cooling

the pressure had dropped to 1.5×10^{-10} torr and the partial pressures of all gases had dropped (figure 5.12c). However, the getter was hardly a success since all surfaces were covered with a layer of adsorbed gas which took several hours of degassing to remove.

A second attempt at gettering was made on a system whose mass spectrum is shown in figure 5.12d. In this case the glass bulb was immersed in liquid nitrogen. During evaporation no pressure rise was recorded, and on switching off the filament the pressure dropped from 1×10^{-9} torr to 4×10^{-10} torr over a period of 30 minutes. The mass spectrum (figure 5.12e) showed that the pressures of all gases were reduced except for water which was increased. Unfortunately, water was the most difficult gas to remove from the system and for this reason it was decided not to continue with the use of getters.

5.3.6 materials used in experimental tubes

Tungsten was the most convenient material from the degassing point of view[264] but initially, because of the difficulty of spot-welding tungsten to tungsten, it was only used for those parts of the electrodes which were heated. Molybdenum was used for supporting the electrodes from the tungsten leadthroughs. In some cases, where there was no likelihood of the electrode becoming hot, nickel (a very 'gassy' material) was utilized. However, after some experience had been gained with spot-welding it was found possible to use tungsten throughout. Briefly, tungsten to tungsten welds were achieved using tungsten spot-welder electrodes and high current, short time, welder settings. In cases of difficulty (eg welding 0.1 mm tungsten foil to 1 mm tungsten rod) a tungsten/tantalum/tungsten sandwich was found to be very

effective. The tantalum, in the form of thin (0.05 mm) sheet cut to the smallest possible size, produced no outgassing problems.

5.3.7 removal of carbon contamination from tungsten

It has been suggested that carbon cannot be removed from tungsten by heating alone[176,278]. Several authors[175,176,279] report that heating tungsten in the presence of oxygen removes carbon with the release of carbon monoxide. However, Zingerman[173] states that carbon is removed by heating tungsten to 3000 K.

A simple experiment was made in which the partial pressures of carbon monoxide and oxygen were monitored with an MS10 mass spectrometer whilst a tungsten filament was heated in oxygen. The filament was already well degassed, as described in section 5.3.1, including flashing to 3000 K for a few seconds. The results are shown in figure 5.13. The filament was heated to 2200 K in 3×10^{-6} torr of oxygen. Immediately on switching on the filament the oxygen pressure dropped to $\sim 5 \times 10^{-7}$ torr while the carbon monoxide pressure rose to a maximum of 4×10^{-7} torr and then dropped (figure 5.13a). The carbon monoxide pressure then gradually built up to a maximum of 3×10^{-7} torr after 14 minutes before falling to a steady value of 6×10^{-8} torr after 280 minutes (figure 5.13b). The oxygen pressure remained constant at 5×10^{-7} torr. The initial burst of carbon monoxide was presumably due to carbon on the surface whereas the second maximum was determined by diffusion of carbon to the surface from the interior. The carbon monoxide pressure of 6×10^{-8} torr remained constant for 24 hours. The temperature of the filament was then increased to 2600 K. The carbon

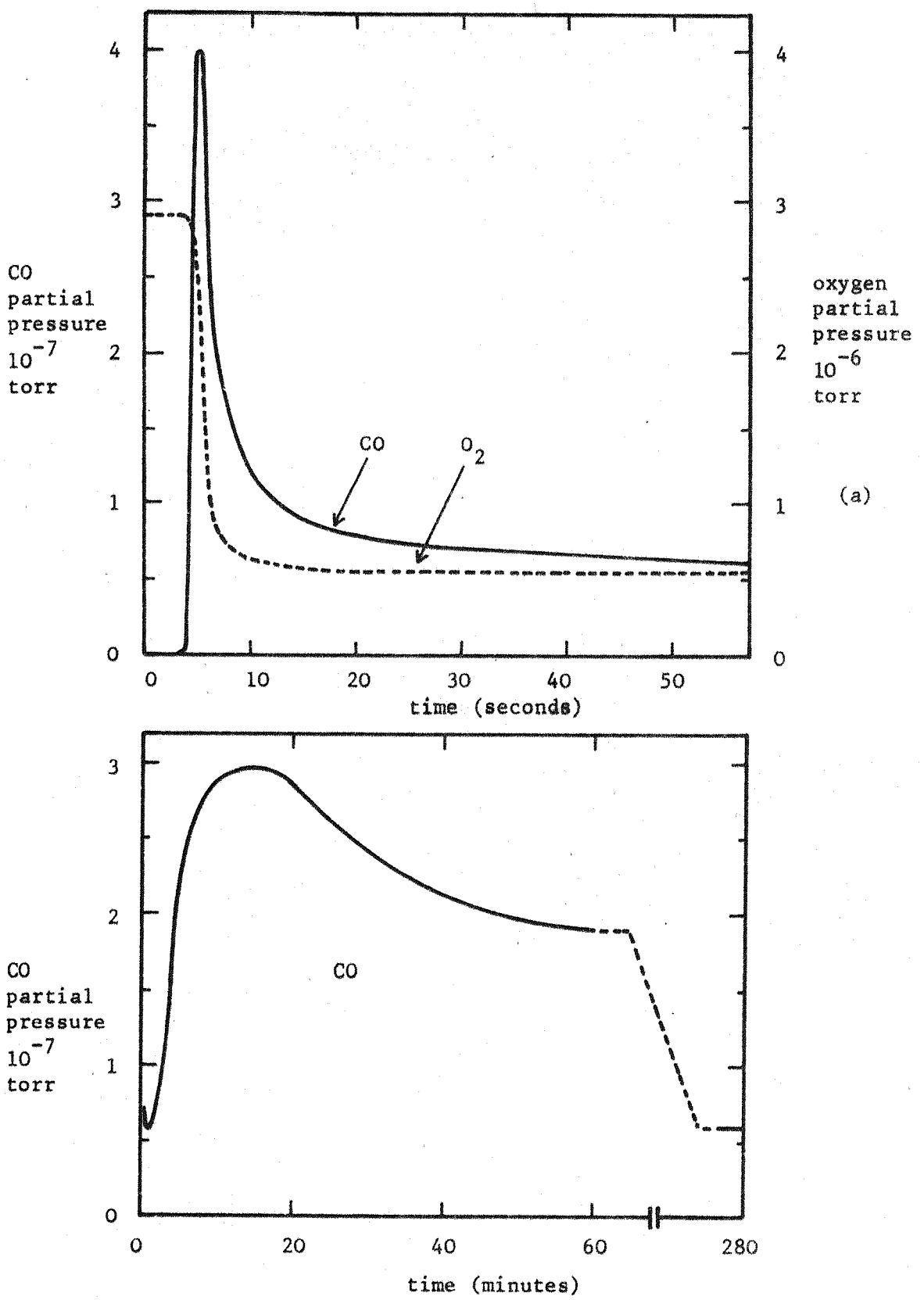

figure 5.13

partial pressures of CO and O_2 whilst heating a well-outgassed tungsten filament to 2200 K

monoxide pressure proceeded to climb to a new maximum before dropping in much the same way as for the 2200 K temperature.

It thus appears that it is difficult to entirely remove carbon from the interior of the metal. This is consistent with the diffusion controlled process by which carbon arrives at the surface, described by Becker et al[175].

CHAPTER 6 PREPARATION AND ASSESSMENT OF SURFACES

6.1 tungsten single crystals

Until recently polycrystalline tungsten foil has been widely used as the substrate in work function measurements of evaporated films[31,87]. Tungsten foil was chosen since it could be readily outgassed (chapter 5) to produce an atomically clean surface[279] with a reproducable work function[265] and is easily obtainable. However, as adsorption theories developed (chapter 2) it became clear that, in order to assess the agreement between theory and experiment, substrates were required whose exact surface geometry was known. Thus, in this work, single crystals with very carefully prepared surfaces were used. The following is an account of how such surfaces were prepared.

Single crystal rods, oriented to within $\pm 3^{\circ}$, were manufactured by Metals Research Limited using the electron beam float zoning technique. The purity was better than 3N (99.999%). The rod was approximately circular in cross-section with a diameter of 6 - 8 mm. A 2 mm length was spark sliced from the rod with a Metals Research Servomet spark machine. A Laue X-ray back reflection photograph taken at this stage is shown in figure 6.1. Spark damage causes the diffuse polycrystalline-type rings but some preferred orientation is evident. Removal of 20 μm from the surface in a sodium hydroxide electro-etch enabled a single crystal-type Laue pattern to be obtained. The crystal was then attached to the X-ray goniometer with an electrically conducting glue (mixture of powdered graphite and formvar) so that it could be spark machined without removal from the goniometer. Laue back reflection photographs were taken and with the aid of a Greninger chart and a Wulff grid[266] the crystal could be oriented to $\pm \frac{1}{2}^{\circ}$. Figures 6.2, 6.3

figure 6.1
Laue back reflection from spark damaged (110) tungsten single crystal

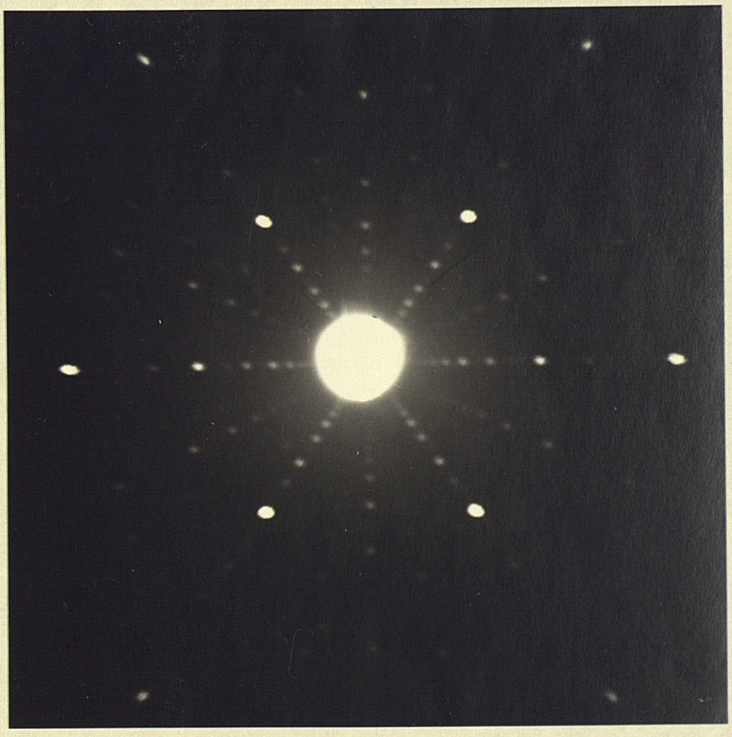

figure 6.2
Laue back reflection from (110) tungsten single crystal prior to use

figure 6.3
Laue back reflection from (100) tungsten single crystal prior to use

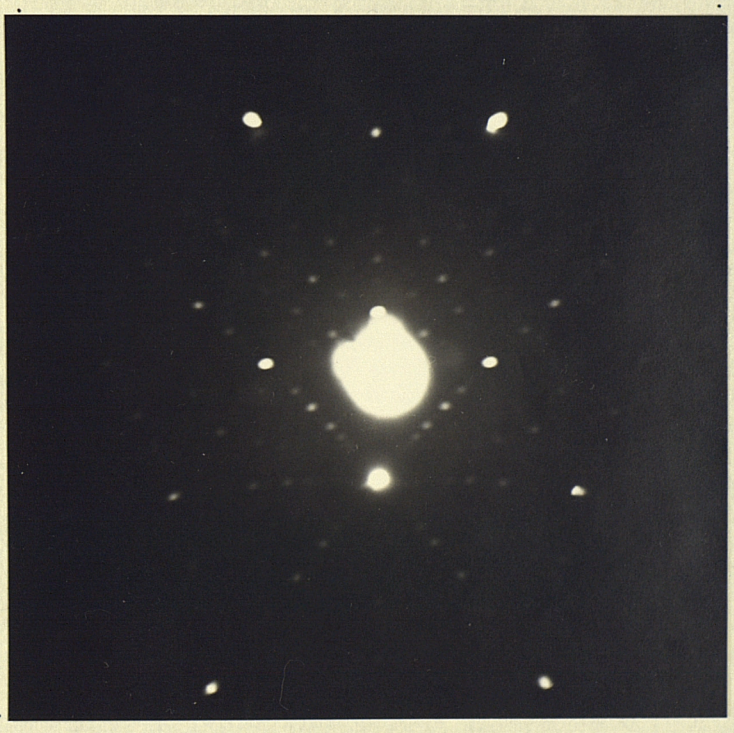

figure 6.4
Laue back reflection from (611) tungsten single crystal prior to use

and 6.4 show Laue photographs of (110), (100) and (611) oriented crystals where the camera length L is 3 cm (see figure 6.21). The crystal, still attached to the goniometer, was then spark planed until its surface was parallel to the desired orientation, finishing on the finest spark setting. An optical micrograph of this surface is shown in figure 6.5. Before polishing, the crystal was spark machined into the required shape (section 7.2.2).

The next stage, mechanical polishing, was accomplished with emery papers and then a lapping machine. In order to prevent the crystal becoming domed during this process it was surrounded by a guard ring of tungsten sheet. This was mounted at the bottom of a moulded epoxy resin disc, the latter designed to fit into the lapping machine. The use of a guard ring to prevent doming was also desirable in the last process: electropolishing. Since electrical contact was then required between the guard ring and the crystal a layer of conducting glue was inserted between the tungsten and the epoxy resin. Finally, the current for electropolishing was fed in through two 2 mm tungsten rods embedded in the conducting glue. The completed 'polishing block' is shown in figure 6.6. Summarizing the procedure:

1 a 25 mm diameter disc was spark machined from 0.020" tungsten sheet and a hole made at the centre to take the crystal;

2 the disc and crystal were placed at the bottom of a plastic mould. A 1 mm layer of conducting glue was poured into the mould and the tungsten rods inserted into it;

3 when the glue set, the mould was filled with epoxy resin;

4 when the resin hardened the block was removed from the mould and a hole drilled in the resin to take the lapping machine spindle.

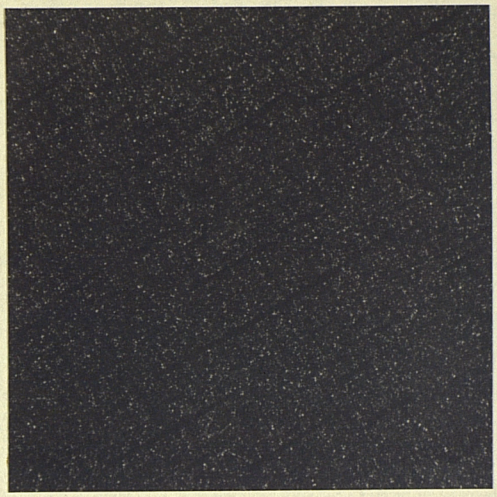

figure 6.5
surface of tungsten crystal
after spark machining (x75)

200 µm

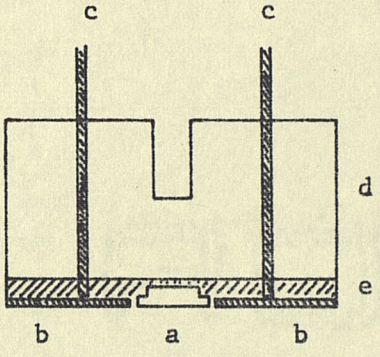

figure 6.6
tungsten single crystal mounted
in 'polishing block'

a spigotted tungsten crystal
b tungsten sheet guard ring
c tungsten rod
d epoxy resin
e conducting glue

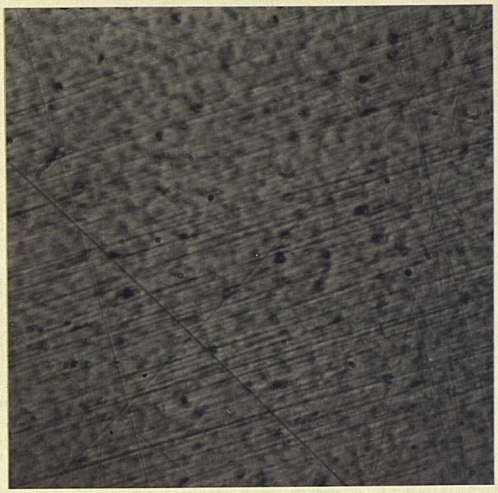

figure 6.7
surface of tungsten crystal after polishing with emery papers
(x600)

25 µm

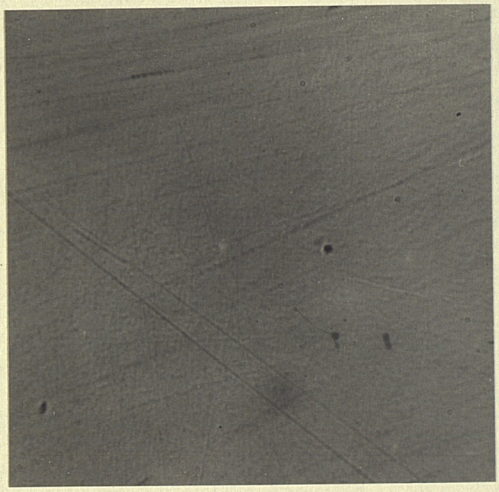

figure 6.8
surface of tungsten crystal after polishing with 3 µm diamond particles on lapping machine
(x600)

25 µm

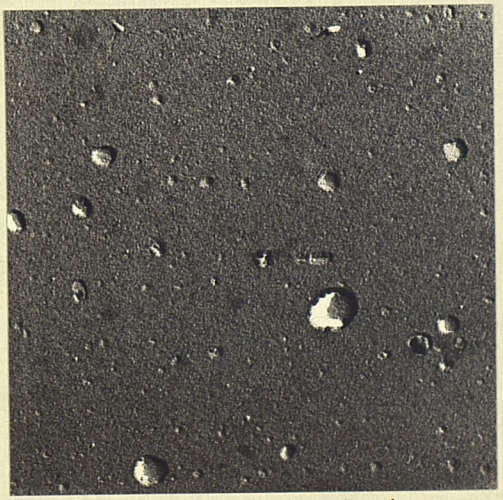

figure 6.9
surface of tungsten crystal after electropolishing
electron micrograph
(x16,000)

1 µm

Polishing with emery paper was carried out manually, starting with grade 0 and finishing with 6/0. The emery paper was laid on a flat surface and the block pressed against it. Figure 6.7 shows the surface after this treatment. The block was then transferred to the lapping machine (Struers DP7) where 3 μm diamond particles brought the surface to the state shown in figure 6.8.

The last step was to remove the mechanically damaged layer by electropolishing[267]. The electrolyte was 0.5N sodium hydroxide and the cathode was a stainless steel plate mounted vertically. Great care was necessary to prevent damage to the surface. The recommended methods[268] used to circulate the electrolyte appeared either to etch the crystal or to produce an 'orange peel' effect. The method used here was to move the crystal back and forth, surface parallel to and 2 cm away from the cathode. This provided continuous arrival of fresh electrolyte at the surface and removed any gas bubbles. The current and voltage settings were critical, electropolishing occurring in the region 9 - 12 V where the current reached a plateau of $\sim$ 4 amp cm^{-2}. The usual method of circulating the electrolyte with the crystal stationary produced a plateau current which varied from 0.5 to 1 amp cm^{-2}. About 20 μm was removed, giving the final surface as shown in the electron micrograph, figure 6.9. A two stage replica process was used in which the carbon film was shadowed at 30° with platinum.

After the outgassing procedure described in chapter 5 the surface was re-examined by means of Laue X-ray back reflection, optical microscopy, electron microscopy and reflection high energy electron diffraction. Laue photographs, figures 6.10, 6.12 and 6.14, show that in all cases the single crystal had broken into small crystallites, retaining the original orientation. The crystallite size must therefore have been less than 100 μm,

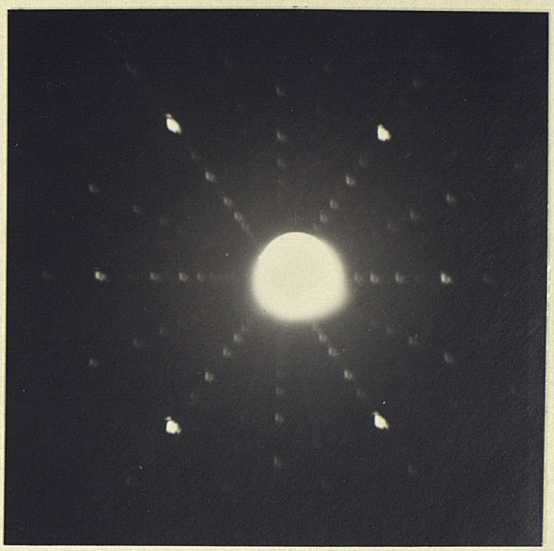

figure 6.10
Laue back reflection from (110) tungsten crystal after measurements

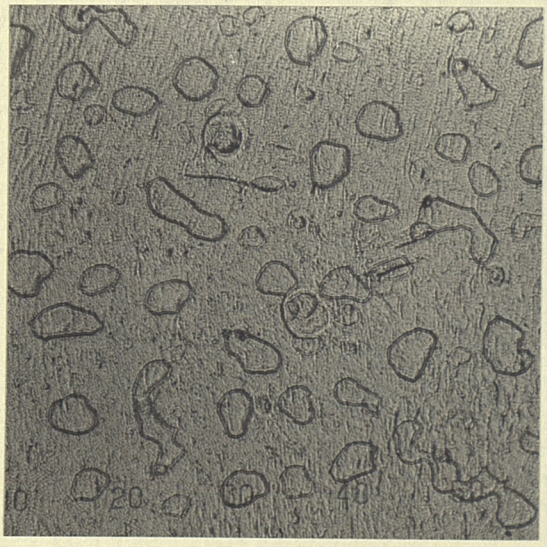

figure 6.11
surface of (110) tungsten crystal after measurements (x75)

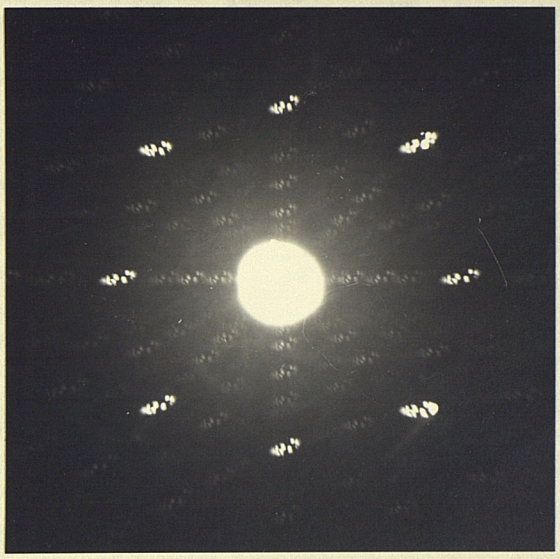

figure 6.12
Laue back reflection from (100) tungsten crystal after measurements

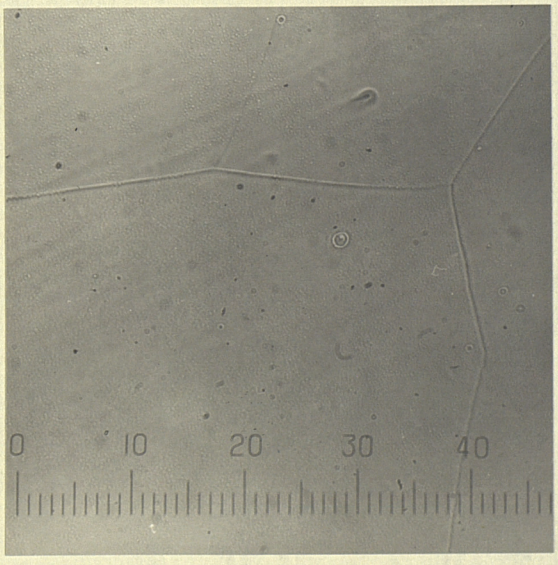

figure 6.13
surface of (100) tungsten crystal after measurements (x150)

100 µm

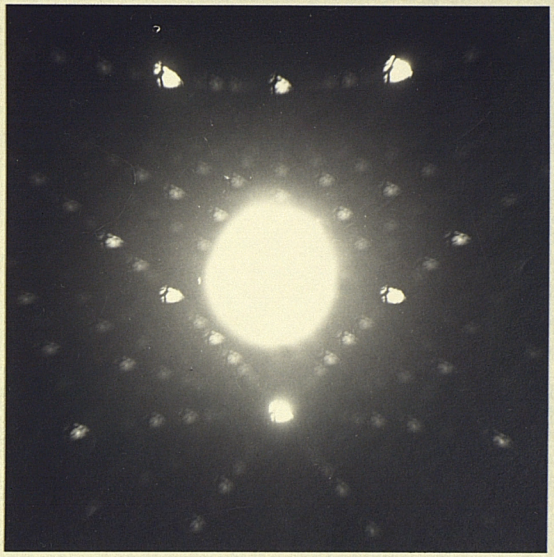

figure 6.14
Laue back reflection from (611) tungsten crystal after measurement

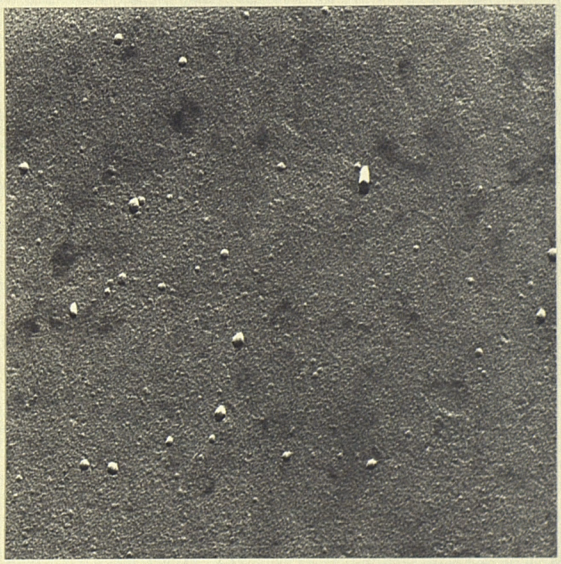

figure 6.15
typical electron micrograph of crystal after measurements (x16,000)

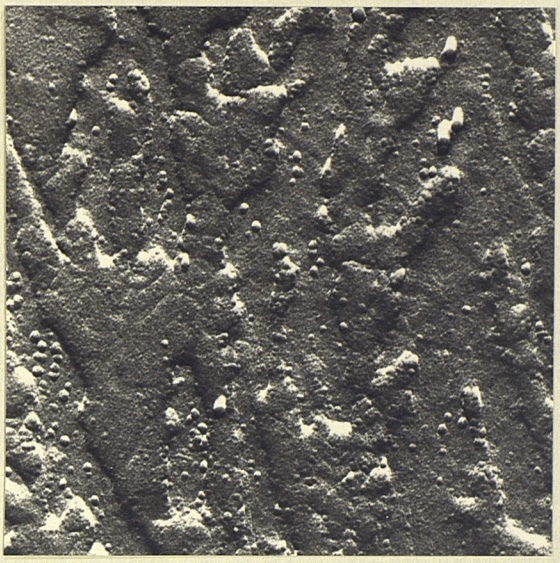

figure 6.16
electron bombardment damage to surface of (611) tungsten crystal

(x16,000)

1 μm

figure 6.17
RHEED pattern from (100) tungsten along [100] azimuth

figure 6.18
RHEED pattern from (100) tungsten along [110] azimuth

the diameter of the X-ray beam. The optical micrograph of the (110) surface, figure 6.11, showed crystallites of 50 - 100 μm size randomly spaced and occupying about 10% of the surface area. A similar photograph of the (100) surface, figure 6.13, shows the whole surface intersected with grain boundaries, the smallest crystallites being 100 μm across. Electron micrographs of all surfaces were very similar, showing that on this scale they were very flat. Figure 6.15 is a typical example, the only features, scattered 'pimples' probably originating from the replicating process. Greater magnification possible with this microscope (AEI EM6G) only resolved the already visible carbon replica structure.

Electron bombardment damage occurred in the first single crystal experiment where stringent precautions were not taken (section 7.2.2.2). This was very obvious as can be seen from the electron micrograph, figure 6.16.

Since X-rays penetrate about 3 μm into tungsten, Laue photographs are not adequate to determine the structure of the last few atomic layers. Consequently, reflection high energy electron diffraction photographs were taken using the electron microscope. The grazing incidence (4^{o}) electron beam, energy 80 KeV, penetrates at the most only 10 atomic layers and so gives a good indication of the state of the true surface. The spacing between rows of atoms in the surface, d, is given by:

$$Rd = \lambda L \qquad 6.1$$

where R is the row spacing of the diffraction pattern, λ is the electron wavelength and L is the camera length. Figures 6.17 and 6.18 show diffraction patterns along the [100] and [110] azimuths respectively for which the appropriate d values are 3.16 and 2.23 Å (figure 6.19). The values calculated from equation 6.1, using R taken from figures 6.17 and

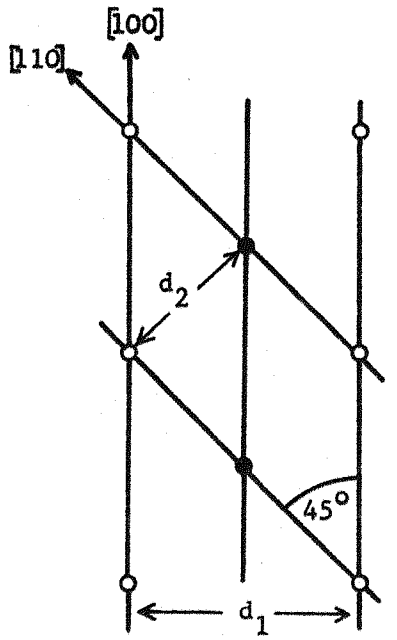

figure 6.19
tungsten (100) orientation showing [100] and [110] azimuths

d_1 = 3.16 Å
d_2 = 2.23 Å

○ atoms in plane of diagram
● atoms in plane $d_1/2$ into surface

6.18, are 3.15 and 2.24 Å, in very good agreement. The directions were at 45° ± 2° to each other. Similarly, for the (110) surface diffraction patterns were obtained for the [110] and [100] azimuths. These were at 90° ± 2° to each other.

Unfortunately the specimen manipulator used in these experiments was at an early stage of development and insufficient movement was available to obtain the best diffraction patterns. The experiment was repeated 6 months later using a modified manipulator but no diffraction patterns could be obtained, presumably because the surfaces had oxidized during their exposure to the atmosphere.

6.2 polycrystalline tungsten foil

Aged polycrystalline tungsten foil has a reproducable work function[110], is easy to prepare and so is suitable for use as a reference material in the

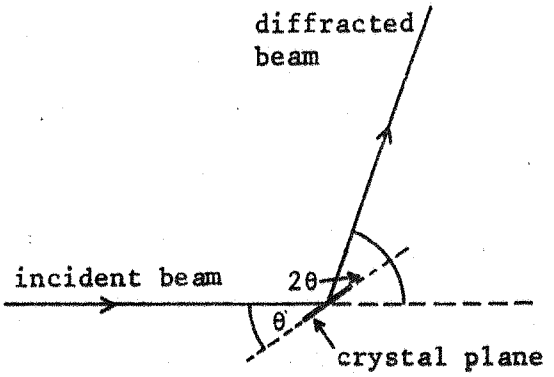

figure 6.20
diagram of X-ray diffractometer

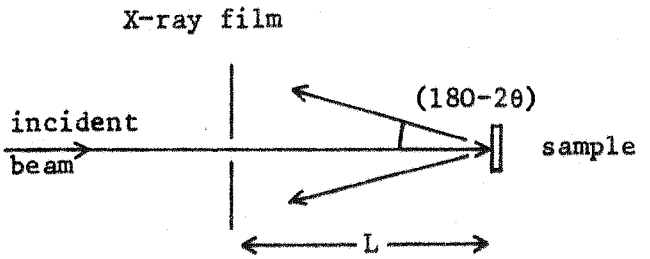

figure 6.21
diagram of Laue X-ray back reflection

L = 3 cm

Kelvin technique. Hopkins and Rivière[265], from the mean of many measurements, suggest the use of 4.55 eV for the area average work function at zero K ($\bar{\phi}$). As long as this value is used consistently throughout Kelvin work its absolute accuracy is not important since it is only used as a reference.

In this work two types of foil were used, 0.1 mm and 0.5 mm thickness, but these appeared to exhibit the same $\bar{\phi}$ even though they were rather different. Foils before and after ageing were investigated by means of Laue back reflection photographs, X-ray diffractometer traces and optical micrographs. X-rays are diffracted according to Bragg's law: $\sin\theta = \lambda/2d$ where d is the distance between lattice planes, λ is the wavelength of the X-rays and θ the

diffraction angle. d can be calculated from[269]:

$$d = a / (h^2 + k^2 + l^2)^{\frac{1}{2}}$$

where a is the lattice constant (a = 3.165 Å for tungsten) and h, k, l are the Miller indices of the crystal plane. In the diffractometer method, figure 6.20, λ is kept constant (CuKα) and θ is varied. In the Laue method (figure 6.21) for each value of d, θ is constant and λ varied (polychromatic X-ray beam).

Figure 6.22 is an optical micrograph of virgin 0.1 mm foil showing very small crystallites. The corresponding Laue photograph, figure 6.23, has continuous rings showing that the crystallite size is small compared with the X-ray beam area (0.1 mm diameter). The fact that the intensity of the rings varies symmetrically implies some degree of preferred orientation probably due to the rolling process in manufacture. After ageing, the optical micrograph (figure 6.24) shows crystallites of 20 - 100 µm size as is confirmed by the Laue photograph (figure 6.25) in which the continuous rings have been replaced by a series of spots, each corresponding to a reflection from an individual crystallite. The 0.5 mm thick foil was somewhat different. The Laue photograph (figure 6.26) before ageing showed no preferred orientation. After ageing the optical micrograph (figure 6.27) showed large crystallites up to 0.1 mm in size. The X-ray beam for the Laue photograph (figure 6.28) was aimed at a large crystallite and it produced an almost perfect (100) single crystal pattern.

The diffractometer results are given in table 6.1. In order that preferred orientation did not affect the readings the specimens were spun about an axis perpendicular to their surface. Virgin 0.1 mm foil was predominantly (100) oriented with a substantial amount of (211). After ageing the (211)

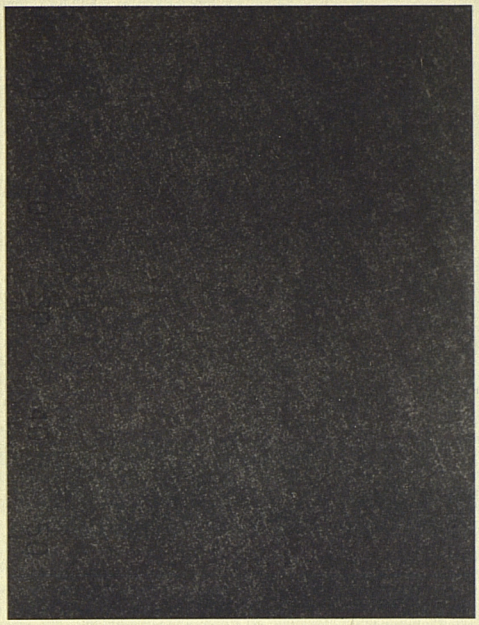

100 μm

figure 6.22
virgin 0.1 mm tungsten foil
(x150)

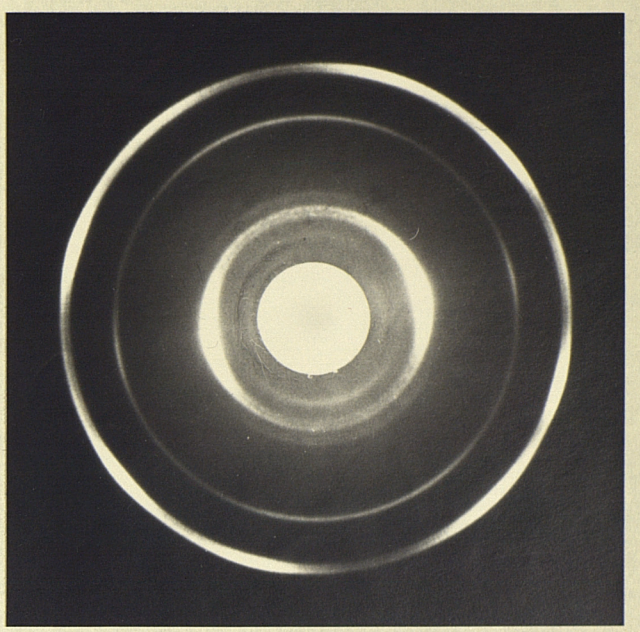

figure 6.23
Laue back reflection from virgin
0.1 mm tungsten foil

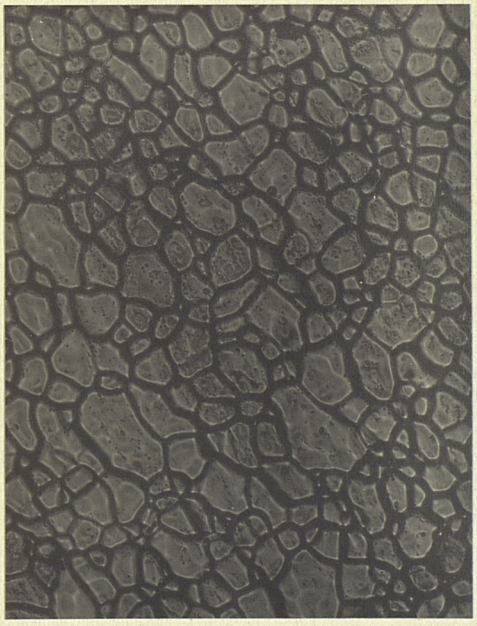

100 μm

figure 6.24
aged 0.1 mm tungsten foil
(x150)

figure 6.25
Laue back reflection from aged
0.1 mm tungsten foil

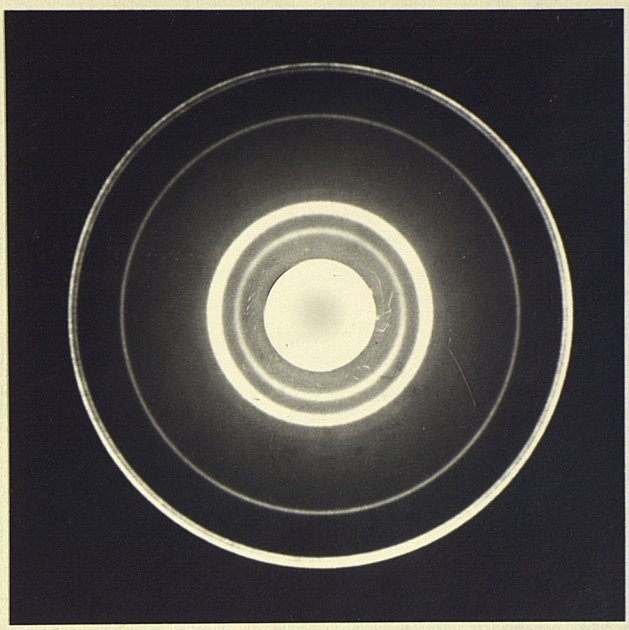

figure 6.26
Laue back reflection from
virgin 0.5 mm tungsten foil

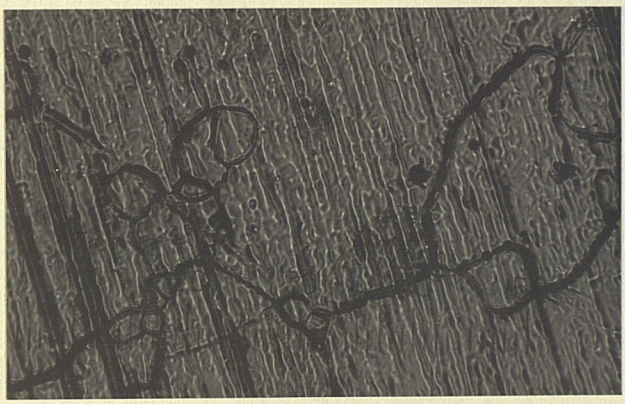

figure 6.27
aged 0.5 mm tungsten foil
(x75)

200 μm

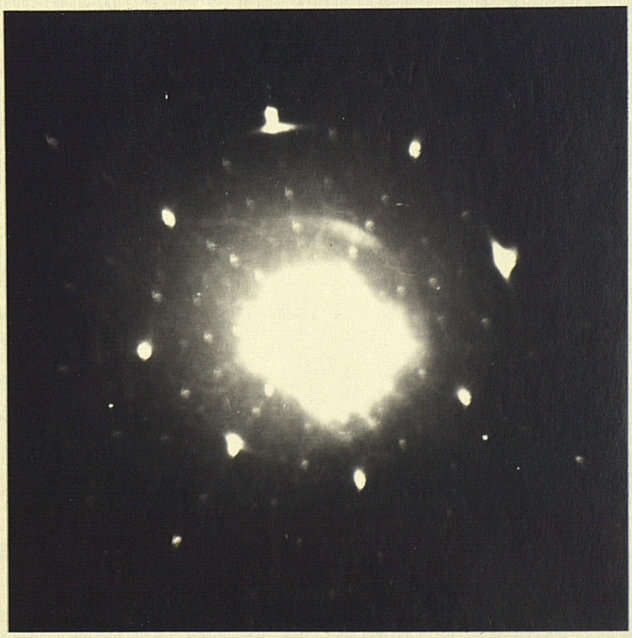

figure 6.28
Laue back reflection from
aged 0.5 mm tungsten foil

intensity was reduced, the surface then being almost entirely (100). Virgin 0.5 mm foil was quite different. Although (100) predominated there was a large (110) component and some (321), neither ever observed in the thinner foil. After ageing only (100) was apparent, confirming the Laue picture.

table 6.1 X-ray diffraction from polycrystalline tungsten foil

reflection	diffraction angle 2θ	intensity for CuKα radiation (uncorrected) sample spun			
		virgin 0.1 mm foil	aged 0.1 mm foil	virgin 0.5 mm foil	aged 0.5 mm foil
110	40.26	-	-	40	-
200	58.25	100	100	100	100
211	73.16	26	10	27	-
220	87.02	-	-	4	-
310	100.64	0.5	3	24	-
222	114.92	5	3	2	-
321	131.20	-	-	13	-
400	153.55	7	29	11	17

$2d\sin\theta = n$ $\quad d = a\,(h^2 + k^2 + l^2)^{-\frac{1}{2}}$ $\quad a = 3.165$ Å for tungsten

Kelvin c p d measurements reproducably gave a work function of 4.65 eV for a (100) tungsten single crystal (section 8.1) where 4.55 eV was assumed for the foil reference. This c p d was unaltered when the reference was changed from 0.1 to 0.5 mm foil. Since the latter was entirely (100) oriented it seems unlikely that the lower work function of foil was due to the presence of other low work function orientations as has been suggested[174,270]. A possible explanation is that the grain boundaries possess very low work functions, as is exhibited by stainless steel[271].

CHAPTER 7 WORK FUNCTION MEASUREMENTS

Two techniques were used in this work: Anderson and Kelvin

They are described in this order

7.1 Anderson (retarding field) measurements

The current in the retarding field region of the characteristic of a diode is given by equation 3.9:

$$i_r = A\, s_c\, (1-r_c)\, T^2 \exp\{-\tfrac{e}{kT}(\phi_c - V_a)\}$$

A plot of log i_r versus V_a should therefore be a straight line. A change $\Delta\phi_c$ in the anode work function, all else remaining constant, causes this line to be displaced along the voltage axis by an amount equal to $\Delta\phi_c$. Thus, if i_r is held constant, $\Delta\phi_c$ is equal to the change in V_a. However, in order that this voltage change at a single value of current accurately reflects $\Delta\phi_c$, it is essential that the log i_r versus V plot is linear. To ensure that the latter condition was obeyed the experimental diode was constructed with close-spaced, plane parallel geometry. A compromise had to be reached between the requirements of close-spacing and the need to be able to evaporate material on to the anode. Anderson's original method[110] overcame this problem using a collimated beam of electrons produced by an electron gun. However, the simple planar diode shown in figure 7.1 was found to be adequate. The emitter and collector were identical, consisting of tungsten foil 2.5 cm long, 3 mm wide, 0.1 mm thick and separated by 4 mm. Both were directly heated. The diode was mounted at 45° to the vertical in order that material could be evaporated from below without being shadowed by the emitter. Initially (tube 1) a thermocouple (W - W/26%Re) was attached to the emitter only, this being necessary to ensure that the

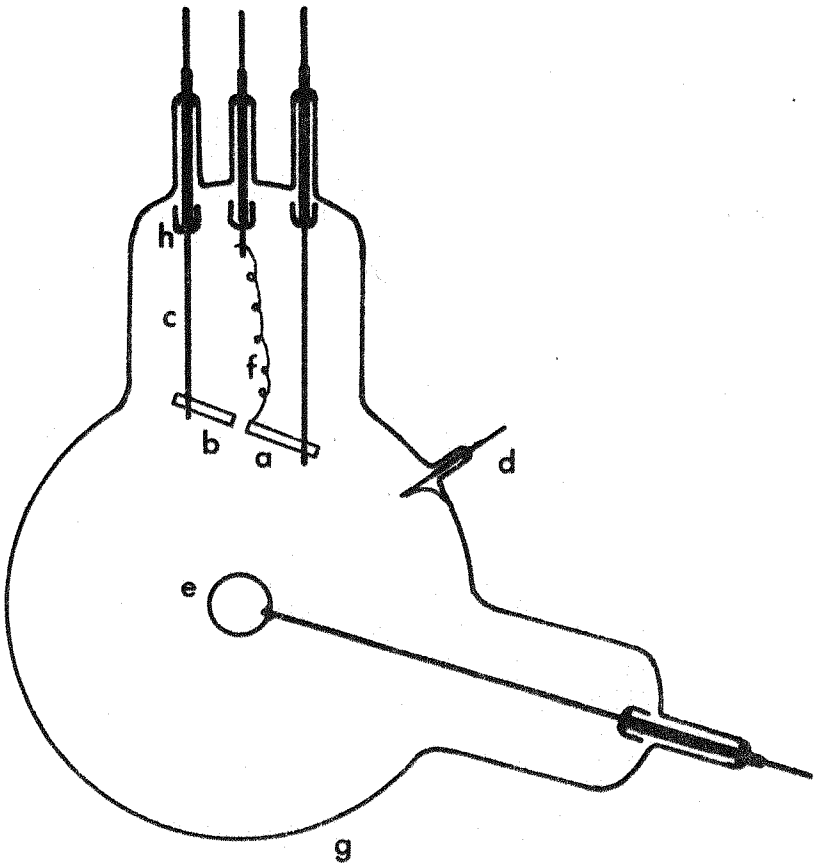

figure 7.1

tube 1 Anderson technique

a emitter

b collector

c tungsten rod

d screen connection

e evaporator coil

f thermocouple

g 1 litre glass envelope

h evaporation shield

temperature, on which the emission critically depends (equation 3.9), was constant. Even so it was found that at least 24 hours 'warm-up' period was required before the emission current stabilized. A 'voltstat' constant voltage transformer on the primary of the transformer supplying the emitter current provided some independence from mains voltage fluctuations.

A retarding field plot, before degassing the electrodes, was found to be far from linear. Invariably the direction of current flow would reverse at high retarding voltages, presumably due to ion currents from the emitter. Well degassed electrodes in a clean system (1×10^{-10} torr) usually produced the required straight line. Some difficulty was experienced at first with (a) electrodes buckling during degassing and (b) electrical leakage caused by evaporation of metal components. The first problem was found to be due to spot welding electrodes under strain and could be eliminated by careful alignment during welding. The second problem was best overcome by the use of glass evaporation shields as shown in figure 7.1.

After degassing was complete, retarding field plots for a range of emitter temperatures were made. The temperature which gave the best linearity in this plot was used in the experiments. The current (operating point) at which the voltage was measured was chosen at the centre of the most linear section of this line. Typically the emitter temperature was 1800 K and the operating point was 10^{-10} amp. A Keithley 610 electrometer used in the constant current mode provided a convenient method of measuring the voltage V_a at the operating point. A 'back-off' voltage supply was included in the circuit (figure 7.2) so that the electrometer voltage range could be set to the desired value, usually 0-1 V. In order that no correction was necessary for the voltage drop across the electrometer, the latter was used at high

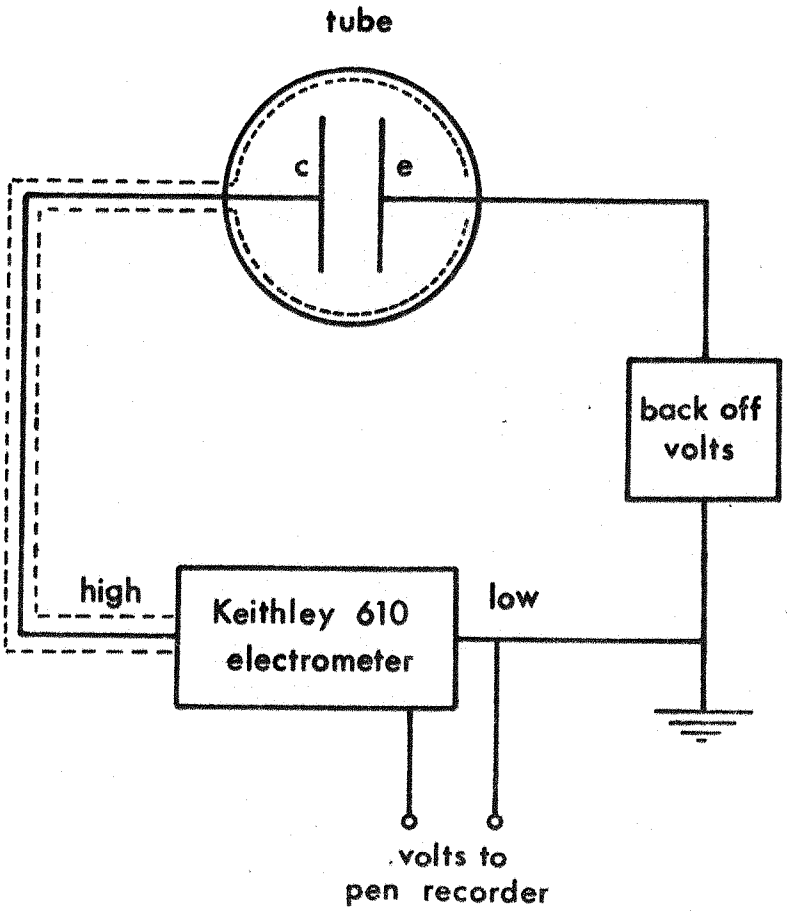

e emitter

c collector

figure 7.2

block diagram of Anderson measurement system

amplification (low input resistance) where the correction, 1 mV, could be neglected. In all cases complete retarding field plots were made both before and after an experiment to ensure that there was no deviation from linearity or parallelism. This determined the accuracy of the measurement.

After thoroughly degassing all parts of the tube the pumps were switched off and the system filled with dried nitrogen. One side arm was removed so that a 1 cm length of zirconium wire 1 mm in diameter could be inserted on to the evaporator. The system was then pumped out and the zirconium fused on to the coil. After charging the evaporator in this way it was not possible to degas it at high temperatures without evaporating all the zirconium. The procedure was to degas all other parts of the tube, and when the pressure was in the low 10^{-10} torr range the evaporator was heated to just below the melting point of zirconium (2120 K) until the pressure again dropped to the low 10^{-10} torr range. Finally the evaporator was flashed for a few seconds at a time to 2600 K, well over the temperature used for evaporation.

The above procedure was partially successful in enabling evaporation to be carried out at low pressures. However, a pressure of 2×10^{-10} torr during evaporation was the best achieved. Since, assuming unit sticking coefficient, this corresponds to a gas coverage of $\sim$ 4 monolayers for a 50 minute evaporation, it is clear that a method of evaporating at lower pressures was essential. A large part of the problem was that zirconium (and, in later experiments, uranium) alloyed with the tungsten evaporator, eventually causing it to part at the points arrowed in figure 7.3. Examination of an evaporator after use revealed that tungsten had been removed from the edges of the zirconium globule and deposited at the bottom of the loop in the centre of the globule. The size of the initial charge of

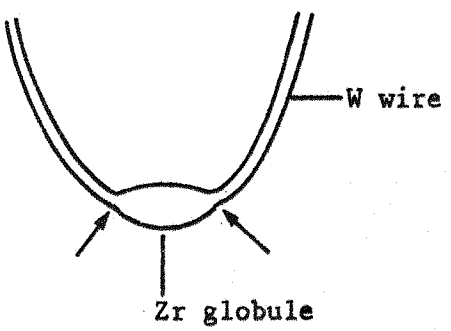

figure 7.3
evaporator indicating the points at which failure occurred

zirconium was critical: too great an amount caused rapid failure; too small an amount resulted in there being no zirconium left at the end of the outgassing procedure. One way of surmounting this difficulty was to outgas the evaporator by electron bombardment, a technique which appeared to retard the rate at which the tungsten was dissolved away. Direct heating was only used for evaporation. This modified evaporator is shown in figures 7.4 and 7.5 (tube 2). Additional advantages of electron bombardment were that (a) it enabled the evaporator support rods to be degassed, thus removing a major source of gas, and (b) zirconium could be evaporated by bombardment heating even after the evaporator failed.

Tube 2 was additionally modified in the following ways:

a a thermocouple was fitted to the collector in order to make desorption measurements on the evaporated films. Since an absolute measurement of temperature was required, the thermocouple cold junctions (ie the tungsten leadthroughs) were moved back into separate side arms where they were shielded from direct radiation from the emitter;

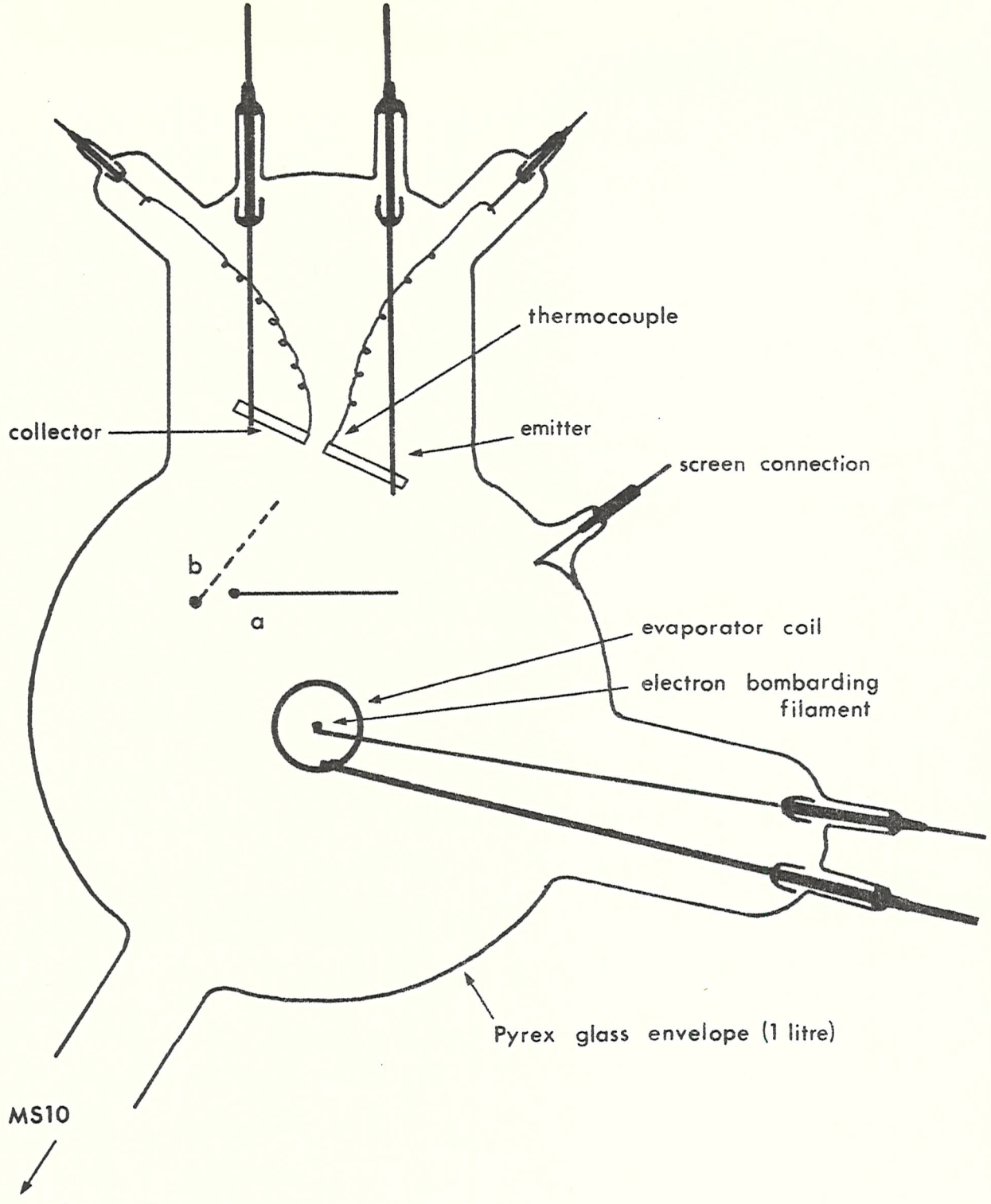

figure 7.4

tube 2 Anderson technique front elevation

a shutter in closed position

b shutter in open position

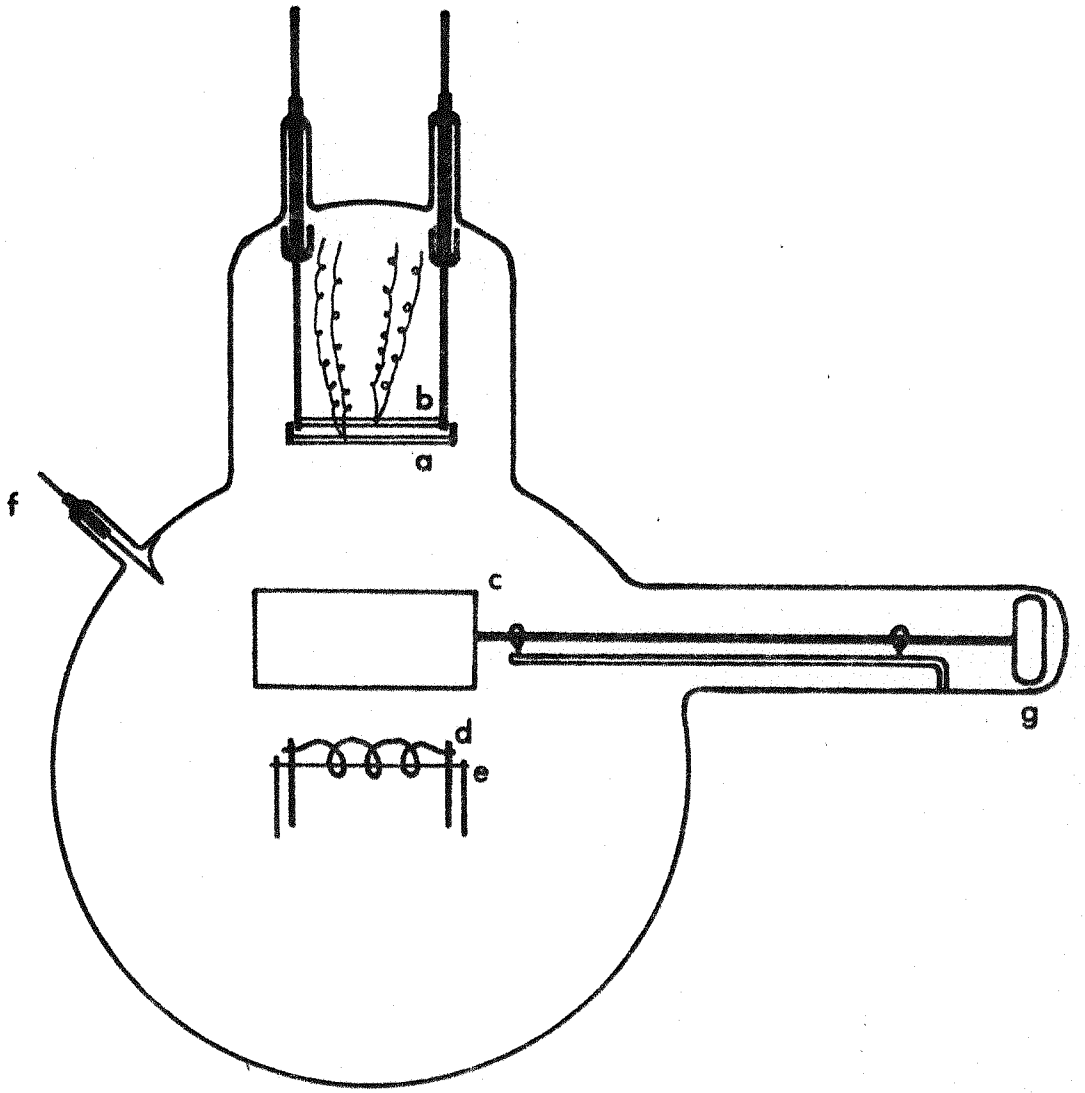

figure 7.5
tube 2 side elevation

a emitter
b collector
c shutter
d evaporator coil
e electron bombarding filament
f screen connection
g encapsulated iron slug

b a magnetically operated shutter was mounted below the diode so that the evaporator could be heated to a steady temperature before allowing any evaporant to reach the collector. This ensured a linear coverage scale in adsorption measurements;

c an extra arm was fitted for connection to an MS10 mass spectrometer used for gas contamination studies.

The complete tube 2 is shown in figures 7.4 and 7.5.

7.1.1 comments on the Anderson technique

Initially this technique was used to measure the variation of work function with coverage of zirconium. The outstanding advantage of the method is that it enables continuous recording of contact potential changes to be made. The evaporant can be deposited in a short time, so minimizing contamination. However, the temperature at which the zirconium evaporator was held ($\sim$ 2500 K) permitted considerable electron emission, some of which reached the collector and gave spurious results. This effect could be easily overcome by maintaining the evaporator at a positive potential (usually 48 V) with respect to the diode. However, this resulted in the collection of positive ions of zirconium at the diode, again affecting the results. In the present work this difficulty was avoided by evaporating comparatively slowly ($\sim$ 1 monolayer in 50 minutes) so that the rate of arrival of zirconium ions was negligible. Thus one of the principle advantages of the method, rapid evaporation, was lost. A possible method of eliminating the effects of both electron and ion currents is the interposition of a 'grid' in the form of a ring between the evaporator and the diode, through which the zirconium flux must pass. If voltages are applied to the electrodes, as

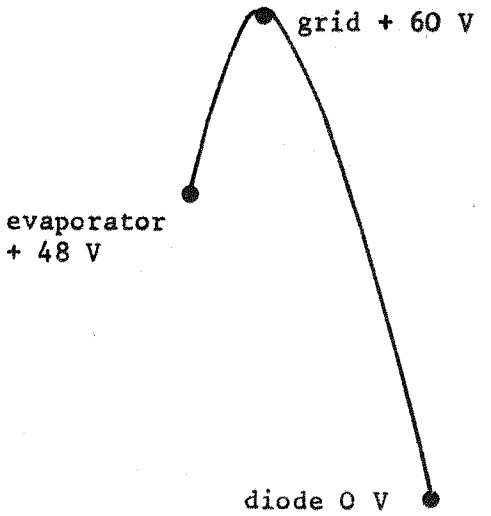

figure 7.6
suggested potentials to suppress ion and electron currents

shown in figure 7.6, then electrons are collected at the grid and ions reflected back to the evaporator.

The use of the Anderson method in the desorption measurements involved heating the collector to successively higher temperatures and measuring the contact potential difference after each period of heating. Originally it was hoped to use this method to detect the small changes in work function which occurred after heating uranium films (section 4.2). However, the scatter of the points obtained after heating the collector made any such observation very difficult. The large scatter was thought to be of two causes:

a contamination in the 15 minute period required for the diode to stabilize;

b slight changes in the geometry of the diode (eg buckling of the anode) which caused the shape of the retarding field characteristic to alter.

Evidence for the latter was provided by the fact that after completely desorbing the film the voltage differed appreciably (as much as 200 mV) from the initial clean tungsten value.

The Anderson method was found to be most useful for gas adsorption studies where the Kelvin technique is difficult to apply because the work functions of both reference and substrate change simultaneously. The technique usually employed in such Kelvin measurements is[224]:

a contaminate both surfaces;

b pump out the gas;

c flash the gas from one surface;

d re-contaminate the cleaned surface.

From the two contact potential difference/coverage curves obtained from steps (a) and (d) it is possible to calculate the work function changes on both surfaces. Assumptions involved in this procedure are:

1 the coverage scales in steps (a) and (d) are exactly equal;

2 no work function change in either surface occurs during pump-out;

3 no gas desorbed (and possibly dissociated) at step (c) adsorbs on to the other electrode;

4 adsorption occurs only on the cleaned electrode at step (d).

In view of these difficulties the use of the Anderson method seems very attractive. However, apart from the problems of patchy surfaces and reflection coefficients discussed in section 3.2 the method has 3 disadvantages:

a the surface under investigation is continually bombarded by low energy electrons which may lead to desorption of weakly bound gases or other processes[272]:

b the collector is heated by radiation from the emitter, again likely to cause desorption or other thermally controlled processes (typically the collector temperature in this work was ∿ 500 K for an emitter temperature of 1800 K). This difficulty is not experienced in an electron gun technique;

c gases may be dissociated at the emitter and then adsorb on the collector.

It is suggested that a combination of the Anderson method (to determine the overall shape of the coverage curve and pressure dependent effects - if any) with the Kelvin technique (to determine the absolute values) would yield the most conclusive results.

7.2 Kelvin measurements

In the Zisman[108] modification of the Kelvin technique used in this work an a.c. voltage is produced across the resistor R connecting the two surfaces. The theoretical amplitude of this signal has been calculated by Macdonald and Edmondson[273] for certain special cases. If C_o is the (stationary) capacitance of the Kelvin electrodes and ω is the frequency of vibration then if $RC_o\omega < 10$ and the stray capacitance $C' = 0$, the signal amplitude is given by:

$$V = 0.86\ (V_{c\ p\ d} - V_a)\ RC_o\omega \qquad 7.1$$

for a modulation constant of 0.5.

In order to reduce the harmonic component of the signal, C' should be minimized.

7.2.1 preliminary measurements

The first Kelvin measurements were made using a very simple system. The experiment tube is shown in figure 7.7 and the circuit shown diagrammatically in figure 7.8. A major problem in this technique is the production of signal amplitudes sufficient for separation from the noise. In order to reduce unwanted signals as far as possible (a) the tube was coated with an internal conducting screen of bright platinum (Johnson-Matthey F104); (b) the high impedance head amplifier was placed as close to the tube as possible; (c) great care was taken to screen all high impedance leads, earth all electrodes other than the Kelvin pair and avoid unwanted vibrations. The signal, after passing through the head amplifier and tuned amplifier, was fed into an oscilloscope. The back-off voltage was simply adjusted until a null was obtained as observed on the oscilloscope. The contact potential difference was then read on a voltmeter across the back-off voltage supply.

The tube used in these measurements (tube 3 - figure 7.7) consisted of a movable high impedance electrode (the substrate) of tungsten foil which could be electron bombarded from below, and an identical reference electrode which could also be bombarded from behind. The substrate was attached to a hinge which allowed it to be moved magnetically from the measurement position under the reference to a position away from the reference where it could be electron bombarded or coated with an evaporated film. The reference was mounted on a spring arrangement constructed from thin (0.1 mm) tungsten foil which gave a natural resonance frequency of $\sim$ 15 hz. Vibration of the reference was initiated by the crude but effective method of tapping the tube. This allowed several minutes for a measurement to be made before

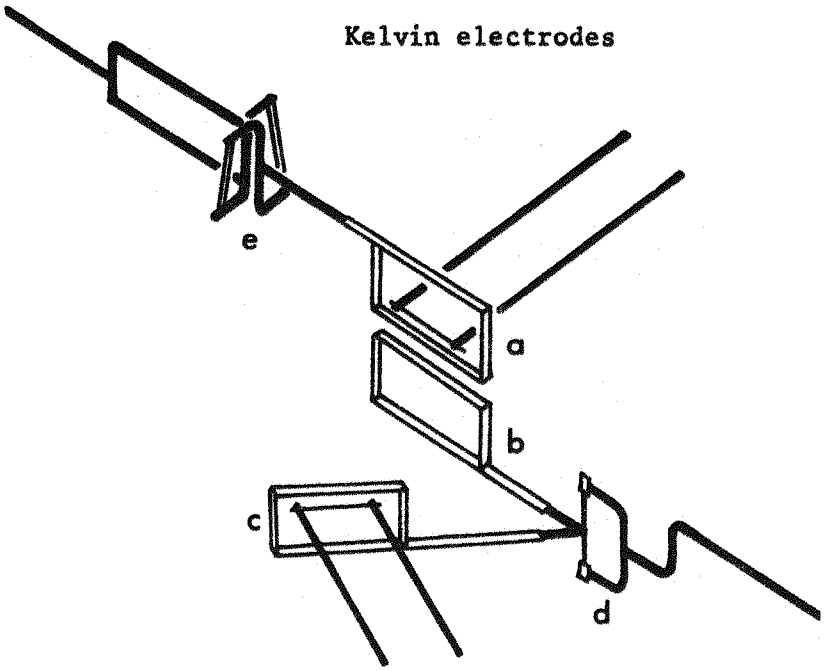

a W foil reference
b W foil substrate in measurement position
c substrate in electron bombardment position
d hinge
e spring

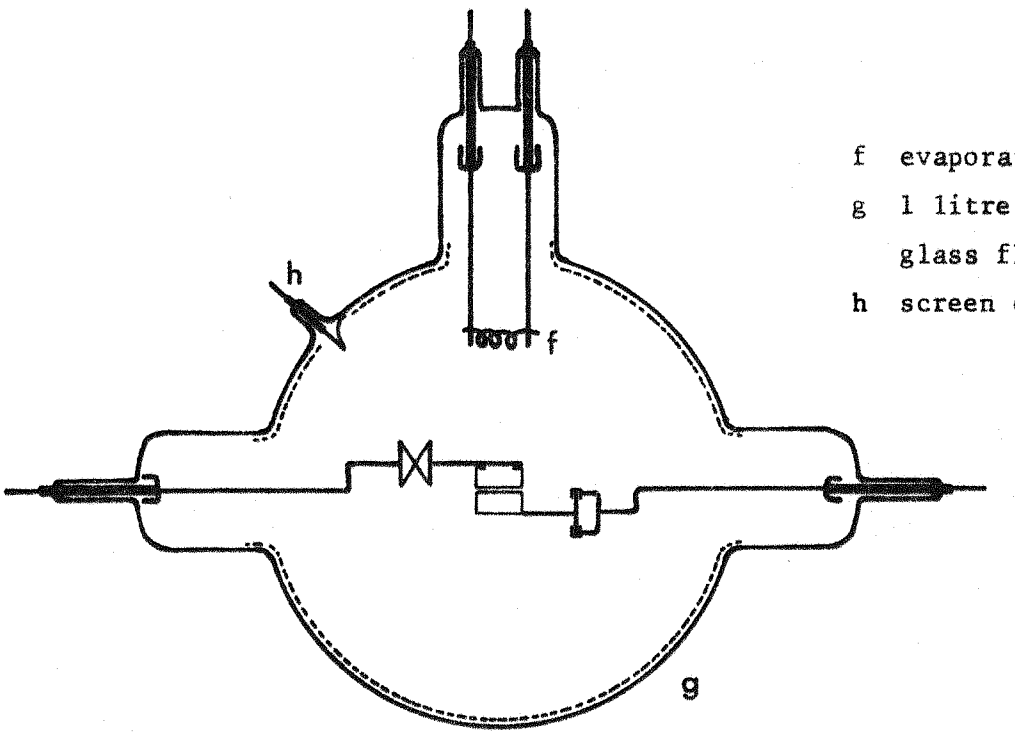

f evaporator
g 1 litre Pyrex glass flask
h screen connection

figure 7.7
tube 3 preliminary Kelvin tube

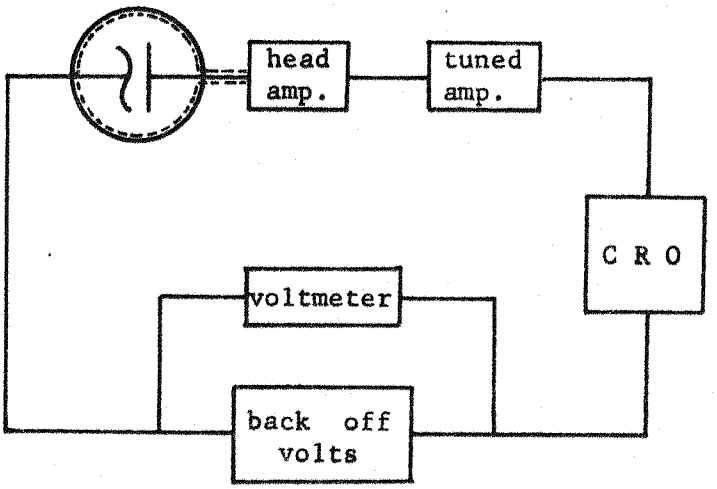

figure 7.8
block diagram of circuit for preliminary Kelvin measurements

the amplitude of vibration became too small. The procedure for measurement of a work function/coverage curve was as follows:

a both electrodes were flashed clean and allowed to cool;

b with the substrate in the position away from the reference, material was evaporated for a measured length of time (usually 30 seconds);

c the reference was flashed and the substrate moved back into the measurement position;

d after measurement the substrate was moved away again and the procedure from step (b) repeated.

The accuracy with which the contact potential difference could be measured with this arrangement was ∿ 20 mV. However, any variation with electrode spacing was not apparent since the substrate was always returned to the same position for measurement. For this reason the reproducibility obtained with this tube was within the measurement error.

The tube design and measurement technique for the major part of the Kelvin

work was considerably more sophisticated than that used for this preliminary experiment. A description of these tubes is followed by an account of the measurement system.

7.2.2 Kelvin tube design

Following the preliminary tube all Kelvin work was performed on tubes in which the substrate was fixed and the reference was movable (tubes 4-8). The latter was mounted on stainless steel bellows which allowed movement both horizontally and vertically, and was attached externally via a perspex rod to a Goodmans electromagnetic vibrator (manufactured by Pye-Ling Limited). With the spring-vibrated reference (tube 3), the use of frequencies higher than $\sim$ 20 hz was prevented by rapid decay of the oscillations. Electromagnetic vibration enabled the frequency to be raised to the 50 - 100 hz range, thus increasing the amplitude of the signal (equation 7.1). Again a natural resonance of the reference electrode was employed so that the oscillation could be maintained with very low vibrator amplitudes. This minimized vibration of other electrodes in the tube which would otherwise give rise to stray signals. As the frequency was increased, greater vibrator amplitudes were required so that in practice 100 hz was the convenient maximum. Very close spacing of the Kelvin electrodes also facilitated the use of lower amplitudes without reducing the modulation constant. An electrode spacing of 0.3 mm with an amplitude of 0.2 mm was typical. The reference electrode could be positioned either in the measurement position at the centre of the tube or to one side where it was possible to electron bombard it on the front face.

A lot of the problems associated with the Kelvin technique appeared to arise from the charging up of bare glass which produced a spurious (and often immense) contact potential difference. As a result, all parts of the glass tube which were visible to the Kelvin electrodes were coated with a conducting layer of bright platinum. As has already been pointed out, such a coating was necessary for electrical screening purposes. However great care was necessary in applying this coating to ensure that all the glass surfaces were rendered conducting. In particular it was important that the inner tubing around the vibrating electrode contained no bare patches.

Apart from the introduction of bellows, combined with careful screening, the other major improvement in tube design was the inclusion of magnetic loading of the evaporator. This simply enabled the material under study to be fed on to the evaporator (after the latter had been degassed) whilst still under vacuum, and resulted in greatly improved evaporation conditions.

7.2.2.1 tube 4 (figure 7.9)

This tube was used on a getter-ion pumped system and was primarily intended for the investigation of gas contamination of uranium films deposited on a polycrystalline tungsten substrate. A second aim was to determine whether there had been any mercury contamination of the uranium in the mercury diffusion pumped system. The preliminary experiment had shown that a major part of the gas evolved during evaporation was desorbed from the glass walls which had been heated by the evaporator. For this reason the evaporator was mounted at the centre of a separate 500 ml bulb. In addition 'outgassing loops' were used for the first time: instead of single support

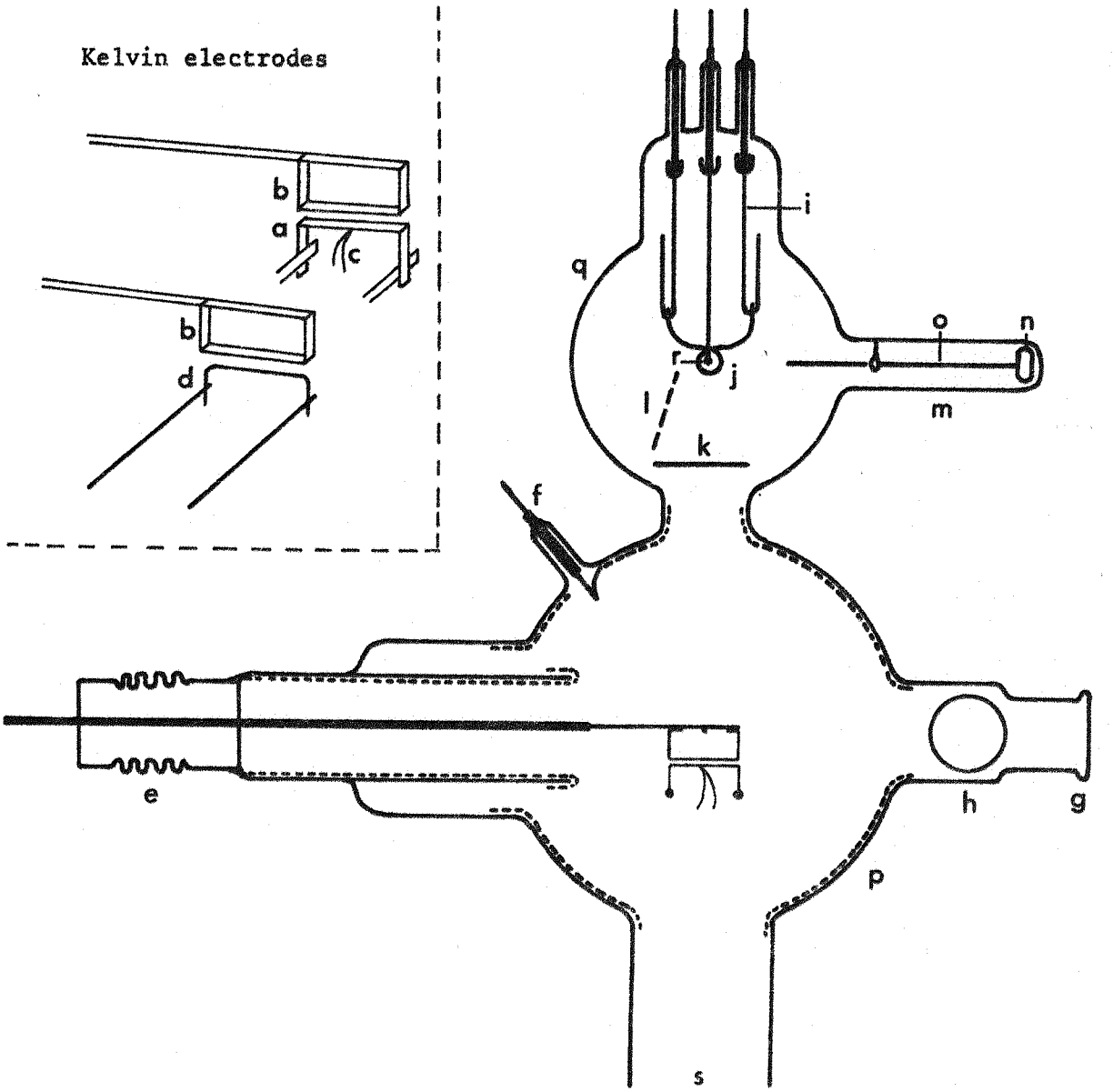

a	W foil substrate	k	shutter closed
b	W foil reference	l	shutter open
c	thermocouple	m	magnetic uranium loader
d	reference electron bombarding filament	n	encapsulated iron slug
e	stainless steel bellows	o	uranium wire
f	screen connection	p	1 litre Pyrex glass flask
g	window	q	500 ml Pyrex glass flask
h	magnetic shutter	r	evaporator electron bombarding filament
i	outgassing loop		
j	evaporator	s	connection to pump

figure 7.9
tube 4 (Kelvin)

wires for the evaporator coil these were made into loops which could be outgassed separately. Thus adsorbed gas could be removed from the supports even after the evaporant material had been fused on to the coil. The substrate, polycrystalline foil, was directly heated and its temperature measured with a W - W/26%Re thermocouple. A shutter was incorporated in the evaporator bulb so that measurements could be made on the gas evolved from the uranium during evaporation whilst preventing uranium itself from being deposited.

7.2.2.2 tube 5

This tube was identical to tube 4 except that the substrate was replaced by a tungsten single crystal. The aim was to determine whether such single crystals could be degassed by electron bombardment without damage to the surface. Figure 7.10 shows the arrangement. The crystal was spark machined to the required orientation and shape (in this case (611) orientation and disc-shaped: 8 mm diameter and 2 mm thickness) and 3 holes machined from the edge towards the centre at 120° to each other. 1 mm wire was inserted in the holes, bent round and spot welded together as shown in figure 7.10. The crystal, supported in this way, was electron bombarded from below with focusing of the electrons provided by a guard ring maintained at a negative voltage with respect to the crystal. In this way it was hoped to prevent electrons reaching the front face of the crystal. However, after the usual degassing procedure the work function was rather higher than would be expected of such a high index plane (see section 8.1).

An electron micrograph (figure 6.16) of the crystal after its removal from

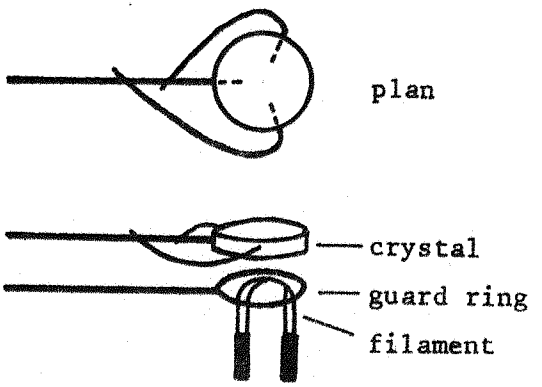

figure 7.10
initial arrangement for electron bombardment heating of the crystal

the tube showed that the surface was damaged. For this reason it was decided to abandon this technique in favour of the 'box' method first used by Lee[228] and described under tube 6.

7.2.2.3 tube 6 (figure 7.11)

Since the measurements on tube 4 had demonstrated (a) that the work function was not affected by mercury contamination, and (b) that the dominant residual gas in the ion pumped system, hydrogen, was also the major source of gas contamination, it was decided to revert to the mercury pumped system. The inset in figure 7.11 shows the 'box' method of mounting the crystal. A tungsten tube was spark machined from rod and the crystal spigotted to fit into the tube. The filament was thus totally enclosed by the box. The crystal temperature was measured with a W - W/26%Re thermocouple welded to the box, and to ensure good thermal contact a strip of tungsten foil etched down to the required thickness was wedged into the gap between the crystal and the tube. Examination of the box after use revealed that this foil had melted, firmly cementing the crystal to the tube. No electron bombardment

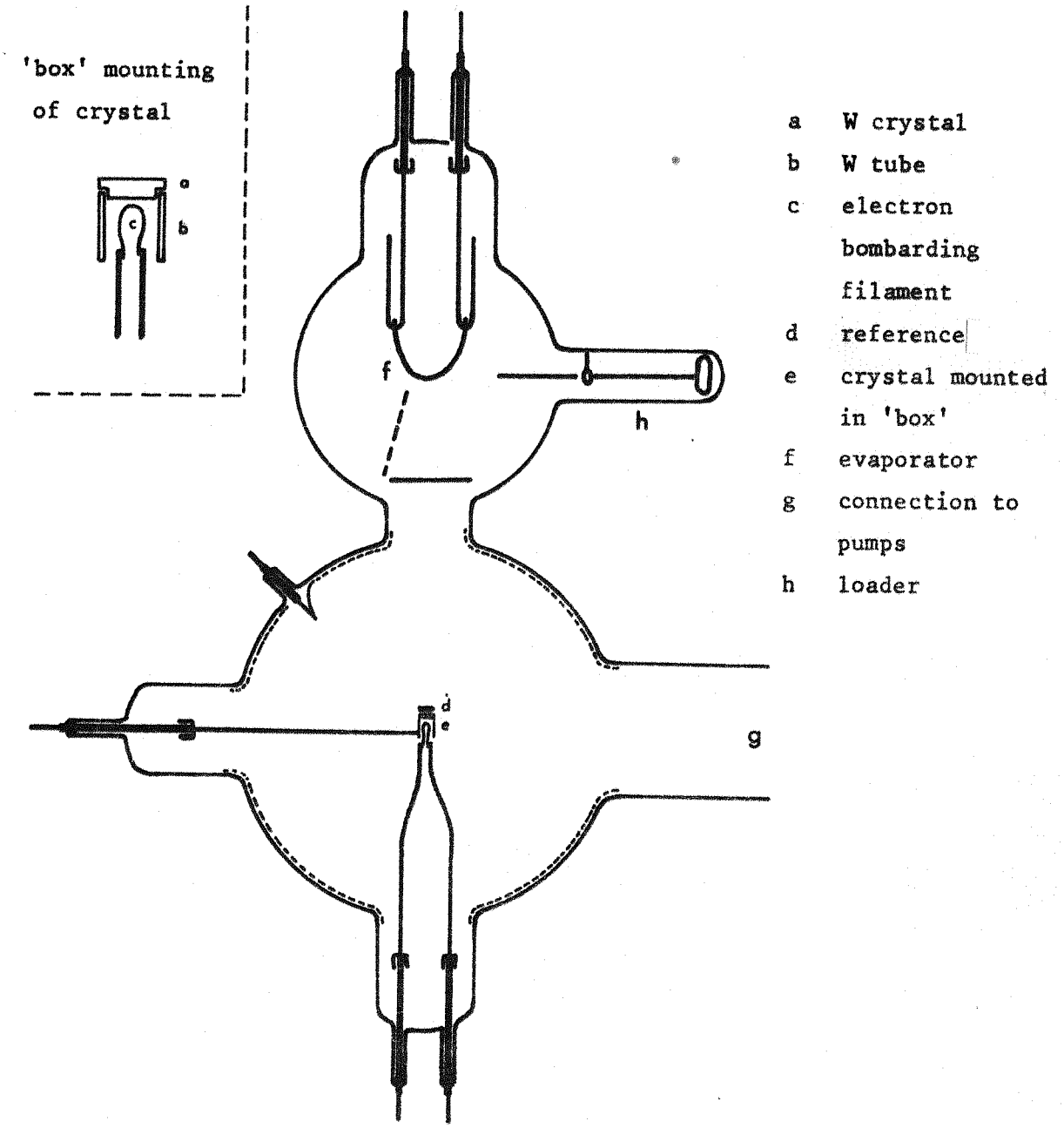

figure 7.11
tube 6 (Kelvin)
reference, bellows and window as in figure 7.9
viewed from window end

damage to the surface of a crystal mounted in this way was ever evident. However this solution provided other problems, the most serious being the tendency for thermal runaway. Above a critical temperature radiation from the box alone was sufficient to heat the filament to a temperature at which considerable emission occurred. This unstable situation resulted either in failure of the filament or melting of the crystal. To overcome this difficulty a temperature controller was installed (West Viscount 3 term) which operated the filament current. This solution was only partially successful because at the runaway situation the filament current dropped to zero while radiation from the box maintained the filament temperature. It was then decided to attempt to control the bombarding voltage rather than the filament current. The filament was used only to initially heat the crystal; as soon as the runaway temperature was reached, the filament was switched off. Again this method was not entirely successful because of difficulties with the response time of the controller. Finally, the most satisfactory solution was found to be a combination of filament current control and careful arrangement of the geometry of the box. A small filament placed exactly at the centre raised the runaway temperature above that used for sustained outgassing.

As shown in figure 6.11, a viewing window was built on to this tube to aid in the alignment of the electrodes. A magnetically operated evaporation shield covered this window when not in use.

7.2.2.4 tube 7 (figure 7.12)

Difficulties had arisen in tube 6 from vibration of the crystal, a

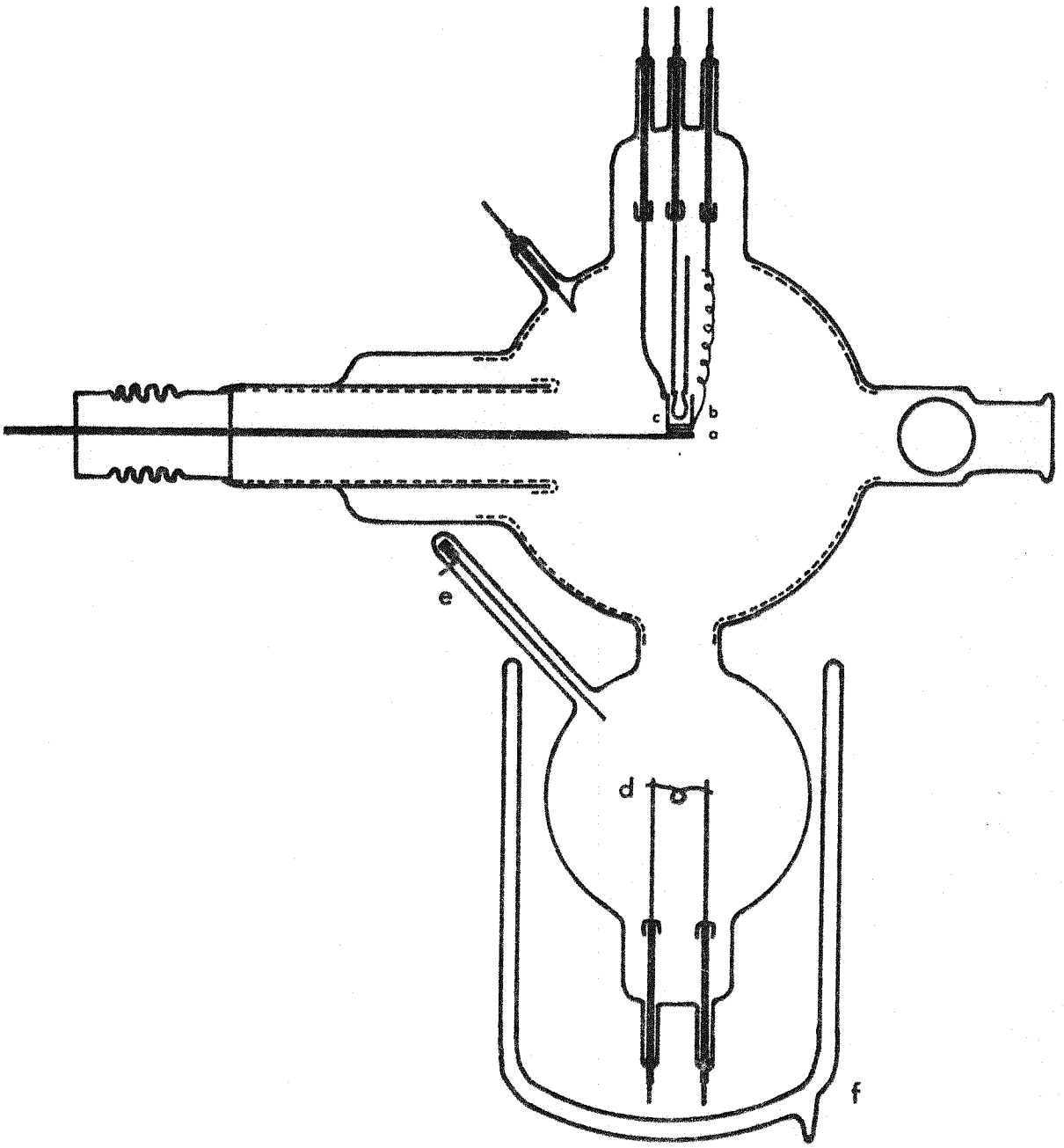

a W foil reference

b thermocouple

c crystal in 'box' mounting

d evaporator

e loader

f dewar

figure 7.12 tube 7 (Kelvin)

consequence of supporting it in the same plane as the vibrator. The use of vertical supports satisfactorily avoided this problem.

Since a large part of the gas evolved during evaporation originated from the glass walls of the evaporator it was decided to cool the latter to liquid nitrogen temperature. This involved inverting the tube so that the evaporator bulb could be inserted into a dewar. The loader side arm was repositioned as shown in figure 7.12. Results obtained with this tube, in which evaporation could be carried out in the 10^{-11} torr pressure range, established that reliable values of work function could only be obtained by evaporating at pressures $\leq 1 \times 10^{-10}$ torr.

7.2.2.5 tube 8 (figures 7.13 and 7.14)

Earlier tubes had all suffered from the problem of evaporator failure. Usually only 2 or 3 measurements could be made under the cleanest conditions before the evaporant dissolved through the filament. Hence in this final tube the evaporator was moved into the main chamber and positioned close to (4 cm) the substrate.

Degassing of the tube and achievement of clean conditions consumed the major part of the experimental time. After an experiment was completed, gettering by the evaporated film ensured ideal vacuum conditions. For these reasons it was decided to incorporate two evaporators (and two loaders) so that both uranium and zirconium could be studied without having to repeat the pumpdown procedure. The evaporators and loaders were carefully positioned so that in the course of experiments neither metal could be contaminated by the other.

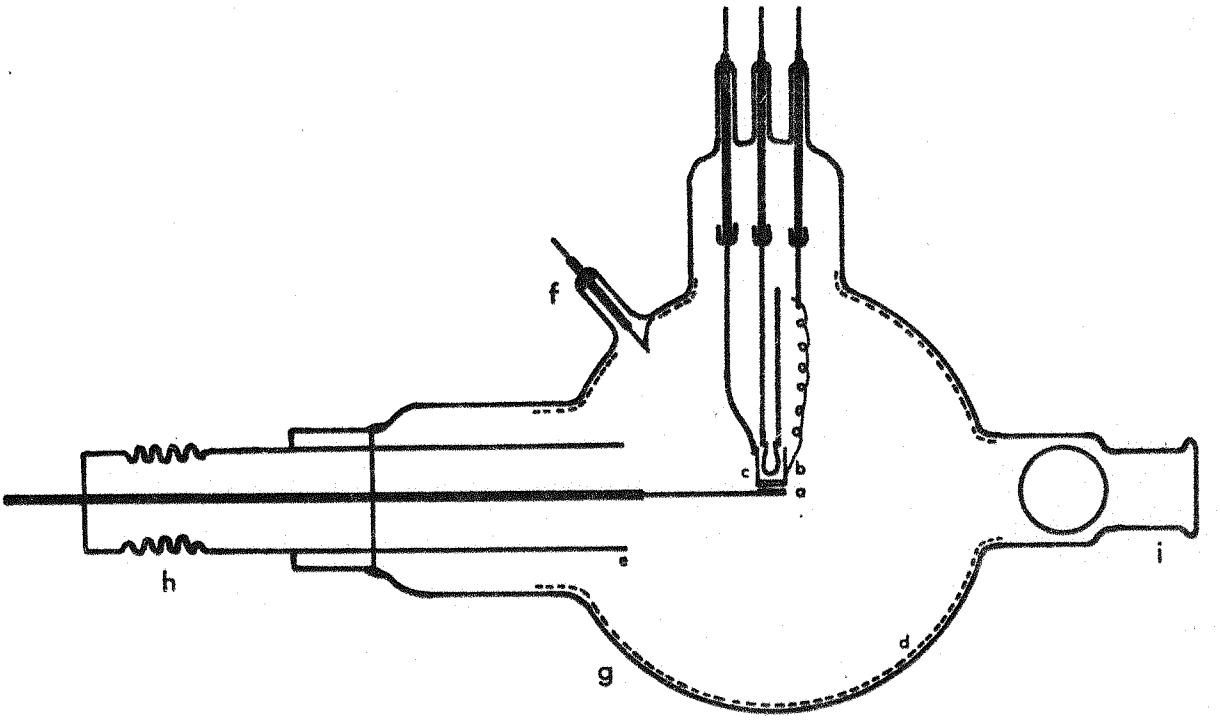

diagram of bellows manipulator

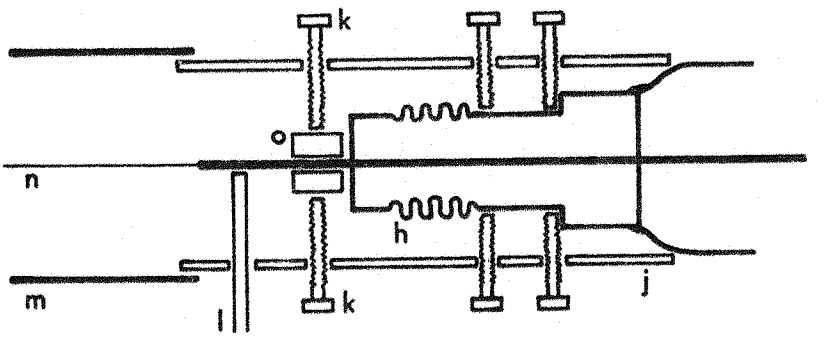

a W foil reference
b thermocouple
c crystal in 'box' mounting
d bright platinum screen
e stainless steel tube
f screen connection
g 1 litre Pyrex glass flask
h stainless steel bellows
i window
j aluminium tube
k bolts for adjusting reference position
l perspex rod from vibrator
m end of canister containing FET pre-amplifier
n electrical connection to pre-amp
o wood block

figure 7.13 front elevation of tube 8 (Kelvin)

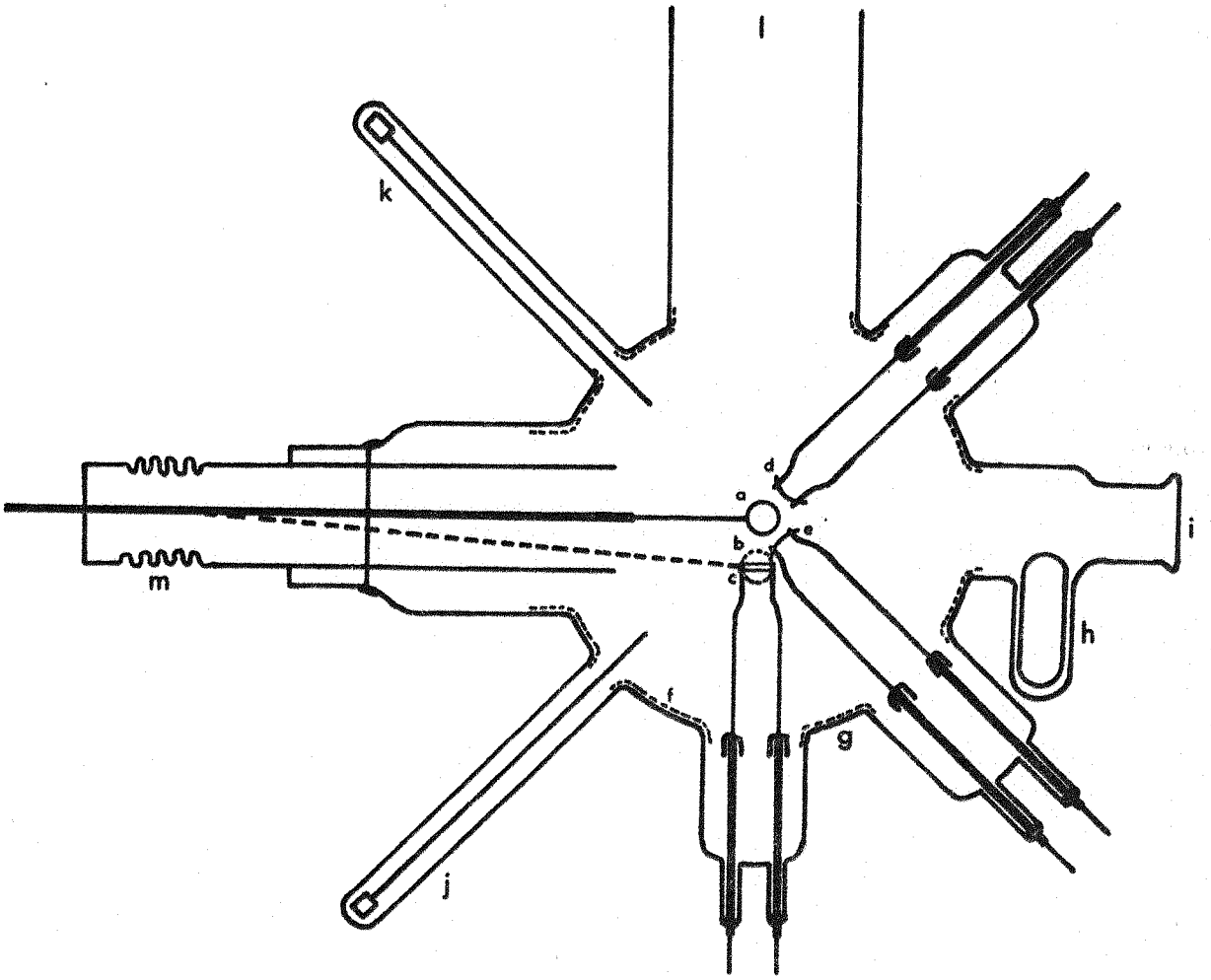

a W foil reference in measurement position beneath crystal (crystal not shown)
b reference in electron bombardment position
c electron bombarding filament
d uranium evaporator
e zirconium evaporator
f bright platinum screen
g 1 litre Pyrex glass flask
h magnetic shutter
i window
j uranium loader
k zirconium loader
l connection to pumps
m stainless steel bellows

figure 7.14 plan of tube 8 (Kelvin)

The reference in this tube was changed from 0.1 mm to 0.5 mm tungsten foil since the former tended to buckle during degassing. No alteration in the contact potential was observed as a result of this change. A final modification was the replacement of the inner glass tube surrounding the vibrating electrode by one of stainless steel. Long periods of outgassing caused the platinum coating on the original glass to peel away, exposing bare glass in the most undesirable position.

The adsorption of uranium and zirconium on both (100) and (110) oriented tungsten crystals was studied in this tube.

7.2.3 Kelvin measurement technique

As already pointed out, the sensitivity of the Kelvin detection system is dependent on the ability to separate the signal from noise. Apart from the usual screening of the high impedance electrode at the tube, the noise level was substantially reduced by attaching the head amplifier directly to the leadthrough supporting the Kelvin electrode. This amplifier[274] was constructed at the bottom of a cylindrical metal canister designed to fit over the Kelvin side arm, and incorporated a field effect transistor input stage with an impedance of 5×10^7 Ω. A standard phase sensitive detection technique[275] was used to overcome the poor signal/noise ratio. A block diagram of the circuit is shown in figure 7.15. The signal from the head amplifier was passed via a low-noise low frequency amplifier to the phase sensitive detector. The oscillator (Advance J2B) provided the signal both for the reference channel of the detector and for the power amplifier (Leak TL/12) which operated the vibrator. The output from the detector was

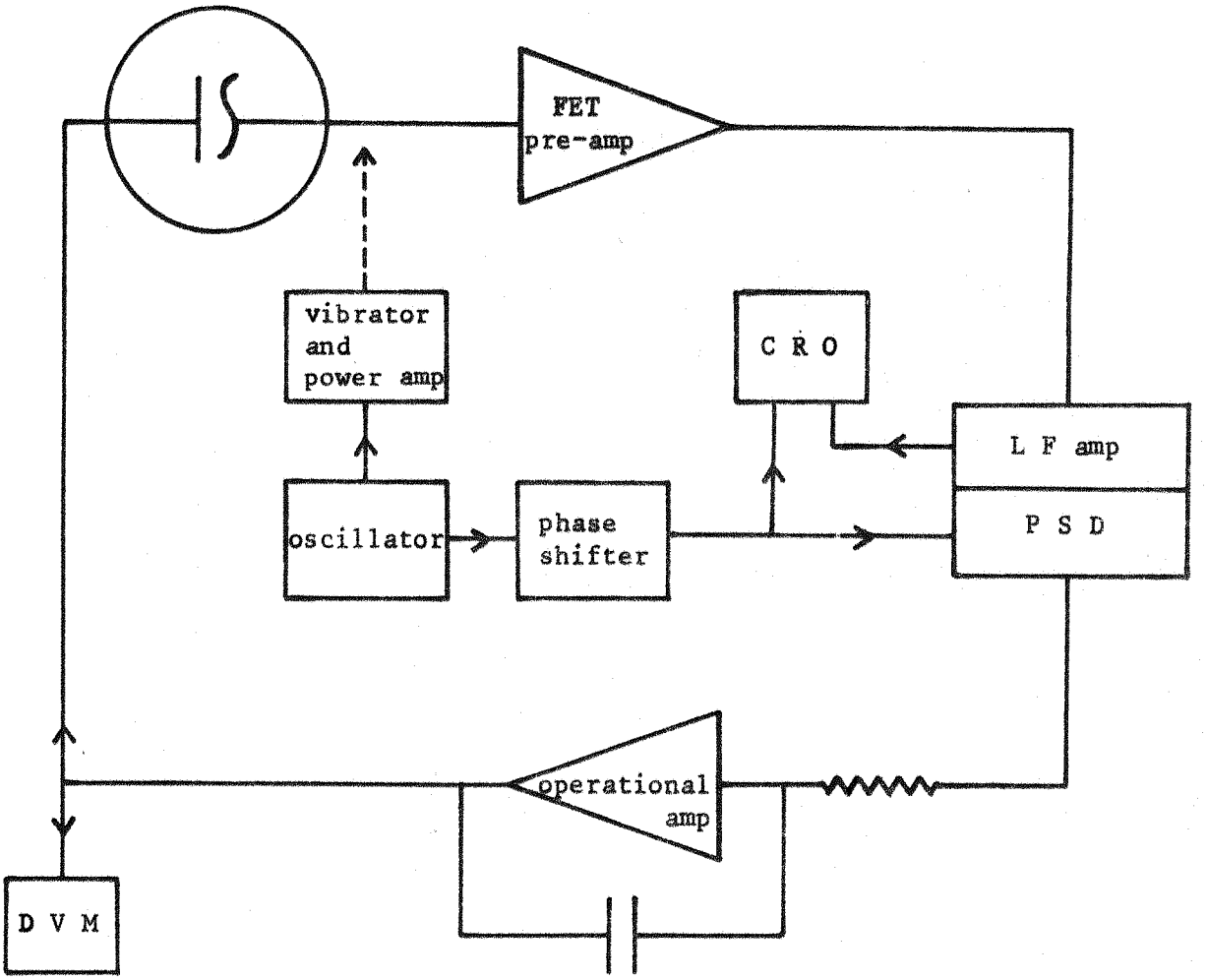

figure 7.15

block diagram of the self-balancing Kelvin detection system

integrated (Fenlow operational amplifier AD2000) and fed back to the low impedance Kelvin electrode, thus providing automatic back-off of the contact potential difference. The feedback voltage was displayed on a digital voltmeter (Solartron LM1619) and, if required, on a chart recorder (Rikadenki 3-31). The phase of the reference signal was adjusted to that of the Kelvin signal by comparison of the 2 traces on a twin beam oscilloscope (Solartron CD1400). The low frequency amplifier and phase sensitive detector were combined in one unit (Brookdeal lock-in amplifier FL355); the phase shifter was combined with a meter unit which displayed the integrated output of the detector (Brookdeal MS320A).

In the initial measurements, the non-vibrating electrode (substrate) was used as the high impedance side. This was because the reference was flashed by electron bombardment after each measurement so that its use as the 'high' would have entailed disconnecting the head amplifier. However, for the desorption/annealing measurements it was in any case necessary to remove the amplifier so that connections to the crystal (for electron bombardment) and to the thermocouple could be made. This was an extremely tedious process but no convenient alternative was found. The use of the reference as the 'high' was possible only in the later experiments (tubes 7,8) where gas contamination was very low. In this case the reference was flashed clean only at the end of a series of measurements. This provided a convenient way of monitoring the total gas contamination: the work function change at this final cleaning was measured. In all cases the results were discarded if this change was detectable (> 5 meV). An important advantage of this procedure was that measurements could be made very much more rapidly, so minimizing exposure to contamination; flashing the reference entailed not only removing and replacing connections but also allowing several minutes for the electrode to cool.

7.2.4 comments on the Kelvin technique

The attraction of this technique is firstly that it measures the area average work function at zero field and ambient temperature (chapter 3), and secondly its obvious simplicity. In practice the latter point is not self-evident because of the problems of:

a low signal amplitude;

b spurious contact potential differences caused by charging up of insulators inside the tube;

c the variation of apparent contact potential difference with separation of the electrodes.

In some cases the last effect was so large as to cause serious error and the tube had to be abandoned. At first it was thought that (b) and (c) were interrelated but experiments with a double modulation system[274] showed conclusively that the dependence on separation was an independent effect, possibly caused by patch fields on rough or non-parallel electrodes, or edge effects. The existence of low work function grain boundaries (section 6.2) below the level of the surface would give rise to just such an effect. It has been suggested[276] that the 'true' contact potential difference is given by an extrapolation of the plot of apparent contact potential difference versus separation to zero. However, this procedure does not give the area average work function if the cause is patch fields.

CHAPTER 8 RESULTS AND DISCUSSION

8.1 tungsten single crystals

The work functions of (100), (110) and (611) single crystals of tungsten were measured with the Kelvin technique. The (611) crystal was used in tube 5 (section 7.2.2.2), having only a guard ring to protect the face of the crystal from electron bombardment damage. As discussed in section 6.1, it suffered some damage as a result even though it did not receive as prolonged outgassing as the others. Only one set of measurements were made on this crystal. The (110) crystal was used in tubes 6 - 8 and in all cases was protected by the 'box' method from bombardment damage (section 7.2.2.3). Measurements on the (100) crystal were made in tube 8, again employing the 'box' mounting technique. Contact potential differences were measured at the beginning and end of every adsorption experiment. Thus a total of 80 measurements on the (110) and 40 on the (100) orientations were made. Before each of these measurements the crystal was flashed to 3000 K. Residual pressures were never worse than 1×10^{-10} torr. Assuming a value of 4.55 eV for the polycrystalline foil reference the measured work functions were:

(110): 5.15 ± 0.01 eV

(100): 4.65 ± 0.01 eV

(611): 4.55 ± 0.05 eV

All three crystals, after removal from the experimental tubes, showed some polygonization (section 6.1). It is difficult to see how the requirements of rigorous outgassing and of true macroscopic single crystals can be compatible. The above values may be compared with previous measurements and those derived from the Steiner and Gyftopoulos theory[18] (table 4.4). It appears that the (100) value is very reproducable and is in good agreement with Steiner and Gyftopoulos.

Previous measurements on the (110) orientation fall into two groups: field emission measurements which are high and measurements on macroscopic crystals which are considerably lower. The present work is in good agreement with the latter values. Steiner and Gyftopoulos predict a (110) work function which is nearer the field emission group. As discussed in section 4.5, it is likely that the work function of the (110) face is very sensitive to the degree of surface perfection on an atomic scale. RHEED patterns obtained recently[285] from (110) tungsten tend to confirm this view. A further possibility is that the very high field emission work functions are a manifestation of the failure of the free electron model on which the Fowler-Nordheim theory is based[277].

The (611) value is a little higher than most measurements on this orientation and is probably a result of surface damage.

The Steiner and Gyftopoulos theory (section 1.5.2) predicts work functions which are in surprisingly good agreement with experiment. The fact that the values for (111), (311) and (611) orientations are identical is a result of the surface atoms having the same number of nearest and next nearest neighbours. Including the third nearest neighbours would distinguish these orientations but the differences would be negligibly small. It is important to realize that Gyftopoulos and Steiner only take into account atoms which are in the plane of the surface. It is likely that in high index planes, where the surface structure is more open, atoms which are below the surface plane contribute to the work function. Finally, it should be pointed out that this theory has an essential empirical basis: Gordy's electronegativity (section 1.3.4).

8.2 uranium

UKAEA, Harwell supplied the natural uranium used in this work in the form of wire, 1 mm diameter. A chemical analysis (before atmospheric oxide contamination) is given below in ppm:

C	700	W	40	Bi	< 5
O	300	N	30	B	< 2
Al	95	Si	15	Mo	< 2
Fe	60	Mn	10		
Ni	50	Cr	8		

Immediately before inserting into the experimental tube the black uranium oxide layer formed on the exterior was removed in an electro-etch consisting of 20% orthophosphoric acid, 40% sulphuric acid and 40% distilled water. However, during pumpdown and bakeout further oxide contamination could not be avoided. For this reason it was necessary to degas the uranium above 2000 K[139]. Before any measurements were begun at least ¾ of the original uranium sample had evaporated. Figure 8.1 shows mass spectra as the uranium was progressively cleaned in a mercury diffusion pumped system. Initially H_2, CH_4, CO, N_2, CO_2 were evolved (figure 8.1a). It was not possible to determine the relative amounts of CO and N_2 since the cracking patterns for these gases were found to be unreliable. During evaporation (figure 8.1d) only H_2 and CO were evolved, approximately in the ratio 1:2. A similar cleaning procedure in the getter-ion pumped system showed (figure 8.2) that hydrogen was in this case always the predominant gas. Noticeable gettering occurred during evaporation with the result that the pressure after completion of an experiment (figure 8.2e) was reduced.

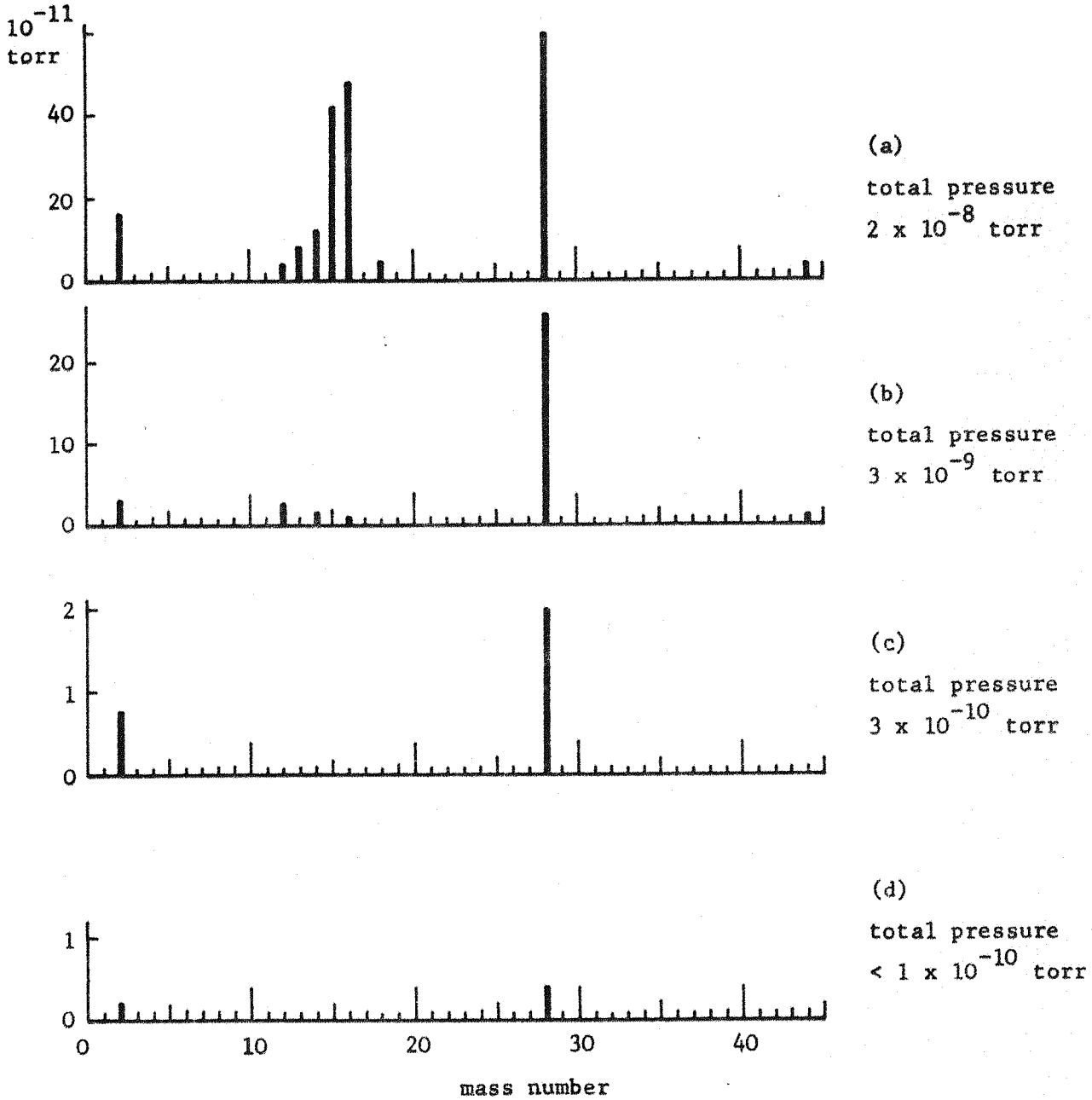

figure 8.1

mass spectra during degassing of uranium in a glass mercury-diffusion pumped system

(a) initial high temperature degas showing H_2, CH_4, CO, N_2, CO_2

(b) further degassing; CH_4 pressure greatly reduced

(c) final degassing; H_2, CO only present

(d) during evaporation

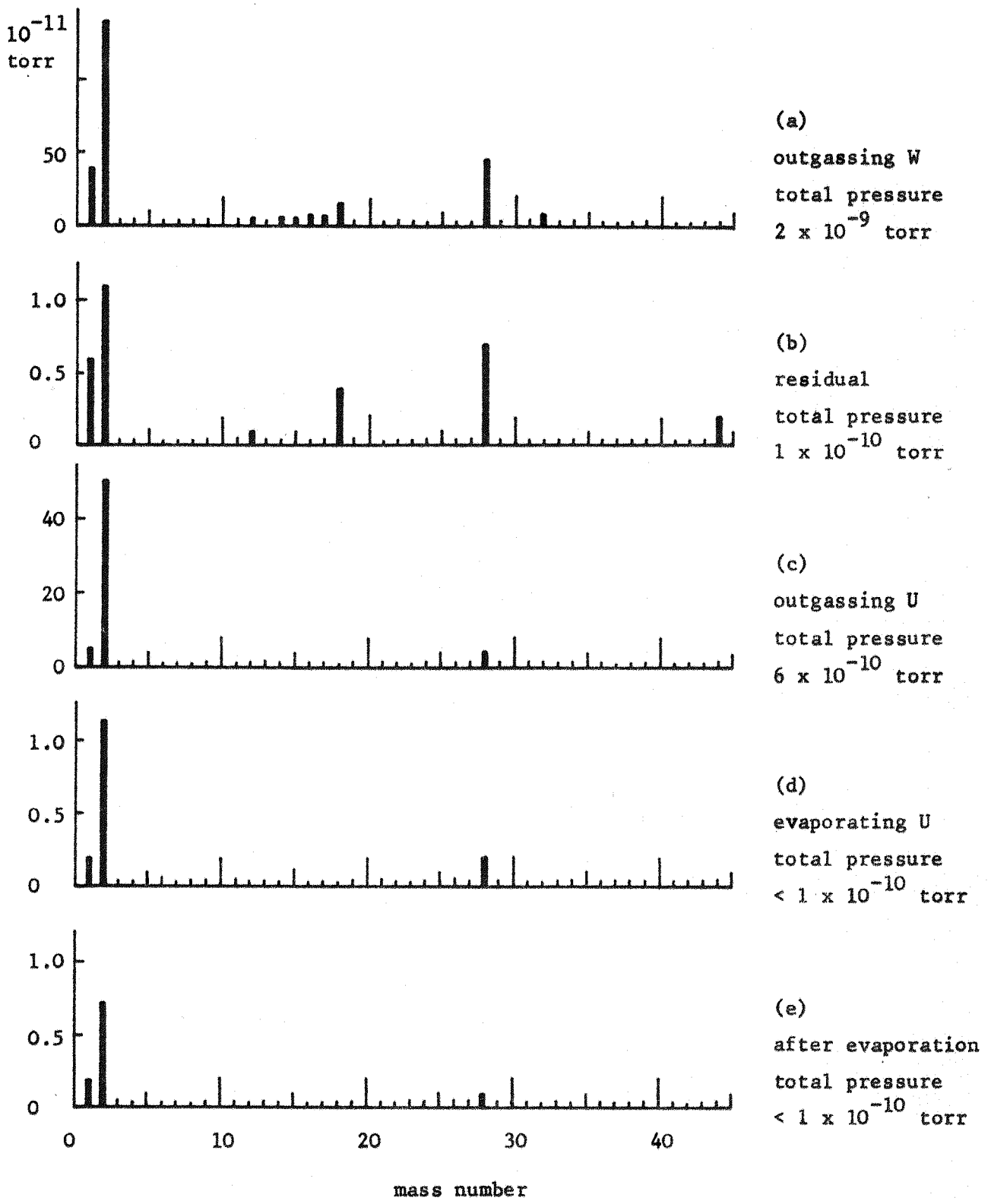

figure 8.2

mass spectra obtained with p p g on getter-ion pumped system

8.2.1 effect of contamination on the work function - uranium on polycrystalline tungsten foil

Experiments in which insufficiently degassed uranium was deposited, and in which uranium was exposed to gas contamination, were made in order to determine how previous measurements may have been affected. These experiments were performed on uranium deposited on polycrystalline tungsten foil.

8.2.1.1 contamination of uranium source

Figure 8.3 shows the variation in work function with coverage measured in tube 2 (Anderson technique) for uranium well degassed and briefly degassed. In the latter case the work function dropped to 3.20 eV at $\sim$ 10 monolayers, which is close to Rivière's (Kelvin) value of 3.19 eV[6]. However this result was not reproducable as it depended markedly on the extent of uranium degassing. In the case of well degassed uranium, the work function, after rising from the minimum, remained constant up to $\sim$ 10 monolayers. This constancy was achieved only after the uranium had been heated to at least 2400 K before deposition.

The residual gases present during the deposition of uranium are mainly hydrogen and carbon monoxide (figures 8.1, 8.2). The effect of both these gases on clean uranium films was investigated.

8.2.1.2 carbon monoxide on uranium - Anderson technique

A glass capsule was filled with spectroscopically pure carbon monoxide and

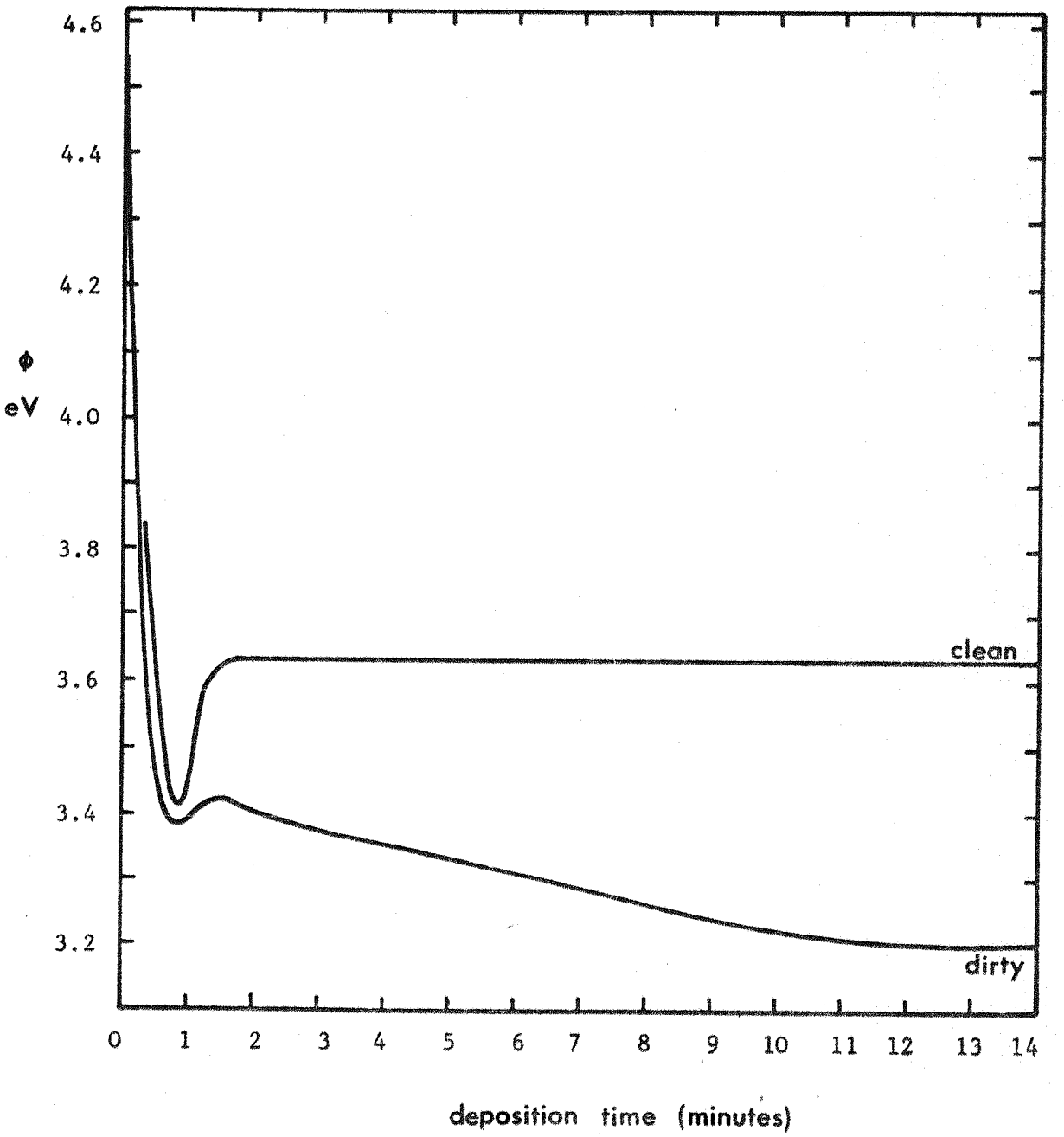

figure 8.3
work function ϕ/coverage for uranium on polycrystalline tungsten measured using the Anderson technique

dirty: insufficiently degassed uranium
clean: well degassed uranium

sealed off. After deposition of a monolayer of clean uranium (tube 2) the capsule was broken magnetically, causing the pressure to rise to $\sim 10^{-2}$ torr. A mass scan taken when the pressure had pumped down to 10^{-8} torr showed that the only impurity was < 0.1% CO_2. The work function of the uranium film dropped by 0.07 ± 0.01 eV.

8.2.1.3 hydrogen on uranium - Kelvin technique

This experiment was performed on the ion-pumped system using tube 4. Hydrogen was introduced into the system by diffusion through a palladium tube. The maximum pressure reached was 10^{-4} torr after which the system was evacuated to 5×10^{-10} torr. A mass scan at 10^{-6} torr showed that the impurities were 0.2% H_2O[225] and < 0.1% CO. The contact potential differences measured were as follows:

a clean monolayer of uranium on polycrystalline foil versus polycrystalline foil: 0.92 ± 0.01 V;

b both surfaces exposed to hydrogen at 10^{-4} torr: 1.39 ± 0.01 V;

c system pumped out to 5×10^{-10} torr: 1.39 ± 0.01 V;

d reference foil flashed clean: 0.75 ± 0.01 V;

e uranium film heated to 800 K and reference flashed: 0.92 ± 0.01 V.

These measurements lead to the result that the work function of the uranium film increases by 0.17 ± 0.02 eV on exposure to hydrogen and returns to the clean value on heating to 800 K. Also, the surface potential of hydrogen on tungsten foil is - 0.64 ± 0.02 V. As pointed out in section 7.1.1, the weakness of Kelvin measurements on gas contamination is that an identical change in the work function of both surfaces during pumpout would not be observed. In order to check this point the work function change caused by hydrogen adsorption on tungsten foil was also measured using the Anderson

technique (tube 1). The result was a surface potential of - 0.66 ± 0.05 V which did not change on pumpout. These results for hydrogen on tungsten are in good agreement with Hopkins and Pender's value[225] for the surface potential: - 0.63 V.

The fact that heating the hydrogen covered uranium film to 800 K caused the work function to return to the clean uranium value suggests that hydrogen is desorbed at low temperatures. This was confirmed by flash desorption measurements (appendix 3) which gave a desorption energy of 14 ± 3 Kcal $mole^{-1}$.

The value for the surface potential of hydrogen on a monolayer uranium film (- 0.17 ± 0.02 V) is not in agreement with a similar measurement by Rivière[283] (- 1.06 V maximum) on a thick uranium film. However this difference appears to have been resolved by the field emission work of Collins and Blott[284]. They found that the magnitude of the surface potential depended critically on the thickness of the initial film. For a film of 12 monolayers the surface potential reached - 0.34 V. Presumably for films of several hundred monolayers, as used by Rivière, the surface potential would be lower still. Rivière suggests that his very low value was associated with the formation of β-UH_3, a structure which would be unlikely to occur in monolayer films.

8.2.1.4 gas contamination of tungsten foil

Since it is possible that in earlier measurements spurious Kelvin work functions were caused by gas contamination of the reference, the effect of such gas contamination on the work function of tungsten foil was investigated. The measurements were made in tube 2 (Anderson technique) with the shutter in

the closed position so that the evaporator could be heated without deposition of uranium on the substrate. The gases evolved were carbon monoxide and hydrogen, as is shown in figure 8.1. The maximum work function change was an increase of 0.70 ± 0.05 eV which occurred when the pressure rose to 10^{-7} torr or above. The surface potential of hydrogen on polycrystalline tungsten was - 0.66 V when measured by the Anderson technique, whereas that for carbon monoxide is - 0.60 V (Kelvin)[227]. However, in view of the replacement of hydrogen by carbon monoxide observed by Robins[280] and Rigby[281] it seems likely that the surface in this experiment was covered by a mixture of carbon monoxide and hydrogen.

8.2.1.5 oxygen contamination of uranium

It was shown in section 8.2.1.1 that insufficiently degassed uranium exhibited work functions lower than clean uranium. This was thought to be due to oxide contamination since this can only be removed by heating to temperatures in excess of 2000 K[139]. Previous measurements (section 4.2) have also demonstrated that oxide contamination produces a lower work function. Rivière[282] found that oxygen admitted on to a thick film of uranium caused a large decrease in the work function which he attributed to penetration of oxygen below the uranium surface.

It is not clear that oxygen adsorbed on to a monolayer film of uranium would cause a similar work function decrease since penetration is unlikely to occur. For this reason such an experiment was undertaken, using tube 2 (Anderson technique). Oxygen, admitted by diffusion through a silver tube, contained 1% CO_2, 0.5% N_2 and 0.5% CO impurities at 10^{-6} torr. The result of this experiment was a large rise in the work function of the monolayer

uranium film. Unfortunately the increase was so large that the operating point of the retarding field diode moved out of the linear part of the log i versus V characteristic so that an accurate measurement was not possible. However, from the shift in the retarding field plots made before and after oxygen adsorption, the surface potential was determined as - 1.5 ± 0.1 V. It was not thought to be worth repeating this experiment since its essential purpose, to find the direction of work function change, was achieved. In addition, difficulty was experienced with leaks in the silver diffusion tube caused by the degassing procedure.

8.2.1.6 discussion of uranium contamination

Summarizing the gas contamination studies, the work function changes on monolayer films of uranium and on tungsten are given below (surface potentials are of opposite sign to work function changes):

	U monolayer on W foil	W foil
hydrogen	+ 0.17 ± 0.02	+ 0.64 ± 0.02
carbon monoxide	- 0.07 ± 0.01	+ 0.60 ± 0.03†
oxygen	+ 1.5 ± 0.1	

† value obtained by Usami[227]

It is clear from the above that the lower work functions produced by insufficiently degassed uranium were not due to gas contamination at the substrate. Presumably the uranium leaving the evaporator was already oxidized. As pointed out by Ackerman et al[139], degassing the uranium above 2000 K was sufficient to remove this oxide. It seems likely that the values found for thick uranium films by Rivière[6] and by Collins[155] were contaminated in this way since in both cases the vacuum conditions were good. In this

work it was found to be very difficult to achieve thick clean films since very little uranium was available for deposition after rigorous outgassing.

It is interesting to note that another possibility exists in the case of Rivière's Kelvin measurements. If both the tungsten foil reference and the uranium film were coated by hydrogen evolved during deposition then the contact potential difference would be 1.36 V, giving an apparent uranium work function of 3.16 eV. If, however, some replacement of hydrogen by carbon monoxide occurred at the reference, producing a surface potential of only - 0.61 V, then the apparent uranium work function would be the observed 3.19 eV. No account of the exact degassing procedure or evaporation conditions are given by Rivière. It is however difficult to see how the work function, if affected by contamination, could be reproducable in the way in which Rivière's was.

8.2.2 uranium on single crystal tungsten substrates

All work on single crystal substrates was performed using the Kelvin technique. The procedure for measurement of a coverage curve was as follows:

a the crystal and reference were flashed to 3000 K for a few seconds, allowed to cool and the contact potential difference measured;

b the reference was moved away and uranium evaporated for a measured length of time (usually 1 minute);

c the reference was moved back to the crystal and the contact potential difference re-measured;

d steps (b) and (c) were repeated until the desired coverage was achieved;

e the reference was flashed clean and the contact potential difference again measured;

f both crystal and reference were flashed clean and one further deposition made. The contact potential difference was compared with that measured after the first deposition.

Step (e) was intended to act as a measure of gas contamination. If any change in the contact potential difference was observed (>5 mV) the measurement was discarded. Step (f) was necessary to ensure that the coverage scale was linear. In practice it was found that the amount of uranium evaporated during each deposition was constant, provided that the deposition time was the same and that the voltage to the transformer supplying the evaporator filament current was kept constant. When the evaporator was exhausted the uranium deposition rate dropped abruptly.

Measurements were also made of coverage curves at elevated substrate temperatures. This involved depositing uranium on a heated substrate; measurements were made at room temperature. After each coverage curve was determined a room temperature curve was measured so that the coverage scales could be related.

Finally the uranium films were annealed. The procedure was to deposit the film at room temperature and then heat it to successively higher temperatures for periods of 1 minute. The work function was measured at room temperature after each period of heating. The measurement of elevated temperature coverage curves and annealing curves was undertaken in order to investigate possible work function changes of the abrupt and irreversible type seen for uranium on polycrystalline tungsten (section 4.2).

8.2.2.1 results - uranium on tungsten single crystals

uranium on (110) tungsten

Coverage curves obtained during the uranium cleaning procedure are shown in figure 8.4. In all cases the pressure conditions were similar ($< 1 \times 10^{-10}$ torr). For an insufficiently degassed source the work function was lower (as in the polycrystalline substrate case), showing no minimum in the coverage curve. The clean coverage curve (figure 8.5) was determined from five independent measurements on the most thoroughly degassed uranium, one on tube 7 and four on tube 8. The time scale for each of these curves was different; the coverages shown in figure 8.5 have been normalized at the minimum. After rising to the monolayer value the work function remained constant up to approximately 8 monolayers (figure 8.7). Figure 8.6 shows the annealing curve. No abrupt changes in work function are evident until the uranium begins to desorb at $\sim$ 1800 K. The clean tungsten value was reached after heating to 2400 K. Finally, the elevated substrate coverage curves are given in figure 8.8. The work functions are generally lower for higher substrate temperatures except at the minimum where they coincide. The monolayer points are in good agreement with the values from the annealing curve.

uranium on (100) tungsten

The work function/coverage curve determined from 3 independent measurements on tube 8 is given in figure 8.9. Figure 8.10 shows that the work function remains constant between 1 and 3 monolayers. The annealing curve, figure 8.11, was only taken up to 1600 K since the temperature could not be measured

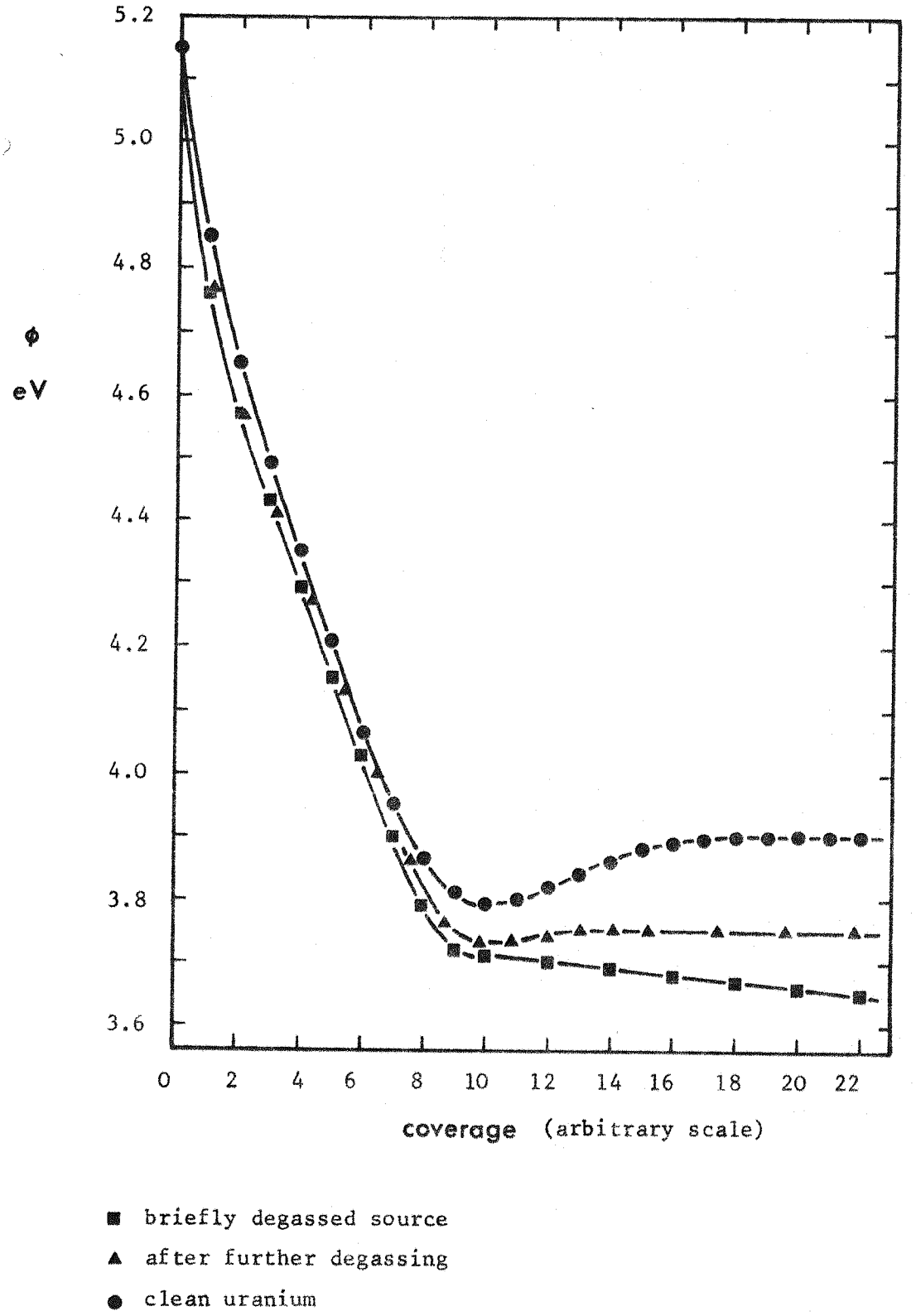

figure 8.4

work function ϕ/coverage for uranium on (110) tungsten

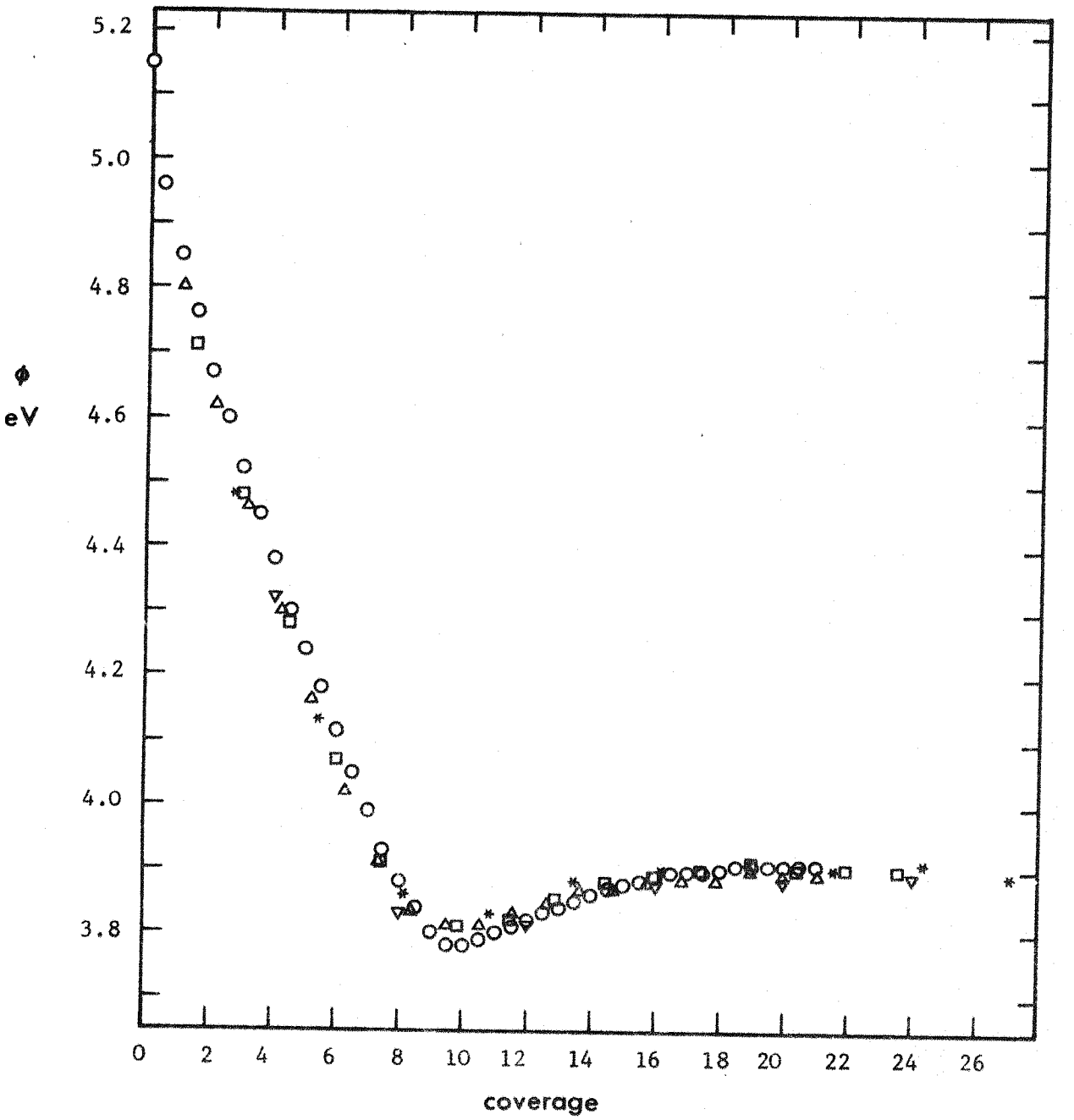

figure 8.5

work function ϕ/coverage for uranium on (110) tungsten for deposition times of:

- ○ 42 minutes
- △ 20 minutes
- □ 15 minutes
- * 11 minutes
- ▽ 7 minutes

coverage scale normalized to minimum

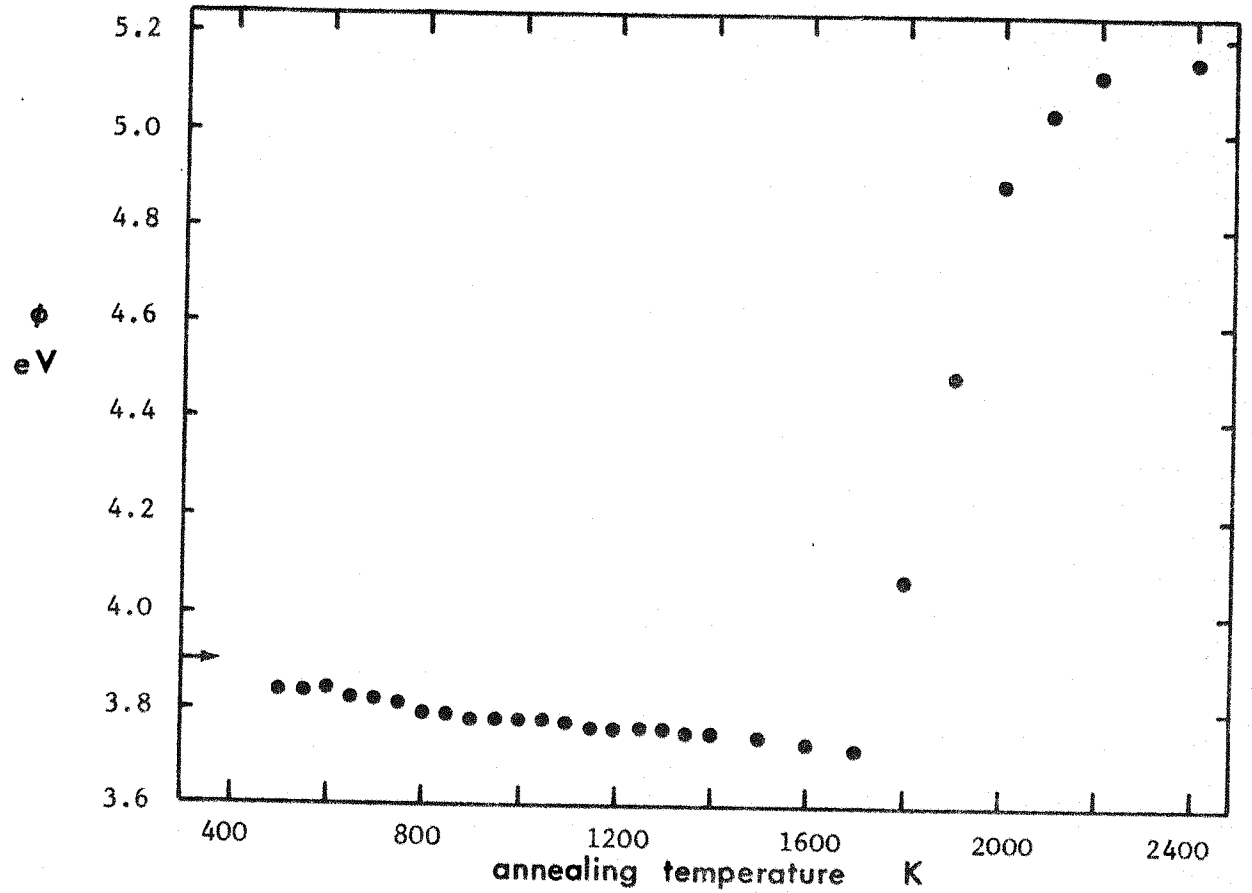

figure 8.6

work function after annealing a monolayer film of uranium on (110) tungsten

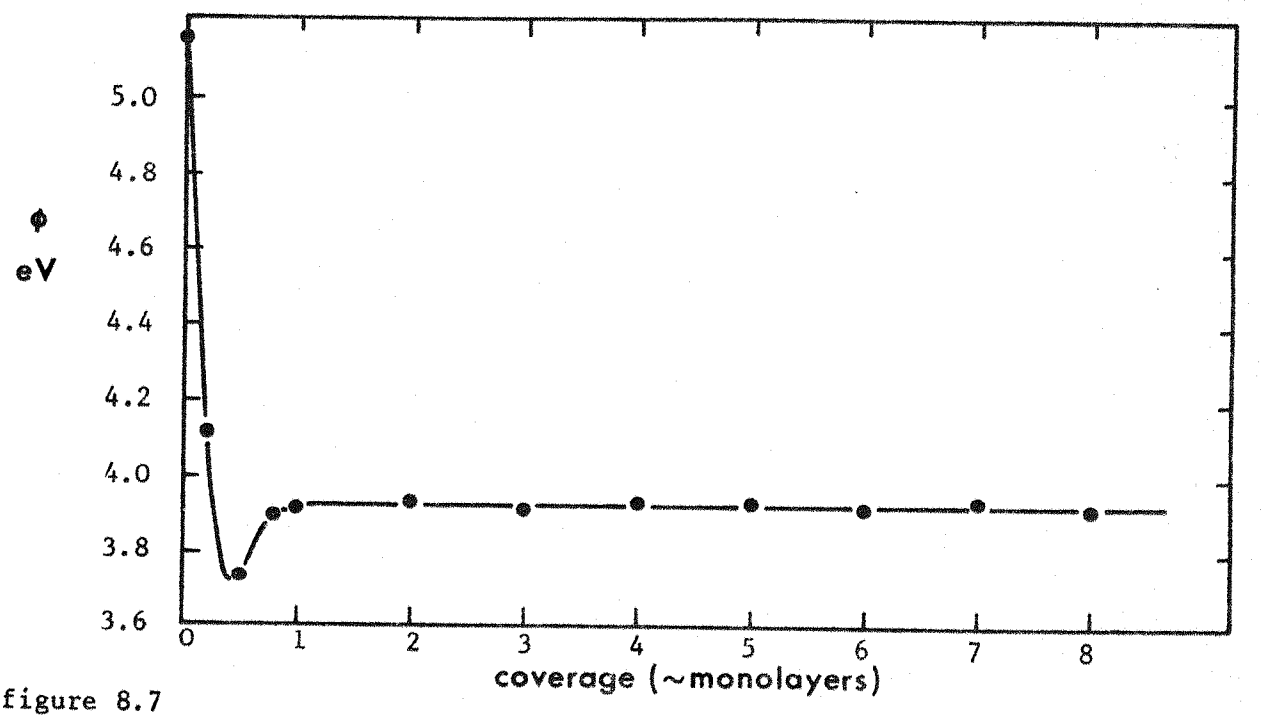

figure 8.7

work function ϕ/coverage for uranium on (110) tungsten

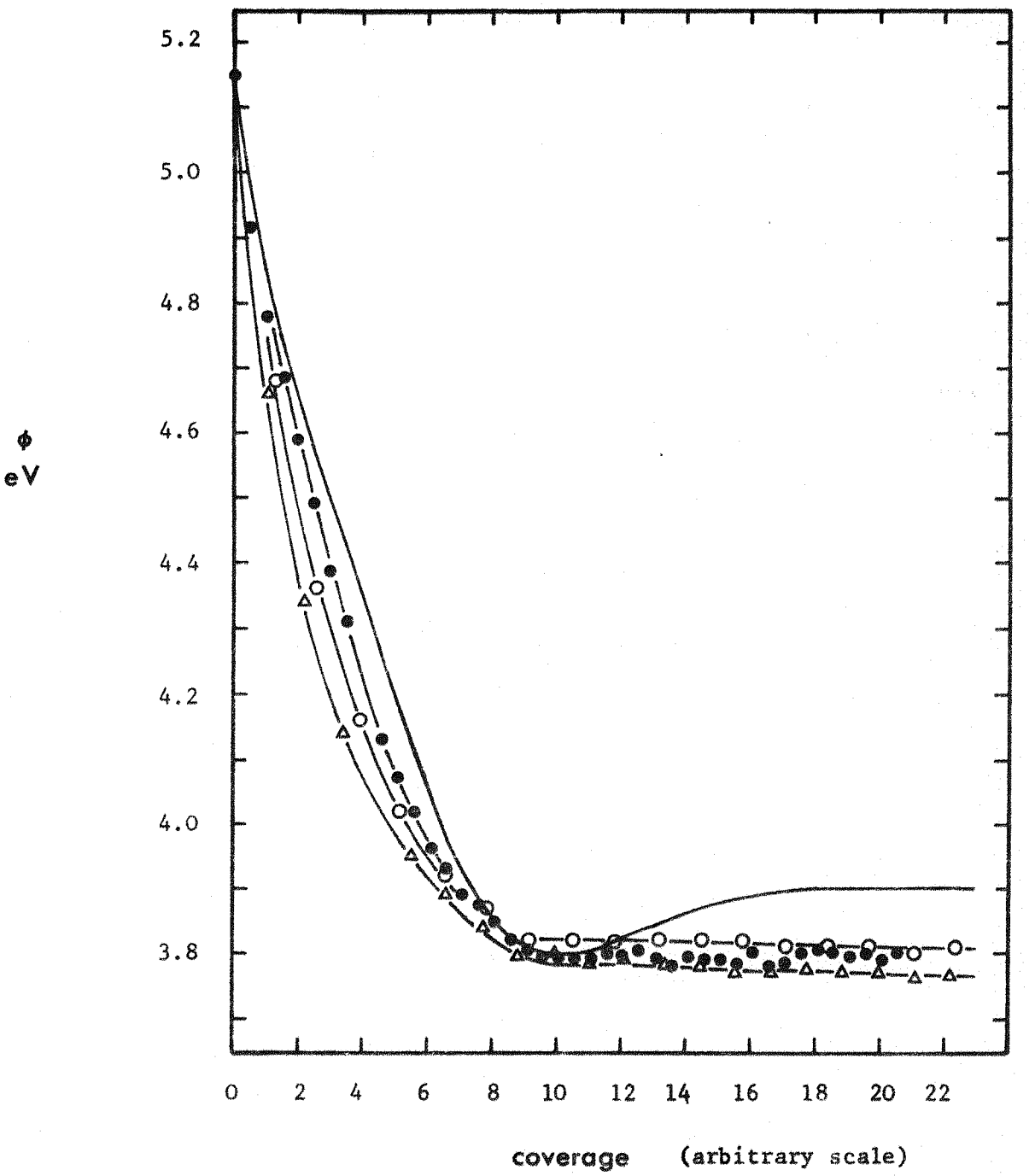

figure 8.8
work function ϕ/coverage for uranium on (110) tungsten
for 4 substrate temperatures

——— 300 K
●●● 850 K
○○○ 1000 K
△△△ 1250 K

accurately beyond this point because of bad thermal contact between the crystal and the supporting tube (the temperature was measured at the latter). However, there is no evidence of abrupt work function changes in the temperature range where bulk crystallographic phase changes occur. The coverage curves at elevated temperatures (figure 8.12) very nearly coincide, none showing a work function minimum. Again the final values agree with those from the annealing curve.

The coverage curves for polycrystalline, (110) and (100) tungsten substrates are summarized in figure 8.13. The coverage scale is normalized at the minimum. The curve for adsorption on polycrystalline tungsten is due to Barry[7] again using the Kelvin technique.

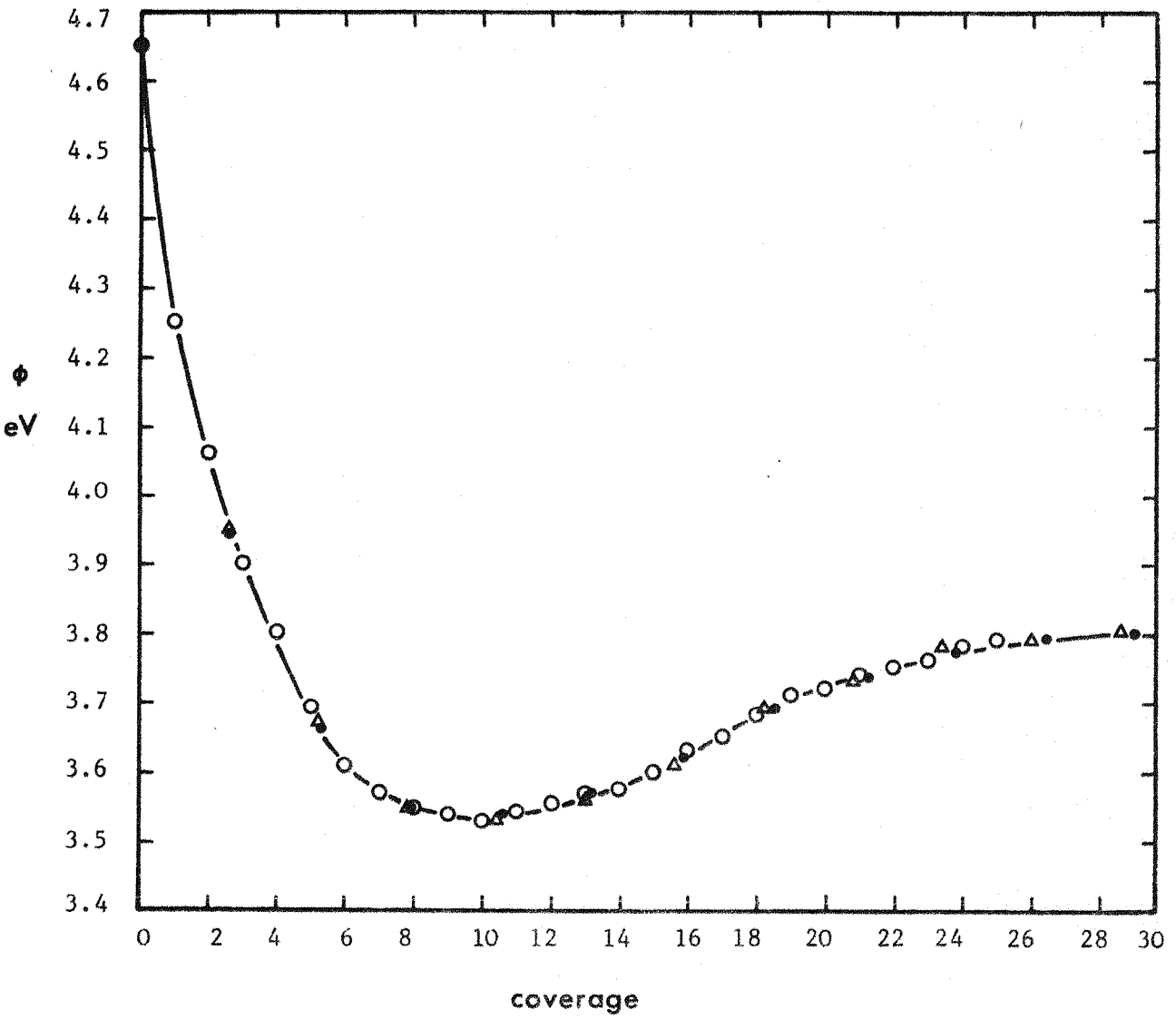

figure 8.9

work function φ/coverage for uranium on (100) tungsten for deposition times of:

- ○ 30 minutes
- △ 12 minutes
- ● 12 minutes

coverage scale normalized to minimum

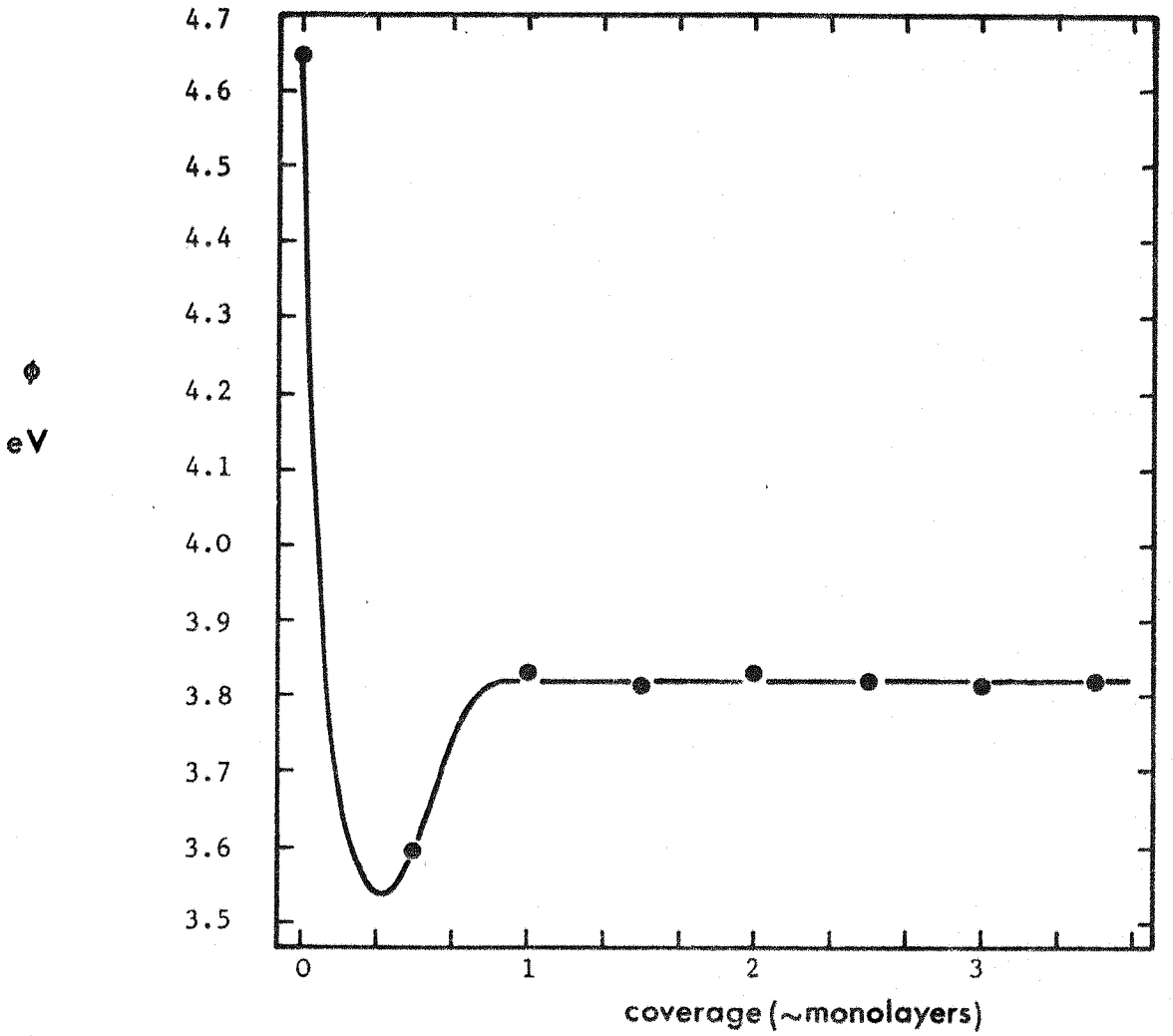

figure 8.10

work function ϕ/coverage for uranium on (100) tungsten

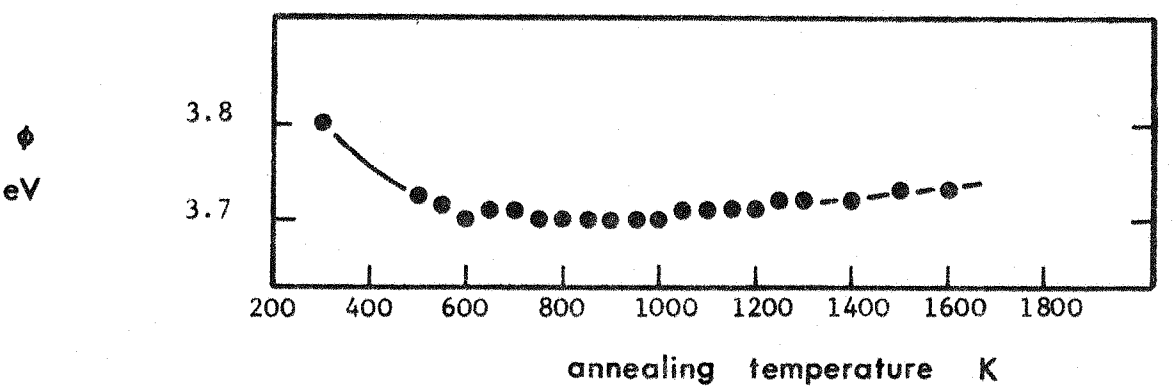

figure 8.11

work function after annealing a monolayer film of uranium on (100) tungsten

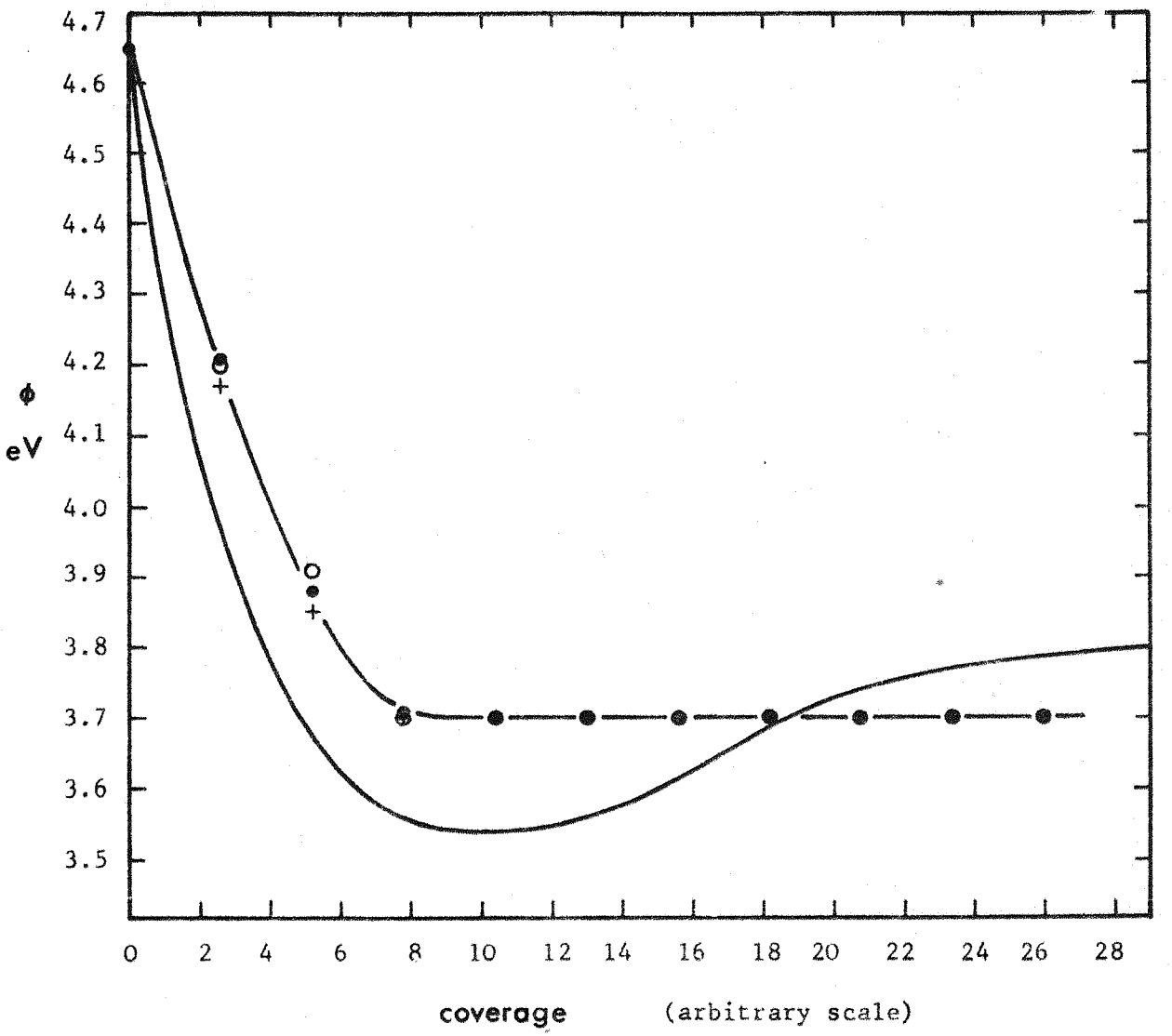

figure 8.12

work function ϕ/coverage for uranium on (100) tungsten

for 4 substrate temperatures

—— 300 K

● 850 K

\+ 1000 K

○ 1250 K

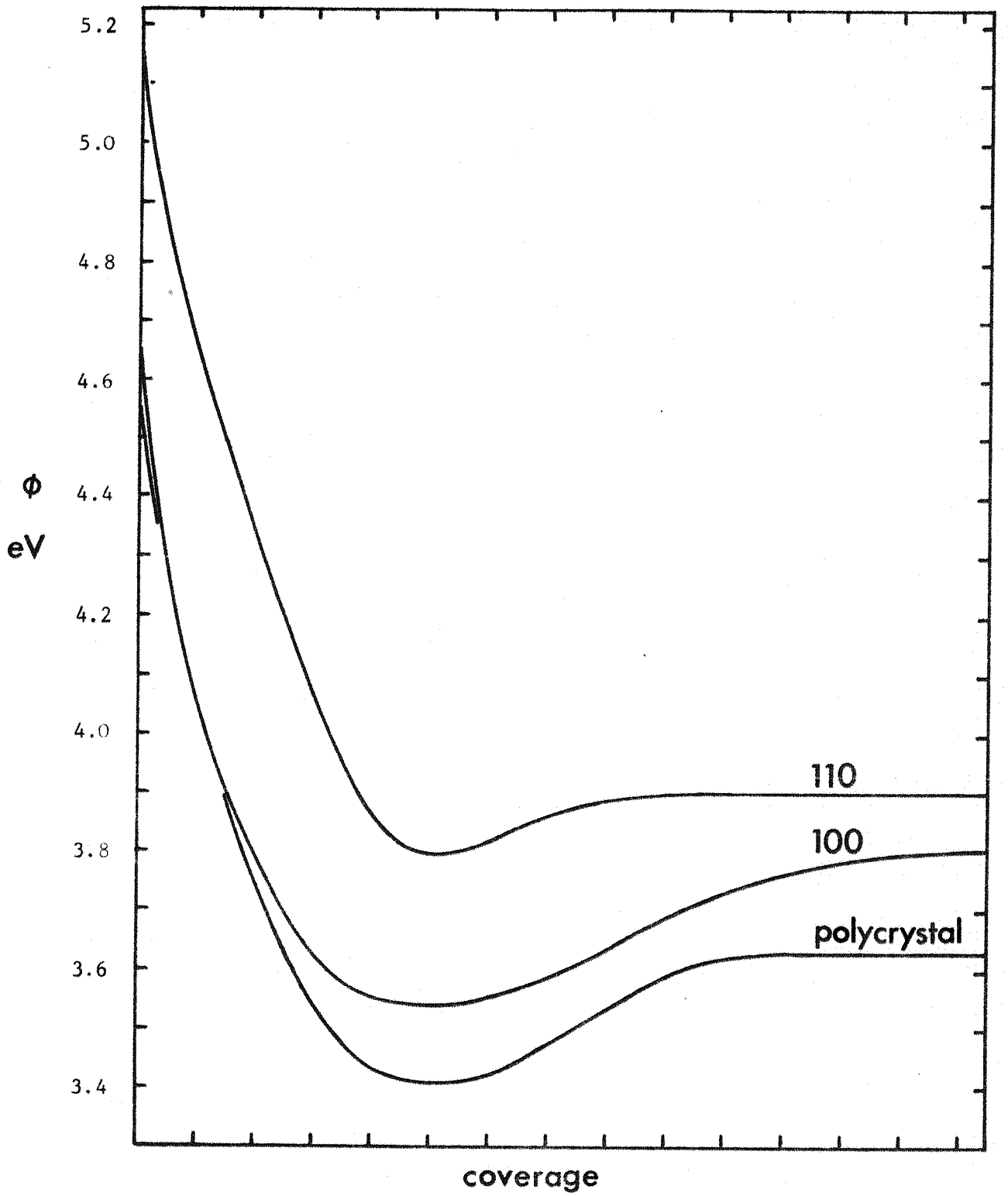

figure 8.13

work function ϕ/coverage: uranium on tungsten (110) crystal, (100) crystal and polycrystal

coverage scale normalized to minima

8.3 zirconium

The zirconium used in the present work was supplied by Koch Light Laboratories Ltd in the form of wire 1 mm diameter and of 99.5% purity. As with uranium, this wire formed an oxide layer on exposure to the atmosphere which was removed immediately before inserting into the experimental tube with a chemical etch consisting of 47% nitric acid, 48% distilled water and 5% hydrofluoric acid (40%). During the cleaning procedure the zirconium was degassed above 2400 K. Figure 8.14 shows the mass spectra obtained during the cleaning process. Initially, most of the gas evolved was hydrogen with some water, methane, carbon monoxide and carbon dioxide (figure 8.14a). During evaporation of the cleanest zirconium only methane and hydrogen were detectable (figure 8.14c).

8.3.1 zirconium on polycrystalline foil - Anderson technique

The work function/coverage curve, measured by the Anderson technique (tube 2), is shown together with the single crystal tungsten substrate results in figure 8.24. Annealing the monolayer films produced the work function changes shown in figure 8.15. As discussed in section 7.1.1 the Anderson technique is not suited for these measurements and consequently the points are subject to some scatter. The work function of the film deposited under the cleanest conditions was constant up to 1700 K where it fell before rising to the clean tungsten value. When gas contamination occurred during deposition the annealing curve displayed maxima at $\sim$ 900 K and $\sim$ 1600 K. These peaks became smaller as the evaporation conditions improved.

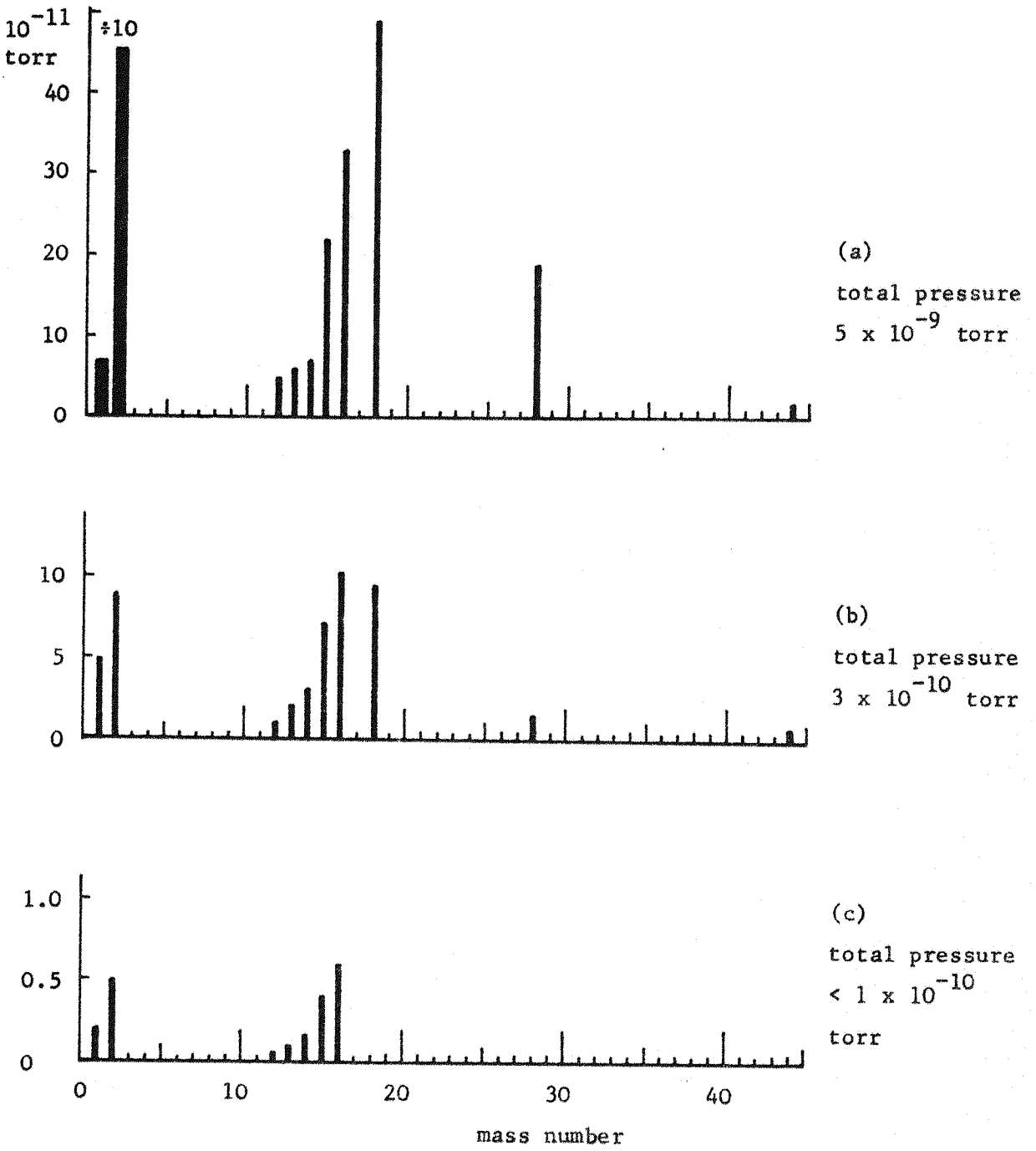

figure 8.14

mass spectra during degassing and evaporation of zirconium

(a) initial degas (masses 1 and 2 are reduced by factor of 10 on diagram)

(b) further degassing

(c) evaporation

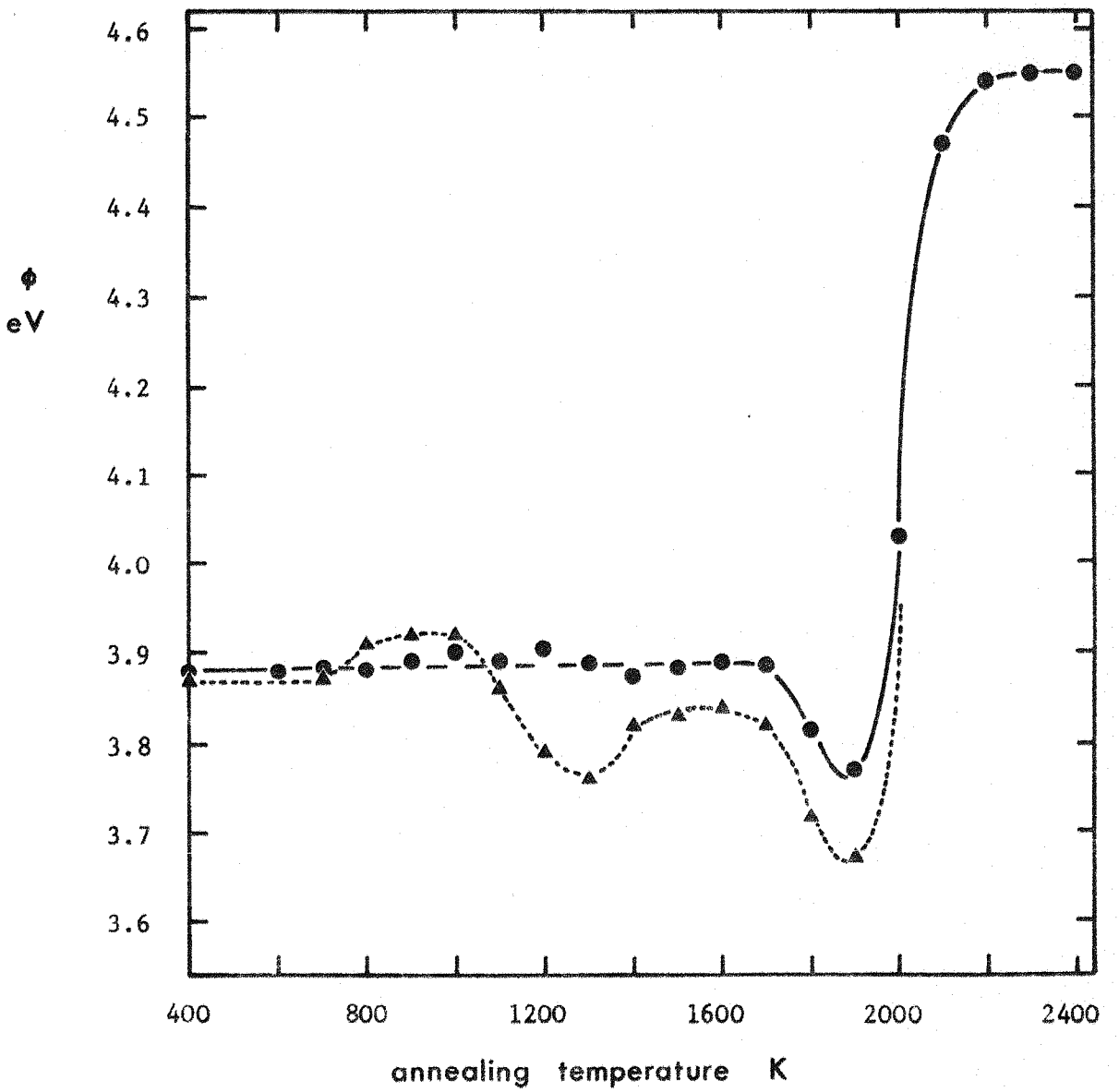

figure 8.15
work function ϕ after annealing a monolayer film of zirconium on polycrystalline tungsten (Anderson technique)

▲ ▲ ▲ contaminated (20 minute deposition at 2×10^{-10} torr)
● ● ● clean (20 minute deposition at $< 1 \times 10^{-10}$ torr)

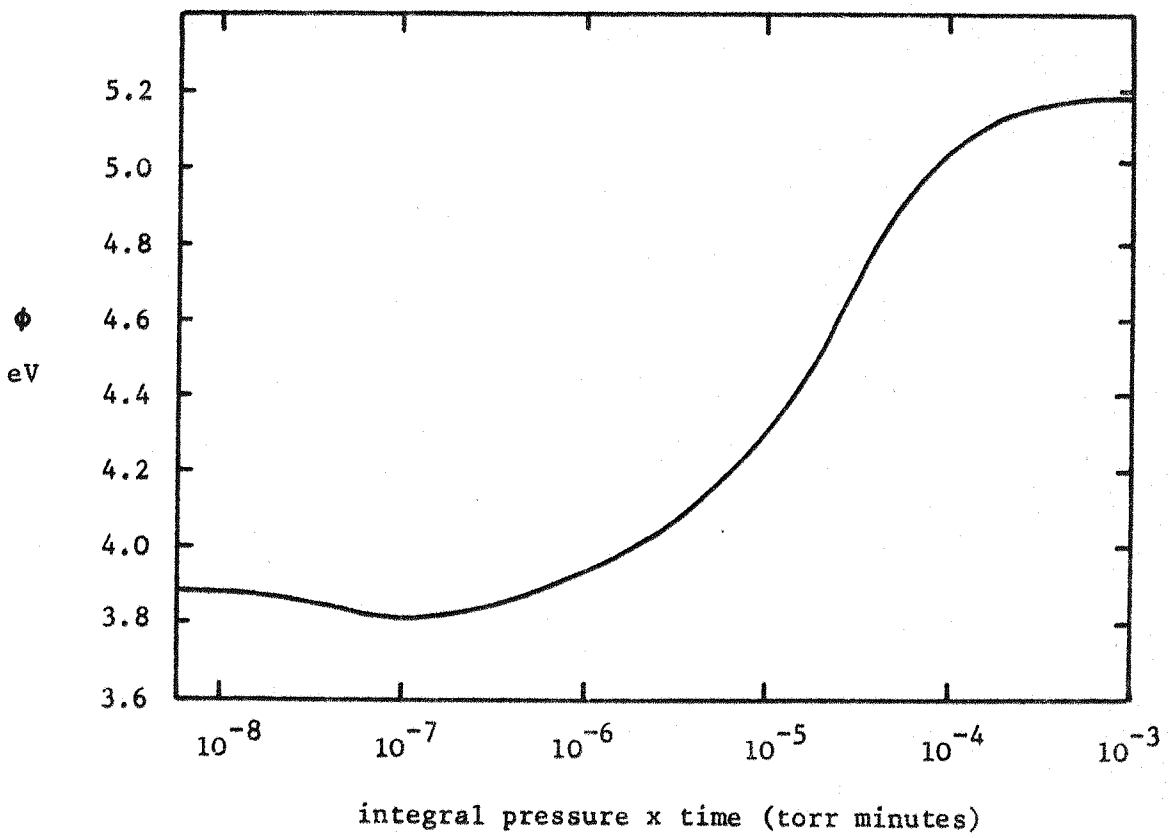

figure 8.16
work function ϕ of zirconium film on exposure to oxygen

8.3.1.1 oxygen contamination of zirconium - Anderson technique

Several investigators[166,286] have reported that oxygen desorption lowers the work function of zirconium. However, Wahl[166] has suggested that this is due to oxygen dissolving into the bulk and that at very high exposures ZrO_2 is formed at the surface, causing the work function to rise. A simple experiment was undertaken in which a glass capsule, filled with spectroscopically pure oxygen and sealed off, was broken magnetically, thus exposing a zirconium film, estimated to be 2 monolayers thick, to oxygen (tube 1). The resulting work function is shown in figure 8.16 where the abscissa is the integrated pressure-time. On breaking the capsule the pressure dropped

rapidly following the initial burst of gas, stabilizing after 1 minute at 4×10^{-8} torr. The contribution of the initial gas burst to the exposure is neglected in figure 8.16. The work function first decreased, reaching a minimum of 3.80 eV after 2 minutes before slowly rising to a final value of 5.18 eV after 40 hours. It seems likely that the small initial drop was caused by penetration of the oxygen through the zirconium and the rise due to the slow formation of zirconium oxide. As in the case of uranium, coverage curves produced by deposition of insufficiently degassed zirconium exhibited a lower work function (see figure 8.18). From this experiment it appears that such an effect is unlikely to be caused by oxygen contamination at the substrate, but rather by evaporation of zirconium already oxide contaminated.

8.3.2 zirconium on tungsten single crystals

A series of Kelvin measurements analogous to those obtained for uranium were made for zirconium on (110) and (100) single crystals using tube 8. The room temperature coverage curves are from 3 independent measurements for the (110) case (figure 8.17), and 2 for the (100) case (figure 8.21). Insufficiently degassed zirconium produced lower work functions (figure 8.18) in the same way as uranium. For (110) tungsten coverage curves at elevated temperatures (figure 8.19) were very similar to the room temperature curve except that no minima were observed. The annealing curve for (110) tungsten (figure 8.20) showed a distinct rise at $\sim$ 800 - 1100 K when the zirconium was insufficiently degassed. Even in the cleanest film this rise was still observable, the work function falling at $\sim$ 1100 K, near the α/β phase transition in bulk zirconium (1137 K). However, it seems clear that this was a contamination effect. The coverage curves at elevated temperatures

for zirconium on (100) tungsten (figure 8.22) were markedly different from the room temperature curve; the work function at all times was considerably higher. The addition of only $\sim$ 1/3 of a monolayer at room temperature to the final high temperature film was sufficient to bring the work function back to the room temperature value. The annealing curve for (100) tungsten (figure 8.23) showed no abrupt work function changes. The temperature in this case was taken only up to 1300 K because bad thermal contact between the crystal and its supporting tube made accurate temperature measurement impossible.

Coverage curves for zirconium on polycrystalline, (110) and (100) tungsten are summarized in figure 8.24. The polycrystalline measurement was made using the Anderson technique; otherwise measurements were by the Kelvin technique.

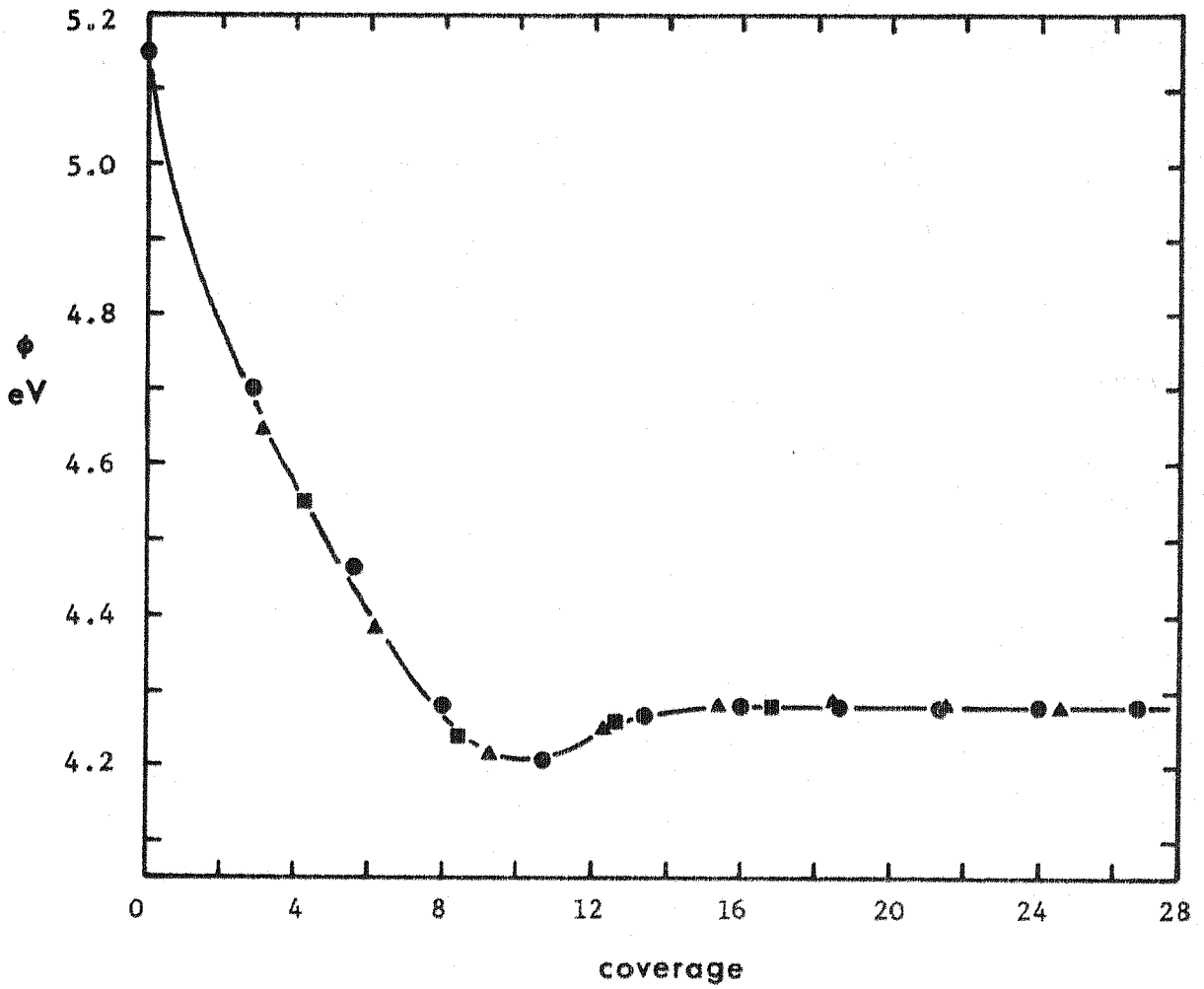

figure 8.17
work function ϕ/coverage for zirconium on (110) tungsten for deposition times of:

- ● 10 minutes
- ▲ 8 minutes
- ■ 4 minutes

coverage scale normalized to minimum

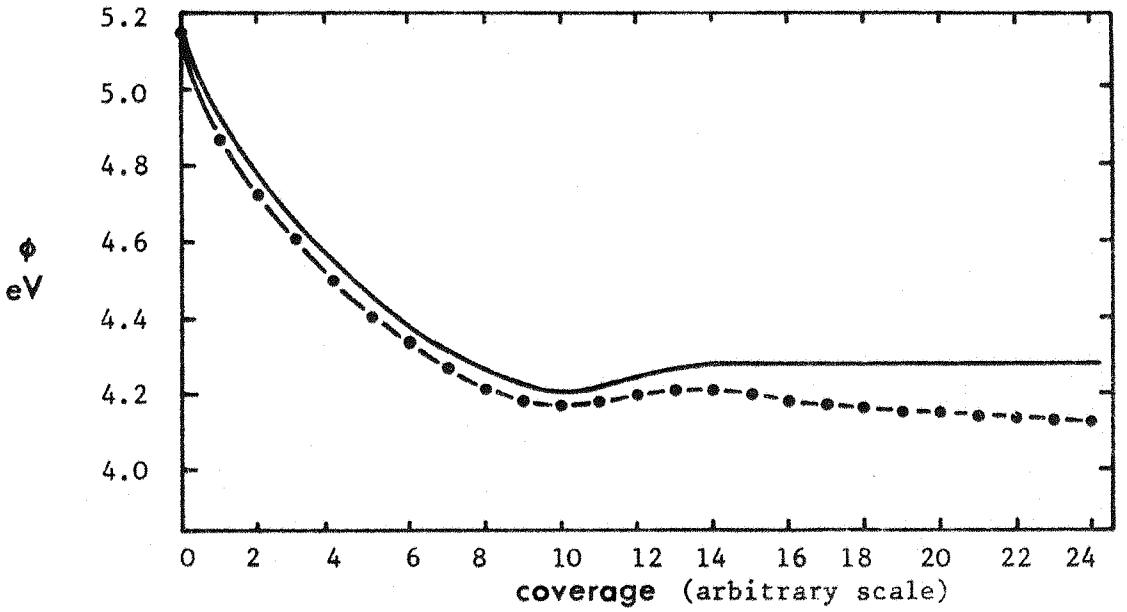

figure 8.18

work function ϕ/coverage for zirconium on (110) tungsten

——— briefly degassed source

• • • well degassed source

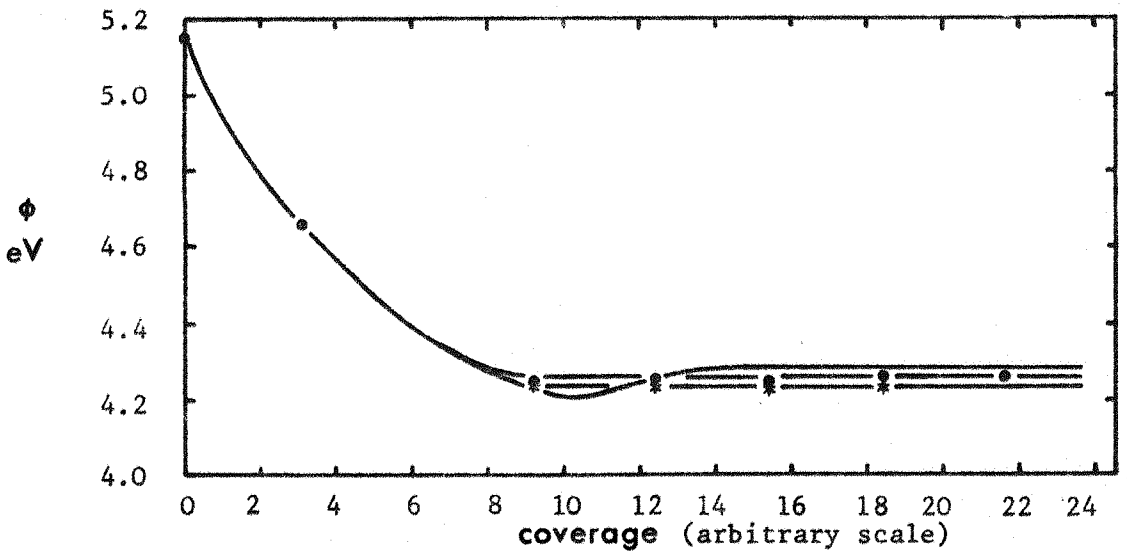

figure 8.19

work function ϕ/coverage for zirconium on (110) tungsten for 3 substrate temperatures:

——— 300 K

• • 1000 K

* * 1250 K

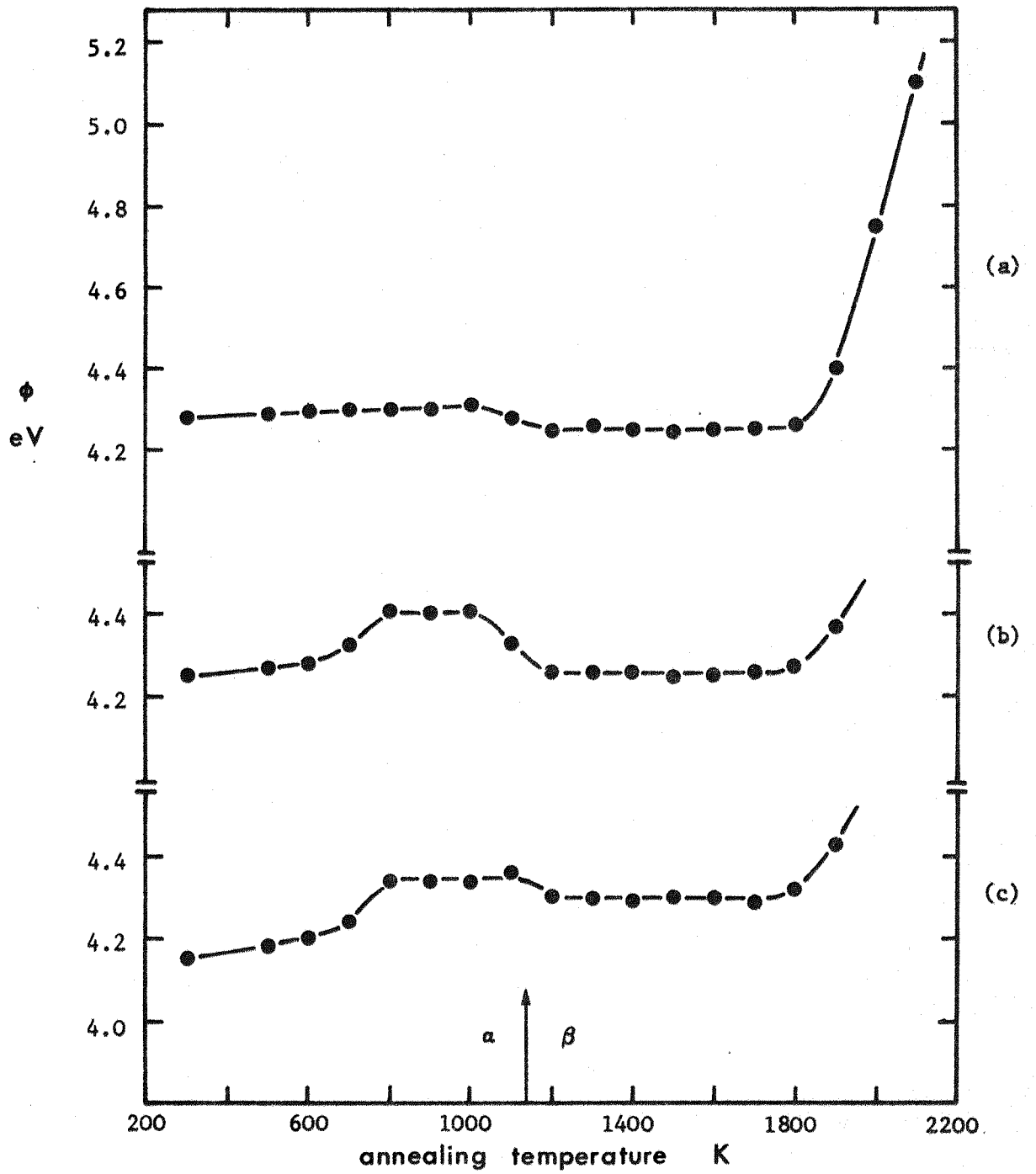

figure 8.20
work function ϕ after annealing a monolayer film of zirconium on (110) tungsten

(a) well degassed source
(b) partially degassed source
(c) briefly degassed source

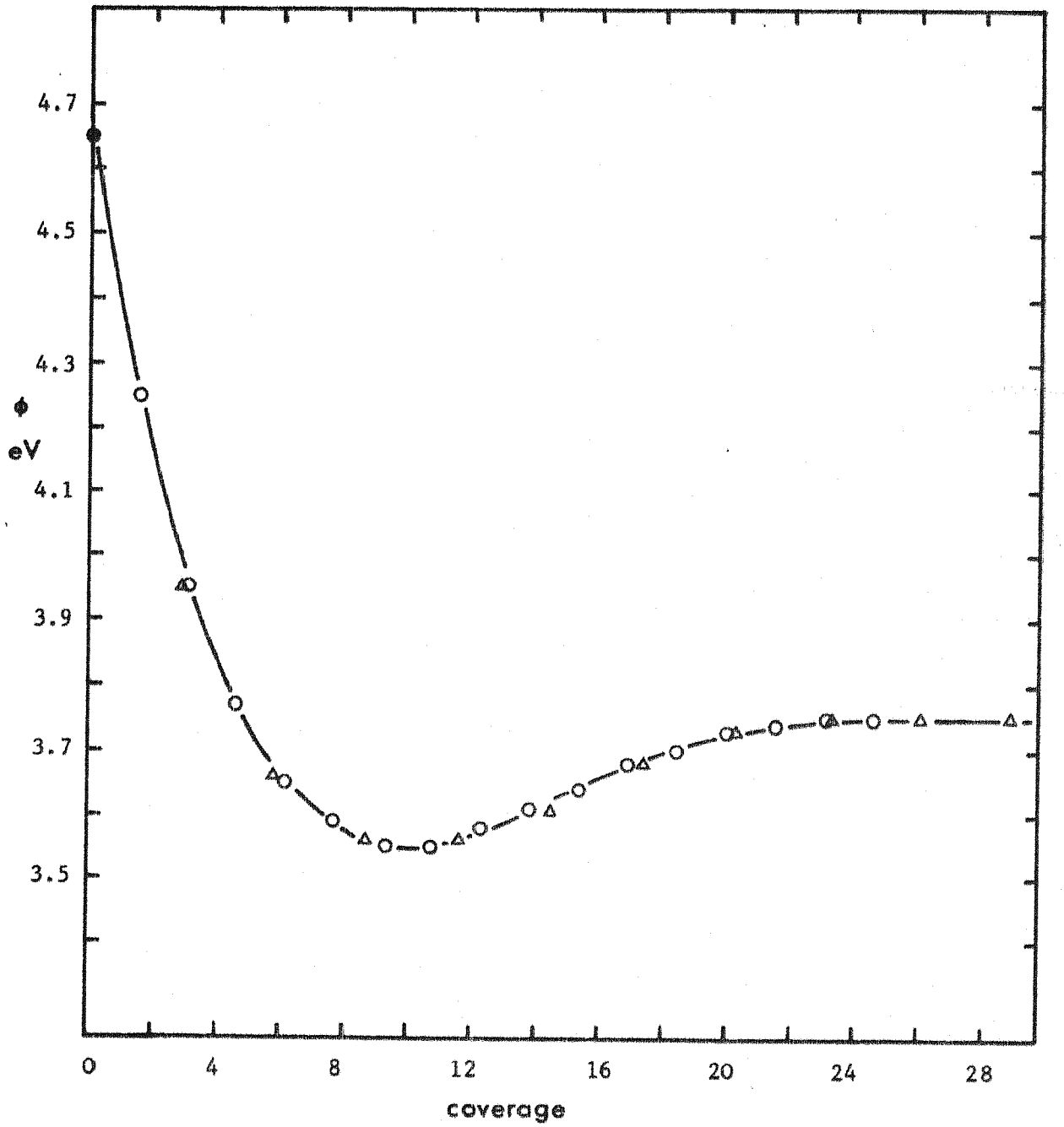

figure 8.21
work function ϕ/coverage for zirconium on (100) tungsten for deposition times of:

- ○ 16 minutes
- △ 10 minutes

coverage scale normalized to minimum

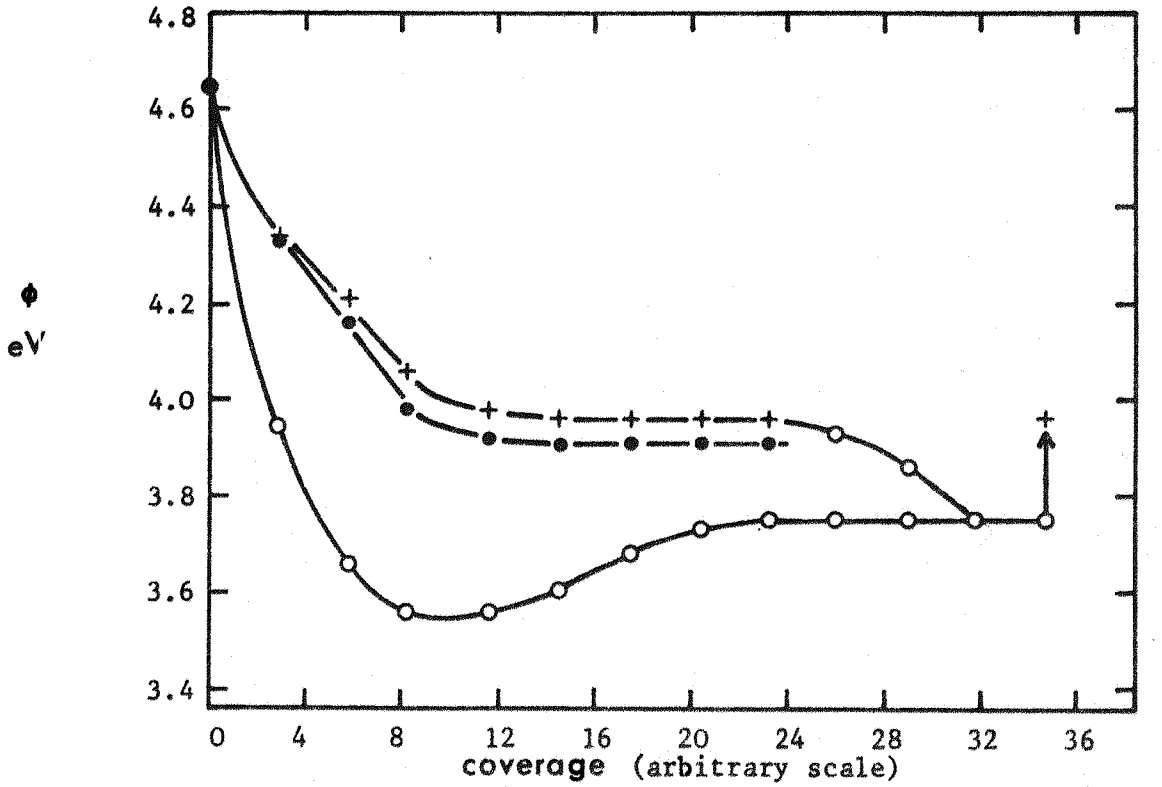

figure 8.22
work function ϕ/coverage for zirconium on (100) tungsten for 3 substrate temperatures:

- ○ 300 K
- ● 850 K
- \+ 1250 K

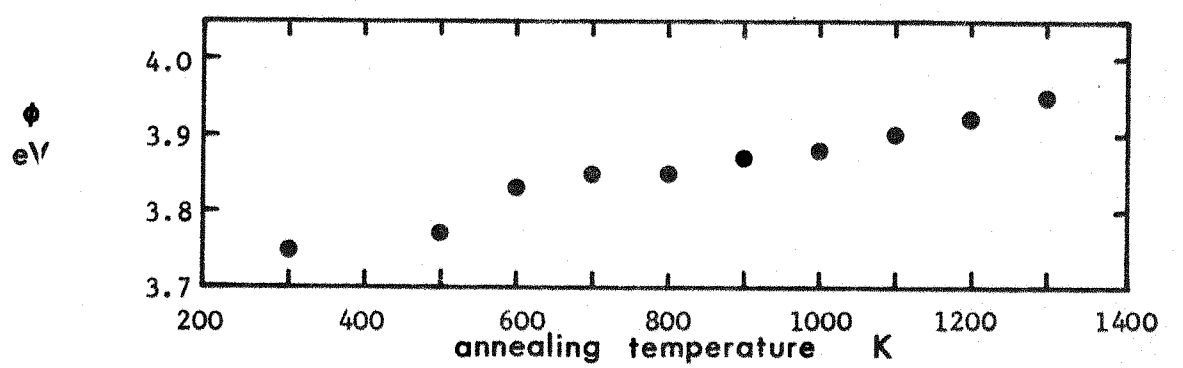

figure 8.23
work function ϕ after annealing a monolayer film of zirconium on (100) tungsten

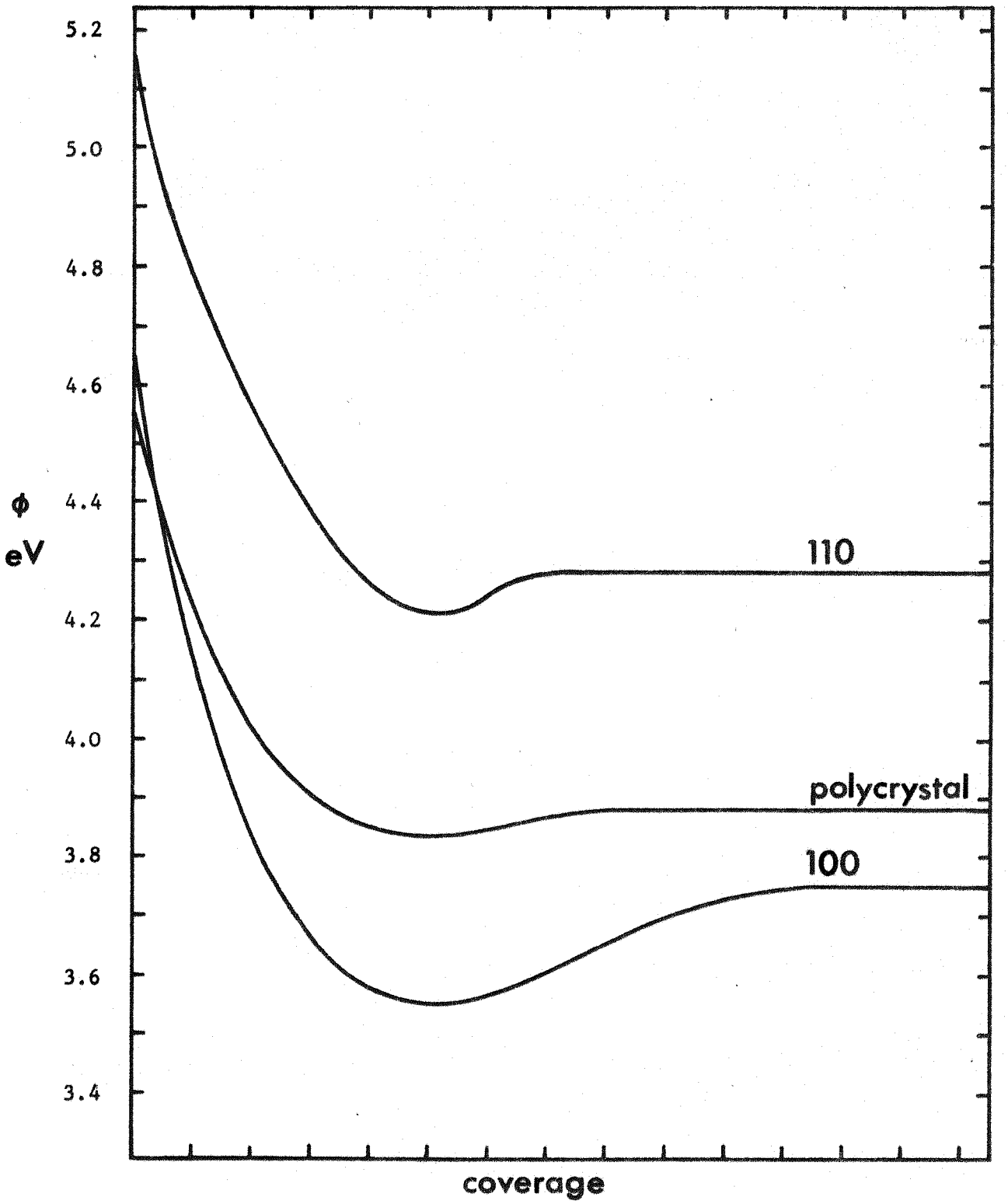

figure 8.24
work function ϕ/coverage: zirconium on tungsten (110) crystal, (100) crystal and polycrystal
coverage scale normalized to minima

8.4 discussion

8.4.1 room temperature measurements

The room temperature coverage curves for both uranium and zirconium display the general shape expected from the adsorption theories discussed in chapter 2. The work function falls to a minimum, followed by a rise to the final (monolayer) value†. The Gyftopoulos and Levine[65] and Gyftopoulos and Steiner[99] theories propose that the monolayer work function is that of the adsorbate and hence, by implication, independent of the substrate. This is clearly not in agreement either with the present results or with other work[124,228-230,289,290]. In ascribing the initial and final work functions to the bulk properties of the substrate and adsorbate the above theories implicitly exclude any dependence on the surface double layer. Lee et al[228] have assumed that the anisotropy of work function with orientation can be attributed entirely to the Smoluchowski 'smoothing' component of the surface double layer (section 1.1), and are thus able to compute the difference between the monolayer work function of caesium on (110) and on (100) tungsten. A simple calculation of this kind is possible only when the ratio of surface densities, σ_f/σ_m, is independent of substrate orientation. In the present case it is proposed (section 9.1) that for both adsorbates $\sigma_f/\sigma_m = 1$ for the (100) tungsten substrate whereas $\sigma_f/\sigma_m = 1/2$ for the (110) substrate. However the magnitude of such structural effects may be assessed in a qualitative way: the decrease in work function $\Delta\phi_s$ due to 'Smoluchowski smoothing' depends on the roughness and hence the density of the surface.

† throughout this thesis monolayer coverage is defined as in section 2.2.1: ie monolayer ($\theta = 1$) occurs when the density of adatoms equals the density of sites σ_f

In the (100) case, since $\sigma_f/\sigma_m = 1$, $\Delta\phi_s$ will be the same for the monolayer film as for the clean surface. In contrast $\sigma_f/\sigma_m = 1/2$ for the (110) surface resulting in a larger $\Delta\phi_s$ for the film than for the clean surface. Thus one would expect the total work function change on adsorption to be greater for the (110) substrate. Further support for this argument is provided by considering the geometry of the surfaces. In the (100) case an adsorbed atom can be partially accommodated in the 'holes' in the surface whereas the depth of such holes on the (110) plane is minimal. Consequently the roughness of the (100) film is less than suggested by the surface density while that of the (110) is more. The experimental values of total work function change $\Delta\phi$ are given below:

U on (110) W:	$\Delta\phi$ = 1.25 eV
U on (100) W:	$\Delta\phi$ = 0.85 eV
Zr on (110) W:	$\Delta\phi$ = 0.87 eV
Zr on (100) W:	$\Delta\phi$ = 0.90 eV

Clearly the above argument is valid only for uranium. However lithium[230], sodium[289], potassium[229], scandium[290], caesium[228], barium[124] all show larger values of $\Delta\phi$ on (110) than on (100) tungsten, indicating that zirconium is anomalous in this respect. The correlation between surface potentials and electronegativity discussed in appendix 2 provides further evidence that zirconium is an unusual case: agreement is obtained for zirconium on (100) tungsten but for the (110) substrate the value of $\Delta\phi$ is smaller than expected. An obvious explanation is that zirconium forms islands on (110) tungsten, producing a patchy surface with an average work function $\bar{\phi}$ between that of zirconium and tungsten. However, it is difficult to see how the work function

of such a surface could remain constant at higher coverages. In addition, the recent field emission work of Collins[156] shows no evidence for nucleation in this case. It thus appears likely that a monolayer film is formed, but for reasons not understood this structure has an unexpectedly high work function.

In summary, for all cases studied here the work function remains constant after rising from the minimum, assuming a value which is dependent on both the adsorbate and substrate. Nucleation has not been observed by Collins[156] for any of these systems. This is consistent with the view of a monolayer film whose work function is determined by the adsorbate but modified by the structural dependence on the substrate.

The concept of a 'monolayer' film is proposed in the 'pseudomorphic' model of Franke and van der Merve[294-296], Finch and Quarrell[297,298] and Rhodin[299], unlike the nucleation models of Hirth and Pound[300-303] and Rhodin and Walton[304]. There is good evidence[305-310] that for bimetallic systems nucleation does not occur until several monolayers have been deposited, the first monolayer at least showing some registry with the substrate. Other investigations have shown that a monolayer[291,311], or a substantial fraction of a monolayer[312-314], is formed prior to nucleation. However, before accepting the 'monolayer' model (ie no island structure at monolayer coverage at which point the work function levels out), experimental work in which both structure and work function have been measured should be examined. Unfortunately, few such measurements have been made. A discussion of these is given below.

8.4.2 correlation of work function with structure for adsorbed films

Intuitively one would expect the structure to be determined by 3 factors:

1 the strength of the adsorbate-substrate bond as opposed to the adsorbate-adsorbate bond. The covalent components of these are given approximately by D_o as calculated by Gyftopoulos and Steiner (section 2.2.5) and the sublimation energy D(f-f) respectively;

2 the magnitude of the adsorbate-substrate dipole. A large dipole causes the adatoms to spread out uniformly because of the long range dipole-dipole interaction. The dipole is given by the initial slope of the work function/coverage curve but relative magnitudes are given approximately by the values of $\Delta\phi/\sigma$ at the work function minimum;

3 the size of the adsorbate particle compared with the substrate lattice. Large radii result in a reduced dependence on the substrate structure.

These 3 factors are interrelated since the existence of a dipole adds an ionic contribution to the adsorbate-substrate bond, as well as reducing the radius of the adatom (r_a) towards that of the ion (r_i). However some insight into the process of formation of monolayer films may be obtained by comparing these parameters. Values of D_o, D(f-f), r_a, r_i and $(\Delta\phi/\sigma)_{min}$ are listed in table 8.1 for the systems considered.

The following conclusions may be drawn:

a caesium is more strongly bonded to the substrate than to itself and so registry with the substrate might be expected. However the large size of the caesium atom means it will be less dependent on the substrate, and at low coverage the strong dipole-dipole interaction will tend to keep the atoms equally spaced;

table 8.1 parameters of adsorbate-substrate systems

system	D_o † (eV)	D(f-f)[102] (eV)	r_a[315] (Å)	r_i[315] (Å)	$\Delta\phi_{min}$ (eV)	σ_{min} (atoms nm^{-2})	$10(\Delta\phi/\sigma)_{min}$	ref
Cs-W (100)	1.75	0.80	2.66	1.69	3.05	1.9	16.1	237
Li-W (110)	2.53	1.66	1.52	0.60	2.3	4.7	4.9	221
Th-Ta(100)	3.57	6.29	1.79	1.02	1.10	3.4	3.24	292
Th-W (100)	3.69	6.29	1.79	1.02	1.36	4.2	3.24	292
Cu-W (110)	3.67	3.51	1.28	0.96	0.75	8.0	0.94	311
U -W (100)	2.21	5.20	1.54	1.05	1.11	3.7	3.00	††
Zr-W (100)	3.71	6.16	1.60	1.09	1.10	4.3	2.56	††
W -W	8.68	8.68	1.37					
Ta-Ta	8.11	8.11	1.65					

† equation 2.63

†† $\Delta\phi_{min}$ from present work; σ_{min} estimated by assuming σ = 10 atoms nm^{-2} at θ = 1

b the lithium atom is very small and much less ionic than caesium. It, too, is strongly bound to the substrate and so registry would be expected. However, apart from the caesium case, the dipole-dipole interaction is larger than in the other systems considered;

c thorium is very strongly bonded to itself and is a little less ionic than lithium. Its diameter can be as small as the tantalum or tungsten lattice constants depending on the ionicity;

d copper is only marginally more strongly bonded to the substrate than to itself and has a low dipole and small size. Thus the substrate would be expected to dominate the structure.

experimental low energy electron diffraction (LEED) and work function studies

1) Cs on W(100)

The work function/coverage curve[237] is similar in shape to those of the present work. MacRae et al[316,325] report that at low coverages caesium is distributed in a roughly hexagonal array before a LEED pattern appears. Presumably the strong dipole-dipole interaction keeps the caesium in this distribution, as discussed in (a) above. The first LEED pattern to appear corresponds to a c(2x2) structure† and occurred at a coverage of 2.5 atoms nm^{-2} (2.5×10^{14} atoms cm^{-2}). After this, MacRae et al report the formation of a second layer which was completed at a total surface density σ of 9.34 atoms nm^{-2}. The final work function corresponds to the completed 'duolayer'. However, this density is more than 3 times that measured by other experimenters[237,318]. (MacRae et al infer their surface density from the LEED patterns; no measurement was made). It seems unlikely that errors in the measurement of σ could be this great. In addition the caesium Auger intensity increased almost linearly with coverage up to $\sigma = 5.0$ atoms nm^{-2}. In view of the extreme sensitivity of Auger emission to thickness[319] a change of slope would be expected at the completion of the first layer. Contamination of the caesium could possibly have caused these discrepancies. However, the important points are that at low coverages caesium is distributed evenly over the surface and that at high coverages caesium structures can be formed which are in registry with the substrate. It is interesting to note that Gerlach and Rhodin[293] have also observed registry, in their case for low coverages ($\theta \ll 0.5$) of caesium on Ni(110). Additional caesium deposition reduced the dependence on the substrate, the completed monolayer showing one-dimensional registry only.

† see Wood[317] for explanation of nomenclature

Thus, in spite of its size and charge caesium appears to form structures related to the substrate. This is probably a result of the strong adsorbate-substrate bond (in comparison with the adsorbate-adsorbate bond) which is augmented by a large ionic component. At low coverages caesium may be distributed evenly, in accordance with (a) above.

2) Li on W(110)

Again the work function/coverage curve[221] displayed the usual shape. LEED measurements have been performed by Gorodetskii[320] but this work is not yet available. However, it has been briefly discussed elsewhere[321]. A p(2x1) structure (where the unit mesh is oblique) was formed at $\sigma_f/\sigma_m = 1/2$ (σ = 7.1 atoms nm^{-2}). This corresponds to a position past the minimum in the work function/coverage curve. After this point lithium atoms 'crowded' on to the surface until $\sigma_f/\sigma_m \simeq 1$ ($\theta = 1$). Registry with the substrate occurred up to $\theta = 0.67$.

Thus the registry expected from (b) above occurs. However, the very small size of the ionic lithium atom permits a more densely packed structure.

NOTE: in the present work a p(2x1) structure is proposed at monolayer coverage on W(110) (section 9.1 - see figure 9.6).

3) Th on Ta(100)

These measurements[291,292] were performed with the substrate heated to 1250 K. The work function/coverage curve[292] again displayed a shape similar to those of the present work. The LEED patterns showed that islands of c(2x2) structure were formed up to σ = 3.4 atoms nm^{-2} (σ_m = 9.3 atoms nm^{-2}) which corresponds to the work function minimum. Further deposition of thorium did not complete this structure (ie did not reach σ = 4.65 atoms nm^{-2}) but produced a deposit in (1x1) registry with the substrate. This

pseudomorphic layer had the final work function. Additional deposition resulted in the epitaxial growth of 3-dimensional islands on the pseudomorphic layer.

Thus, in spite of the very strong adsorbate-adsorbate bond, pseudomorphism can occur. The ionicity of the adsorbate-substrate bond must reduce the radius to the required 1.65 Å. At low coverages the strong adsorbate-adsorbate bond is evident since islands are formed.

4) Th on W(100)

The majority of this work was carried out on substrates at room temperature[322-324] but recently a heated substrate has been studied[292]. The room temperature work function/coverage curve showed an abrupt change at the minimum which appeared to correspond to an incomplete c(2x2) structure (σ = 4.2 atoms nm^{-2}), similar to that on the tantalum substrate. Deposition of one monolayer produced the hexagonal structure of Th(111), but with a slightly expanded lattice (thorium radius 1.82 Å rather than 1.79 Å found in bulk) in order to give registry in one dimension. This structure corresponded to the final work function. The rather linear work function change to the minimum implies near-constancy of dipole-dipole depolarization possibly due to island formation. However, no direct evidence of islands was observed.

Deposition on a substrate at 1200 K[292] removed the abrupt change in the work function/coverage curve at the minimum and resulted in a final work function which corresponded to a (1x1) structure.

Thus the strong adsorbate-adsorbate bond is evident in the formation of a structure characteristic of bulk thorium. However, it seems that this is not an important parameter since heating to 1200 K (with presumably an increase in the size of the substrate lattice) produces a pseudomorphic layer. The thorium radius in this layer is 1.58 Å.

5) Cu on W(110)

Moss and Blott[311] suggest that the monolayer coverage (σ_f = 16.0 atoms nm^{-2}, σ_m = 14.1 atoms nm^{-2}) occurs at the lowest work function. The structure is Cu(111) which is constrained to give registry with the substrate in one dimension - [001]. Since the interatomic distance in the copper lattice (2.56 Å) is smaller than the tungsten lattice constant (3.16 Å), the Cu(111) structure is expanded in the [001] and compressed in the [110] directions (see figure 9.6). Further deposition resulted in the formation of normal Cu(111), the work function rising as the surface density increased to that of Cu(111), 17.9 atoms nm^{-2}.

Since the adsorbate-substrate bond has a very low ionic content there is little dipole-dipole depolarization. This could account for the lack of a minimum in the work function/coverage curve up to the monolayer point. Copper is interesting in that on the basis of bond strengths one would expect the structure to be principally determined by the substrate. However, the small size of the copper atom seems to be the important factor.

In summary, it appears that the relative strengths of adsorbate-substrate and adsorbate-adsorbate bonds is an unimportant factor in determining the structure. However, the size of the adsorbate particle seems crucial. An increase in the size of the substrate lattice on raising the temperature may explain the Th on W(100) structures. The magnitude of the dipole moment is critical in determining the size of the adsorbate particle but otherwise appears to be important only at low coverages where the long range dipole-dipole interaction tends to keep the adatoms apart.

The U on W(100) and Zr on W(100) systems studied in this work are clearly most similar to the Th on W(100) case (see table 8.1). Since there will be a substantial reduction in radii due to ionicity, the adatom sizes are

likely to be less than the 1.58 Å required for the (1x1) structures. However, for the U on W(110) and Zr on W(110) systems the adatom sizes are too large to allow 1:1 registry. Detailed consideration of the adsorption sites is given in section 9.1, but it is pertinent to note here that a p(2x1) structure is proposed, similar to that observed for Li on W(110) at $\theta = 0.5$. As has been pointed out above, the dissimilarity in bond energies (ie for Li on W and for U, Zr on W) does not appear to be important.

A considerable amount of work on bimetallic systems has been undertaken in the USSR. Zingerman and others[219,326-329] have studied Ba, Sr, Ca and Mg on tungsten foil and found that a work function minimum exists when these materials are deposited on a room temperature substrate. Evaporation on to a heated substrate resulted in a monotonic work function/coverage curve. Since the residual pressures were in the 10^{-9} torr range it was concluded that the work function minimum was caused by electronegative gas contamination. At elevated substrate temperatures this gas was desorbed. Shrednik[169,330,331], however, suggests that for Cs, Na, K, Ba, Th and Zr on tungsten the work function minimum corresponds to 'optimal packing' of the adsorbate atoms. Further deposition causes the work function to rise as the surface density decreases to that of the bulk adsorbate.† Vedula et al[332], from studies of the Ba-W and U-W systems, conclude that the dependence on substrate temperature observed by Zingerman et al could not be due to contamination but was associated with the structure of the substrate. Tishin and Tsarev[333], in a thorough investigation of the adsorption of Ba, Ca and Cs on tungsten, have eliminated all sources of contamination as the cause of work function minima. However, rough surfaces tended to reduce the sizes of the minima.

† this is contrary to the dependence proposed by Smoluchowski[13]

It is curious that none of these experimenters have considered dipole-dipole depolarization as the cause of work function minima. The dependence on surface roughness can easily be explained in these terms since, on atomically rough surfaces, the depolarization will be considerably reduced.

A complete account of the fitting of coverage curves to adsorption theories is discussed in chapter 9.

Since the completion of the present experimental work a project was undertaken by Lea[125] in which coverage curves obtained by Kelvin, photoelectric and Anderson techniques were compared for the uranium on tungsten system. Both (110) and (100) substrates were used in this work. The values obtained for the minimum and final work functions are given below, together with the field emission results of Collins[156] and, for comparison, the values from the present work:

		U on (110) W		U on (100) W	
		minimum	final	minimum	final
present work	(Kelvin)	3.79	3.90	3.54	3.80
Lea[125]	(Kelvin)	3.68	3.90	3.65	3.73
Collins[156]	(field emission)	3.90	3.99	3.64	3.88

For the sake of this comparison the field emission (110) values have been lowered by 0.05 eV since Collins assumed 5.20 eV for the clean tungsten work function whereas 5.15 eV was used in the Kelvin work. It is clear that there is some disagreement between the 2 Kelvin measurements. Lea finds a deeper minimum for (110) tungsten but a shallower one in the (100) case. The final values for (110) tungsten agree while Lea's final value for (100) tungsten is lower. It is possible that these differences arise from the use of the Anderson technique since, as was pointed out in section 7.1.1, during

such measurements the substrate is heated by radiation from the emitter and is also bombarded by low energy electrons. In addition, each point on the coverage scale involved making 4 measurements so that the total time taken to complete one monolayer was presumably considerably longer. A surprising result is that the shape of the field emission curves is in good agreement with the present measurements although the values, after the initial fall in work function, appear to be displaced upwards by ∿ 0.1 eV. Recent field emission work[334] has shown that at the initial deposition there is a marked change in the value of the Fowler-Nordheim pre-exponential, an effect which may well explain this last result.

A comparison of the values obtained for zirconium in the present work and in Collins' field emission measurements[156] is given below. Again the (110) field emission values have been corrected so that both measurements refer to the same clean tungsten value:

		Zr on (110) W		Zr on (100) W	
		minimum	final	minimum	final
present work	(Kelvin)	4.21	4.28	3.55	3.75
Collins[156]	(field emission)	4.32	4.41	3.75	3.87

As in the uranium case, the shape of the curves measured by the two techniques are similar although the field emission values are considerably higher. It is interesting that the anomalously high Kelvin value obtained for zirconium on (110) tungsten is also evident in the field emission work.

work function of films after the monolayer point

It must be assumed that as the film thickness is increased the work function becomes independent of the substrate and characteristic only of the adsorbate.

figure 8.25
electron micrograph of a (110) tungsten surface after deposition of ∿ 10 monolayers of zirconium
(x50,000)

0.3 μm

Experimentally, the region in which this occurs is difficult to ascertain since after rigorous degassing very little evaporant is available for deposition. Thicker films could only be achieved in the present work by inadequate outgassing of the source which resulted in lower work functions. The cleanest films, however, showed no variation up to ∿ 10 monolayers. Presumably a change to the bulk value occurs either very slowly or at greater thicknesses. Electron micrographs of substrates after deposition of 10 monolayers showed smooth featureless surfaces. However, because of the loss of resolution in the replicating process no structure < ∿ 200 Å size would be observed. A typical micrograph is shown in figure 8.25.

8.4.3 measurements at elevated temperatures

These measurements were undertaken to determine the nature of the abrupt, irreversible work function changes observed for uranium on polycrystalline

tungsten (section 4.2). Initially[7] it was thought that these were associated with crystallographic phase changes in the bulk metal. Thus a great deal of time was spent investigating the way in which the work function changed around the α/β and β/γ phase transition temperatures in uranium and the α/β transition temperature in zirconium. The temperatures involved are 938 K, 1043 K and 1135 K respectively. However, the annealing curves for the single crystal substrates (figures 8.6, 8.11, 8.20, 8.23) show only gradual changes to values consistent with the end points of the elevated temperature coverage curves. The only abrupt change occurs for zirconium on (110) tungsten but this appears to be a contamination effect (see figure 8.20). The annealing curve for zirconium on polycrystalline tungsten foil also displays curious changes (figure 8.15) when the zirconium is contaminated, but, unlike the (110) single crystal case, it is possible to eliminate these effects by careful degassing. Thus it must be concluded that uranium on polycrystalline foil is an isolated example of abrupt work function changes, presumably associated with the tungsten grain boundaries. It seems unlikely that the initial explanation in terms of phase changes 'frozen-in' to the thin film is correct for two reasons:

1 no monolayer film can be expected to display effects characteristic of structures as complex as those of uranium (see figure 4.0);

2 there is no evidence that thin films of uranium change phase irreversibly (see section 4.1).

In the absence of structural measurements little can be said about the elevated temperature coverage curves that is not mere speculation. However, the following points are of interest:

a all coverage curves above room temperature are monotonic (figures 8.8, 8.12, 8.19, 8.22). This result is to be expected if island formation

occurs. The work function is then the area average of the island work function and that of the tungsten, and will decrease monotonically as the island size increases until a monolayer is formed. An alternative description is that the dipole-dipole depolarization term (which normally causes the work function to rise) is constant when the separation between adatoms is unchanged, as it is within the islands. The final work function will then depend on the structure of the coalesced film. A similar disappearance of the work function minimum for deposition on heated substrates has been observed for Li and Th on tungsten[221] and for Ba, Sr, Ca and Mg on tungsten[326,327];

b in the case of zirconium on (100) tungsten the work function at elevated temperatures (figure 8.22) is always considerably above that at room temperature. The addition of only $\sim$ 1/3 of a monolayer at room temperature reduces the high temperature monolayer work function to the room temperature value. Such an effect will occur if islands form but do not coalesce, growth occurring normal to the surface. Only 1/3 of a monolayer is then required to bridge the bare tungsten areas. The final work function before addition of this 1/3 monolayer is then given by simple 2-patch theory. It is interesting to note that, because of the large size of the zirconium atom and the (proposed) high density of sites on (100) tungsten, the adatoms are more closely packed in this case than in any of the other systems studied in the present work. The resulting dipole-dipole interaction may be large enough to reduce the binding energy at the adsorption sites by an amount sufficient to allow increased adatom mobility at elevated substrate temperatures;

c for uranium on (100) tungsten the coverage curves (figure 8.12) intersect in a way similar to those for uranium on polycrystalline tungsten[7]. This is to be expected since foil is predominantly (100) oriented;

d the annealing curves for both adsorbates on polycrystalline tungsten (figures 4.2, 8.15) reflect the coverage curves in that the work function falls before rising to the clean tungsten value. The single crystal annealing curves (measurements over this temperature range were made only on (110) tungsten, figures 8.6, 8.20) rise abruptly at the onset of desorption in the same way as the high temperature coverage curves abruptly level out during adsorption.

The formation of islands as suggested above implies mobility of adatoms on the tungsten surface. In addition, both Good and Müller[186] and Collins[156] have observed migration of uranium and zirconium on tungsten field emitter tips at high temperatures. For these reasons an attempt was made to observe migration on the macroscopic single crystals used in this work. Uranium and zirconium were evaporated on to a (110) crystal which was partially shadowed from the vapour stream by the reference electrode. The crystal was then heated to progressively higher temperatures for periods of 5 minutes. The reference was not moved during this process so that initially it was facing clean tungsten. At the onset of mobility it was hoped to see the work function fall as the adsorbate migrated across the crystal. However, no change was detected until the film began to desorb ($\sim$ 1700 K for uranium, $\sim$ 1800 K for zirconium). It can only be assumed from this experiment that the adsorbates migrate over distances small in comparison with the dimensions of the Kelvin electrodes.

CHAPTER 9 FITS TO ADSORPTION THEORIES

An important prerequisite to the use of all the adsorption theories discussed in this thesis is the knowledge of the geometry of the substrate-adsorbate system. The adsorption sites on the substrate surface are taken as the positions of highest binding energy as calculated by the pair-wise interaction model of Neustadter and Bacigalupi[105]. The position of these sites, together with a knowledge of the sizes of the adsorbate atom and the substrate lattice, permits an estimation of the maximum (ie monolayer) adsorbate surface density σ_f.

The atomic radii in metal crystals are usually taken as half the observed minimum atomic separation[287]. For α-uranium, α-zirconium and tungsten these are:

α-U 1.38 Å α-Zr 1.59 Å W 1.37 Å

However, in the case of α-uranium the electron configuration of the atom is strongly asymmetric so that this radius is not representative of the 'hard-sphere' volume of the atom. Zachariasen[288] has calculated the metal radii from the volume average per atom corrected to a ligancy of 12 (L12). For uranium, zirconium and tungsten these values are:

U 1.54 Å Zr 1.60 Å W 1.39 Å

Zachariasen's atomic radii are used in the following work.

The calculations involved in fitting the following adsorption theories to the experimental results were made on an ICL 1907 computer at the University of Southampton Computation Department. The programming language was ALGOL.

9.1 Neustadter and Bacigalupi

As discussed in section 2.3 the normalized potential energy ζ between an adatom and substrate atoms i is given by the summation:

$$\zeta = \frac{E}{4E_o} = \frac{1}{4}\left(\frac{R}{a}\right)^{12}\sum_i\left(\frac{1}{d_i}\right)^{12} - \frac{1}{2}\left(\frac{R}{a}\right)^{6}\sum_i\left(\frac{1}{d_i}\right)^{6} \qquad 9.1$$

where $R = r_m + r_f$, the sum of the adsorbate and substrate atomic radii, 'a' is the substrate lattice constant (a = 3.16 Å for tungsten) and d_i is the distance in units of 'a' between the adatom and the substrate lattice atom i. Values of ζ are calculated as the adsorbate position is moved along an axis perpendicular to the surface. The binding energy is then defined by the minimum in this curve. The summation in equation 9.1 was carried out for substrate atoms situated within a hemisphere, radius 5a, centred on the adsorption site. It is clear from equation 9.1 that the ratio R/a defines the system. For uranium on tungsten and for zirconium on tungsten this ratio is 0.927 and 0.851 respectively.

Topographical maps of the normalized energy ζ were constructed for the 4 cases U-(100)W, U-(110)W, Zr-(100)W and Zr-(110)W. Since the features of these maps are similar for both uranium and zirconium adsorbates only the latter are reproduced here. Figure 9.1 is of the (100) unit mesh and figure 9.3 the (110) unit mesh. In both cases the substrate atoms are situated at the points marked A, B, C, D. Figure 9.2 shows the potential energy variation along the lines AB and CD of figure 9.1, both passing through the central maximum. Similarly, the potentials along the lines AB, CD and BE (figure 9.3) are shown in figure 9.4. It is clear that in the (100) case there is a single pronounced energy maximum at the centre of each unit mesh, whereas in the (110) unit mesh two maxima exist, separated by a small energy

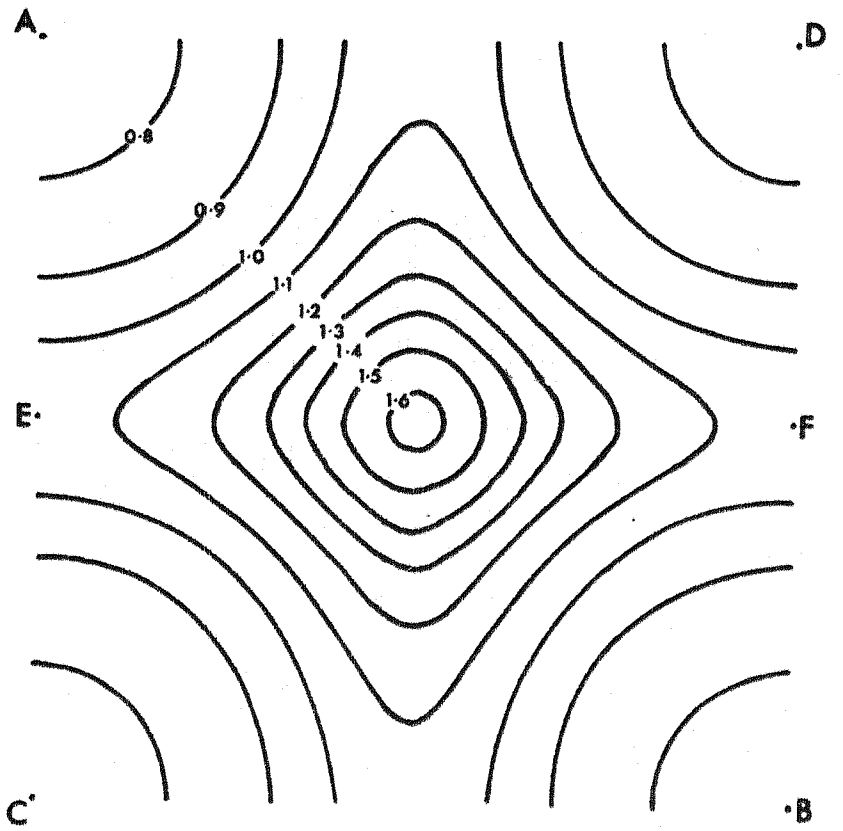

figure 9.1

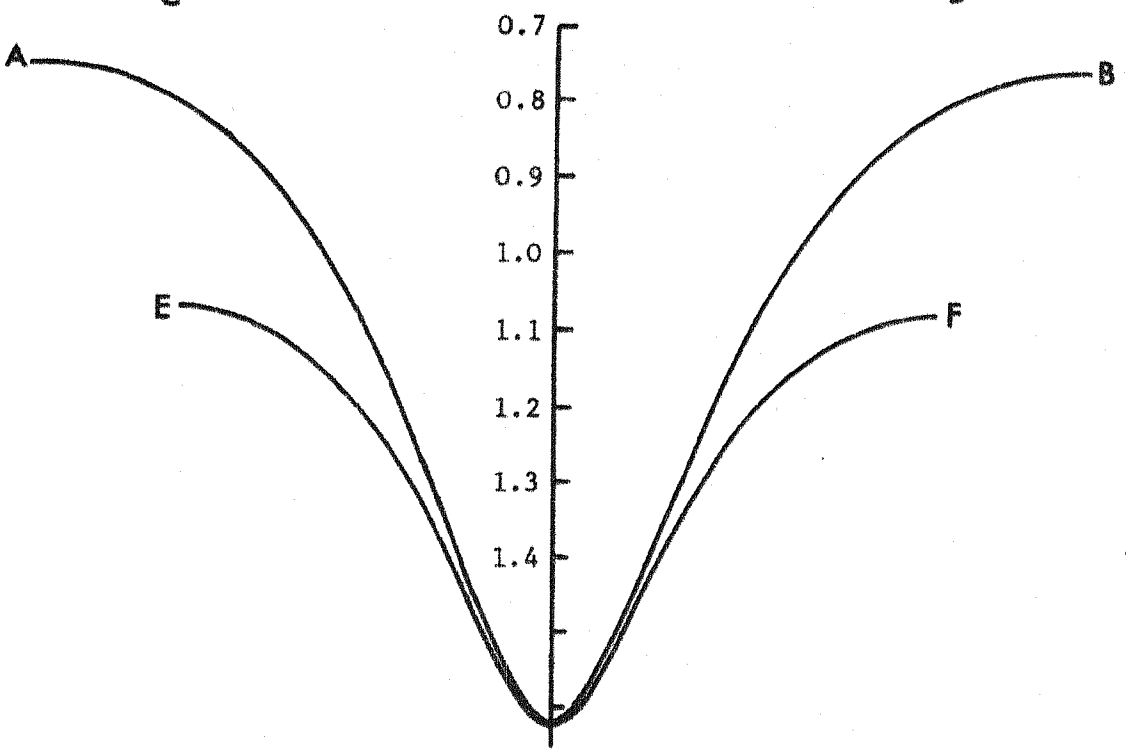

figure 9.2
normalized binding energy ζ for the (100) unit mesh
zirconium on tungsten

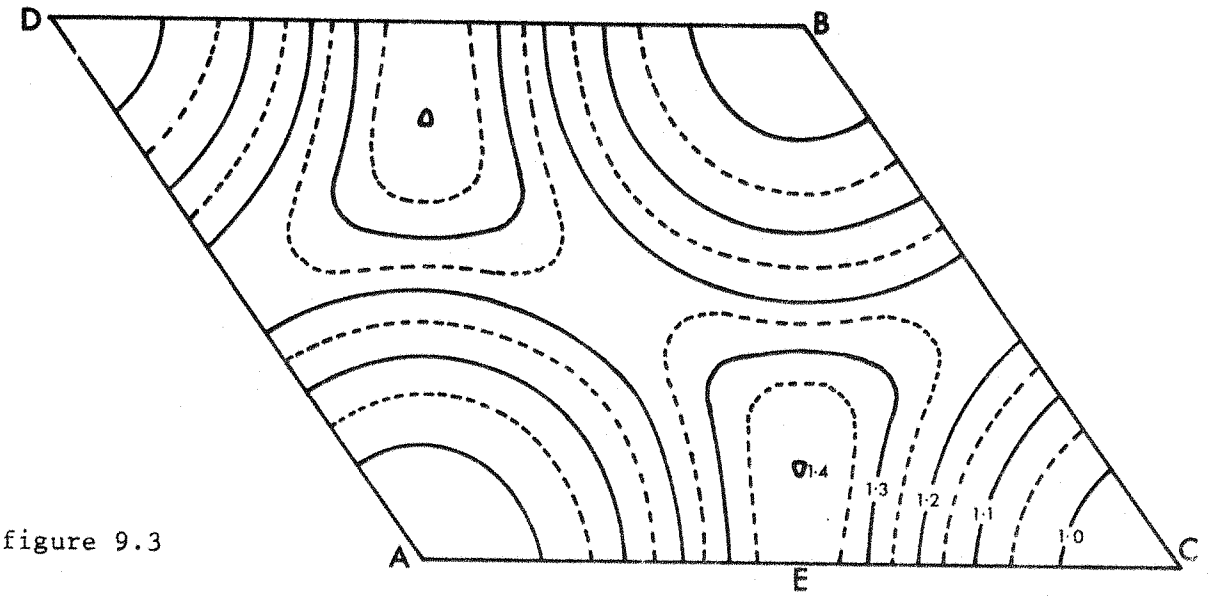

figure 9.3

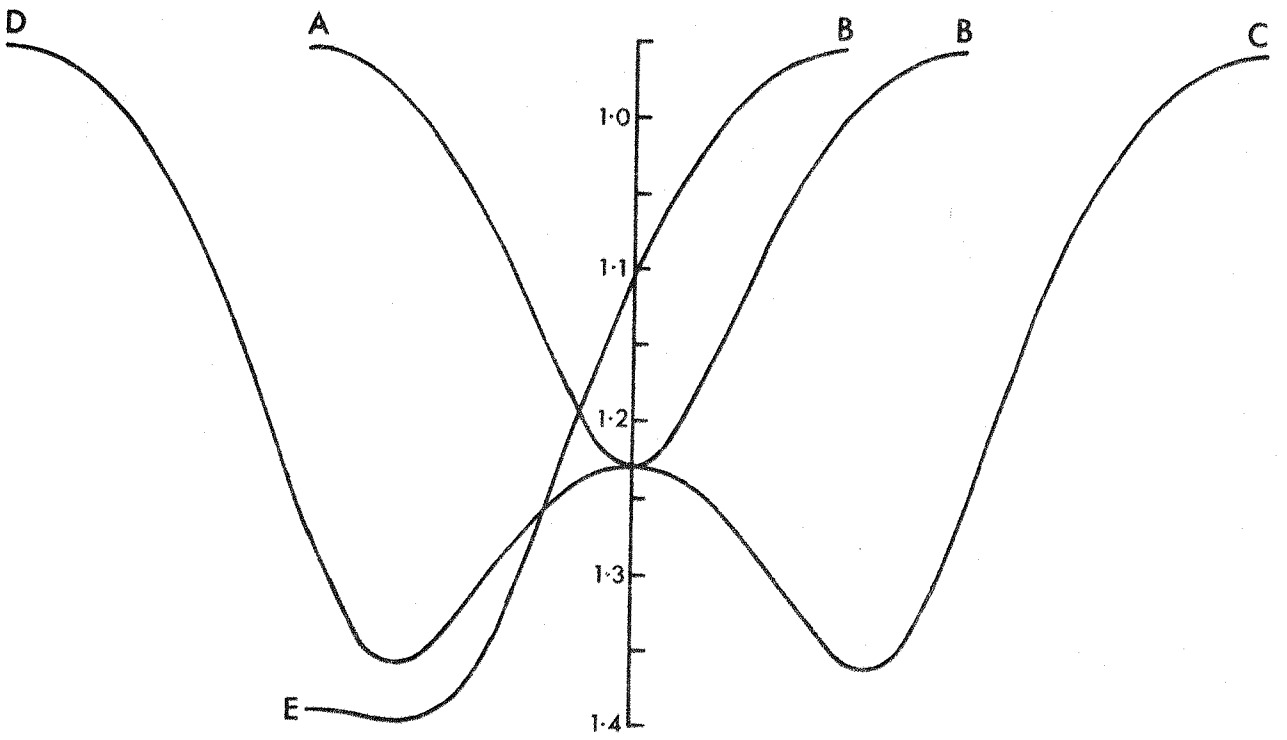

figure 9.4

normalized binding energy ζ for the (110) unit mesh zirconium on tungsten

barrier; the line EB passes through one of these maxima. Figures 9.5 and 9.6 demonstrate the hard-sphere model of the two surfaces showing the unit meshes and adsorption sites. The (100) case is unambiguous: the distance between adsorption sites equals the lattice constant, 3.16 Å. Although the 'hard-sphere' diameter of the zirconium atom (L12) is 3.20 Å it is possible for adatoms to fill every site since the L12 radius represents the maximum possible size of the covalently bonded atom. In reality an adatom has a ligancy[68] $L < 12$ and in addition is partially ionically bonded to the substrate. Uranium atoms, diameter 3.08 Å (L12), can be accommodated in the same way with no reduction in radius. Thus, in both cases the ratio $\sigma_f/\sigma_m = 1$.

For the (110) surface, because the adsorbate atoms are larger than those of the substrate, it is not possible to accommodate one adatom in each unit mesh. If all adatoms are situated in sites of the same type (sites (a) or (b) in figure 9.6) then there is one atom in every other unit mesh and the ratio $\sigma_f/\sigma_m = 1/2$. As in the (100) case, the atoms are separated in the [001] direction by a distance equal to the lattice constant 3.16 Å. If, however, atoms are situated as shown in figure 9.6 - that is: site (a) filled in mesh 1, site (b) filled in mesh 2, none filled in mesh 3 - then the ratio $\sigma_f/\sigma_m = 2/3$. It is usual[65] in the case of the (110) surface to take as the adsorption sites the positions mid-way between adjacent sites (a) and (b). Only alternate sites can then be filled, giving $\sigma_f/\sigma_m = 1/2$. Although the binding energy is not as great for such sites they may be energetically more favourable for a monolayer film because of reduced dipole-dipole effects due to:

a lower surface density σ_f;

b equal spacing between adatoms in the [110] direction.

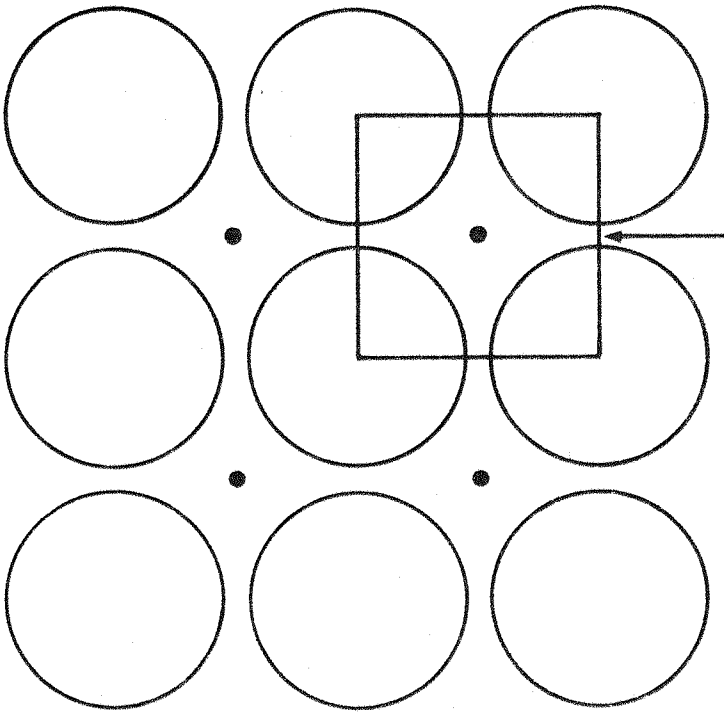

figure 9.5
tungsten (100) surface

● proposed sites

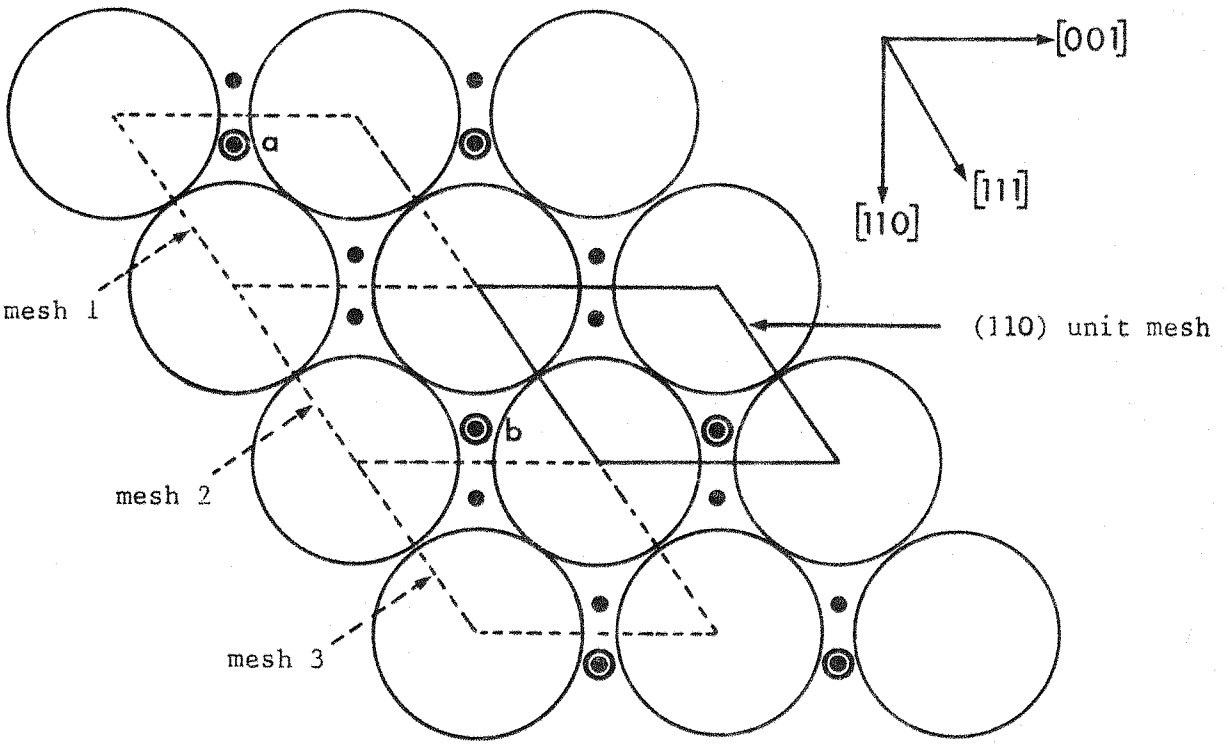

figure 9.6
tungsten (110) surface

● possible sites ◉ sites filled for $\sigma_f/\sigma_m = 2/3$

However, once in the mid-way position a lower energy state would be achieved by adatoms filling alternate sites of the same type, as discussed initially. Thus the following mechanism is suggested:

1 adatoms first fill sites (a) and (b) at random;

2 as the coverage increases, the dipole-dipole interaction causes the adatoms to move towards positions mid-way between (a) and (b) sites;

3 at monolayer coverage $\sigma_f/\sigma_m = 1/2$ and all sites are of the same type.

This process involves movement of some adatoms from (a) to (b) type sites or vice versa. As pointed out in section 8.4.2, LEED measurements of the Li - W(110) system have demonstrated that adatoms can adsorb in this arrangement.

9.2 Rasor and Warner

Since the Rasor and Warner theory can be expected to describe accurately only highly ionic systems (see chapter 2), a comparison of the theory with experiment was performed for only one of the present cases, that of zirconium on (100) tungsten. This was sufficient to determine the adequacy of the theoretical approach.

In the derivation of the theory, Rasor and Warner assumed a model in which the ratio of ions/atoms on the surface was determined by an exponential dependence on the surface ionization energy E, where (equation 2.30):

$$E = E_o - (1-f)\Delta\phi + \Delta\phi_a$$

They then showed that for the case of caesium on tungsten the atom adsorption energy ϕ_a (or, in the terminology of Levine and Gyftopoulos[102], the covalent part of the bond energy, H_{cc}) was independent of coverage so that $\Delta\phi_a = 0$. Since this may not be true for the less ionic systems studied in the present

work, it was suggested in section 2.2.3 that as a first approximation $\Delta\phi_a = -c\Delta\phi$, where c is a constant, was reasonable.

A computer program, similar to that developed by Lee[97], was used to calculate Σd^2, the sum of the squares of the deviations between theory and experiment for 21 points at 0.05 monolayer intervals. For given values of the parameters σ_f (adsorbate surface density), E_o (zero coverage surface ionization energy), ℓ (ion-imaging plane distance), and c (atomic adsorption constant), the program was designed to minimize Σd^2 with respect to the polarizability α_i. Initially c was set at zero (ie as Rasor and Warner) and the surface density was taken as that proposed in section 9.1 (σ_f = 10 atoms nm^{-2}). This left only E_o and ℓ as adjustable parameters. In addition, the position on the coverage scale chosen as the monolayer point could be altered. The parameters then giving the best fit, as determined by the minimum Σd^2, are shown in the first row of table 9.1. Σd^2 was insensitive to the position of the monolayer point, the best fit occurring just after the work function reached the final value. In this region, changes in the monolayer position had an insignificant effect on the 'best-fit' values of ℓ and E_o. For these reasons this parameter was not subsequently adjusted. The agreement between theory and experiment is surprisingly good, the maximum deviation (case (a) in figure 9.7) being only $\sim$ 40 mV. This agreement could be only marginally improved by adjusting the value of c (case (b) in figure 9.7); the parameters emerging in this case are shown in the second row of table 9.1. Evidently the agreement for the c = 0 case is so good that any improvement due to inclusion of a non-constant ϕ_a is obscured. It is perhaps worth noting that the calculation of Levine and Gyftopoulos[102] shows that ϕ_a increases slowly with coverage; this is consistent with the small negative value of c determined from the best fit. In addition, Levine and

Gyftopoulos calculate E_o (the ionic component of the bond energy, H_{ii}, at zero coverage). For caesium on (100) tungsten the value obtained is E_o = 1.17 eV, which compares well with the values found from the best fits of the theory to the experimental data of Taylor and Langmuir[86] (E_o = 1.05 eV)[91], and of Lee[97] (E_o = 1.2 eV). For zirconium on (100) tungsten the result is 0.254 eV, considerably above the experimental-fit value. Because of the exponential dependence on E_o the theory is very sensitive to small changes in this parameter. Consequently, the use of E_o = 0.254 eV would lead to a very much lower final work function.

table 9.1

parameters from fit of Rasor and Warner theory to Zr on (100) W results†

σ_f atoms nm^{-2}	ℓ Å	E_o eV	c	polarizability 10^{-40} Fm^2	α_i Å^3	Σd^2	fig 9.7 case
10.0	0.40	0.168	0.000	21.4	19.2	0.0080	(a)
10.0	0.36	0.161	-0.033	30.3	27.5	0.0048	(b)
3.9	1.00	0.260	0.000	92.7	83.4	0.0036	(c)

† parameter underlined held constant

According to the proposed model, ℓ should equal the ionic radius of the adsorbate. For alkali adsorbates this appears to be true[97,359]. However, for zirconium $\ell \approx 0.4$ Å, considerably below the univalent radius (1.09 Å) or even the quadrivalent radius (0.80 Å)[315]. Since $\sigma_f \ell \approx$ constant (equation 2.34), ℓ may be fixed at a realistic value and the best fit found for σ_f. The third row of table 9.1 shows the parameters emerging when ℓ is set at 1.00 Å; although the fit is slightly improved (case (c) in figure 9.7),

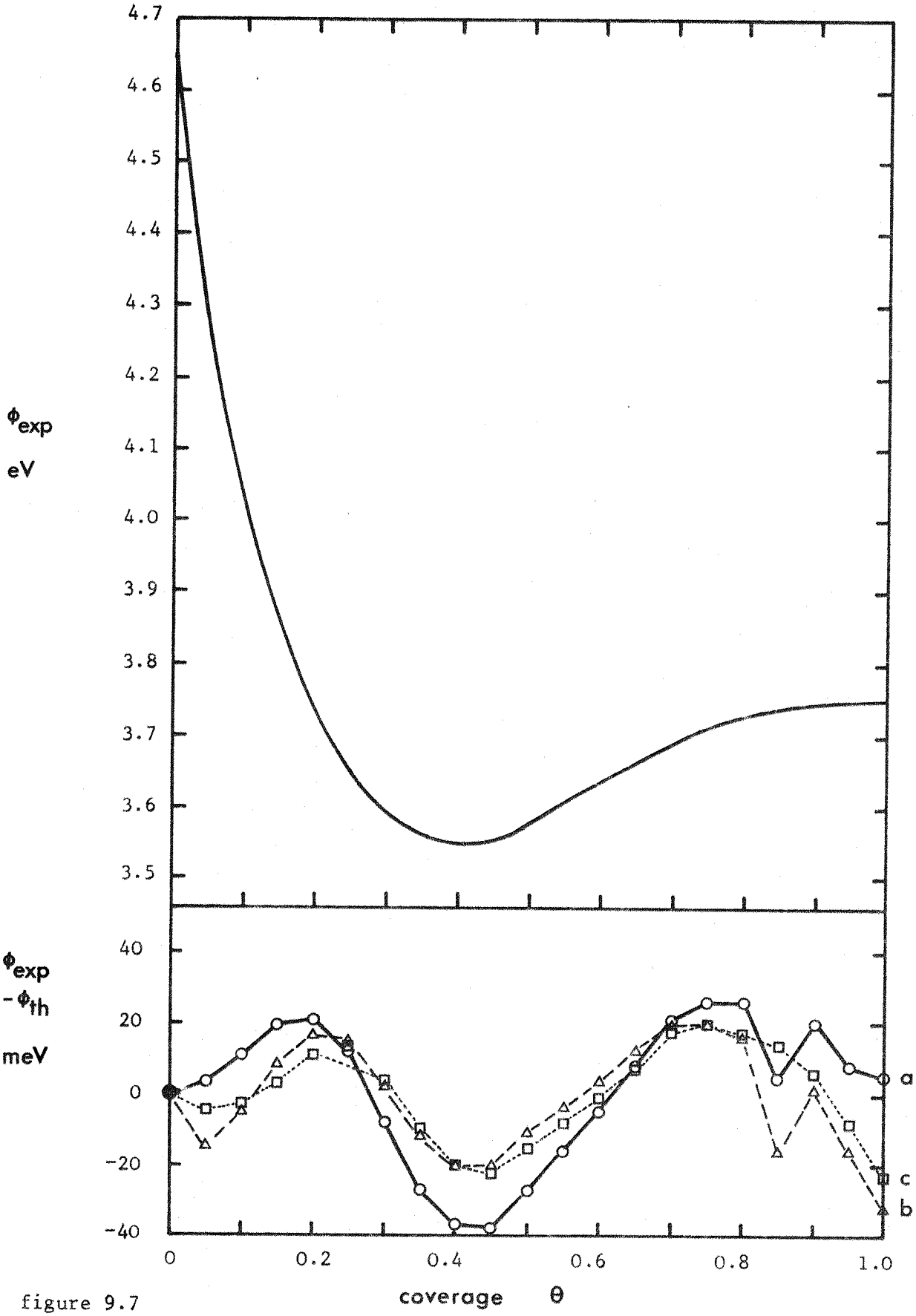

figure 9.7

zirconium on (100) tungsten data fitted to the theory of Rasor and Warner parameters in cases a, b and c as in table 9.1

σ_f falls to $\sim$ 1/3 of the expected value and the polarizability α_i rises to an unlikely magnitude. Of all the parameters α_i is the least well established. In the physical model it is proposed that α_i is the ionic polarizability of the adatom. However, in order to account for the high value required for caesium on tungsten, Rasor and Warner suggest that the total polarizability is the sum of adsorbate and substrate components. The former, being the ionic polarizability, is small and hence the polarizability of the electron cloud at the substrate surface is the dominant term. Consequently, as pointed out by Fehrs[359], the polarizability is then determined only by the substrate as long as the adsorbate ionic polarizability is small. Thus the value determined by Rasor and Warner for caesium on tungsten (31×10^{-40} Fm^2) should be approximately the same as in the present case. In fact the agreement, particularly for case (b) in table 9.1, is good. However, it should be noted that these values are very large; they are higher even than the atomic polarizabilities quoted by Gyftopoulos and Levine[65] for either tungsten or zirconium or the sum of the two.

In summary, although there is no reason to suppose that the theory should describe adsorption systems which are not predominantly ionic, the fit to the present data is remarkably good. However, the physical parameters which emerge, particularly the dipole length, are not in accordance with the model. In addition, the claim that the theory is more useful than others, in that it predicts the temperature dependence of work function, has been thrown into some doubt by the recent measurements of Lee et al[360].

9.3 Gyftopoulos and Levine

The theory of Gyftopoulos and Levine has been fitted to experimental results

for several adsorbates on single crystal tungsten substrates[97,125,238]. The fit is in all cases good but the surface density required is not always that expected from geometrical considerations.

A computer program, similar to that described by Lee[97], was used to determine the best fit. This program minimized the sum of the squares of the deviations, Σd^2, with respect to the constants k_1 and k_2 (equation 2.44). The values of k_1, k_2 and Σd^2 were then plotted as a function of the position on the coverage scale chosen as the monolayer point. The best fits, as determined by the minimum values of Σd^2, are shown in table 9.2. The coverage scales are those given in figures 8.13 and 8.24 as well as those tabulated in appendix 5 (ie normalized to the work function minimum, defined as a coverage of 10). Also shown in this table are the values of surface density σ_f, and polarizability α, calculated from k_1 and k_2^* (equation 2.45), as well as the approximate coverage at which the experimental work function levels out.

table 9.2
parameters from least squares fits of data to the theory of Gyftopoulos and Levine

system	k_1	k_2	σ_f atoms nm^{-2}	$\alpha^{\dagger\dagger\dagger}$ 10^{-40} Fm^2	mono-layer point	approx. final ϕ coverage	Σd^2
Zr - poly W[†]	4.73	2.30	11.6	7.17	16.1	16	0.00015
Zr - (100)W	7.68	3.45	18.1	5.56	21.1	23	0.00046
Zr - (110)W	3.81	1.64	8.2	8.58	17.0	15	0.00556
U - poly W[††]	6.65	2.50	15.9	4.86	21.0	22	0.00057
U - (100)W	12.56	6.17	29.9	4.66	24.9	28	0.00055
U - (110)W	3.29	1.10	7.0	7.28	17.2	18	0.00866

† measurement by Anderson technique
†† measurement due to Barry[7] (Kelvin)
††† 1 Fm^2 = $(10^{10})^3/4\pi\varepsilon_o$ $Å^3$ = 0.9×10^{40} $Å^3$

* the values of R used in this calculation are those given in table 9.3

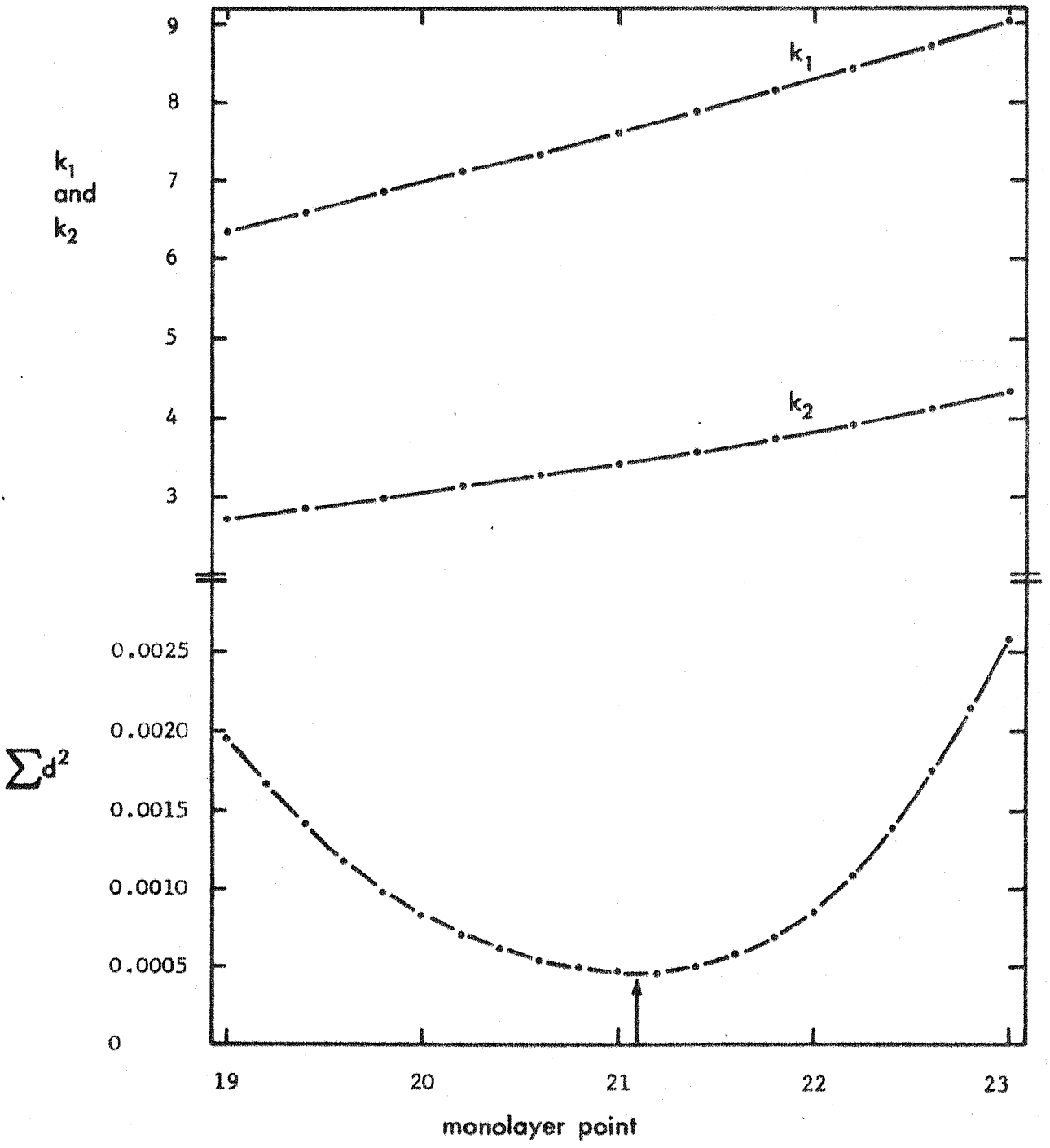

figure 9.8

values of the Gyftopoulos and Levine fitting constants k_1 and k_2, and the sums of the squares of the deviations between theory and experiment (Σd^2) for a range of monolayer positions

zirconium on (100) tungsten

Figure 9.8 shows a typical plot of the kind described above, in this case for zirconium on (100) tungsten. Clearly, although k_1 and k_2 are sensitive to the monolayer position, the latter point is well defined. In addition, the best-fit monolayer point occurs in all cases near to the coverage at which the work function reaches the final value. The deviations between theory and experiment are shown in figures 9.9 and 9.10 for zirconium on (100) and (110) tungsten respectively. The maximum deviation occurs in the (110) case and is then only 33 meV. Similar plots are obtained for uranium adsorption but they are not reproduced here since they are very like those for zirconium.

Having demonstrated that the theory can accurately describe the experimental results, it is necessary to compare the parameters which emerge with those expected from the physical situation. According to Gyftopoulos and Levine[65], quantum mechanical calculations of heats of adsorption[361] suggest that in their case the polarizability should be taken as the electronic polarizability α of the adsorbate. This may be estimated from:

$$\alpha = 4\pi\varepsilon_o n r_f^3 \qquad 9.2$$

where r_f is the covalent radius of the adsorbate and n is a number to account for the effects of the electronic shell structure. For metals other than alkalis n is taken as 1.65[362]. Both MacDonald and Barlow[363] and Gyftopoulos and Levine[65] have pointed out the approximate nature of equation 9.2, but in the absence of data on the polarizability of metallic surface dipoles this expression must suffice. The covalent radii[364] used by Gyftopoulos and Levine[102] are somewhat smaller than the atomic radii usually quoted[336]. As discussed at the start of this chapter, Zachariasen's values[288] are here preferred because of the asymmetric nature of the uranium α-lattice.

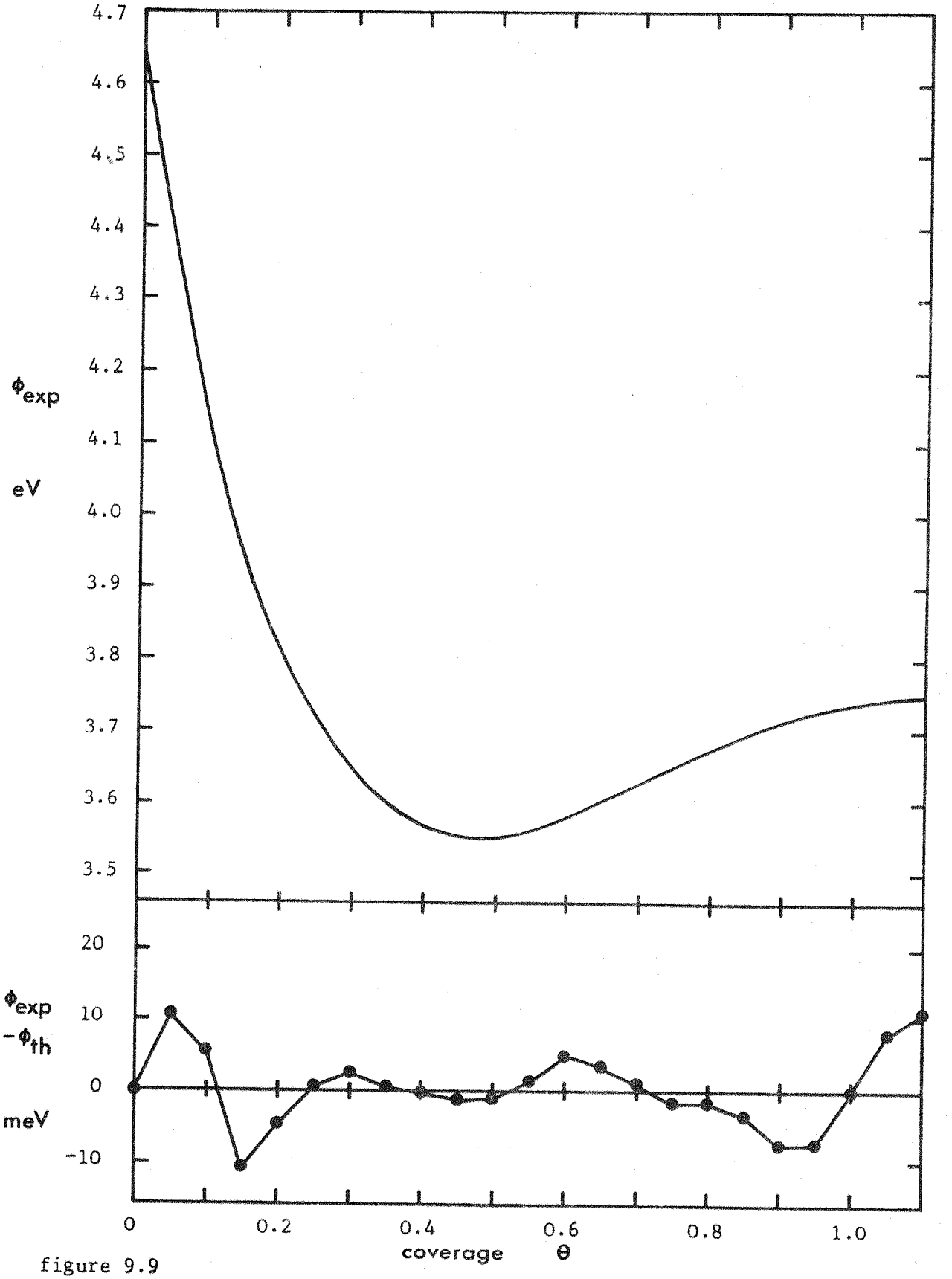

figure 9.9

zirconium on (100) tungsten data fitted to the theory of Gyftopoulos and Levine parameters as in table 9.2

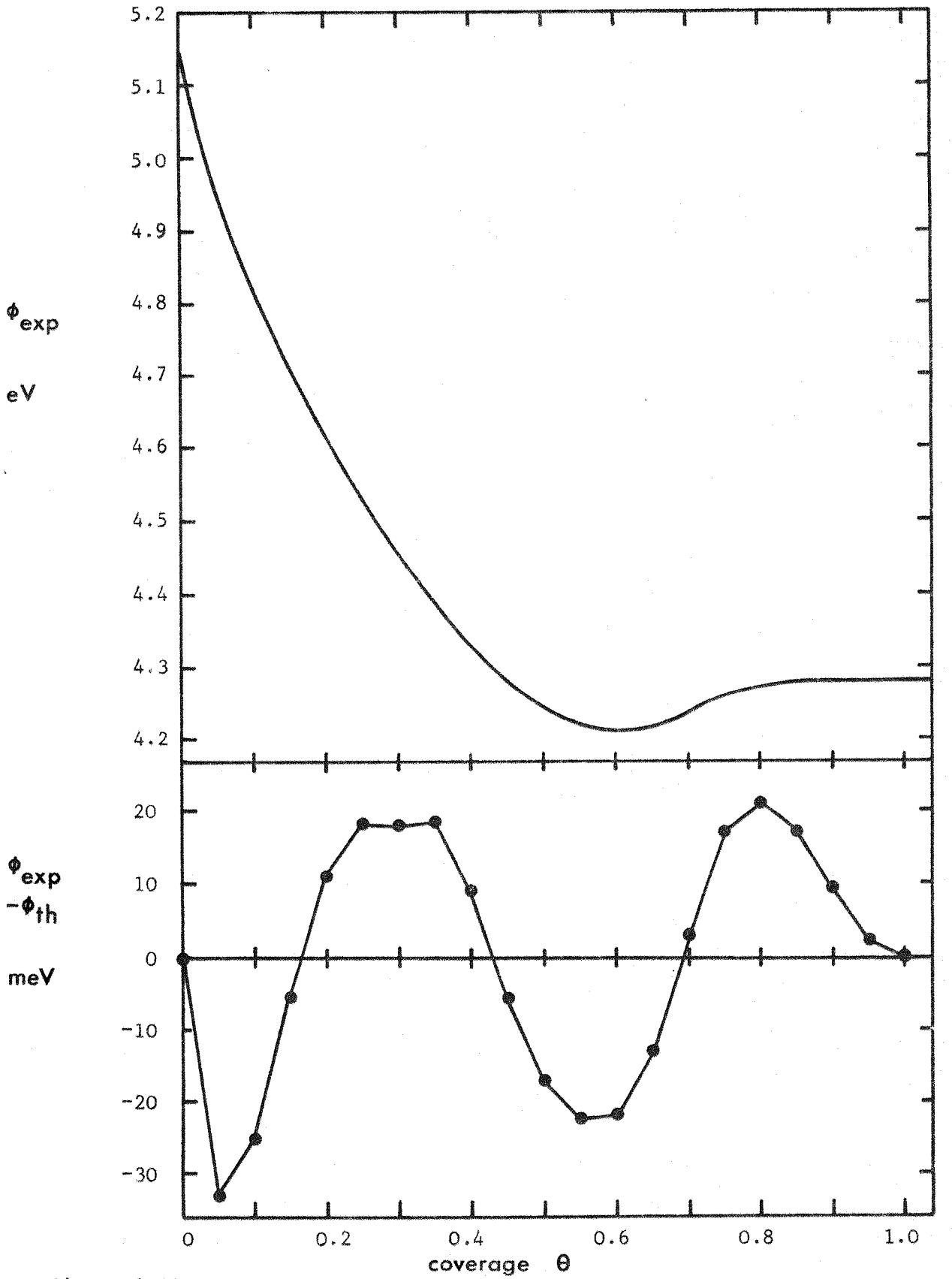

figure 9.10

zirconium on (110) tungsten data fitted to the theory of Gyftopoulos and Levine parameters as in table 9.2

The values of the following parameters are collected together in table 9.3: σ_f as proposed in section 9.1, $R = r_m + r_f$, $\cos B = (1-1/2\sigma_m R^2)^{\frac{1}{2}}$ (see figure 2.7), and α as calculated from equation 9.2. In addition, the values of k_1 and k_2 calculated from these parameters (equation 2.45) are listed on the right of the table.

table 9.3
theoretical values of parameters used in the theory of Gyftopoulos and Levine

system	σ_f atoms nm^{-2}	R Å	cosB	α 10^{-40} Fm^2	k_1	k_2
Zr - (100)W	10.0	2.99	0.66	6.76	4.03	1.92
Zr - (110)W	7.1	2.99	0.78	6.76	3.37	1.14
U - (100)W	10.0	2.93	0.64	6.03	3.95	1.72
U - (110)W	7.1	2.93	0.77	6.03	3.36	1.02

Comparing tables 9.2 and 9.3 it is clear that for both adsorbates on the (100) surface the values of σ_f derived experimentally are considerably higher than those proposed in the theoretical model. For the (110) surface, however, the agreement is good. In order to explain the high values of σ_f, required to fit the theory to the data of Taylor and Langmuir (Cs on polycrystalline W)[86] and Brattain and Becker (Th on polycrystalline W)[365], Gyftopoulos and Levine proposed a 'fictitious bumpy surface' for polycrystalline tungsten which has a density of surface sites $\sqrt{3}$ times that of (100) tungsten. In the present work the values of σ_f for the polycrystalline substrates are lower than for the (100)s, an observation which is in agreement with Lee (Cs on W)[97], but which disagrees with Smith (Ba on W)[238]. In addition, it should be noted that Lee used the Kelvin technique for both polycrystalline and (100) substrates, whereas Smith used this technique only in the case of the (100); for the polycrystalline substrate the Anderson method was employed. The use of the latter leads to smaller initial slopes

in the work function/coverage curves[125,347] and hence a lower apparent σ_f. The same comment naturally applies to the present (Anderson) work on the zirconium-polycrystalline tungsten system. However, the uranium and caesium work, all of which was carried out using the Kelvin technique, suggests that the 'bumpy surface' may indeed be fictitious.

Lee[97] finds that σ_f determined experimentally is approximately twice that proposed in the models for both (100) and (110) surfaces; Smith[238], however, finds fair agreement. As noted above, good agreement in the present work is obtained only for the (110) surface. Thus it must be concluded that either the models used to determine σ_f, or the Gyftopoulos and Levine approach to the problem is inadequate to explain the experimental results. It should be pointed out, however, that Lea and Mee[125] find good agreement for uranium on both (110) and (100) surfaces, indicating that the values of σ_f are very dependent on the exact experimental procedure.

Other than σ_f, the only parameter required in the theory is the polarizability α. Comparison of tables 9.2 and 9.3 reveals that the experimental values are in fair agreement with those derived from equation 9.2. The adoption of this last equation implies that α is independent of the substrate, an assumption which is not in agreement either with the present results or with others[97,125,238]. This fault is rectified in the Gyftopoulos and Steiner theory discussed below.

9.4 Gyftopoulos and Steiner

The Gyftopoulos and Steiner theory is a recent extension of the Gyftopoulos and Levine theory in which most of the faults of the latter are eliminated.

These have been considered briefly in section 2.2.5 and are elaborated below:

1 Gyftopoulos and Levine propose that electronegativity is an invariant property of an atom whereas Gyftopoulos and Steiner have considered the orbital dependence. The result is that the electronegativity becomes a function of the charge states of the orbitals in question;

2 the magnitude of the dipole barrier in the Gyftopoulos and Levine theory was estimated from empirical relations: Malone and Gordy-Thomas. No dependence on dipole length or adsorbate valence was included. Gyftopoulos and Steiner calculate the dipole explicitly in terms of the charge transfer Fe, dipole length R, and the number of bonding orbitals per adatom z, of the adsorbate-substrate bond. The important parameter F is found by maximizing the bond energy with respect to F. The result is an expression for F in terms of D_o (the pure covalent bond energy), D_1 (energy parameter), and the total work function change $(\phi_m - \phi_f)$. The inclusion of D_1 and $(\phi_m - \phi_f)$ in this expression is a direct result of the dependence of electronegativity on the charge states of the bonding orbitals. Unfortunately D_1 cannot be evaluated since it involves quantities - ionization potentials and electron affinities of particular bonding orbitals - whose values are not known. In the present work D_1 is adjusted to give the best fit to the theory;

3 the Gyftopoulos and Levine shape factor $G(\theta)$ combines the two extreme situations - initial dipole dominated, and final adsorbate electronegativity dominated - in the region $0 < \theta < 1$ in the simplest way consistent with the three boundary conditions. Gyftopoulos and Steiner attempt a more detailed physical description in terms of the covalent adsorbate-adsorbate interaction. Specifically $G(\theta)$ is replaced by $1-M(\theta)$ where M is the Morse function (M is proportional to the covalent

bond energy). In this case only one boundary condition, $\phi(\theta=1) = \phi_f$, is required.

Before the theory can be applied, the following parameters must be evaluated: σ_f, R, cosB, z, D_o. σ_f, R and cosB are the same as in the Gyftopoulos and Levine theory (see table 9.3). As proposed by Gyftopoulos and Steiner, z is taken as half the adsorbate metallic valence[367]. D_o is calculated from equations 2.63 and 2.64, expressions which involve the 'angular strength' S, and the sublimation energy D(f-f) of both adsorbate (f) and substrate (m). These quantities have been tabulated by Levine and Gyftopoulos[102] for both tungsten and zirconium, but not for uranium. Smithells[368] lists sublimation energies for tungsten and zirconium similar to those given by Levine and Gyftopoulos, and in addition includes uranium. These values are used in the present work. The most difficult problem is the assignment of a value to S. The discussion in the appendix of reference 102 indicates that S for uranium is likely to be between 2 and 3 (S for W and for Zr is 2.62). In addition, for the transition elements nearest to uranium in the periodic table (Th, Ta, W, Re) S = 2.62. Furthermore, D_o is not very sensitive to the values of S in the range 2 - 3: for S = 2, D_o = 2.13 eV; for S = 3, D_o = 2.19 eV; for S = 2.62, D_o = 2.21 eV. For these reasons the last value of S is chosen, giving D_o = 2.21 eV.

Finally, the values of all the parameters discussed above are collected in table 9.4.

The computer program reproduced in appendix 4 was used to calculate Σd^2, the sums of the squares of the deviations between theory and experiment for 21 points at 0.05 monolayer intervals. For a range of values of the monolayer position and of D_1, the program minimizes Σd^2 with respect to the

table 9.4

values of parameters in Gyftopoulos and Steiner theory

system	σ_f† atoms nm^{-2}	R† (Å)	cosB†	z	D_o(eV)
Zr-(100)W	10.0	2.99	0.66	2	3.71
Zr-(110)W	7.1	2.99	0.78	2	3.71
U -(100)W	10.0	2.93	0.64	3	2.21
U -(110)W	7.1	2.93	0.77	3	2.21

† values as in Gyftopoulos and Levine theory (see table 9.3)

polarizability α. In this way the values of monolayer point and D_1 giving the best fit could be ascertained.

As discussed in sections 2.1.2.2 and 2.2.5, the theory may be derived from consideration of either of two extreme cases: zero overlap (S=0) and complete overlap (S=1) in the adsorbate-substrate bond. In general, the use of the latter results in better agreement between theory and experiment because of the less restrictive resulting expression for the charge transfer F (equations 2.68, 2.69). For zirconium and uranium on the (100) surface the theory was fitted for both cases (S=0 and S=1).

Gyftopoulos and Steiner point out that the value of ad_o in the Morse function (equation 2.66) lies in the range 2.29 - 3.65, and they suggest the use of an average value, 2.97, for all systems. In the present work ad_o was adjusted to give the best fit.

Table 9.5 shows the best-fit parameters for each system. For zirconium on (100) tungsten the theory was first fitted for the case of zero overlap (S=0) and ad_o = 2.97 (1st row of table 9.5). The deviations are shown in figure 9.11. Although the agreement is improved by adjusting ad_o to an

optimum value of 2.22 (2nd row of table 9.5), this is outside the physically realistic range of ad_o given by Gyftopoulos and Steiner. However, a similar procedure for the case of complete overlap (S=1) produces a more reasonable value of ad_o (2.52) as well as an improved fit (3rd row in table 9.5, figure 9.12). Figure 9.13 shows the deviations for zirconium on (110) tungsten for the S=1 case using this same value of ad_o.

table 9.5
parameters from least squares fit of data to the theory of Gyftopoulos and Steiner

system	overlap S	ad_o ††	D_1(eV)	α (10^{-40} Fm^2)	mono-layer point	approx. final coverage	Σd^2	figure
Zr-(100)W	S=0	2.97	-1.18	16.5	21.35	23	0.00170	9.11
	S=0	2.22	-1.39	16.6	23.65	23	0.00046	-
	S=1	2.52	-4.67	14.9	23.35	23	0.00037	9.12
Zr-(110)W	S=1	2.52	-3.14	14.8	19.05	15	0.00853	9.13
Zr-poly W†	S=1	2.52	-2.64	10.2	17.20	16	0.00030	-
U -(100)W	S=0	2.97	-0.48	27.7	24.20	28	0.00293	-
	S=0	1.78	-1.03	32.1	28.35	28	0.00103	-
	S=1	2.73	-2.65	28.1	27.35	28	0.00038	9.14
U -(110)W	S=1	2.73	3.73	9.9	18.75	18	0.00552	9.15
U -poly W†	S=1	2.73	0.62	10.9	22.30	22	0.00090	-

† polycrystalline surface assumed to be (100) oriented
†† parameters underlined held constant

The results from fitting to the uranium data are also given in table 9.5; they are very similar to those for zirconium. The deviations for the (100) and (110) surfaces are shown in figures 9.14 and 9.15 for the S=1 case.

Unlike the Gyftopoulos and Levine fitting constants k_1 and k_2 (see figure

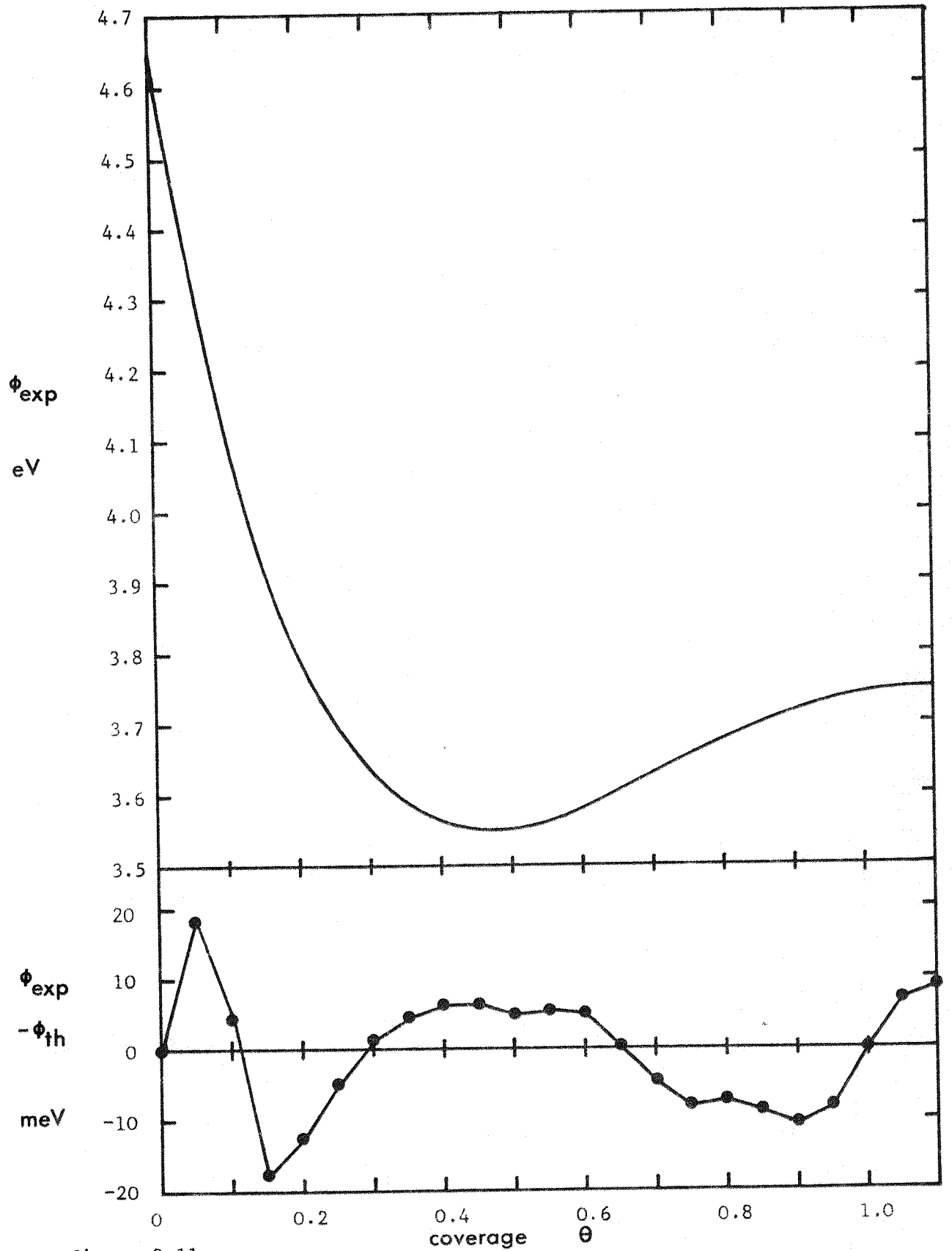

figure 9.11

zirconium on (100) tungsten data fitted to the theory of Gyftopoulos and Steiner; parameters as given in table 9.5 - zero overlap(S=0), ad_o=2.97

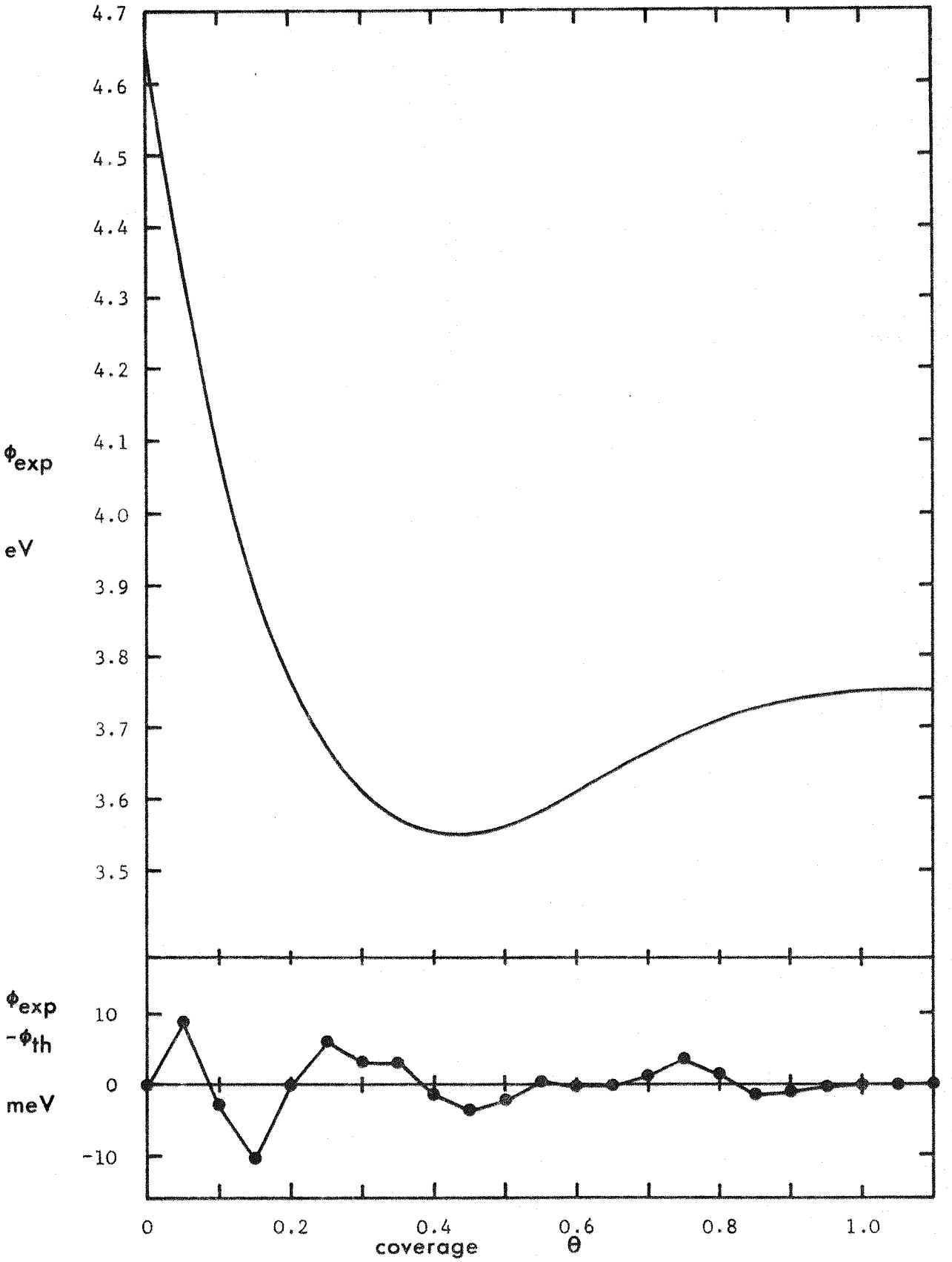

figure 9.12

zirconium on (100) tungsten data fitted to the theory of Gyftopoulos and Steiner; parameters as given in table 9.5 - complete overlap(S=1), ad_o=2.52

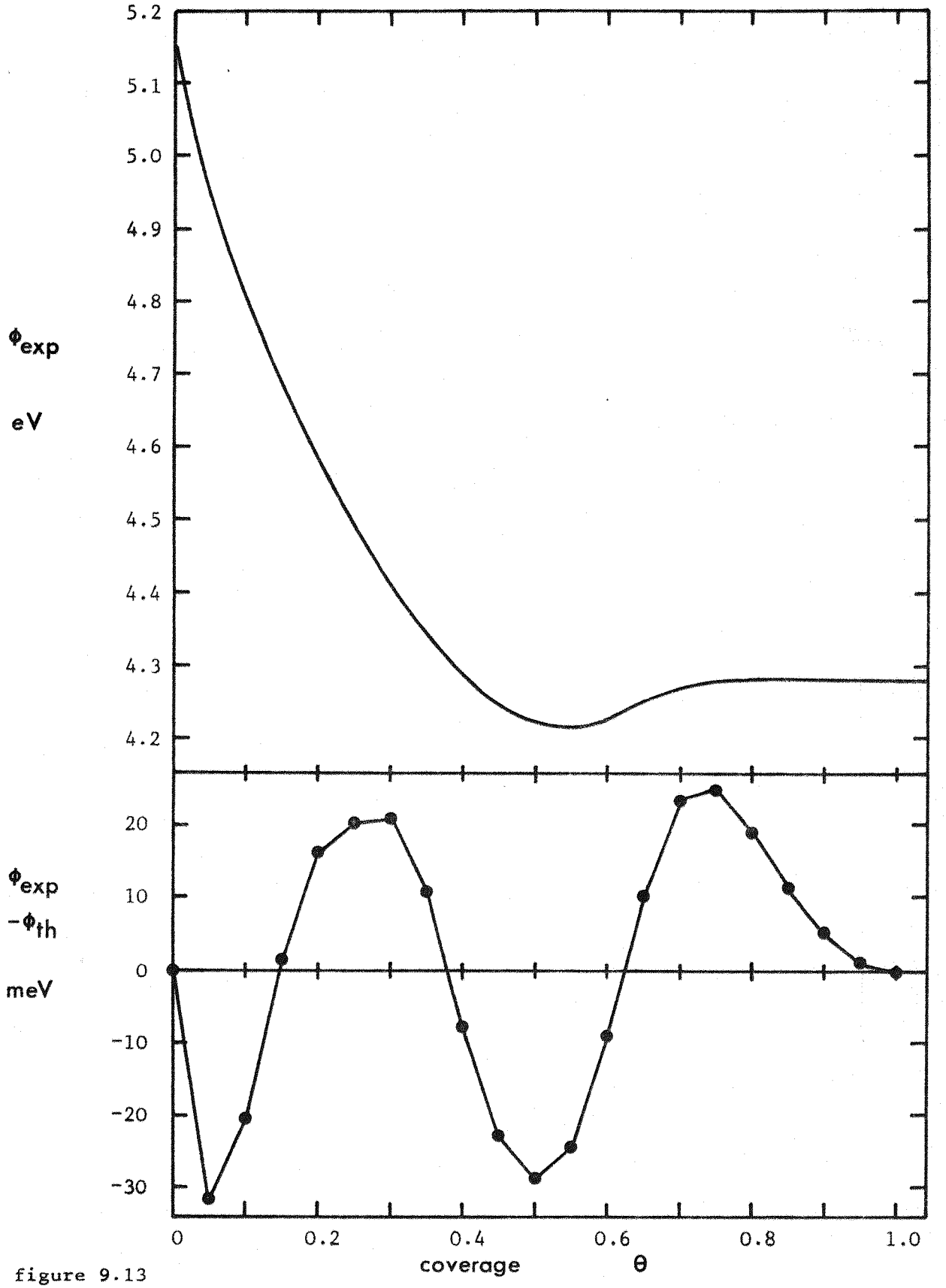

figure 9.13

zirconium on (110) tungsten data fitted to the theory of Gyftopoulos and Steiner; parameters as given in table 9.5 - complete overlap(S=1), ad_o=2.52

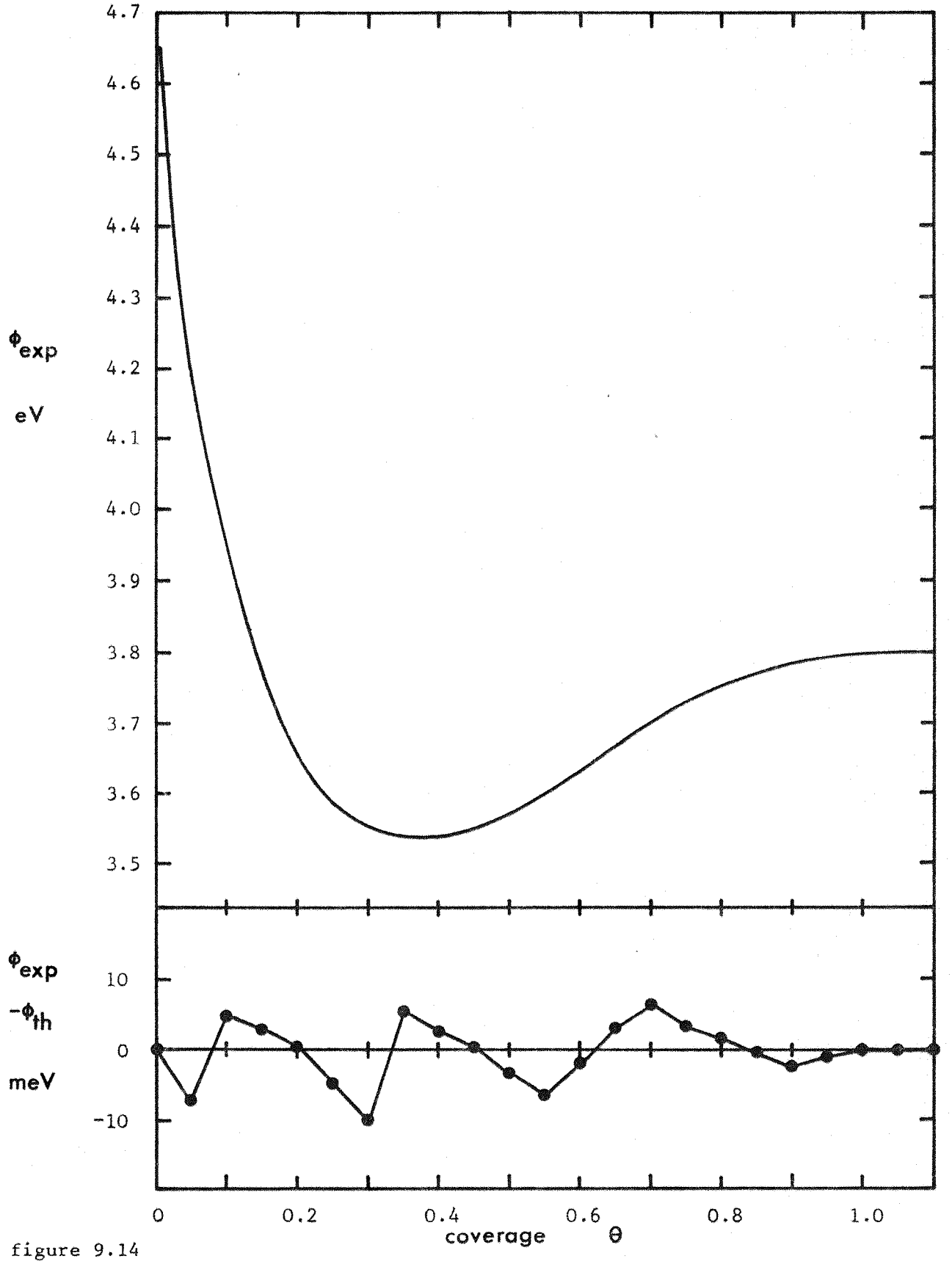

figure 9.14

uranium on (100) tungsten data fitted to the theory of Gyftopoulos and Steiner; parameters as given in table 9.5 - zero overlap(S=0), ad_o=2.73

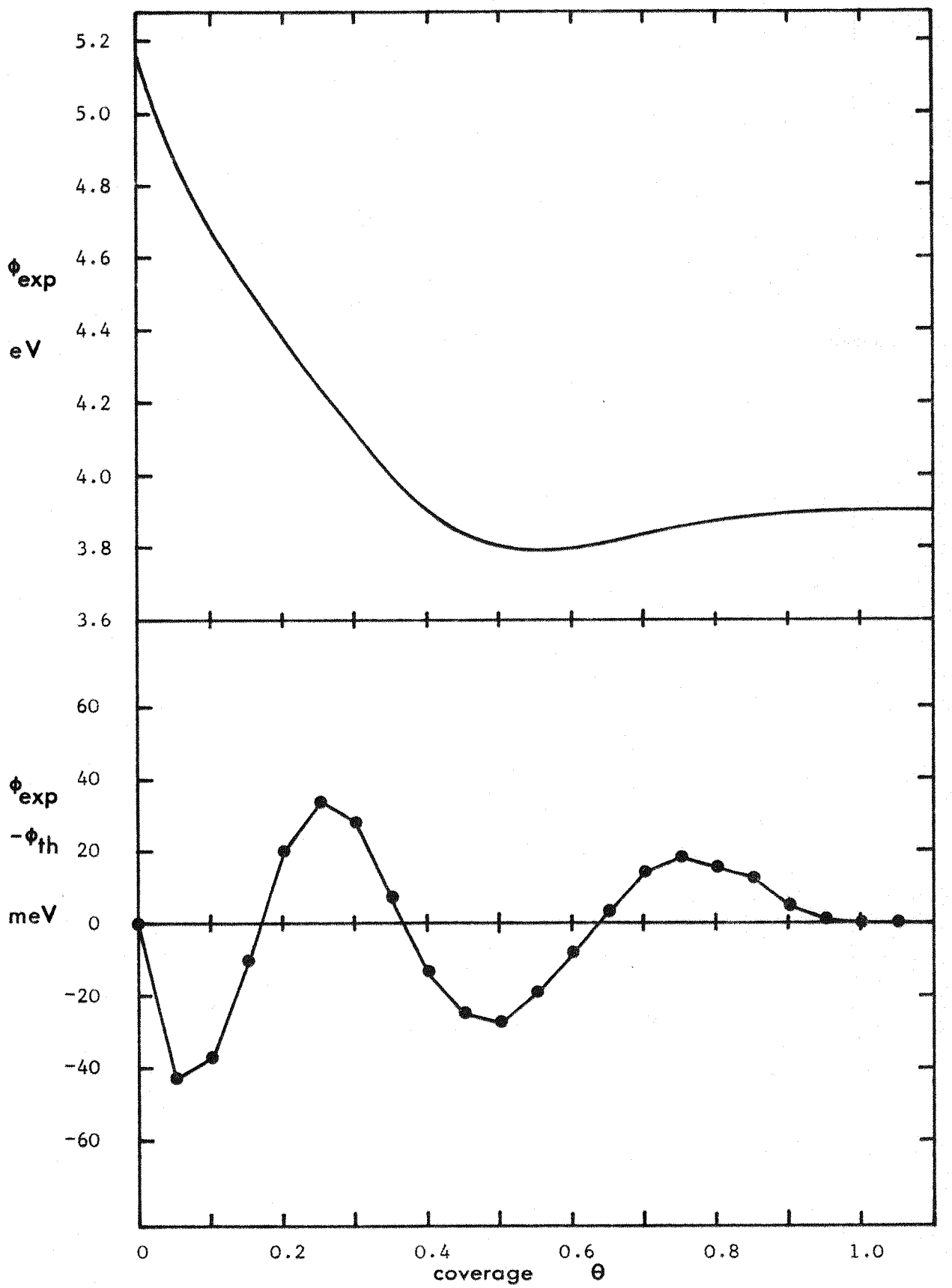

figure 9.15

uranium on (110) tungsten data fitted to the theory of Gyftopoulos and Steiner; parameters as given in table 9.5 - complete overlap(S=1), ad_o=2.73

9.8), α is insensitive to the position of the monolayer point. In figure 9.16, Σd^2 and α are plotted against monolayer position for zirconium on (100) tungsten, demonstrating that α is indeed well defined. Figure 9.17 shows how the best fit monolayer point, α, and Σd^2 vary with the value of D_1. Again the best fit, and hence α, is well defined. Finally, in order to demonstrate that for S=1 the optimum value of ad_o lies within the range 2.92 - 3.16, Σd^2 is plotted in figure 9.18 against ad_o for a fixed value of D_1 and monolayer position.

The above discussion indicates that in spite of the more detailed physical model on which the theory is based, it describes the experimental data at least as well as does the Gyftopoulos and Levine theory. However, in order to ascertain the validity of the model it is necessary to compare the parameters which emerge with those expected from the physical situation. It has already been pointed out that ad_o lies within the expected range. The other parameters which determine the accuracy of the fit are D_1 and α. Neither of these quantities have been experimentally determined. Gyftopoulos and Steiner suggest that α should be equal to the electronic polarizability of the adsorbate as proposed by Gyftopoulos and Levine (equation 9.2), plus the electronic polarizability of the substrate calculated in an analogous manner,

ie $\alpha = \alpha_f + \alpha_m$ 9.3

where $\alpha_i = 4\pi\varepsilon_o n r_i^3$ for i = f or m.

Equation 9.3 gives $\alpha = 12.4 \times 10^{-40}$ Fm^2 for the Zr-W system

and $\alpha = 11.6 \times 10^{-40}$ Fm^2 for the U-W system

From table 9.5 it can be seen that these values are in fair agreement in all cases except that of uranium on (100) tungsten where the experimental value

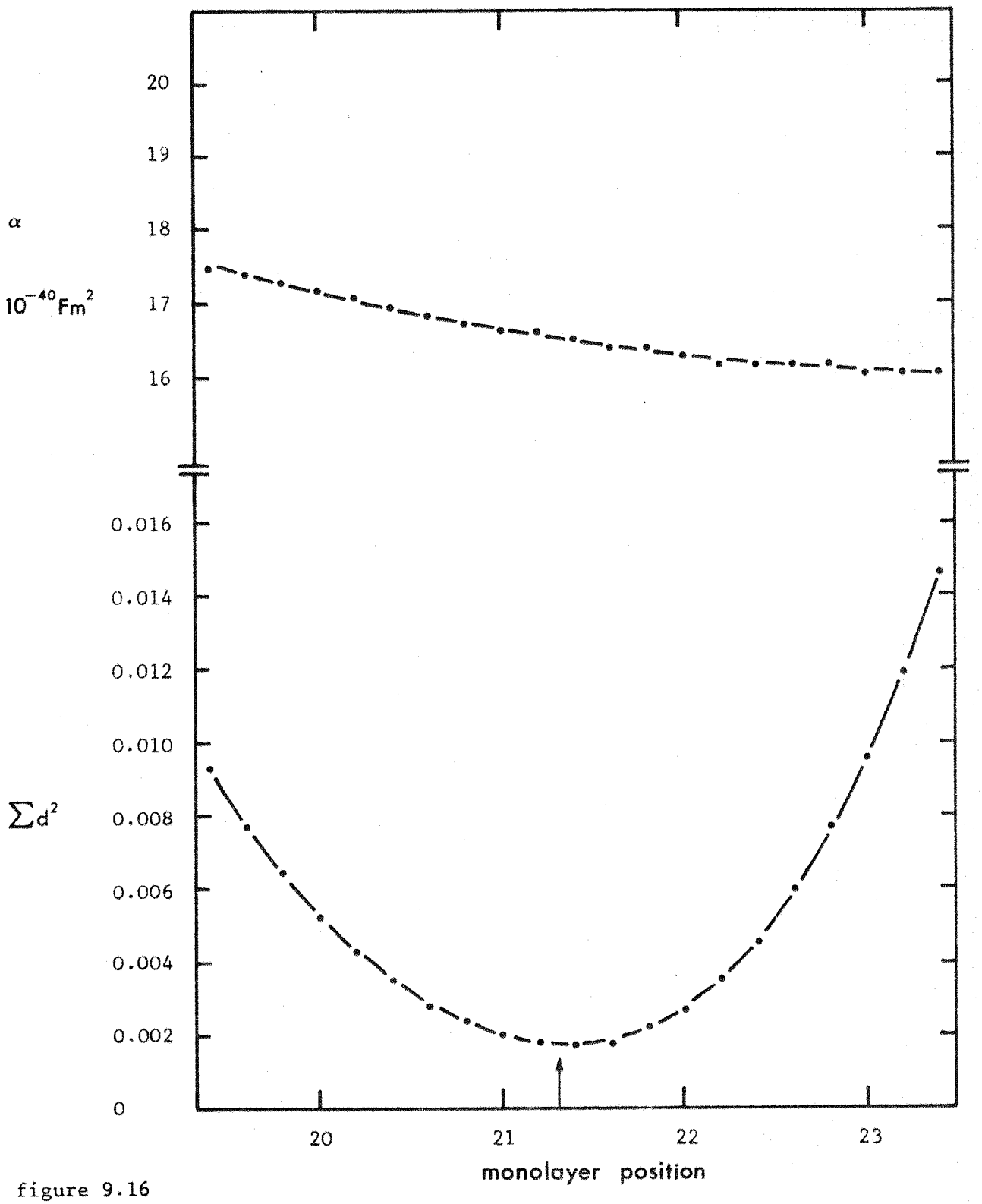

figure 9.16
values of Σd^2 and α from the best fit of the Gyftopoulos and Steiner theory, for constant D_1 for a range of monolayer positions (S=0 case)

zirconium on (100) tungsten

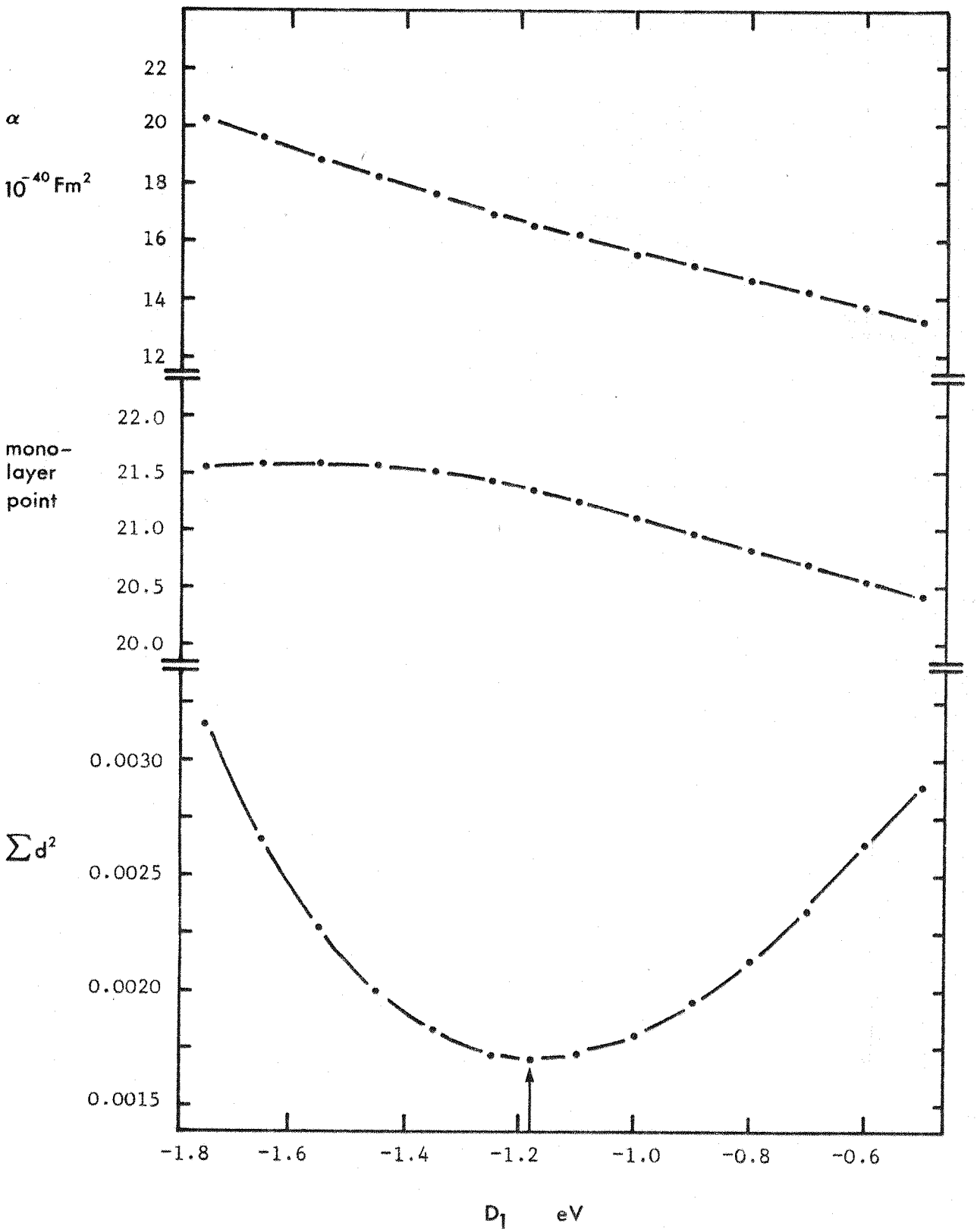

figure 9.17

values of Gyftopoulos and Steiner best fit polarizability α, monolayer point, and Σd^2 as a function of D_1 (S=0 case)

zirconium on (100) tungsten

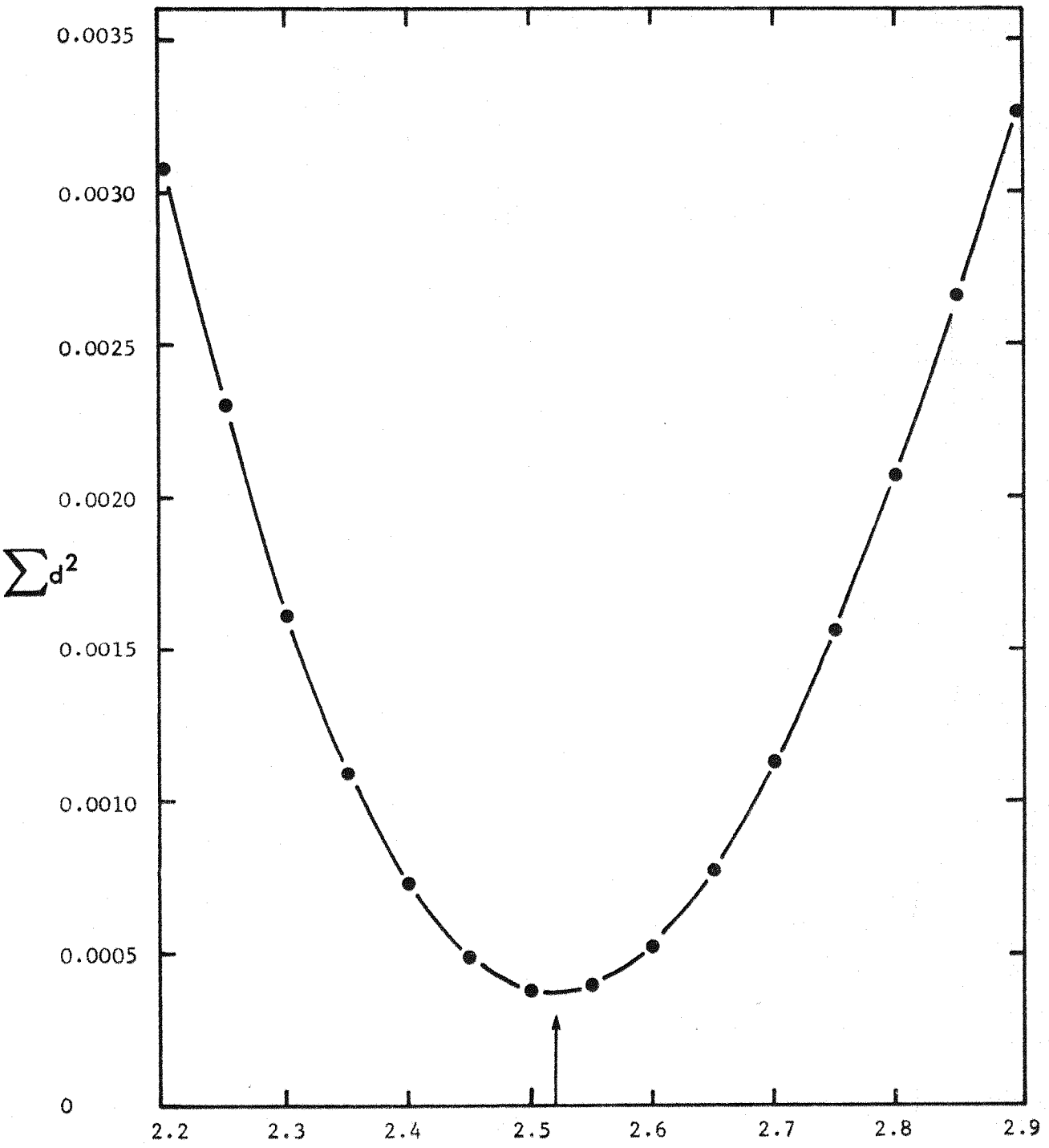

figure 9.18

Gyftopoulos and Steiner theory for the S=1 case: sums of the squares of the deviations between theory and experiment Σd^2, as a function of ad_o (Morse potential) for constant D_1 and monolayer point

zirconium on (100) tungsten

is considerably too large. At first sight this appears to be contrary to the results of the Gyftopoulos and Levine theory where the experimental polarizability was too small (see tables 9.2 and 9.3). However, examination of equations 2.45 shows that the Gyftopoulos and Levine fitting constants k_1 and k_2 are related in such a way that discrepancies in α may be manifest as discrepancies in σ_f. In fact, for uranium on (100) tungsten, σ_f was considerably larger than expected. Since (equation 2.45) $k_2 = 9\alpha\sigma_f^{3/2}/4\pi\varepsilon_o$, a large value of σ_f can be alternatively interpreted as a large value of α.

The second parameter D_1 cannot be evaluated theoretically without a detailed knowledge of the energy band structure of both the adsorbate and substrate materials. Gyftopoulos and Steiner state that such calculations indicate D_1 is dependent only on the adsorbate and substrate materials and is independent of substrate orientation. The present results, however, show a marked variation of D_1 with orientation, especially in the case of uranium. It should be noted that because of the different way in which the covalent bond energy is defined for the S=0 and S=1 cases (see section 2.1.2.2), the corresponding values of D_1 cannot be equated. For the same reason, Gyftopoulos and Steiner's empirical method of estimating D_1 (ie putting $k = 1$, $I_m - A_m = c\phi_m$, $I_f - A_f = c\phi_f$, and $c = 1.3$, in equation 2.62) cannot be applied to the S=1 case.

If it is assumed that D_1 is independent of substrate orientation then the value derived from the best fit to the (100) data should be applicable to the (110) case. However, the predicted coverage curve using the (100) value of D_1 has a work function considerably below the experimental work function in the region of the minimum. Thus it appears that it is possible to fit the theory accurately to the data only if no restriction is placed on D_1.

Since at present D_1 cannot be independently evaluated there is no way of determining the extent of the agreement between theory and experiment.

The fact that through adjusting D_1 the theory can adequately describe even the anomalous (see section 8.4.1) zirconium on (110) case illustrates that as long as D_1 cannot be evaluated, the theory is not specific enough to allow its use to predict work function/coverage data. Thus, although Gyftopoulos and Steiner have improved on the theory of Gyftopoulos and Levine in that the physical model is more detailed, this advantage is lost because of the introduction of the extra undetermined parameter D_1. For comparison, the quantities which must be evaluated for the two theories are given below, where the depolarization parameters R, α, σ_f (which are required for both theories) are omitted.

theory	parameters required			
Gyftopoulos and Levine	$\sigma_f \cos B$	ϕ_f		
Gyftopoulos and Steiner	$zR\sigma_f \cos B$	ϕ_f	D_o	D_1

Clearly in the Gyftopoulos and Steiner case, even assuming D_o is accurately known, D_1 still remains to be determined.

A final point concerning the Gyftopoulos and Steiner theory is that for the highly ionic caesium on tungsten system the predicted initial slope in the work function/coverage curve is not as great as that measured experimentally[97], even for a charge transfer of unity (F=1). Since

$$\left.\frac{d\phi}{d\theta}\right|_{\theta=0} = -\frac{FezR\cos B\sigma_f}{2\varepsilon_o(1+\alpha/4\pi\varepsilon_o R^3)} \qquad 9.4$$

this implies that either σ_f is underestimated or that the Helmholtz formula (equation 2.10) on which equation 9.4 is based is not applicable to this case. In order to obtain the agreement shown in figure 2.8, σ_f was increased from the proposed value of 3.54 atoms nm^{-2} to 5.43 atoms nm^{-2}. It is interesting that the use of zero overlap (S=0) effectively confines F to less than unity (see equation 2.68), whereas for S=1 the best fit value of D_1 can give rise to the physically impossible situation F>1 (see equation 2.69). Thus it is important, when using the latter case, to ensure that the best fit corresponds to a physically real situation. In this context it is worth noting Gadzuk's remark[369]: 'One must be careful not to fall into the trap of believing that reproduction of numbers in agreement with experiment constitutes understanding'. The present work illustrates that this situation can easily arise. However, it has been emphasized throughout this chapter that 'fitting parameters' must be compared with those expected from the physical model on which the theory is based.

SUMMARY AND CONCLUSIONS

As discussed in section 2.2.6, the classical ion-image model of adsorption is only applicable in the limiting case of a perfect conductor. For a real metal, screening is not complete, and as a result volume polarization effects must be taken into account. This has the effect of increasing the apparent dipole length by an amount dependent on the substrate electron density. According to Gadzuk's calculations[370], for caesium on tungsten the effective increase in the ionic radius is ~ 0.7 Å, giving an ion imaging-plane distance of ~ 2 Å. It is important to realize that the use of the Helmholtz formula (equation 2.10) with the factor 2 in the denominator implies that the metal completely screens half the dipole field. The total dipole length

is taken by Rasor and Warner as the ion-image distance and by Gyftopoulos and Steiner as the component of R ($R = r_m + r_f$) normal to the surface, RcosB. Consequently the half dipole length is different in the two cases. It should also be noted that both Rasor and Warner, and Gyftopoulos and Levine suggest that only the adsorbate particle is polarized, whereas Gyftopoulos and Steiner include in the polarizable entity the substrate surface atom. Even in this last case it is implied that polarization does not affect the substrate below the outermost atomic layer.

It is apparent from the discussion in this chapter that, as yet, no theory is capable of accurately predicting work function/coverage curves. The theories described have been dictated by technological requirements for forecasting electron emission for bimetallic systems. As such, the Gyftopoulos and Levine, and Gyftopoulos and Steiner theories are not as useful as was hoped since the assumption that the final work function is equal to that of the bulk adsorbate has been shown to be false. The Rasor and Warner theory makes no assumptions about the final work function, but at the expense of good agreement in the high coverage region. From the physical viewpoint the Gyftopoulos and Steiner theory is probably the most advanced but, as discussed above, is limited by the lack of knowledge of the energy parameter D_1.

It is clear that a truly rigorous assessment of adsorption theories requires a precise knowledge of the geometrical arrangement at the surface, in particular the surface density, as well as information about the nature and magnitude of polarization. In addition, since work function is so sensitive to contamination it is essential to be able to monitor the exact composition of the surface. Several techniques are becoming available

which enable these quantities to be measured. LEED[375,377] and RHEED[376] can be used to determine structure. LEED combined with Auger spectroscopy has proved to be a powerful tool for investigating structure, density and composition[319,371,372]. Recently, ellipsometry combined with LEED has been demonstrated as a sensitive method of determining both surface density and structure[373]. Future work function studies must be combined with techniques of this kind if the measurements are to be interpreted unambiguously.

Finally, preliminary measurements on the zirconium on (100) tungsten system, using a combined LEED/RHEED technique[374], indicate that, as proposed in this thesis, the monolayer film is pseudomorphic.

APPENDIX 1 GYFTOPOULOS AND STEINER THEORY FOR ELECTRONEGATIVE ADSORBATES

In section 2.2.5 it was pointed out that the Gyftopoulos and Steiner theory can be applied to systems other than bimetallic. This is a consequence of defining the work function of a surface as the neutral electronegativity since this overcomes the problem of assigning a value to the final (monolayer) point. This is taken as the perturbed neutral electronegativity of the substrate surface where the perturbation arises from the interaction of substrate and adsorbate valence orbitals. Steiner[103] has employed the theory for both electronegative adsorbates and for combinations of electronegative and metallic adsorbates.

The work function of the bimetallic system is given by equation 2.65:

$$\phi = \phi_m - (\phi_m - \phi_f)M + bF$$

For electronegative adsorbates the interaction between adsorbed atoms (Morse function, M) is negligible because, even at high coverages, the average distance between adatoms is much larger than the equilibrium distance characteristic of the electronegative species in chemical combination. For example, the equilibrium distance between oxygen atoms in molecular oxygen is 1.2 Å[101] whereas the average distance between oxygen atoms at one monolayer coverage on (100) tungsten (assuming $\phi_f/\phi_m = 1$) is 3.16 Å. For this reason M is taken as zero and equation 2.65 becomes:

$$\phi = \phi_m + bF \qquad \text{A1.1}$$

where b is given by equation 2.67:

$$b = - \frac{ezR \cos B \, \sigma_f \theta}{2\varepsilon_o \left(1 + \frac{\alpha}{4\pi\varepsilon_o R^3}\right)\left(1 + \frac{9\alpha\sigma_f{}^{3/2}\theta^{3/2}}{4\pi\varepsilon_o}\right)} \qquad \text{A1.2}$$

(ie mobile case: H = 1.5) and where z, the number of bonding orbitals per adatom, is taken as the adsorbate valency. F is given by equations 2.68 and 2.69 with M = 0 and with the adsorbate work function ϕ_f replaced by the neutral orbital electronegativity $(I_f + A_f)/2$:

$$F = \frac{\phi_m - (I_f + A_f)/2}{D_{o/e}(1-f^2)^{-\frac{1}{2}} + D_{1/e}} \qquad \text{A1.3}$$

for zero overlap, and

$$F = \frac{\phi_m - (I_f + A_f)/2}{2D_{o/e} + D_{1/e}} \qquad \text{A1.4}$$

for complete overlap. Here D_o is given by[335]:

$$D_o = \tfrac{1}{2}\{D(m - m)/6 + D(f - f)\} \qquad \text{A1.5}$$

where D(m - m) is the heat of sublimation of the substrate and D(f - f) is the single bond energy of the electronegative gas molecule. D_1 is given by equation 2.62:

$$D_1 = I_m - A_m + I_f - A_f - ke/R \qquad \text{A1.6}$$

An approximate estimate of D_1 can be made by putting[103]:

$$k = 1, \qquad I_m - A_m = c_1\phi_m \quad \text{and} \quad c_1 = 1.3 \; . \qquad \text{A1.7}$$

cosB in equation A1.2 is evaluated from the geometry of the surface as for the bimetallic system. However, for adsorbates of small size on planes of low surface density (eg oxygen on (100) tungsten) the exact geometry is not obvious. In these cases cosB is estimated by assuming that the electronegative adsorbate rests on a hypothetical plane which is tangent to the sub-surface atoms of the substrate as shown in figure A1.1.

The results from this theory for oxygen and the halogens adsorbed on (100) tungsten are shown in figure A1.2 where the parameters used (table A1.1) are those given by Steiner and where equation A1.3 has been used to calculate F.

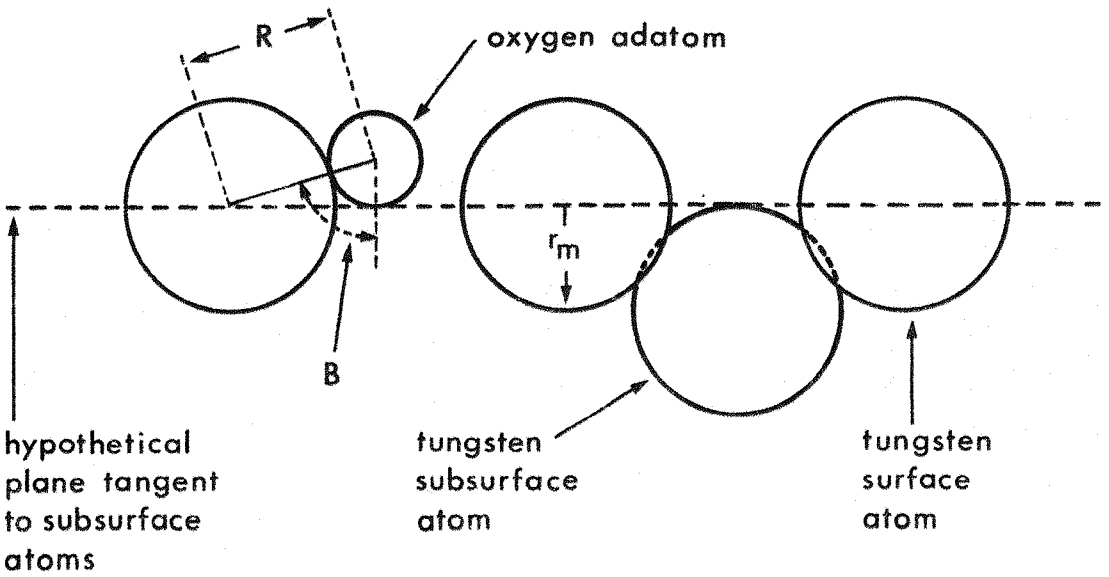

$R = r_m + r_f$

figure A1.1
diagram showing hypothetical geometric arrangement of an oxygen adatom on the (100) plane of tungsten

table A1.1

parameters used in figure A1.2

Gyftopoulos and Steiner for electronegative adsorbates

adsorbate	z	r_f[336] Å	cosB	α_f (Å^3)	$(I_f+A_f)/2$[337] (eV)	I_f-A_f[337] (eV)	D(f-f)[338] (eV)	σ_f (Å^{-2})	D_o (eV)	D_1 (eV)
oxygen	2	0.6	0.19	0.216	9.65	15.27	1.52	0.1	1.48	6.53
fluorine	1	0.5	0.146	0.125	12.18	17.36	1.56	0.1	1.50	7.83
chlorine	1	1.00	0.31	1.00	9.38	11.30	2.48	0.1	1.96	5.04
bromine	1	1.15	0.45	1.52	8.40	9.40	1.97	0.1	1.70	3.88
iodine	1	1.40	0.58	2.74	8.10	9.15	1.54	0.1	1.49	4.73

$R = r_m + r_f$ $\qquad$ r_m = 1.35 Å for tungsten[336]

$\alpha = \alpha_m + \alpha_f$ $\qquad$ α_m = 4.06 Å^3 for tungsten[65]

ϕ_m = 4.60 eV for (100) tungsten[220]

The work function increases resulting from halogen adsorption decrease in the order $I_2 > Br_2 > Cl_2 > F_2$. This is because the atomic radii and hence RcosB decrease in this order and override the effect of the increase in F due to the increasing electronegativity difference $\phi_m - (I_f + A_f)/2$. This result is not in agreement with experiment (appendix 2) since the work function increases decrease in the order $Cl_2 > Br_2 > I_2$. Clearly a greater dependence on the electronegativity difference is required. This would occur if the substrate electronegativity ϕ_m was very much larger; the results obtained using ϕ_m = 8.30 eV (see appendix 2),but all else unchanged, are shown in figure A1.3. The order in which the work functions change is

then in agreement with experiment. Quantitative agreement would not be expected in view of the arbitrary way in which D_1, cosB, and ϕ_f are estimated.

It must be concluded from these results that neutral electronegativity and work function cannot be equated. This would not be evident in the bimetallic system since electronegativity does not appear explicitly in the theory. An estimate of the electronegativity of a surface could be made by choosing the value which gives the best agreement with experiment.

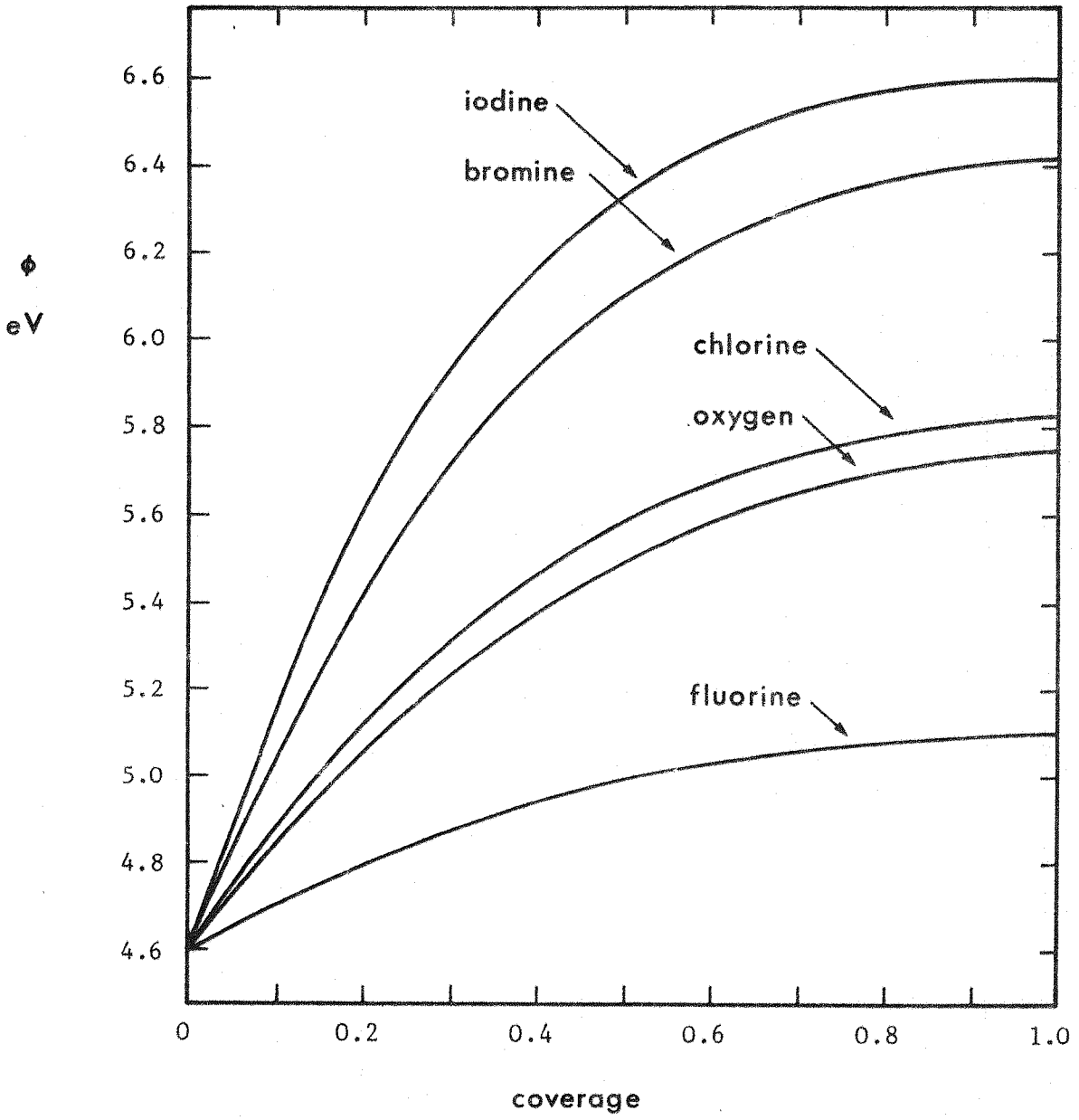

figure A1.2

work function ϕ/coverage for electronegative adsorbates on (100) tungsten

Gyftopoulos and Steiner theory

absolute electronegativity of substrate equal to the work function, 4.60 eV

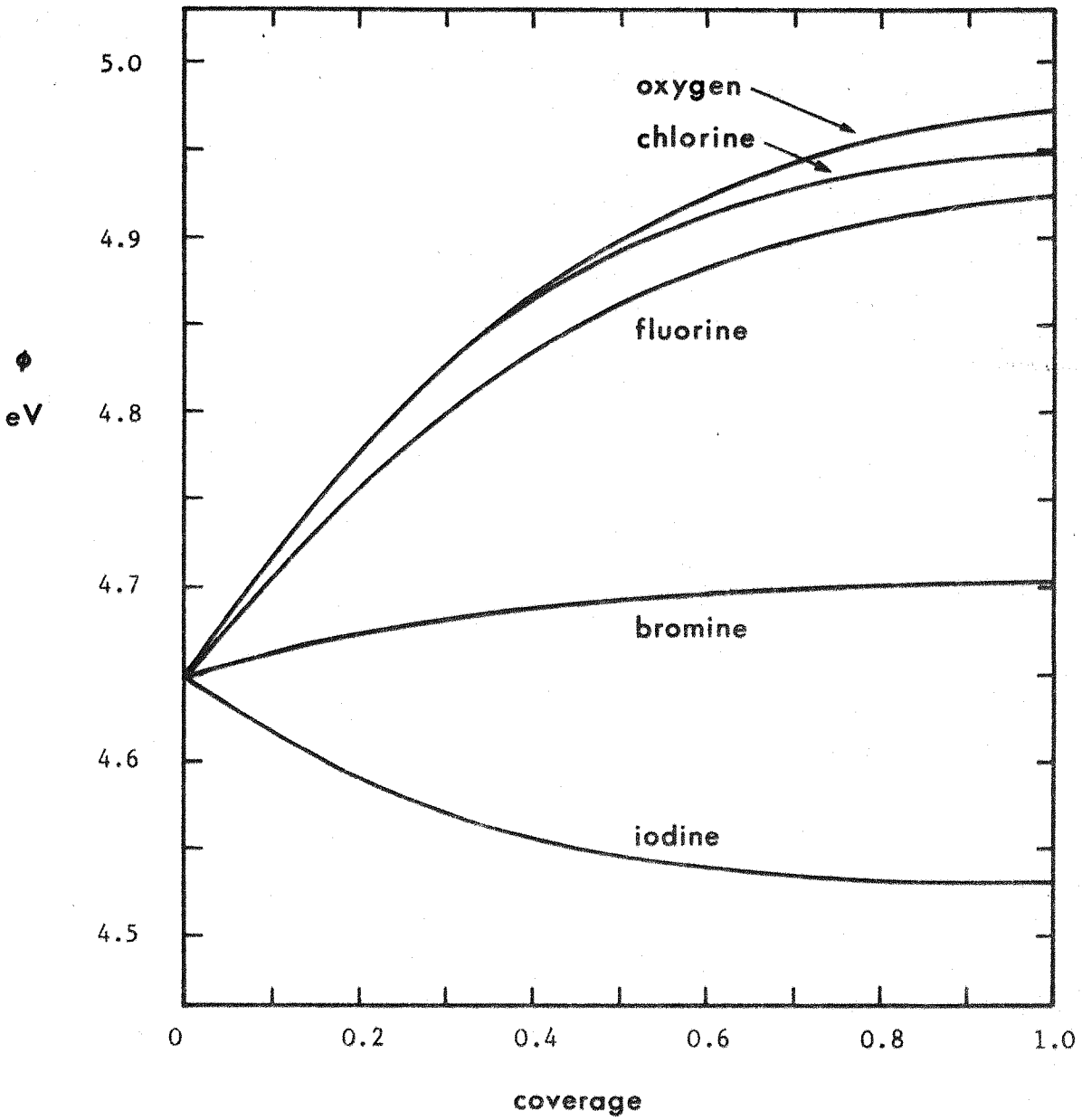

figure A1.3

work function ϕ/coverage for electronegative adsorbates on (100) tungsten

Gyftopoulos and Steiner theory

absolute electronegativity of substrate = 8.30 eV

APPENDIX 2 A CORRELATION BETWEEN SURFACE POTENTIAL AND ELECTRONEGATIVITY

A2.1 introduction

Explanations of the surface potentials (SP) due to adsorbed atoms on metal surfaces in terms of the electronegativity difference between the adsorbate and adsorbent are not new[339,340]. In the past, however, they have been applied to ill-defined metal surfaces generally prepared by vapour deposition techniques. In recent years it has become increasingly clear that the SP of a particular species is, to a remarkable extent, dependent on the crystallographic orientation of the adsorbent surface. Several instances are now known[218,225,234,341] in which there is a complete reversal of dipole for the same adsorbate between differing faces of the same crystal. The dependence of the electronegativity of the substrate on its orientation has recently been discussed by Steiner and Gyftopoulos[18] and Fehrs and Stickney[342]. The purpose of this appendix is to present a simple discussion of SP in the light of recent developments in both the reliability of SP data and in the understanding of the electronegativity of metal surfaces. The discussion has been restricted to tungsten substrates since in this case clean single crystal surfaces can be achieved with the greatest reliability. For this same reason most SP data on single crystals relate to tungsten. A number of gross assumptions are made in the present correlation, particularly regarding the selection of appropriate SPs from complex work function versus coverage curves and in allotting radii to the adsorbates. In view of the remarkably simple relationship that emerges, it appears that these may be justified.

Wherever available, SPs measured by the Kelvin technique have been utilized

since, for the reasons discussed in chapter 3, these are considered to be the most reliable. Four tungsten substrates, (110), (211), (100) and (111), and nine adsorbates, caesium, barium, uranium, zirconium, iodine, bromine, chlorine, oxygen and water vapour are included in this correlation. These cover the range from the least electronegative adsorbate, caesium, to the most electronegative, OH^-, that can be handled conveniently.

A2.2 previous correlations

Previous correlations by Broeder et al[339] and by Mignolet[340] assumed that the absolute electronegativity of the substrate was equal to the work function. This was based on an empirical relation between experimentally observed SPs of gases on various polycrystalline metallic adsorbates and the electronegativity difference $\Delta\chi$. Broeder et al used the Helmholtz equation for the dipole moment, M, in terms of the potential change v:

$$v = SP = \frac{\sigma_f M}{\varepsilon_o} \qquad A2.1$$

where σ_f is the adsorbate density. The dipole moment and electronegativity difference were related via Malone's[54] empirical equation:

$$M = \Delta\chi_p \qquad A2.2$$

where χ_p is in Pauling units and M is in Debye. As discussed in section 1.3.3, equation A2.2 has little experimental foundation and clearly does not take account of the dipole length. Adopting the absolute electronegativity ($\chi_a = 3.15\ \chi_p$, section 1.3.2) of the substrate as equal to the work function ϕ:

$$M = \frac{1}{3.15}(\phi - \chi_f) \qquad A2.3$$

where χ_f is the absolute electronegativity of the adsorbate. Hence, combining equations A2.1 and A2.3:

$$SP = 1.2 \times 10^{-19} \sigma_f(\phi - \chi_f) \qquad A2.4$$

Measurement of σ_f is difficult and to a first approximation had to be taken as equal to the substrate surface density. This expression shows little quantitative agreement with experiment, and in the case of adsorbates of intermediate χ_f often gave the wrong sign. Agreement for hydrogen on polycrystalline nickel and tantalum and for nitrogen on polycrystalline tantalum could be obtained if the expression was multiplied by the arbitrary reduction factors 0.03, 0.09 and 0.08 respectively.

A2.3 the present model

The formulation of a model that will predict, in quantitative terms, the sign and approximate magnitude of the SP of any adsorbed species is not easy. Many of the difficulties are clear from the brief discussion of the model of Broeder et al. The major problems are: (1) the charge state of the adsorbate; (2) the surface density of the adsorbate; (3) the geometry of the system (ie what is the dipole length?); (4) the electronegativity of differing single crystal faces of the substrate material. These four factors are clearly interrelated.

To make any progress, drastic assumptions have to be made since, in general, all of the above are unknown. In formulating this correlation it is assumed: (a) that caesium, barium, uranium and zirconium exist on tungsten surfaces as singly charged positive ions, and that iodine, bromine, chlorine, oxygen and water exist as singly charged negative ions. The appropriate radii are then taken from published data[315,343]; (b) in selecting the appropriate SP data the maximum excursion of the work function from its clean value during exposure has been adopted (see below). The adsorbate densities appropriate

to these points are then required. In all cases, with the possible exception of caesium (see section 8.4.2), these are unknown and it would be possible only to speculate. In view of this it is assumed that the adsorbate densities are constant and independent of both adsorbate and adsorbent; (c) there has been much speculation about the penetration of various adsorbates below the surface of the adsorbent. The evidence for this is usually from SPs[344-346] in which the observed dipole has the wrong or unexpected sign. There are several such examples in the present analysis: both bromine and chlorine give the 'expected' work function increases on the (111) and (100) planes, but on the (110) give reductions. Iodine, however, gives a work function decrease on all three planes[341]. It seems unlikely that penetration into the bulk is a feasible explanation for the halogens since (a) the ions or even atoms are usually too big, and (b) penetration should be most effective on the open (111) plane whereas the SP shows it to take place on the (110). Thus, in none of the systems contained in this correlation is bulk penetration by the adsorbate considered. As indicated below, however, this may be possible with hydrogen and nitrogen. There will, of course, be the kind of slight penetration of the adsorbate into the 'billiard ball' model surface 'holes' more evident on the (111) and (211) than the (110) and (100) planes. To take this into account in the estimation of dipole length presumes a detailed knowledge of the surface structure which is at present unknown. In this correlation it is simply assumed that the adsorbent completely screens half the ion-image dipole so that the dipole length is just the adsorbate ionic radius, r_i.

The physical basis of the model is therefore that atomic adsorption takes place until, at a constant coverage independent of the adsorbent or adsorbate, a maximum SP is observed. This is due to a uniform array of

dipoles whose length is determined solely by the singly charged ionic radius, positive ions for metals, negative ions for non-metals. The dipole moment, and hence the magnitude of the SP, is determined by the charge transfer in the adsorbent-adsorbate bond. This will be the sum of at least two major contributions: (a) the polarization of the adsorbed entity in the field of the metal - rather like physical adsorption of the inert gases. This will give rise to a dipole positive outwards and hence a work function reduction. The magnitude of this component will depend critically (as r^3) on the radius of the adsorbed entity; (b) the charge transfer due to the electronegativity difference between the adsorbate and adsorbent. There will, of course, be contributions due to depolarization and other effects. Contribution (a) will clearly apply to any adsorbed species but will be particularly effective for the larger ions, I^-, Br^- and Cl^-. It is because of this contribution and the small electronegativity difference that, for the halogens, it is possible to have externally adsorbed negative ions giving rise to a work function decrease. However quantitative estimates for (a) are not at present possible. In the following discussion the only contribution to the dipole considered is that due to (b).

A2.4 discussion of the data

In general, work function versus coverage curves are not simply monotonic but may contain maxima, minima or plateaux. On single crystal surfaces these may represent different rates of adsorption, depolarization and other effects. For the present purposes the information required from the experimental curve is the maximum surface potential change due to a single state of atomic adsorption. Usually the only evidence is the shape of the work function curves themselves, sudden changes in slope being taken to

indicate the onset of some new process.

In the cases of the metallic adsorbates, caesium[97], barium[347], uranium† and zirconium†, all of the work function/coverage curves show a rather similar shape with a minimum work function followed by a rise to a steady final level. For use in the correlation the minimum in the curve is adopted as an approximation to the value which would be obtained without depolarization effects (see chapter 2).

For the halogens, the desorption measurements of Fehrs and Stickney[342] for iodine and bromine on (100) tungsten, and of McCarol1[348] for iodine on polycrystalline tungsten, indicate that for atomic adsorption the coverage curve is monotonic. Subsequent adsorption does take place after this initial atomic state but this is generally thought to be a molecular state and gives rise to work function change in the opposite sense to the atomic state. Thus, the SPs adopted for the halogens[341] are the maximum changes in all cases with the exception of chlorine on the (100). With this system the Kelvin measurements of Jowett and Hopkins[341] showed a rapid increase in work function to a plateau value, followed by a further small increase at very high chlorine exposures. In this case the plateau value of -0.58 V rather than the maximum change of -0.70 V has been chosen. Fehrs and Stickney, using the Anderson technique, did not see this slow increase but recorded a final SP of -0.635 V.

In the case of bromine on (100) tungsten, the results of Fehrs and Stickney and of Jowett and Hopkins differ appreciably. The former observe a two stage adsorption with an initial plateau at -0.41 V. This initial atomic phase was

† present work

followed by a further change to ∿ -0.8 V. In the results of Jowett and Hopkins a monotonic change to -0.8 V was observed. It is preferred therefore to use the value of -0.41 V due to Fehrs and Stickney.

Oxygen on the (110) face shows an inflection at approximately half the final SP[16]. This has been shown[16,349] to be caused by an abrupt change in the sticking coefficient. In this case the final, maximum SP has been used.

There is much evidence in the literature[350-353] that the adsorption of water vapour is dissociative: hydrogen is released with OH^- remaining on the surface bonded through oxygen. Thus, the SP data of Jowett[15] relates to water on tungsten but is interpreted as OH^-. The water adsorption curves are very similar to those of oxygen on tungsten[16] but with overall higher SPs. In particular the (110) curve shows the same inflection as for oxygen and, as in that case, the maximum SP change is taken.

Rather less Kelvin data is available for the (111) and (211) surfaces and in particular there is no metallic data. The value for chlorine on (111) was obtained using a retarding field technique[342]. Field emission measurements of uranium on tungsten have, however, been made by Collins[156]. The SPs observed on the (100) and (110) planes differed by a factor of 1.1 from the present Kelvin results (section 8.4). An estimate of the (111) and (211) values has been obtained by applying the same correction factor to Collins' values.

The SPs finally used are collected together in table A2.1.

It is easy to 'select' appropriate electronegativity values from the

table A2.1

orientation of substrate	adsorbate	surface potential experimental SP (volts)	references	ionic radius[315] r_i (Å)	SP/r_i	adsorbate electronegativity[315] χ_f (eV)	$\chi_w - \chi_f$	surface potential calculated (V)
(110)	Cs^+	3.17	97	1.69	1.88	2.36	7.10	3.13
	Ba^+	2.60	347	1.53	1.70	2.84	6.62	2.64
	U^+	1.36	††	1.05	1.30	4.41	5.05	1.38
	Zr^+	0.94	††	1.09	0.86	4.73	4.73	1.35
	I^-	0.78	341	2.16	0.36	7.88	1.58	0.89
	Br^-	0.32	341	1.95	0.16	8.82	0.64	0.32
	Cl^-	0.26	341	1.81	0.14	9.45	0.01	0.00
	O^-	-0.85	16	1.76	-0.48	11.03	-1.57	-0.72
	OH^-	-1.01	15	1.76†	-0.57	12.29	-2.83	-1.30
	H	0.14	225	2.08		6.63	2.83	
	N	-0.20	16	2.47		9.45	0.01	
(211)	U^+	1.26	156	1.05	1.20	4.41	4.44	1.18
	O	-1.04	177	1.76	-0.59	11.03	-2.18	-1.17
(100)	Cs^+	2.85	97	1.69	1.69	2.36	5.94	2.76
	Ba^+	2.28	347	1.53	1.49	2.84	5.46	2.30
	U^+	1.11	††	1.05	1.06	4.41	3.89	1.12
	Zr^+	1.10	††	1.09	0.92	4.73	3.57	1.07
	I^-	0.18	341	2.16	0.08	7.88	0.42	0.25
	Br^-	-0.41	342	1.95	-0.21	8.82	-0.52	-0.28
	Cl^-	-0.58	341	1.81	-0.32	9.45	-1.15	-0.57
	O^-	-1.18	16	1.76	-0.67	11.03	-2.73	-1.32
	OH^-	-1.40	15	1.76	-0.80	12.29	-3.99	-1.93
	H	-0.54	225	2.08		6.63	1.67	
	N	0.52	16	2.47		9.45	-1.15	
(111)	U^+	0.84	156	1.05	0.80	4.41	3.06	1.00
	I^-	0.15	341	2.16	0.07	7.88	-0.41	-0.03
	Br^-	-0.88	341	1.95	-0.45	8.82	-1.35	-0.53
	Cl^-	-1.10	341	1.81	-0.61	9.45	-1.98	-0.81
	O^-	-1.65	16	1.76	-0.94	11.03	-3.56	-1.56
	H	-0.30	225	2.08		6.63	0.84	
	N	-0.17	218	2.47		9.45	-1.98	

† since the H^+ radius is vanishingly small, OH^- radius is taken as the O^- radius (see page 451 of reference 315)

†† present work

literature. In order to avoid this, the original Pauling[315] scale was employed though this presents some limitations as the values are rounded to the first decimal place. The electronegativity of the OH^- radical was calculated according to the relation given by Wilmshurst[354] using a value for the covalent radius of oxygen in the O-H bond of 0.66 Å[315]. The adsorbate electronegativity values used in the correlation are shown in absolute units in table A2.1; in addition those for metals are given in table 1.2.

A2.5 present correlation

Dipole moment (and hence SP) is given by the product of charge transfer and dipole length. As discussed in section A2.3, the former is determined by the electronegativity difference and the latter is taken as the ionic radius r_i. Hence:

$$SP \propto r_i(\chi_w - \chi_f) \qquad A2.5$$

where χ_w is the electronegativity of the tungsten substrate. Since equation A2.5 can be written:

$$SP/r_i \propto \chi_w - \chi_f \qquad A2.6$$

SP/r_i is plotted against χ_f in figure A2.1 for the four surfaces. It is clear from this plot that equation A2.6 holds remarkably well, but that the effective electronegativity of the tungsten substrates (the intersection on the abscissa) differs for each orientation with values of 9.46, 8.85, 8.30 and 7.47 eV for the (110), (211), (100) and (111) surfaces respectively. The measured work function values[15,16,234,241] of the surface are: 5.15 ± 0.02 eV, 4.77 ± 0.02 eV, 4.65 ± 0.02 eV and 4.45 ± 0.02 eV respectively†. Thus, on the basis of the Steiner and Gyftopoulos[18] concept

† (110) and (100) values from present work

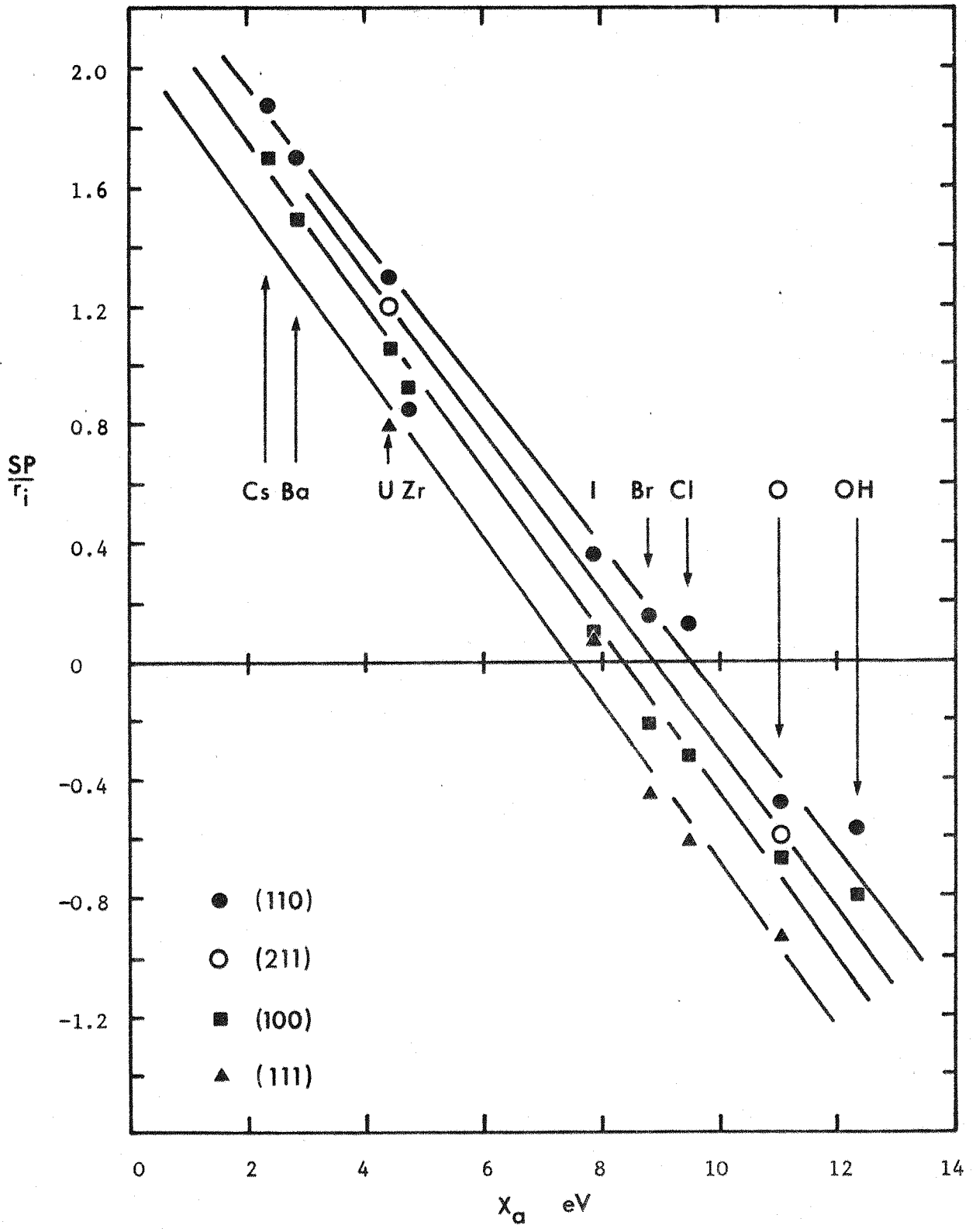

figure A2.1
surface potential/ionic radius versus absolute electronegativity for 9 adsorbates on 4 tungsten single crystal substrates

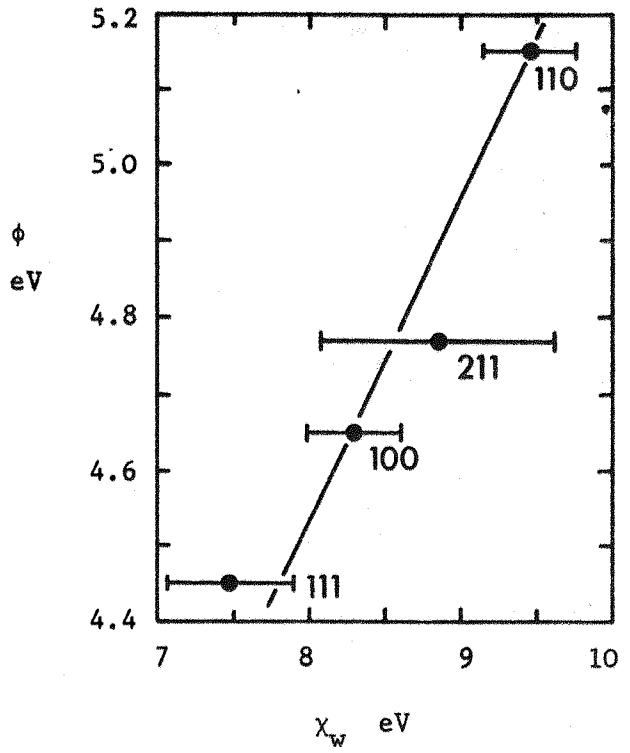

figure A2.2
work function ϕ versus effective electronegativity χ_w of the tungsten substrate

of electronegativity these values should also be the appropriate absolute electronegativities of the surfaces. It is clear that the effective electronegativities are appreciably higher. Such a situation would occur if the adsorbate-adsorbent bond were very strong and weakened the binding of the surface tungsten atom to the bulk. The surface tungsten atom will then behave rather more like a free atom. The implication is that the effective electronegativity of a free tungsten atom is very high. Fehrs and Stickney[342] have made an approximate calculation of this electronegativity using the tungsten-tungsten bond energies from field ion microscopy studies[355,356] of the binding of single tungsten atoms. Their estimates lie within the range 7.5 to 9.5 eV, suggesting that the tungsten surface atoms in these chemisorption experiments can be considered as nearly isolated. Figure A2.2 illustrates that a linear relationship exists between the experimentally determined tungsten surface electronegativity

and the measured work functions. The line on this figure is given by:

$$\chi_{hk\ell} = 2.32\phi - 2.49 \qquad \text{A2.7}$$

It is also of interest to note that the slopes of the four lines in figure A2.1, given by $K_{hk\ell} = \Delta SP/r_i \Delta\chi_f$, are in the order $K_{111} = 0.277 \pm 0.018$ -> $K_{100} = 0.275 \pm 0.009$ > $K_{211} = 0.270 \pm 0.022$ > $K_{110} = 0.261 \pm 0.008$. This is in reverse order of the work function and appears to be a lowering of the efficiency with which electronegativity difference produces charge transfer as the work function increases. Such an effect is to be expected since the tungsten atoms are more strongly bound on high work function surfaces and so are less able to participate in charge transfer.

Finally, in figure A2.3 the spread in the data is represented by putting all of the points on one line. The ordinate is the experimental surface potential and the abscissa that calculated (column 9, table A2.1) from:

$$SP\ (calc) = K_{hk\ell} r_i\ (\chi_{hk\ell} - \chi_f) \qquad \text{A2.8}$$

where $\chi_{hk\ell}$ is given by equation A2.7.

Two major anomalies in this correlation occur for hydrogen and nitrogen; hydrogen on (100) and (111) and nitrogen on (110) and (100) tungsten produce SPs of the 'wrong' sign. This may well be due to penetration of the substrate by the adsorbate. No quantitative assessment can be made if this is the case since there is no way of ascertaining the final location of the adatom; consequently there can be no meaningful value of ionic radius. The fact that hydrogen on (110) tungsten gives a SP of the 'correct' sign may be because it cannot penetrate this very densely packed surface.

In conclusion, mention should be made of the recent work of Steiner[103] in which an attempt is made to calculate the SPs due to the halogens (see

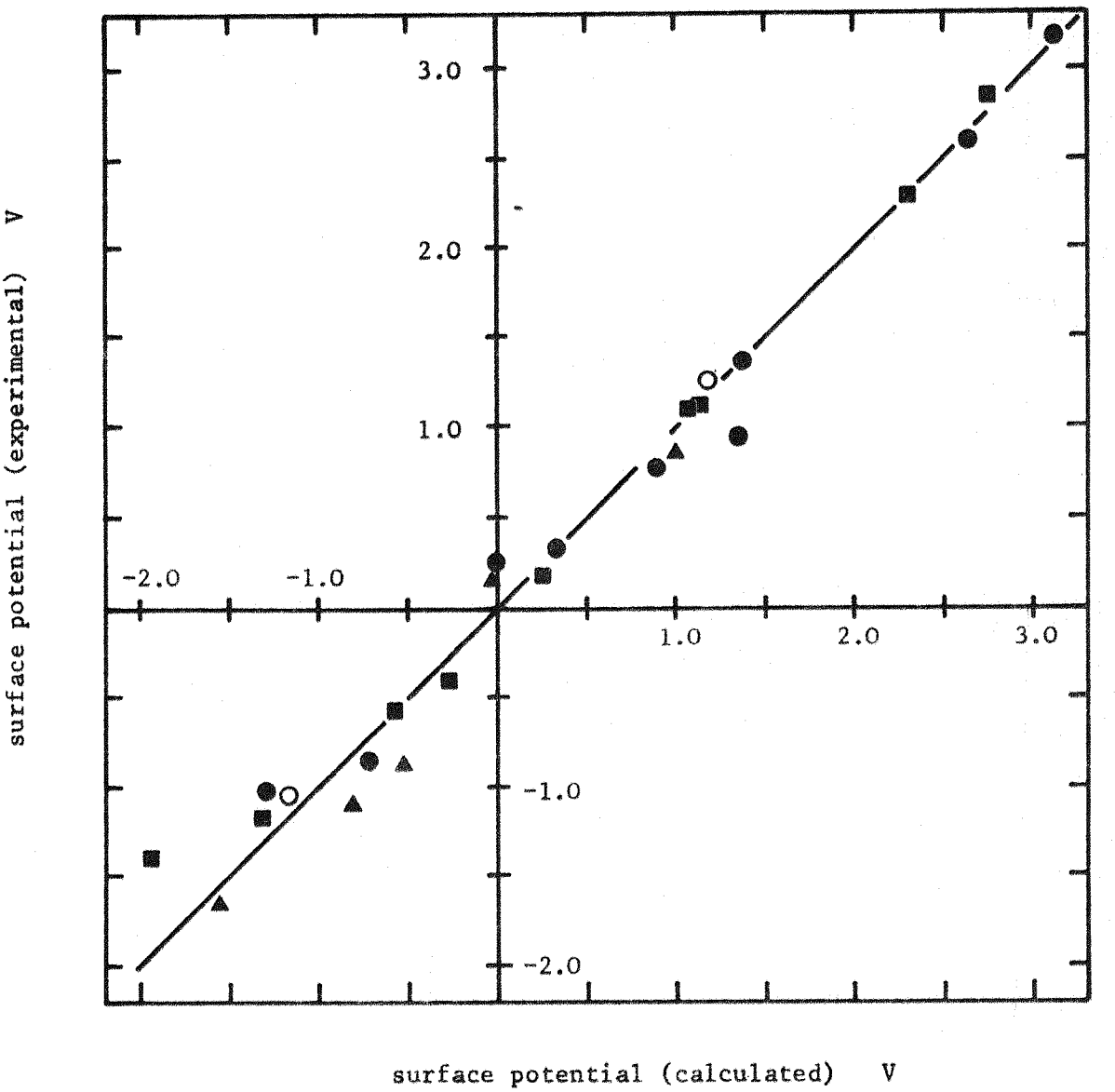

figure A2.3
calculated surface potential (equation A2.8) versus experimental surface potential

appendix 1). The SP is derived from the product of the dipole length, adsorbate density and the charge transfer, taking into account depolarization effects. Charge transfer is calculated by maximizing the bond energy, but the result is mainly determined by the electronegativity difference between the adsorbate and substrate. The substrate electronegativity is taken as the work function (4.60 eV for the (100) plane). Adopting this low electronegativity value results in the dipole length being the dominant term in the SP. Consequently, for the (100) plane of tungsten the SPs increase in the order I > Br > Cl > F. Fehrs and Stickney[342] have pointed out that this is opposite to experiment which shows a sequence Cl > Br > I. If, however, the present experimental value of 8.30 eV for the substrate electronegativity is used for (100) tungsten the results are closer to those observed. The values obtained using both 4.60 and 8.30 eV for the substrate electronegativity are shown in table A2.2, together with the experimental results.

table A2.2
predicted[103] surface potentials due to halogen adsorption on (100) tungsten

adsorbate	surface potential		
	for χ_w = 4.6	for χ_w = 8.30	experimental (see table A2.1)
I	-2.00	+0.12	+0.18
Br	-1.82	-0.05	-0.41
Cl	-1.23	-0.30	-0.58
F	-0.50	-0.28	-

A2.6 summary

Surface potential data for the atomic adsorption of eight materials, ranging from caesium to water vapour, on to four single crystal planes of tungsten have been correlated with electronegativity differences between the substrate and adsorbates. It has been demonstrated that for each surface an effective electronegativity exists which may be used to predict SPs due to the adsorption of materials covering the whole electronegativity range. In addition, a linear relation between this effective electronegativity and work function is found. The physical interpretation suggests that penetration of the surface by hydrogen and nitrogen may occur.

APPENDIX 3 DESORPTION OF HYDROGEN FROM A MONOLAYER URANIUM FILM

During the investigation of gas contamination of uranium films discussed in section 8.2.1 it was noted that heating a monolayer film of uranium after exposure to hydrogen caused the work function of the film to return to the clean uranium value (section 8.2.1.3). Consequently it was decided to monitor the desorption of hydrogen with a mass spectrometer and hence determine the desorption energy. Measurements were made on tube 4 which contained a directly heated polycrystalline tungsten foil substrate fitted with a W - W/26%Re thermocouple. Hydrogen was introduced to the system by diffusion through a palladium tube, its partial pressure being measured on a Varian PPG. After outgassing the palladium tube at a temperature well above that at which it was subsequently used for hydrogen diffusion, a high final hydrogen purity could be achieved. A typical mass scan, taken at a total pressure of $\sim 10^{-6}$ torr, showed the main impurities were 0.2% water vapour[225] and < 0.1% carbon monoxide.

The desorption energy was calculated using the method described by Booth[357] which required the measurement of the maximum desorption rate T_{max} at two values of heating rate b. The desorption energy E_d could then be found from the relation:

$$E_d = \left(\log_e \frac{b_1}{b_2} + 2 \log_e \frac{T_{max(1)}}{T_{max(2)}} \right) \frac{T_{max(1)} \times T_{max(2)}}{T_{max(1)} - T_{max(2)}} \; k$$

where $b = (dT/dt)$ at T_{max} and k is Boltzman's constant.

Hydrogen was admitted to a maximum pressure of $\sim 10^{-4}$ torr and then allowed to pump away for 12 hours. The substrate was then heated at a rate determined by a motor-driven Variac, whilst the partial pressure of hydrogen

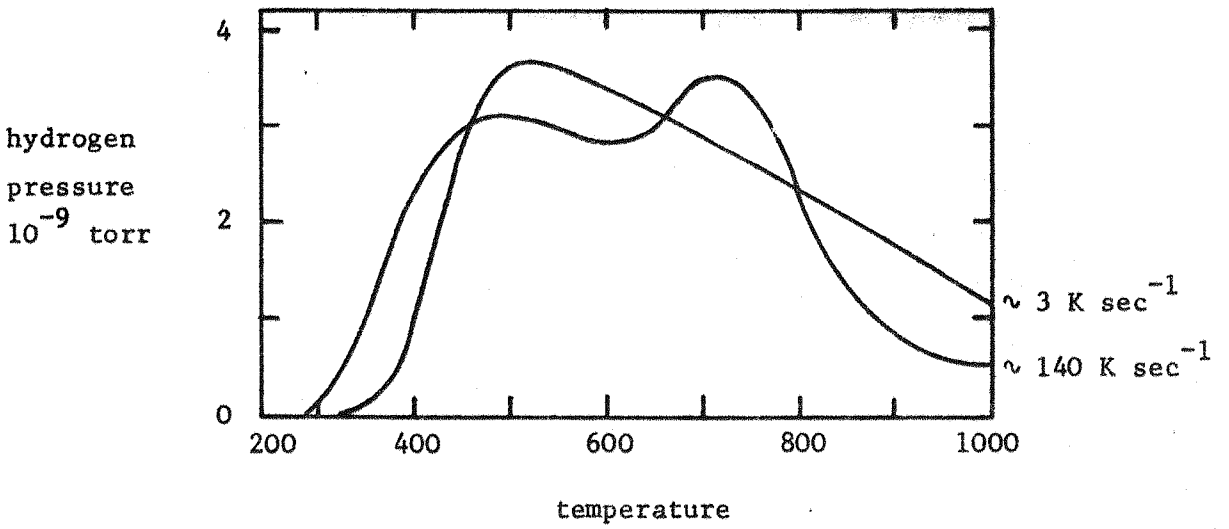

figure A3.1
desorption of hydrogen from a monolayer uranium film at 2 heating rates
pressure scale at lower heating rate has been multiplied by 10

was monitored. The results for a monolayer uranium film substrate are shown in figure A3.1. The temperature of the maximum desorption rate increased from 514 K at a heating rate of 3 K sec^{-1}, to 723 K at a heating rate of 140 K sec^{-1}. The first maximum at the higher heating rate is probably due to a very weakly bound physisorbed state which was not detectable at the lower heating rate. The desorption energy calculated from the above figures is 0.68 ± 0.13 eV. As a check, a similar measurement was made on tungsten foil, giving a value of 1.95 ± .43 eV. This compares with the measurements of Hickmott[149] and Beeck[358] of 0.87 and 1.43 eV at complete coverage.

This method of determining desorption energies is somewhat crude and the values must be regarded with some suspicion. However, the results indicate that hydrogen is completely desorbed from uranium after only a few seconds at 800 K. This is consistent with the observation that after heating to this temperature the work function returns to that of clean uranium.

APPENDIX 4 ALGOL PROGRAM FOR LEAST SQUARES GYFTOPOULOS AND STEINER FIT

The program is designed to calculate Σd^2, the sums of the squares of the deviations between theory and experiment for 21 points at 0.05 monolayer intervals. Σd^2 is then minimized with respect to the polarizability α for a range of values of monolayer point, D_1 and ad_o.

INPUTS (see equations 2.66 - 2.68)

identifier in program	parameter	units
ADO	ad_o	
VF	z	
R	R	Å
COSB	cosB	
SIGF	σ_f	atoms $Å^{-2}$
DO	D_o	eV
T	H	mobile adsorbates H = 1.5; immobile H = 1.0
N		one less than number of data points
NM		maximum position of monolayer point (θ = 1)
L		minimum position of monolayer point (θ = 1)
I		intervals between monolayer points
D1B	eV	initial value of D_1
DD1	eV	intervals in D_1
W		optional printout/no printout of work function/ coverage. If W = 0, no printout.
ADOI		initial value of ad_o
ADOF		final value of ad_o
DADO		intervals in ad_o
DATA[U]		work function data (N+1) points
SG[U]		data weighting factor (N+1) points

OUTPUT for W = 0 (no work function/coverage printout)

For each value of ad_o the calculation is made for five values of D_1, starting at D1B with increments of DD1. For these five D_1 values, Σd^2 and α are calculated for the range of monolayer values. Only ad_o, D_1 (eV), monolayer point, Σd^2 and α ($\AA^3$) are printed out. If the charge transfer F is not found to within ±0.00001 after completion of 99 loops (Newton's method) F FAIL is output. If in the process of minimizing Σd^2, α becomes negative or more than 50 loops are completed, ALPH FAIL is output.

OUTPUT for non-zero W

The calculation is performed for only one value of D_1: D1B.

In addition to the parameters printed for the W = 0 case, the following are output for each of 21 points on the coverage scale at 0.05 monolayer intervals: coverage (θ), charge transfer (F), coverage (experimental scale), theoretical work function (ϕ_{th} eV), experimental work function (ϕ_{exp} eV:- interpolated value), experimental minus theoretical work function ($\phi_{exp} - \phi_{th}$ eV).

The following is a completed compilation of the program.

```
STATEMENT
        0       'SEND TO' (ED,SEMICOMPFILE(26  ),.PROGRAM FILE)
        0       'PROGRAM'           (P15FP15)
        0       'BEGIN'
        1       'REAL'  L, NM, I, T, AD0, VF, R, COSB, SIGF, ALPH,
        1       D1, D0, K3, J, Z, DZF, SUMY, SUMDY, DEL, D1B,     UT,
        1       DD1,DIFF,S,TH,NSUMDY,U,W1,AD0I,AD0F,DAD0;
        1       'ARRAY' PHI, SIG, M, P, Q[0:20];
        2       'INTEGER' W,C,V,N;
        3       'PROCEDURE'  TIMENOW;  'EXTERNAL' ;
        4       START;
        5       SELECT INPUT (3);
        6       AD0 := READ;  VF:= READ; R:= READ;  COSB := READ;
       10       SIGF:= READ;  D0:= READ;  T:=READ;
       13       N:=READ;  NM:=READ;    L:=READ;  I:=READ;
       17       D1B:=READ;  DD1:=READ;  W:=READ;
       20       AD0I:=READ; AD0F:=READ; DAD0:=READ;
       23       'IF' W=0 'THEN' W1:=4 'ELSE' W1:=.9;
       24       K3:= 18*3.14159*1.602*VF*R*COSB*SIGF/D0;
       25       'BEGIN'
       25       'ARRAY'   DATA, SG[0:N];
       25       'FOR' U:=0 'STEP' 1 'UNTIL' N 'DO'
       27       DATA[U] := READ;
       28       'FOR' U:=0 'STEP' 1 'UNTIL' N 'DO'
       29       SG[U] := READ;
       30       'IF' I<0 'THEN' 'GOTO' CONTINUE;
       31       I:=-I;
       32       CONTINUE;
       32       'IF' AD0I>0 'THEN' 'GOTO' OK;
       33       AD0I:=-AD0I;
       34       OK;
       34       'FOR' AD0:=AD0I 'STEP' DAD0 'UNTIL' AD0F 'DO'
       35       'BEGIN'
       35       SELECT OUTPUT(0);
       37       WRITE TEXT  ('('P15B%%ADRIAN%SARGOOD%%SURFACE%PHYSICS%%%GYFTOPOULOS%&%
       37       STEINER%%LEAST%SQ%FIT%ALPHA%FOR%GIVEN%D1%%%AD0%='')'); PRINT(AD0,1,2);
       39       WRITE TEXT ('('('('3C')'D1%%VALUE%%%%%%')');
```

```
40      D1:=D1B;
41      'FOR' U:=0 'STEP' 1 'UNTIL' W1 'DO'
42      'BEGIN'
42      PRINT (D1,2,3); SPACE(13);
45      D1:=D1 +DD1;
46      'END';
47      NEWLINE(2); WRITE TEXT ('('MONOLAYER%PT'('C')'')');
49      'FOR' C:= 0 'STEP' 1 'UNTIL' 20 'DO'
50      'BEGIN'
50      J:=C/20;
52      'IF' C=0 'THEN' M[C]:=0 'ELSE'
52      M[C]:= 2*EXP(AD0*(1-1/SQRT(J)))-EXP(2*AD0*(1-1/SQRT(J)));
53      Q[C]:= (1-M[C])*K3*J;
54      'END';
55      'FOR' UT:= NM 'STEP' I 'UNTIL' L 'DO'
56      'BEGIN'
56      PRINT(UT,2,2); SPACE(2);
59      'FOR' C:=0 'STEP' 1 'UNTIL' 20 'DO'
60      'BEGIN'
60      V:=ENTIER(C*UT/20);
62      PHI[C]:=DATA[V]+(C*UT/20-V)*(DATA[V+1]-DATA[V]);
63      SIG[C]:=SQRT((SG[V]↑2+SG[V+1]↑2)/2);
64      'END';
65      'FOR' C:=0 'STEP' 1 'UNTIL' 20 'DO'
66      P[C]:=(PHI[C]-PHI[0])/(PHI[20]-PHI[0])-M[C];
67      D1:=D1B;
68      'FOR' UT=0 'STEP' 1 'UNTIL' W1 'DO'
69      'BEGIN'
69      'ARRAY'  N, F, X, DX[0:20];
69      'FOR' C:=0 'STEP' 1 'UNTIL' 20 'DO'
71      'BEGIN'
71      DZF:=(PHI[20]-PHI[0])*(1-M[C]);
73      J:=.1;
74      F[C]:=0;
75      V:=0;
76      FINDF;
76      N[C]:=D1/D0+1/SQRT(1-F[C]↑2);
```

```
77        'IF'  C=20  'THEN'  'GOTO'  FITAL;
78        Z:=D0*F[C]*H[C]+DZF;
79        F[C]:=F[C]+J;
80        H[C]:=D1/D0+1/SQRT(1-F[C]↑2);
81        DIFF:=D0*F[C]*H[C]+DZF;
82        'IF' DIFF=0 'THEN' 'GOTO' FITAL;
83        'IF' ABS(J)<0.00001 'THEN' 'GOTO' FITAL;
84        'IF' DIFF*Z<0 'THEN'
84        J:=-J/2    'ELSE'
84        'IF' ABS(DIFF)>ABS(Z) 'THEN'
84        'BEGIN'
84        F[C]:=F[C]-J;
86        J:=-J;
87        'END';
88        V:=V+1;
89        'IF' V>99 'THEN' 'GOTO' FFAIL;
90        'GOTO' FINDF;
91        FITAL;
91        'END';
92        V:=0;
93        DEL:=0.8;
94        ALPH:=0;
95        MINALPH:  SUMDY:=0;
96        'FOR'  C:=0 'STEP' 1 'UNTIL' 20 'DO'
97        'BEGIN'
97        J:=C/20;
99        X[C]:=(1+ALPH/R↑3)*(1+9*ALPH*SIG↑1.5*J↑T);
100       DX[C]:=1/R↑3+9*SIG↑1.5*J↑T*(1+2*ALPH/R↑3);
101       S:=(P[C]-Q[C]/(X[C]*H[C]))*Q[C]*DX[C]/(H[C]*X[C]↑2*SIG[C]↑2);
102       SUMDY:=SUMDY+S;
103       'END';
104       ALPH:=ALPH+DEL;
105       'IF'ALPH<0 'THEN' 'GOTO' NOTIN;
106       NSUMDY:=0;
107       'FOR'  C:=0 'STEP' 1 'UNTIL' 20 'DO'
108       'BEGIN'
108       J:=C/20;
```

```
110       X[C]:=(1+ALPH/R↑3)*(1+9*ALPH*SIGF↑1.5*J↑T);
111       DX[C]:=1/R↑3+9*SIGF↑1.5*J↑T*(1+2*ALPH/R↑3);
112       S:=(P[C]-Q[C]/(X[C]*H[C]))*Q[C]*DX[C]/(H[C]*X[C]↑2*SIG[C]↑2);
113       NSUMDY:=NSUMDY+S;
114       'END';
115       'IF' ABS(DEL)<.06 'THEN' 'GOTO' FOUND;
116       'IF'  SUMDY*NSUMDY<0  'THEN'  DEL:=-DEL/2
116       'ELSE'
116       'IF' ABS(NSUMDY)>ABS(SUMDY) 'THEN'
116       'BEGIN'
116       DEL:=-DEL;
118       ALPH:=ALPH+DEL;
119       'END';
120       V:=V+1;
121       'IF' V>50 'THEN' 'GOTO' NOTIN;
122       'GOTO' MINALPH;
123       FOUND:  SUMY:=0;
124       'IF' W=0 'THEN' 'GOTO' NOPRINT;
125       WRITE TEXT ('('''('3C')'THETA%%%CHARGE%TRANSFER%%%COVERAGE%%%%%%
125       THEORETICAL%%%%%%EXPERIMENTAL%%%%%%EX%MINUS%TH'('3C')''')');
126       NOPRINT:
126       'FOR' C:=0 'STEP' 1 'UNTIL' 20 'DO'
127       'BEGIN'
127       J:=C/20;
129       SUMY:=SUMY+((P[C]-Q[C]/(X[C]*H[C]))/SIG[C])↑2;
130       'IF' W=0 'THEN' 'GOTO' NOVAL;
131       TH:=PHI[0]+(PHI[20]-PHI[0])*(M[C]+(1-M[C])*K3*J/(X[C]*H[C]));
132       PRINT(J,1,2);  SPACE(5);  PRINT(F[C],1,4);  SPACE(6);
136       PRINT(J*UT,2,2);  SPACE(6);
138       PRINT(TH,2,3);  SPACE(8);
140       PRINT(PHI[C],2,3);  SPACE(9);
142       PRINT(PHI[C]-TH,1,5);  NEWLINE(1);
144       NOVAL:
144       'END';
145       'IF' W=0 'THEN' 'GOTO' HELL;
146       WRITE TEXT ('('''('2C')'SUM%DEVN%SQRD%%ALPHA'('C')''')');
147       HELL:
```

```
147         PRINT(SUMY,2,6);
148         PRINT(ALPH,3,2);  SPACE(1);
150         'GOTO' FINISH;
151         FFAIL;  WRITE TEXT ('('FXFAIL'('S')'')');
152         PRINT(C,2,0);  SPACE(1);  PRINT(F[C],1,3);  SPACE(1);
156         'GOTO' FINISH;
157         NOTIN;    WRITE TEXT ('('XXALPHXFAIL'('S')'')');
158         PRINT(ALPH,3,2);  SPACE(1);
160         FINISH;
160         D1:=D1+DD1;
161         'END';
162         'IF' W=0 'THEN' NEWLINE(1) 'ELSE' SPACE(10);
163         TIMENOW;  NEWLINE(1);
165         'END';
166         NEWLINE(6);
167         'END';
168         FREEOUTPUT;  FREEINPUT;
170         'END';
171         'END';
NO OF BUCKETS USED    38
COMPILED   #P15FP15        EC
```

APPENDIX 5 TABULATED RESULTS WORK FUNCTION/COVERAGE

coverage†	work function eV					
	uranium adsorbate			zirconium adsorbate		
	poly W	(110)W	(100)W	poly W	(110)W	(100)W
0	4.55	5.15	4.65	4.55	5.15	4.65
1	4.27	4.86	4.27	4.375	4.925	4.37
2	4.05	4.655	4.06	4.225	4.78	4.145
3	3.89	4.49	3.90	4.11	4.665	3.955
4	3.75	4.345	3.78	4.015	4.56	3.83
5	3.64	4.203	3.69	3.95	4.465	3.735
6	3.543	4.065	3.62	3.90	4.39	3.665
7	3.48	3.945	3.575	3.865	4.32	3.61
8	3.43	3.862	3.55	3.85	4.26	3.577
9	3.41	3.81	3.541	3.84	4.225	3.555
10	3.405	3.795	3.54	3.835	4.21	3.55
11	3.41	3.80	3.541	3.84	4.217	3.553
12	3.42	3.815	3.55	3.845	4.24	3.57
13	3.442	3.84	3.565	3.855	4.265	3.59
14	3.47	3.86	3.58	3.87	4.277	3.61
15	3.50	3.875	3.60	3.878	4.28	3.632
16	3.535	3.888	3.625	3.88	4.28	3.655
17	3.56	3.893	3.655	3.88	4.28	3.68
18	3.585	3.898	3.68	3.88	4.28	3.70
19	3.605	3.90	3.705	3.88	4.28	3.714
20	3.62	3.90	3.725	3.88	4.28	3.726
21	3.628	3.90	3.74	3.88	4.28	3.738
22	3.63	3.90	3.757	3.88	4.28	3.747
23	3.63	3.90	3.77	3.88	4.28	3.75
24	3.63	3.90	3.78	3.88	4.28	3.75
25	3.63	3.90	3.787	3.88	4.28	3.75
26	3.63	3.90	3.795	3.88	4.28	3.75
27	3.63	3.90	3.798	3.88	4.28	3.75
28	3.63	3.90	3.80	3.88	4.28	3.75
29	3.63	3.90	3.80	3.88	4.28	3.75
30	3.63	3.90	3.80	3.88	4.28	3.75

† coverage scale is arbitrarily normalized at the work function minimum which is defined as 10

measurements by Kelvin technique using polycrystalline tungsten foil reference (work function = 4.55 eV)
uranium on polycrystalline foil measurement due to Barry[7] (Kelvin)
zirconium on polycrystalline foil - measurement by Anderson technique

APPENDIX 6 GLOSSARY OF SYMBOLS

a	lattice constant, subscript referring to atoms
a_o	Bohr radius = $h^2/(4\pi^2 me^2)$ = 5.29×10^{-11} m
A	Richardson constant, electron affinity
A_f	Fowler-Nordheim pre-exponential
A^*	apparent Richardson constant
B	angle
c	velocity of light = 2.998×10^{8} m sec^{-1}
C	capacitance
d	distance between lattice planes, deviation $\phi_{exp} - \phi_{th}$
d_i	distance between adsorbate atom and substrate atom i
D	dipole moment/unit area
D_o	covalent bond energy
$D(A-A)$	single bond dissociation energy between atoms A-A
$D(f-f)$	sublimation energy (adsorbate)
e	electronic charge = 1.602×10^{-19} C
E	field, energy
E_o	zero coverage surface ionization energy (Rasor and Warner)
E_d	depolarizing field
E_f	Fermi energy
E_n	'natural' field at a metal surface
E_p	patch field
f	subscript referring to adsorbate, fraction of dipole layer penetrated by an ion
F	charge transfer
$G(\theta)$	Gyftopoulos and Levine shape factor
h	Planck's constant = 6.625×10^{-34} J sec
H	constant in Topping summation; H = 1 for immobile adsorbates H = 1.5 for mobile adsorbates
i	emission current, subscript referring to ions
I	ionization potential
k	Boltzman's constant = 1.380×10^{-23} J K^{-1}
ℓ	half dipole length (ion - imaging plane distance)
L	radius (in lattice constants) of Neustadter and Bacigalupi summation
m	electronic mass = 9.107×10^{-31} Kg
M	dipole moment, molecular weight

$M(\theta)$	Morse function
n	number of valence electrons, fractional bond number
N	electron density
P	pressure
q	charge
Q	overlap charge
r	radius
r_c	reflection coefficient at collector
r_e	reflection coefficient at emitter
r_f	adsorbate atomic radius
r_m	substrate atomic radius
r_s	interelectron separation
R	sum of adsorbate and substrate atomic radii ($r_m + r_f$)
s	subscript referring to substrate, emitter area
s_c	collector area
S	exchange integral, angular bond strength
t	time
T	temperature (Kelvin)
v	valence
V	voltage
V_a	applied voltage
V_{cpd}	contact potential difference
W	depth of potential energy well
x	distance from the surface of the metal
z	units of charge, valence, number of bonding orbitals per adatom

α	polarizability
α_i	ionic polarizability
β	Fowler-Nordheim geometrical factor
Γ	bandwidth of broadened atomic energy level
δ	extra-ionic or resonance energy
ε	effective dielectric constant
ε_o	permittivity of free space = 8.854×10^{-12} Fm^{-1}
ζ	normalized binding energy (Neustadter and Bacigalupi)
θ	coverage, angle
θ_a	atomic coverage
θ_i	ionic coverage
λ	wavelength
μ	chemical potential
ν	frequency
ν_o	photoelectric cut-off frequency
σ	surface density
σ_f	adsorbate surface density at $\theta = 1$
σ_m	substrate surface density
ϕ	work function
ϕ_a	atom adsorption energy
ϕ_c	collector work function
ϕ_e	emitter work function
ϕ_E	effective work function
ϕ_f	adsorbate work function
ϕ_i	ion adsorption energy, true work function of ith patch
ϕ_i^*	zero field apparent work function of the ith patch
ϕ_m	substrate work function
$\bar{\phi}$	area averaged work function
ϕ^*	zero field apparent work function
χ	electronegativity
χ_a	absolute (Mulliken) electronegativity
χ_p	Pauling electronegativity
Ψ	wave function
ω	frequency

ACKNOWLEDGEMENTS

The author has great pleasure in thanking Dr Barry Blott for his help and encouragement throughout this work and in particular for his guidance with computer programming.

Sincere gratitude is also expressed to the author's parents without whose financial and moral support this work could not have been completed.

Thanks are due to Dr B J Hopkins for his supervision of this project, to the Professors of the Physics Department for the provision of laboratory facilities and to the Science Research Council for a maintenance grant.

The author also wishes to express his gratitude to Caroline Rees for ably typing this thesis and for successfully managing to maintain a much needed sense of humour.

'Words pay no debts'

Troilus and Cressida act 3 scene 2 line 56

(apologies to W Shakespeare and D Steiner)

REFERENCES

1 J M HOUSTON, H F WEBSTER
Adv. in Electronics and Electron Physics 17 125 1962

2 P D DUNN, J MYATT, C RICE, L G SANDERS
ENEA-IEE Int. conf. thermionic power generation, London 1965

3 E WOLF, W HAUG
IEEE conf. thermionic conversion, Framingham, Mass. USA 1968 p305

4 B H BLOTT
PhD thesis, University of Southampton 1964

5 D E BARRY
private communication

6 J C RIVIERE
Proc. Phys. Soc. 80 116 1962

7 D E BARRY, B J HOPKINS, A J SARGOOD
Surface Science 7 365 1967

8 C KITTEL
'Introduction to Solid State Physics', Wiley, NY 1966. Appendix C

9 C KITTEL
'Introduction to Solid State Physics', Wiley, NY 1966. p205

10 C HERRING, M H NICHOLS
Rev. Mod. Phys. 21 185 1949

11 J ANDERSON, W E DANFORTH, A J WILLIAMS
J. Appl. Phys. 34 2260 1963

12 M ABRAHAM, R BECKER
'The classical theory of electricity and magnetism',
Blackie and Sons Ltd. London 1937. p29

13 R SMOLUCHOWSKI
Phys. Rev. 60 661 1941

14 I N STRANSKI, R SUHRMAN
Ann. d. Phys. 1 153 1947

15 C W JOWETT
PhD thesis, University of Southampton 1969

16 C B WILLIAMS
PhD thesis, University of Southampton 1969

17 A MULLER, M DRECHSLER
15th Ann. field emission symp. Bonn 1968

18 D STEINER, E P GYFTOPOULOS
Report on 27th Ann. Conf. Phys. Elec. Cambridge MIT 1967 p160

19 E WIGNER, F SEITZ
Phys. Rev. 46 509 1934

20 E WIGNER, J BARDEEN
Phys. Rev. 48 84 1935

21 W OLDEKOP, F SAUTER
Z. Phys. 136 534 1954

22 J BARDEEN
Phys. Rev. 49 653 1936

23 F SEITZ
'The modern theory of solids', McGraw-Hill, NY 1940

24 E WIGNER
Phys. Rev. 46 1002 1934

25 H HELLMANN, W KASSATOTSCHKIN
J. Chem. Phys. 4 324 1936

26 R G SACHS, D L DEXTER
J. Appl. Phys. 21 1304 1950

27 H J JURETSCHKE
Phys. Rev. 92 1140 1953

28 T L LOUCKS, P H CUTLER
J. Phys. Chem. Sol. 25 105 1964

29 J M ZIMAN
Adv. Phys. 13 89 1964

30 J BARDEEN
Surface Science 2 381 1964

31 J C RIVIERE
AERE report R5526 1967

32 H B MICHAELSON
J Appl. Phys. 21 536 1950

33 I LANGMUIR
Trans. Am. Electrochem. Soc. 29 125 1916

34 F ROTHER, H BOMKE
Z. Phys. 86 231 1933

35 H BOMKE
Z. Phys. 90 542 1934

36 J F CHITTUM
J. Phys. Chem. 38 79 1934

37 E WIGNER, J BARDEEN
Phys. Rev. 48 84 1935

38 E H B BARTELINK
Physica 3 193 1936

39 P GOMBAS
Nature 157 668 1946

40 C G BEDREAG
Comptes Rendus 223 354 1946

41 J BOCKRIS
Nature 159 539 1947

42 I G HERMAN, P S WAGNER
'Oxide-coated cathode' volume 2, Chapman and Hall, London 1951

43 W M H SACHTLER
Z. Electrochem. 59 119 1955

44 W GORDY, W THOMAS
J. Chem. Phys. 24 439 1956

45 R M VASENIN
Nauch. Trudy. Moskov. Tekhnol. Inst. Legkol. Prom. 11 208 1958

46 J H O VARLEY
Phil. Mag. 5 64 1960

47 L PAULING
'Nature of the chemical bond', Cornell Univ. Press, Ithaca, NY 1960 p88

48 L PAULING, J SHERMAN
J. Am. Chem. Soc 59 1450 1937

49 M HAISSINSKY
J. Phys. Radium 7 7 1946

50 H O PRITCHARD, H A SKINNER
Chem. Rev. 55 745 1955

51 R MULLIKEN
J. Chem. Phys. 2 782 1934; 3 573 1935; J. Chim. Phys. 46 497 1949

52 R MULLIKEN
J Chem. Phys. 3 375 1935; 3 573 1935

53 C A COULSON
'Valence', Oxford University Press, London 1961. 2nd edition. p139

54 J G MALONE
J. Chem. Phys. 1 197 1933

55 R MULLIKEN
J. Chem. Phys. 3 573 1935

56 E S RITTNER
J. Chem. Phys. 19 1030 1951

57 C A COULSON
Trans. Faraday Soc. 38 433 1942

58 J W SMITH
'Electric dipole moment', Butterworth, London 1955 p93

59 W GORDY
Phys. Rev. 69 604 1946

60 J C SLATER
Phys. Rev. 36 57 1930

61 J HINZE, M A WHITEHEAD, H H JAFFE
J. Am. Chem. Soc. 85 148 1963

62 R T SANDERSON
'Chemical Periodicity', Reinhold Publishing Corporation, NY 1960 p37

63 V S FOMENKO
'Handbook of thermionic properties', Plenum Press, NY 1966

64 B M PALYUKH, L L SIVERS
Sov. Phys. Solid State 10 1585 1969

65 E P GYFTOPOULOS, J D LEVINE
J. Appl. Phys. 33 67 1962

66 E P GYFTOPOULOS, G N HATSOPOULOS
Proc. Nat. Acad. Sci. 60 786 1968

67 C A COULSON
'Valence', Oxford University Press, London 1961. 2nd edition. p336

68 L PAULING
J. Am. Chem. Soc. 69 542 1947; Proc. Roy. Soc. A 196 343 1949

69 G EHRLICH
J. Chem. Phys. 31 1111 1959

70 F LONDON
Z. Physik 63 245 1930

71 J E LENNARD-JONES
Trans. Faraday Soc. 28 333 1932

72 A A ABRAHAMSON
Phys. Rev. 130 693 1963

73 W HEITLER, F LONDON
Z. Physik 44 455 1927

74 P M MORSE
Phys. Rev. 34 57 1929

75 M DRECHSLER, J F NICHOLS
J. Phys. Chem. Sol. 28 2609 1967

76 G MIE
Ann. Phys. 25 377 1908

77 R S MULLIKEN
J. Phys. Chem. 56 295 1952

78 C A COULSON
Proc. Roy. Soc. A 169 419 1939

79 R FERREIRA
J. Phys. Chem. 68 2240 1964

80 D A DOWDEN
Research 1 239 1948

81 L PAULING
Proc. Roy. Soc. A 196 343 1949

82 E W PLUMMER, T N RHODIN
J. Chem. Phys. 49 3479 1968

83 D R HARTREE
Camb. Phil. Soc. 24 89 1928

84 V FOCK
Z. Physik 61 126 1930

85 C J F BOTTCHER
'Theory of electric polarization' Elsevier Pub. Co. Holland 1952 p61

86 J B TAYLOR, I LANGMUIR
Phys. Rev. 44 423 1933

87 R V CULVER, F C TOMPKINS
Adv. in Cat. 11 67 1959

88 R W GURNEY
Phys. Rev. 47 479 1935

89 R GOMER, L W SWANSON
J. Chem. Phys. 38 1613 1963

90 J W GADZUK
Surface Science 6 133 1967

91 N S RASOR, C WARNER
J. Appl. Phys. 35 2589 1964

92 H UTSUGI, R GOMER
J. Chem. Phys. 37 1720 1962

93 I LANGMUIR
Phys. Rev. 43 224 1933

94 J TOPPING
Proc. Roy. Soc. A 114 67 1927

95 J R MACDONALD, C A BARLOW
J. Chem. Phys. 39 412 1963; 40 237 1964; 43 2575 1965; 44 202 1966;
Surface Science 4 381 1966

96 L N DOBRETSOV
'Electronic and ionic emission' Veb Verlag Technik, Berlin 1954

97 T J LEE
PhD thesis, University of Southampton 1967

98 M KAPLIT, G L SCHRENK, L W ZELBY
Adv. Energy Conv. 7 177 1967

99 E P GYFTOPOULOS, D STEINER
Report on 27th Ann. Conf. Phys. Elec. Cambridge MIT 1967 p169

100 R S MULLIKEN
J. Chem. Phys. 23 1833, 1841, 2338, 2343 1955

101 J C SLATER
'Introduction to chemical physics' McGraw-Hill, NY 1963

102 J D LEVINE, E P GYFTOPOULOS
Surface Science 1 171 1964

103 D STEINER
PhD thesis, MIT 1967

104 J W GADZUK
private communication

105 H E NEUSTADTER, R J BACIGALUPI
Surface Science 6 246 1967

106 H E NEUSTADTER, K P LUKE, T SHEAHAN
NASA report TN D-2431 1964

107 J W GADZUK, E N CARABATEAS
J. Appl. Phys. 36 357 1965

108 W A ZISMAN
Rev. Sci. Instr. 3 367 1932

109 LORD KELVIN
Phil. Mag. 46 82 1898

110 P A ANDERSON
Phys. Rev. 47 958 1935

111 E B HENSLEY
J. Appl. Phys. 32 301 1961

112 R A ARMSTRONG
Can. J. Phys. 44 1753 1966

113 I H KHAN, J P HOBSON, R A ARMSTRONG
Phys. Rev. 129 1513 1963

114 R J ZOLLWEG
Surface Science 2 409 1964

115 A EINSTEIN
Ann. d. Phys. 17 132 1905

116 R H FOWLER
Phys. Rev. 38 45 1931

117 R H FOWLER, L W NORDHEIM
Proc. Roy. Soc. A 119 173 1928

118 L W NORDHEIM
Proc. Roy. Soc. A 121 626 1928

119 E GUTH, C J MULLIN
Phys. Rev. 59 867 1941

120 D W JUENKER
Phys. Rev. 99 1155 1955

121 D W JUENKER
J. Appl. Phys. 28 1398 1957

122 Ya P ZINGERMAN, V A MOROZOVSKII
Sov. Phys. Solid state 3 88 1961

123 P A ANDERSON
Phys. Rev. 88 655 1952

124 B J HOPKINS, B J SMITH
J. Appl. Phys. 39 213 1968

125 C LEA, C H B MEE
J Appl. Phys. 39 5890 1968

126 A N HOLDEN
'Physical metallurgy of uranium' Addison-Wesley USA 1958

127 C W TUCKER
Trans. Am. Soc. Metals 42 762 1950

128 C W TUCKER
Science 112 448 1950

129 C W TUCKER
Acta Cryst. 4 425 1951

130 C W TUCKER
Acta Cryst. 5 395 1952

131 A S WILSON, R E RUNDLE
Acta Cryst. 2 126 1939

132 A N HOLDEN
Acta Cryst. 5 182 1952

133 P DUWEZ
J. Appl. Phys. 24 152 1953

134 S N CHATTERJEE
Acta Cryst. 11 679 1958

135 J DONOHUE
Acta Cryst. 14 327 1961

136 J C RIVIERE
UKAEA report AERE - R 3991 1962

137 L D KOLOMIETS
Sov. Phys. Cryst. 12 132 1967

138 W J DEISS
Comptes Rendus Acad. Sci. 256 671 1963

139 R J ACKERMAN, E G RAUH, R J THORN
J. Chem. Phys. 37 2693 1962

140 S DUSHMAN
Phys. Rev. 21 623 1923

141 S DUSHMAN, D DENNISON, N B REYNOLDS
Phys. Rev. 29 903 1927

142 H C RENTSCHLER
Trans. Am. Inst. Elec. Eng. 49 576 1930

143 O KLEIN, E LANGE
Z. Electrochem. 44 542 1938

144 W L HOLE, R W WRIGHT
Phys. Rev. 56 785 1939

145 E G RAUH, R J THORN
J. Chem. Phys. 31 1481 1959

146 R K FRY, A B CARDWELL
Phys. Rev. 125 471 1962

147 H C RENTSCHLER, D E HENRY
J. Opt. Soc. Am. 26 30 1936

148 J A BECKER
Solid State Phys. 7 379 1958

149 T W HICKMOTT
J. Chem. Phys. 32 810 1960

150 H C RENTSCHLER, D E HENRY, K O SMITH
Rev. Sci. Instr. 3 794 1932

151 G A HAAS, J T JENSEN
J. Appl. Phys. 34 3451 1963

152 B H BLOTT, B J HOPKINS
Brit. J. Appl. Phys. 16 1215 1965

153 C LEA, C H B MEE
Surface Science 8 417 1967

154 R A COLLINS, B H BLOTT
Surface Science 9 1 1968

155 R A COLLINS, B H BLOTT
Surface Science 13 401 1969

156 R A COLLINS
PhD thesis, University of Southampton 1968

157 E G RAUH
USAEG report ANL 5534 1956

158 G L MILLER
'Metallurgy of the rarer metals - zirconium' Butterworths, London 1957

159 C ZWIKKER
Physica Eindhoven 6 361 1926

160 J H deBOER, J D FAST
Rec. Trav. Chim. 55 459 1936

161 W G GULDEN, L A WOOTON
J. Electrochem. Soc. 93 223 1949

162 J FITZWILLIAM, A R KAUFMAN, C F SQUIRES
J. Chem. Phys. 9 678 1941

163 J D FAST
Foote-Prints 13 22 1940

164 D CUBICCIOTI
J. Am. Chem. Soc. 72 4138 1950

165 C ZWIKKER
Physik Z. 30 578 1929

166 A WAHL
Techn. rept. no.1 US Naval contract N6 our - 27010 NRO74-333 1951

167 D A WRIGHT
Proc. Inst. Elec. Eng. 100 part 3 125 1953

168 H MALAMUND, A KRUMBEIN
J. Appl. Phys. 25 591 1954

169 V N SHREDNIK
Bull. Nat. Acad. Sci. USSR Phys. series 22 592 1958

170 V N SHREDNIK
Sov. Phys. Solid State 1 1037 1959

171 B Ch DYUBUA, B N POPOV
Rad. Eng. Electronic Phys. 7 1454 1962

172 R A COLLINS, B H BLOTT
Surface Science 10 349 1968

173 Ya P ZINGERMAN, V A ISHCHUK
Sov. Phys. Solid State 6 904 1964

174 C LEA
PhD thesis, University of Southampton 1968

175 J A BECKER, E J BECKER, R G BRANDES
J. Appl. Phys. 32 411 1961

176 R M STERN
Appl. Phys. Lett. 5 218 1964

177 J C TRACY, J M BLAKELY
Surface Science 15 257 1969

178 R D YOUNG, H E CLARK
Appl. Phys. Lett. 9 265 1966

179 E W PLUMMER, T N RHODIN
Appl. Phys. Lett. 11 194 1967

180 M H NICHOLS
Phys. Rev. 57 297 1940

181 C HERRING, M H NICHOLS
Rev. Mod. Phys. 21 202 1949

182 E W MULLER
Z. Physik 120 261 1943

183 L APKER, E TAFT, J DICKEY
Phys. Rev. 73 46 1948

184 A A BROWN, L J NEELANDS, H E FARNSWORTH
J. Appl. Phys. 21 1 1950

185 J A BECKER
Bell Systems Tech. J. 30 907 1951

186 R H GOOD, E W MULLER
Handb. der Physik 21 176 1956

187 B G SMIRNOV, G N SHUPPE
Zh. Tekhn. Fiz. 22 973 1952

188 I S ANDREEV
Zh. Tekhn. Fiz. 22 1428 1952

189 M K WILKINSON
J Appl. Phys. 24 1203 1953

190 M DRECHSLER, E W MULLER
Z. Phys. 134 208 1953

191 W P DYKE, J K TROLAN, W W DOLAN, F J GRUNDHAUSER
J. Appl. Phys. 25 106 1954

192 G F SMITH
Phys. Rev. 94 295 1954

193 A R HUTSON
Phys. Rev. 98 889 1955

194 G F SMITH
Phys. Rev. 100 1115 1955

195 E W MULLER
J. Appl. Phys. 26 732 1955

196 J M HOUSTON
PhD thesis MIT 1955

197 G N SHUPPE, E P SYTAYA, R M KADYROV
Bull. Acad. Sciences USSR Phys. series 20 1035 1956

198 J EISINGER
J. Chem. Phys. 27 1206 1957

199 J EISINGER
J. Chem. Phys. 28 165 1958

200 J EISINGER
J. Chem. Phys. 29 1154 1958

201 F L HUGHES, H LEVINSTEIN, R KAPLAN
Phys. Rev. 113 1023 1959

202 H GIENAPP
Z. Angew. Phys. 12 254 1960

203 R L ANTHONY, G GARDNER, E A COOMES
Bull. Am. Phys. Soc. 6 422 1961

204 H M LOVE, G L DYER
Can. J. Phys. 40 1837 1962

205 E P SYTAYA, M I SMORODINOVA, N I IMANGULOVA
Sov. Phys. Solid State 4 750 1962

206 V M GAVRILYUK, V K MEDVEDEV
Sov. Phys. Solid State 4 1737 1963

207 I GOFMAN
Dokl. Akad. Nauk. Uzbek USSR 6 26 1962

208 R D YOUNG, E W MULLER
J. Appl. Phys. 33 91 1962

209 I GOFMAN
Sov. Phys. Solid State 4 4171 1963

210 F L REYNOLDS
J. Chem. Phys. 39 1107 1963

211 A van OOSTROM
Phys. Lett. 3 34 1963

212 D F STAFFORD, A H WEBER
J. Appl. Phys. 34 2667 1963

213 V M SULTANOV
Rad. Eng. Elec. Phys. 9 252 1964

214 D A GORODETSKII, A M KORNEV, Yu P MEL'NIK
Bull. Acad. Sci. USSR Phys. series 28 1241 1964

215 A A HOLSCHER
J. Chem. Phys. 41 579 1964

216 T OGURI
J. Phys. Soc. Japan 19 83 1964

217 J FINE, T E MADEY, M D SCHEER
Surface Science 3 227 1965

218 T A DELCHAR, G EHRLICH
J. Chem. Phys. 42 2686 1965

219 U V AZIZOV, G N SHUPPE
Sov. Phys. Solid State 7 1591 1966

220 O D PROTOPOPOV, E V MIKHEEVA, B N SHEINBERG, G N SHUPPE
Sov. Phys. Solid State 8 909 1966

221 V M GAVRILYUK, V K MEDVEDEV
Sov. Phys. Solid State 8 1439 1966

222 L D SCHMIDT, R GOMER
J. Chem. Phys. 45 1605 1966

223 B J HOPKINS, K R PENDER
Brit. J. Appl. Phys. 17 281 1966

224 B J HOPKINS, K R PENDER
Surface Science 5 155 1966

225 B J HOPKINS, K R PENDER
Surface Science 5 316 1966

226 H M LOVE, J R WILSON
Can. J. Phys. 45 225 1967

227 B J HOPKINS, S USAMI
Nuovo Cim. Suppl. 5 535 1967

228 T J LEE, B H BLOTT, B J HOPKINS
Appl. Phys. Lett. 11 361 1967

229 A P OVCHINNIKOV
Sov. Phys. Solid State 9 483 1967

230 V M GAVRILYUK, V K MEDVEDEV
Sov. Phys. Solid State 9 259 1967

231 A van OOSTROM
J. Chem. Phys. 47 761 1967

232 L W SWANSON, L C CROUSER
Phys. Rev. 163 622 1967

233 W ERMICH
Philips Res. Repts. Suppl. 3 1967

234 B J HOPKINS, K R PENDER, S USAMI
Fundermentals of gas-surface interactions, Academic Press NY 1967 p284

235 T E MADEY, J T YATES
Nuovo Cim. Suppl. 5 482 1967

236 L D SCHMIDT
J. Chem. Phys. 46 3830 1967

237 L W SWANSON, R W STRAYER
J. Chem. Phys. 48 2421 1968

238 B J SMITH
PhD thesis University of Southampton 1968

239 B J HOPKINS, S USAMI
Proc. Con. Struc. Chem. Solid Surfaces, Berkeley 1968

240 A E ABEY
J. Appl. Phys. 39 120 1968

241 B J HOPKINS, S USAMI
J. Appl. Phys. 39 3500 1968

242 M I SMORODINOVA, E P SYTAYA
Tashkent Univ. Sci. Trans. no. 221 123 1963

243 V M SULTANOV, G N SHUPPE
Izv. AN UzbSSR ser. fiz. mat. nauk, no. 4 53 1965

244 S DUSHMAN
'Scientific foundations of vacuum technique' Wiley, London 1962 p14

245 R T BAYARD, D ALPERT
Rev. Sci. Instr. 21 571 1950

246 J H SINGLETON
J. Vac. Sci. Tech. 4 103 1967

247 W B NOTTINGHAM
Rept. 7th Ann. Conf. Phys. Electr. MIT 1947

248 P A REDHEAD
J Vac. Sci. Tech 4 57 1967

249 A VENEMA, M BANDRINGA
Philips Tech. Rev. 20 145 1958

250 K ERENTS, G CARTER
Vacuum 15 573 1965

251 P H DAWSON, N R WHETTON
J. Vac. Sci. Tech. 4 482 1967

252 J H SINGLETON, W J LANGE
J. Vac. Sci. Tech. 2 93 1965

253 D ALPERT, R S BURITZ
J. Appl. Phys. 25 202 1954

254 S B NORNES, E E DONALDSON
J. Chem. Phys. 44 2968 1966

255 GEC - AEI (electronics)
pub. no. 2015 - 13 EdA 5MO468

256 G BERNARD, J C MERLIVAT, B SWINERS
Le Vide 123 207 1966

257 R CALDER, G LEWIS
Brit. J. Appl. Phys. 18 1459 1967

258 P DELLA PORTA, C PISANI
Le Vide 132 331 1967

259 E E HUBER
Appl. Phys. Lett. 8 169 1966

260 U R BANCE, R D CRAIG
Vacuum 16 647 1966

261 P A REDHEAD, E V KORNELSON, J P HOBSEN
Can. J. Phys. 40 1814 1962

262 A G JACKSON, T W HAAS
J. Vac. Sci. Tech. 4 42 1967

263 G M McCRACKEN
Vacuum 15 433 1965

264 W H KOHL
'Materials and techniques for electron tubes' Reinhold, NY 1960

265 B J HOPKINS, J C RIVIERE
Proc. Roy. Soc. 81 590 1963

266 R SCHEIDIGGER, G GALETTI
Brown Boveri Rev. 53 48 1966

267 J W FAUST
Surface Science 13 60 1969

268 W J M TEGART
'The electrolytic and chemical polishing of metals in research and industry' Pergamon, London 1956

269 E A WOOD
'Crystal orientation manual' Columbia Univ. Press NY 1963

270 M CAMP, S M A LECCHINI
Proc. Phys. Soc. 85 815 1965

271 E A HAAS, R E THOMAS
Surface Science 4 64 1966

272 D MENZEL
Surface Science 3 424 1965

273 J R MacDONALD, D E EDMONDSON
Proc. I. R. E. 49 453 1961

274 B H BLOTT, T J LEE
J. Sci. Instr. (J. Phys. E) 2 785 1969

275 E A FAULKNER, D W HARDING
J. Sci. Instr. 43 97 1966

276 J PRITCHARD
private communication

277 A G J van OOSTROM
Philips Res. Repts. Suppl. no. 1 1966

278 N J TAYLOR
Surface Science 2 544 1964

279 H D HAGSTRUM, C d'AMICO
J. Appl. Phys. 31 715 1960

280 J L ROBINS
Trans. Am. Vacuum Soc. 9 510 1962

281 L J RIGBY
Can. J. Phys. 43 1020 1965

282 J C RIVIERE
Brit. J. Appl. Phys. 15 1341 1964

283 J C RIVIERE
Nuovo Cim. Suppl. 5 466 1967

284 R A COLLINS, B H BLOTT
Surface Science 11 149 1968

285 P C WILMER
private communication

286 H C RENTSCHLER, D E HENRY
Trans. Electrochem. Soc. 87 289 1945

287 R W WYCOFF
'Crystal Structures' Interscience Pub. Inc. NY vol. 1 chapter 2 p27

288 W H ZACHARIASEN
Acta Crystall. 5 660 1952

289 V N SHREDNIK, E V SNEZHKO
Sov. Phys. Solid State 6 1173 1964

290 V B VORONIN
Sov. Phys. Solid State 9 1758 1968

291 J H POLLARD, W E DANFORTH
J. Appl. Phys. 39 4019 1968

292 J H POLLARD, W E DANFORTH
private communication

293 R L GERLACH, T N RHODIN
Surface Science 17 32 1969

294 F C FRANK, J H van der MERVE
Proc. Roy. Soc. A 198 205, 216 1949; 200 125 1949

295 J H van der MERVE
Proc. Phys. Soc. A 63 616 1950

296 J H van der MERVE
J. Appl. Phys. 34 117 1963

297 G I FINCH, A G QUARRELL
Proc. Roy. Soc. A 141 398 1933

298 G I FINCH, A G QUARRELL
Proc. Phys. Soc. (London) 46 148 1934

299 T N RHODIN
Disc. Faraday Soc. no. 5 216 1949

300 J P HIRTH, E M POUND
'Condensation and evaporation' Macmillan and Co. 1963
Progr. Materials Science 11 41 1963

301 D W PASHLEY, M J STOWELL, M H JACOBS, T J LAW
Phil. Mag. 10 127 1964

302 D W PASHLEY
Adv. Phys. 14 327 1965

303 G A BASSETT
'Condensation and evaporation of solids' Gordon and Breach NY 1964

304 T N RHODIN, D WALTON
'Metal surfaces' Am. Soc. Metals 1963 p259

305 J B HUDSON, J S SANDEJAS
J. Vac. Sci. Tech. 4 230 1967

306 R D GRETZ
Phys. Stat. Sol. 23 453 1967

307 J W MATTHEWS
Phil. Mag. 13 1207 1966

308 J W MATTHEWS, W A JESSER
Acta Met. 15 595 1967

309 W A JESSER, J W MATTHEWS
Phil. Mag. 17 461, 475, 595 1968

310 W M FRANKLIN, K R LAWLESS
'Fundamentals of gas-surface interactions' Academic Press NY 1967

311 A R L MOSS, B H BLOTT
Surface Science 17 240 1969

312 K L MOAZED, G M POUND
Trans. AIME 230 234 1964

313 R D GRETZ
PhD thesis Carnegie Institute of Technology 1963

314 A J MELMED
J. Chem. Phys. 38 1444 1963

315 L PAULING
'Nature of the chemical bond' Cornell Univ. Press,Ithaca NY 1960

316 A U MacRAE, K MULLER, J J LANDER, J MORRISON
Surface Science 14 465 1969; 15 483 1969

317 E A WOOD
J. Appl. Phys. 35 1306 1964

318 D L FEHRS, T J LEE, R E STICKNEY
Report IEEE conf. thermionic conversion, Framingham, Mass. USA 1968 p10

319 N J TAYLOR
J. Vac. Sci. Tech. 6 241 1969

320 D A GORODETSKII, Yu P MELNIK, A A YASKO
Sov. Phys. Uspekhi 12 649 1967

321 V M GAVRILYUK, A G NAUMOVETS, A G FEDORUS
Sov. Phys. JETP 24 899 1967

322 P J ESTRUP, J ANDERSON, W E DANFORTH
Appl. Phys. Lett. 7 122 1965

323 P J ESTRUP, J ANDERSON, W E DANFORTH
Surface Science 4 286 1966

324 P J ESTRUP, J ANDERSON
Surface Science 7 255 1967

325 A U MacRAE et al
Phys. Rev. Lett. 22 1048 1969

326 Ya P ZINGERMAN, V A ISHCHUK, V A MOROZOVSKII
Sov. Phys. Solid State 2 2030 1960

327 Ya P ZINGERMAN, V A ISHCHUK, V A MOROZOVSKII
Sov. Phys. Solid State 3 760 1961

328 Yu V ZUBENKO, I L SOKOL'SKAYA
Sov. Phys. Solid State 3 1133 1961

329 Ya P ZINGERMAN, V A ISHCHUK
Sov. Phys. Solid State 4 1618 1963

330 V N SHREDNIK
Rad. Eng. Elec. Phys. 5 10 1960

331 V N SHREDNIK
Sov Phys. Solid State 3 1268 1961

332 Yu S VEDULA, V M GAVRILYUK, V K MEDVEDEV
Sov. Phys. Solid State 4 1870 1963

333 E A TISHIN, B M TSAREV
Sov. Phys. Solid State 8 2547 1967

334 R B D WHITCUTT
PhD thesis, University of Southampton 1969

335 D O HAYWARD, B M W TRAPNELL
'Chemisorption' Butterworths, Washington USA 2nd edition 1964 p202

336 J C SLATER
'Quantum theory of molecules and solids' volume 2 McGraw-Hill NY 1965 p103

337 J E HUHEEY
J. Phys. Chem. 69 3284 1965

338 G KLOPMAN
J. Am. Chem. Soc. 86 4450 1964

339 J J BROEDER, L L van REIJEN, W M H SACHTLER, G G A SCHUIT
Z. Electrochem. 60 838 1956

340 J C P MIGNOLET
Bull. Soc. Chem. Belg. 65 837 1956

341 C W JOWETT, B J HOPKINS
Surface Science (in press)

342 D L FEHRS, R E STICKNEY
Surface Science (in press)

343 V M GOLDSCHMIDT
Chem. Ber. 60 1263 1927

344 D F KLEMPERER
J. Appl. Phys. 33 1532 1962

345 D L FEHRS, R E STICKNEY
Surface Science 8 267 1967

346 M J DUELL, R L MOSS
Trans. Farad. Soc. 61 2262 1965

347 B J HOPKINS, B J SMITH
J. Chem. Phys. 49 2136 1968

348 B McCARROLL
J. Appl. Phys. 40 1 1969

349 Ya P ZINGERMAN, V A ISHCHUK
Sov. Phys. Solid State 8 728 1966

350 R J HILL
Vacuum 11 260 1961

351 V N AGEEV, N I IONOV, Yu K USTINOV
Sov. Phys. Tech. Phys. 9 1581 1965

352 H IMAI, C KEMBALL
Proc. Roy. Soc. A 302 399 1968

353 Yu K USTINOV, N I IONOV
Sov. Phys. Tech. Phys. 12 1506 1968

354 J K WILMSHURST
J. Chem. Phys. 27 1129 1957

355 E W PLUMMER
PhD thesis, Cornell University 1968

356 G EHRLICH C F KIRK
J. Chem. Phys. 48 1465 1968

357 A H BOOTH
Can. J. Chem. 32 214 1954

358 O BEECK
Adv. in Catalysis 2 151 1950

359 D L FEHRS
PhD thesis, MIT 1968

360 T J LEE, B J HOPKINS, B H BLOTT
J. Appl. Phys. 40 3825 1969

361 E J R PROSEN, R G SACHS
Phys. Rev. 61 65 1942

362 J W SMITH
'Electric dipole moment' Butterworth, London 1955

363 first paper of reference 95

364 A R von HIPPEL
'Molecular science and engineering' Wiley, NY 1959 p148

365 W H BRATTAIN, J A BECKER
Phys. Rev. 43 428 1933

366 J C TRACY, J M BLAKELY
Surface Science 13 313 1969

367 reference 315 p403

368 C J SMITHELLS
'Metals reference book' volume 1 Butterworths Pub., London
4th ed. 1967 p224

369 J W GADZUK
NASA report TR - R283 May 1968

370 J W GADZUK
J. Chem. Phys. Sol. 30 2307 1969

371 R E WEBER, W T PERIA
J. Appl. Phys. 38 4355 1967

372 L A HARRIS
J. Appl. Phys. 39 1419 1968

373 J J CARROLL, A J MELMED
Surface Science 16 251 1969

374 G E HILL, J MARTINSSON
Chalmers Univ. of Technology, Department of Physics,
Gothenburg, Sweden
private communication (to be published)

375 P A REDHEAD, J P HOBSON, E V KORNELSEN
'The physical basis of ultrahigh vacuum' Chapman and Hall, London 1968 p145

376 B M SIEGEL, J F MENADUE
Surface Science 8 206 1967

377 E BAUER
Surface Science 7 351 1967

ALPHABETICAL AUTHOR INDEX

The reference number is given in parenthesis after the author and date, followed by the page(s) on which the reference appears

de Boer J H, Fast J D 1936 (160) 86
Bomke H 1934 (35) 7
Booth A H 1954 (357) 282
Böttcher C J F 1952 (85) 31
Brattain W H, Becker J A 1933 (365) 240
Broeder J J et al 1956 (339) 267, 268
Brown A A, Neelands L J, Farnsworth H E 1950 (184) 90
Calder R, Lewis G 1967 (257) 118
Camp M, Lecchini S M A 1965 (270) 142
Carroll J J, Melmed A J 1969 (373) 259
Chatterjee S N 1958 (134) 77
Chittum J F 1934 (36) 7
Collins R A 1968 (156) 81, 85, 88, 210, 218, 219, 223, 273, 274
Collins R A, Blott B H 1968 (154) 81, 85, 87
Collins R A, Blott B H 1968 (172) 86, 87
Collins R A, Blott B H 1968 (284) 181
Collins R A, Blott B H 1969 (155) 81, 85, 183
Coulson C A 1939 (78) 28
Coulson C A 1942 (57) 11
Coulson C A 1961 (53) 10, 19
Cubiccioti D 1950 (164) 86
Culver R V, Tompkins F C 1959 (87) 32, 95, 127
Dawson P H, Whetton N R 1967 (251) 113
Deiss W 1963 (138) 78
Delchar T A, Ehrlich G 1965 (218) 92, 267, 274
Della Porta P, Pisani C 1967 (258) 119
Dobretsov L N 1954 (96) 41
Donohue J 1961 (135) 77
Dowden D A 1948 (80) 30
Drechsler M, Müller E W 1953 (190) 90
Drechsler M, Nichols J F 1967 (75) 26
Duell M J, Moss R L 1965 (346) 270
Dunn P D, Myatt J, Rice C 1965 (2) 1
Dushman S 1928 (140) 79, 87
Dushman S 1962 (244) 95
Dushman S, Dennison D, Reynolds N B 1927 (141) 79, 87
Duwez P 1953 (133) 76

Dyke W P et al 1954 (191) 90
Dyubua B Ch, Popov B N 1962 (171) 87
Ehrlich G 1959 (69) 21
Ehrlich G, Kirk C F 1968 (356) 277
Einstein A 1905 (115) 69
Eisinger J 1957 (198) 91
Eisinger J 1958 (199) 91
Eisinger J 1958 (200) 91
Erents K, Carter G 1965 (250) 110
Ermich W 1967 (233) 93
Estrup P J, Anderson J 1967 (324) 215
Estrup P J, Anderson J, Danforth W E 1965 (322) 215
Estrup P J, Anderson J, Danforth W E 1966 (323) 215
Fast J D 1940 (163) 86
Faulkner E A, Harding D W 1966 (275) 169
Faust J W 1969 (267) 133
Fehrs D L 1968 (359) 232, 234
Fehrs D L, Lee T J, Stickney R E 1968 (318) 213
Fehrs D L, Stickney R E 1967 (345) 270
Fehrs D L, Stickney R E t b p (342) 267, 272, 273, 274, 277, 280
Ferreira R 1964 (79) 28, 54
Finch G I, Quarrell A G 1933 (297) 210
Finch G I, Quarrell A G 1934 (298) 210
Fine J, Madey T E, Scheer M D 1965 (217) 64, 92
Fitzwilliam J, Kaufman A R, Squires C F 1941 (162) 86
Fock V 1930 (84) 30
Fomenko V S 1966 (63) 14, 16, 17
Fowler R H 1931 (116) 69
Fowler R H, Nordheim L W 1928 (117) 69
Fry R K, Cardwell A B 1962 (146) 79
Frank F C, van der Merve J H 1949 (294) 210
Franklin W M, Lawless K R 1967 (310) 210
Gadzuk J W 1967 (90) 33, 36
Gadzuk J W 1968 (369) 257
Gadzuk J W 1969 (370) 257
Gadzuk J W 1969 (104) 36, 59
Gadzuk J W, Carabateus E N 1965 (107) 44

Gavrilyuk V M, Medvedev V K 1963 (206) 91
Gavrilyuk V M, Medvedev V K 1966 (221) 92, 212, 214, 222
Gavrilyuk V M, Medvedev V K 1967 (230) 92, 208, 209
Gavrilyuk V M, Naumovets A G, Fedorus A G 1967 (321) 214
GEC-AEI 1968 (255) 118
Gerlach R L, Rhodin T N 1969 (293) 213
Gienapp H 1960 (202) 91
Gofman I 1962 (207) 91
Gofman I 1963 (209) 91
Goldschmidt 1927 (343) 269
Gombas P 1946 (39) 7
Gomer R, Swanson L W 1963 (89) 33, 36
Good R H, Muller E W 1956 (186) 223
Gordy W 1946 (59) 11
Gordy W, Thomas W 1956 (44) 7, 12, 13, 16, 17
Gorodetskii D A, Kornev A M, Mel'nik Yu P 1964 (214) 91
Gorodetskii D A, Mel'nik Yu P, Yasko A A 1967 (320) 214
Gretz R D 1963 (313) 210
Gretz R D 1967 (306) 210
Gulden W G, Wooton L A 1949 (161) 86
Gurney R W 1935 (88) 32
Guth E, Mullin C J 1941 (119) 73
Gyftopoulos E P, Hatsopoulos G N 1968 (66) 18
Gyftopoulos E P, Levine J D 1962 (65) 14, 36, 44, 59, 95, 208, 228, 234, 237, 263
Gyftopoulos E P, Steiner D 1967 (99) 50, 59, 208
Haas G A, Jensen J T 1963 (151) 81, 82
Haas G A, Thomas R E 1966 (271) 142
Hagstrum H D, d'Amico C 1960 (279) 124, 127
Haïssinsky M 1946 (49) 9
Harris L A 1968 (372) 259
Hartree D R 1928 (83) 30
Hayward D O, Trapnell B M W 1964 (335) 261
Heitler W, London F 1927 (73) 26
Hellman H, Kassatotschkin W 1936 (25) 5, 18
Hensley E B 1961 (111) 66
Herman I G, Wagner P S 1951 (42) 67

Herring C, Nichols M H 1949 (10) (181) 3, 64, 71, 72, 74, 90
Hickmott T W 1960 (149) 80, 283
Hill G E, Martinsson J t b p (374) 259
Hill R J 1961 (350) 273
Hinze J, Whitehead M A, Jaffé H H 1963 (61) 12
von Hippel A R 1959 (364) 239
Hirth J P, Pound E M 1963 (300) 210
Holden A N 1952 (132) 76
Holden A N 1958 (126) 76
Hole W L, Wright R W 1939 (144) 79
Holscher A A 1964 (215) 91
Hopkins B J, Pender K R 1966 (223) 92
Hopkins B J, Pender K R 1966 (224) 92, 153
Hopkins B J, Pender K R 1966 (225) 92, 180, 181, 267, 274, 282
Hopkins B J, Pender K R, Usami S 1967 (234) 93, 267, 275
Hopkins B J, Rivière J C 1963 (265) 127, 140
Hopkins B J, Smith B J 1968 (124) 75, 93, 208, 209
Hopkins B J, Smith B J 1968 (347) 241, 272, 274
Hopkins B J, Usami S 1967 (227) 92, 182, 183
Hopkins B J, Usami S 1968 (239) 93
Hopkins B J, Usami S 1968 (241) 93, 275
Houston J M 1955 (196) 90
Houston J M, Webster H F 1962 (1) 1
Huber E E 1966 (259) 119
Hudson J B, Sandejos J S 1967 (305) 210
Hughes F L, Levinstein H, Kaplan R 1959 (201) 91
Huheey J E 1965 (337) 263
Hutson A R 1955 (193) 90
Imai H, Kemball C 1968 (352) 273
Jackson A G, Haas T W 1967 (262) 121
Jessa W A, Matthews J W 1968 (309) 210
Jowett C W 1969 (15) 6, 93, 273, 274, 275
Jowett C W, Hopkins B J t b p (341) 267, 270, 272, 274
Juenker D W 1955 (120) 73
Juenker D W 1957 (121) 73
Juretschke H J 1953 (27) 5, 18
Kaplit M, Schrenk G L, Zelby L W 1967 (98) 48

Kelvin, Lord 1898 (109) 64
Khan I H, Hobson J P, Armstrong R A 1963 (113) 68
Kittel C 1966 (8) (9) 3
Klein O, Lange E 1938 (143) 87, 143
Klemperer D F 1962 (344) 270
Klopman G 1964 (338) 263
Kohl W H 1960 (264) 123
Kolomiets L D 1967 (137) 78
Langmuir I 1916 (33) 7
Langmuir I 1933 (93) 37
Lea C 1968 (174) 88, 93, 142
Lea C, Mee C H B 1967 (153) 81, 85
Lea C, Mee C H B 1968 (125) 75, 218, 235, 241
Lee T J 1967 (97) 47, 57, 58, 231, 232, 235, 240, 241, 256, 272, 274
Lee T J, Blott B H, Hopkins B J 1967 (228) 92, 208, 209
Lee T J, Hopkins B H, Blott B H 1969 (360) 234
Lennard-Jones J E 1932 (71) 22
Levine J D, Gyftopoulos E P 1964 (102) 56, 212, 230, 231, 237, 243
London F 1930 (70) 22
Loucks T L, Cutler P H 1964 (28) 5, 18
Love H M, Dyer G L 1962 (204) 91
Love H M, Wilson J R 1967 (226) 92
McCarroll B 1969 (348) 272
McCracken G M 1965 (263) 121
MacDonald J R, Barlow C A 1963-1966 (95) 38, 49, 59, 237
MacDonald J R, Edmondson D E 1961 (273) 273
MacRae A U, Müller K, Lander J J, Morrison J 1969 (316) 213
MacRae A U, Müller K, Lander J J, Morrison J 1969 (325) 213
Madey T E, Yates J T 1967 (235) 93
Malamund H, Krumbein A 1954 (168) 168
Malone J G 1933 (54) 10, 268
Matthews J W 1966 (307) 210
Matthews J W, Jessa W A 1967 (308) 210
Melmed A J 1963 (314) 210
Menzel D 1965 (272) 153
van der Merve J H 1950 (295) 210

van der Merve J H 1963 (296) 210
Michaelson H B 1950 (32) 7, 13, 14, 16, 17
Mie G 1908 (76) 26
Mignolet J C P 1956 (340) 267, 268
Miller G L 1957 (158) 85
Moazed K L, Pound G M 1964 (312) 210
Morse P M 1929 (74) 26
Moss A R L, Blott B H 1969 (311) 210, 212, 216
Müller E W 1943 (182) 90
Müller E W 1955 (195) 90
Müller A, Drechsler M 1968 (17) 5
Mulliken R S 1934, 1935, 1949 (51) 10
Mulliken R S 1935 (52) 10
Mulliken R S 1952 (77) 28
Mulliken R S 1955 (100) 51
Neustadter H E, Bacigalupi R J 1967 (105) 61, 224
Neustadter H E, Luke K P, Sheahan T 1964 (106) 62
Nichols M H 1940 (180) 90, 94
Nordheim L W 1928 (118) 69
Nornes S B, Donaldson E E 1966 (254) 116
Nottingham W B 1947 (247) 96
Oguri T 1964 (216) 92
Oldekop W, Sauter F 1954 (21) 5, 18
van Oostrom A G J 1963 (211) 91
van Oostrom A G J 1967 (231) 92
van Oostrom A G J 1966 (277) 174
Ovchinnikov A P 1967 (229) 92, 208, 209
Palyukh B M, Sivers L L 1969 (64) 14, 16
Pashley D W, Stowell M J, Jacobs M H, Law T J 1964 (301) 210
Pashley D W 1965 (302) 210
Pauling L 1947, 1949 (68) 19, 30, 228
Pauling L 1960 (47) (315) (367) 8, 212, 232, 243, 269, 274, 275
Pauling L, Sherman J 1937 (48) 9, 56
Plummer E W 1968 (355) 277
Plummer E W, Rhodin T N 1967 (179) 88
Plummer E W, Rhodin T N 1968 (82) 30
Pollard J H, Danforth W E 1968 (291) 210, 214

Pollard J H, Danforth W E 1969 (292) 212, 214, 215
Pritchard H O, Skinner H A 1955 (50) 9, 10, 12, 15, 16, 17
Pritchard J 1969 (276) 172
Prosen E J R, Sachs R G 1942 (361) 237
Protopopov O D, Mikheeva E V, Sheinberg B N, Shuppe G N 1966 (220) 92, 263
Rasor N S, Warner C 1964 (91) 36, 40, 59, 232
Rauh E G 1956 (157) 82
Rauh E G, Thorn R J 1959 (145) 79, 81, 82
Redhead P A 1967 (248) 96
Redhead P A, Hobson J P, Kornelsen E V 1968 (375) 259
Redhead P A, Kornelsen E V, Hobson J P 1962 (261) 121
Rentschler H C 1930 (142) 79
Rentschler H C, Henry D E 1936 (147) 80
Rentschler H C, Henry D E 1945 (286) 199
Rentschler H C, Henry D E, Smith K O 1932 (150) 81, 82, 87
Reynolds F L 1963 (210) 91
Rhodin T N 1949 (299) 210
Rhodin T N, Walton D 1963 (304) 210
Rigby L J 1965 (281) 182
Rittner E S 1951 (56) 11
Rivière J C 1962 (6) 1, 79, 81, 82, 178, 183
Rivière J C 1962 (136) 77, 78
Rivière J C 1964 (282) 182
Rivière J C 1967 (31) 7, 14, 16, 17, 64, 127
Rivière J C 1967 (283) 131
Robins J L 1962 (280) 182
Rother F, Bomke H 1933 (34) 7
Sachs R G, Dexter D L 1950 (26) 18
Sachtler W M H 1955 (43) 7
Sanderson R T 1960 (62) 13
Scheidigger R, Galetti G 1966 (266) 127
Schmidt L D 1967 (236) 93
Schmidt L D, Gomer R 1966 (222) 92
Seitz F 1940 (23) 5, 18
Shrednik V N 1958 (169) 86, 87, 217
Shrednik V N 1959 (170) 86, 87
Shrednik V N 1960 (330) 217

Shrednik V N 1961 (331) 217
Shrednik V N, Snezhko E V 1964 (289) 209
Shuppe G N, Sytaya E P, Kadyrov R M 1956 (197) 90
Siegel B M, Menadue J F 1967 (376) 259
Singleton J H 1967 (246) 96
Singleton J H, Lange W J 1965 (252) 115
Slater J C 1930 (60) 12
Slater J C 1963 (101) 52, 260
Slater J C 1965 (336) 237, 263
Smirnov B G, Shuppe G N 1952 (187) 90
Smith B J 1968 (238) 93, 235, 240, 241
Smith G F 1954 (192) 90, 94
Smith G F 1955 (194) 90, 94
Smith J W 1955 (58) (362) 11, 237
Smithells C J 1967 (368) 243
Smoluchowski R 1941 (13) 4, 217
Smorodinova M I, Sytaya E P 1963 (242) 94
Stafford D F, Weber A H 1963 (212) 91
Steiner D 1967 (103) 59, 260, 261, 278
Steiner D, Gyftopoulos E P 1967 (18) 5, 6, 14, 18, 89, 93, 173, 267, 275
Stern R M 1964 (176) 88, 124
Stranski I N, Suhrman R 1947 (14) 5, 6
Sultanov V M 1964 (213) 91, 94
Sultanov V M, Shuppe G N 1965 (243) 94
Swanson L W, Crouser L C 1967 (232) 93
Swanson L W, Strayer R W 1968 (237) 93, 212, 213
Sytaya E P, Smorodinova M I, Imangulova M I 1962 (205) 91, 94
Taylor J B, Langmuir I 1933 (86) 32, 37, 232, 240
Taylor N J 1964 (278) 124
Taylor N J 1969 (319) 213, 259
Tegart W J M 1956 (268) 133
Tishin E A, Tsarev B M 1967 (333) 217
Topping J 1927 (94) 37
Tracy J C, Blakely J M 1969 (366) 88
Tracy J C, Blakely J M 1969 (177) 274
Tucker C W 1950 (127) 76
Tucker C W 1950 (128) 76
Tucker C W 1951 (129) 76

Tucker C W 1952 (130) 76
Ustinov Yu K, Ionov N I 1968 (353) 273
Utsugi H, Gomer R 1962 (92) 36
Varley J H O 1960 (46) 7
Vasenin R M 1958 (45) 7
Vedula Yu S, Gavrilyuk V M, Medvedev V K 1963 (332) 217
Venema A, Bandringa M 1958 (249) 101
Voronin V B 1968 (290) 208, 209
Wahl A 1951 (166) 87, 199
Weber R E, Peria W T 1967 (371) 259
Wilmshurst J K 1957 (354) 275
Whitcutt R B D 1969 (334) 219
Wigner E 1934 (24) 5, 18
Wigner E, Bardeen J 1935 (20) 5, 7, 18
Wigner E, Seitz F 1934 (19) 5, 18, 31
Wilkinson M K 1953 (189) 90
Williams C B 1969 (16) 6, 93, 273, 274, 275
Wilmer P C 1969 (285) 174
Wilson A S, Rundle R E 1939 (131) 76
Wolf E, Haug W 1968 (3) 1
Wood E A 1963 (269) 141
Wood E A 1964 (317) 213
Wright D A 1953 (167) 87
Wyckoff R W (287) 224
Young R D, Clark H E 1966 (178) 88, 92
Young R D, Müller E W 1962 (208) 91
Zachariasen W H 1952 (288) 224, 237
Ziman J M 1964 (29) 5, 18
Zingerman Ya P, Ishchuk V A 1963 (329) 217
Zingerman Ya P, Ishchuk V A 1964 (173) 88, 113
Zingerman Ya P, Ishchuk V A 1966 (349) 273
Zingerman Ya P, Ishchuk V A, Morozovskii V A 1960 (326) 217, 222
Zingerman Ya P, Ishchuk V A, Morozovskii V A 1961 (327) 217, 222
Zingerman Ya P, Morozovskii V A 1961 (122) 74
Zisman W A 1932 (108) 64, 71, 154
Zollweg R J 1964 (114) 68
Zubenko Yu V, Sokol'skaya I L 1961 (328) 217
Zwikker C 1926 (159) 85
Zwikker C 1929 (165) 87